The Advanced Virgo Gravitational wave detector : Study of the optical design and development of the mirrors

Romain Bonnand

N°d'ordre: 147-2012 Année 2012

THÈSE de l'UNIVERSITÉ DE LYON

Délivrée par

Université Claude Bernard Lyon 1

Ecole Doctorale 52: Physique et Astrophysique

DIPLOME DE DOCTORAT

(arrêté du 7 août 2006)

Physique: champs, particules, matières

Thèse soutenue publiquement

le 27 · 09 · 2012

au Laboratoire des Matériaux Avancés (LMA)

The Advanced Virgo Gravitational Wave Detector: Study of the optical design and development of the mirrors.

Romain BONNAND

Thèse dirigée par M. Raffaele FLAMINIO et M. Laurent PINARD

Jury:			
	M.	Jean Claude PLÉNET,	Président
	Mme.	Edwige TOURNEFIER,	Rapporteur
	M.	Fabian ZOMER,	Rapporteur
	M.	Francesco FIDECARO,	Examinateur
	M.	André RINCHET,	Examinateur
	M.	Raffaele FLAMINIO,	Directeur de thèse
	M.	Laurent PINARD,	Directeur de thèse

UNIVERSITE CLAUDE BERNARD - LYON 1

Président de l'Université	**M. François-Noël GILLY**
Vice-président du Conseil d'Administration	M. le Professeur Hamda BEN HADID
Vice-président du Conseil des Etudes et de la Vie Universitaire	M. le Professeur Philippe LALLE
Vice-président du Conseil Scientifique	M. le Professeur Germain GILLET
Secrétaire Général	M. Alain HELLEU

COMPOSANTES SANTE

Faculté de Médecine Lyon Est Claude Bernard	Directeur : M. le Professeur J. ETIENNE
Faculté de Médecine et de Maeutique Lyon Sud - Charles Mérieux	Administrateur provisoire : M. le Professeur G. KIRKORIAN
HUFR dOdontologie	Directeur : M. le Professeur D. BOURGEOIS
Institut des Sciences Pharmaceutiques et Biologiques	Directeur : Mme la Professeure C. VINCIGUERRA.
Institut des Sciences et Techniques de la Réadaptation	Directeur : M. le Professeur Y. MATILLON
Département de formation et Centre de Recherche en Biologie Humaine	Directeur : M. le Professeur P. FARGE

COMPOSANTES ET DEPARTEMENTS DE SCIENCES ET TECHNOLOGIE

Faculté des Sciences et Technologies	Directeur : M. le Professeur F. De MARCHI
Département Biologie	Directeur : M. le Professeur F. FLEURY
Département Chimie Biochimie	Directeur : Mme le Professeur H. PARROT
Département GEP	Directeur : M. N. SIAUVE
Département Informatique	Directeur : M. le Professeur S. AKKOUCHE
Département Mathématiques	Directeur : M. le Professeur A. GOLDMAN
Département Mécanique	Directeur : M. le Professeur H. BEN HADID
Département Physique	Directeur : Mme S. FLECK
Département Sciences de la Terre	Directeur : Mme la Professeure I. DANIEL
UFR Sciences et Techniques des Activités Physiques et Sportives	Directeur : M. C. COLLIGNON
Observatoire de Lyon	Directeur : M. B. GUIDERDONI
Polytech Lyon	Directeur : M. P. FOURNIER
Ecole Supérieure de Chimie Physique Electronique	Directeur : M. G. PIGNAULT
Institut Universitaire de Technologie de Lyon 1	Directeur : M. C. VITON
Institut Universitaire de Formation des Matres	Directeur : M. R. BERNARD
Institut de Science Financière et d'Assurances	Directeur : Mme la Professeure V. MAUME-DESCHAMPS

À mes parents, à mes grand-parents,
À ma soeur, à mon frère,
À mes ami-e-s,

"L'humour est une affirmation de la dignité, une déclaration de la supériorité de l'homme face à ce qui lui arrive."
La promesse de l'aube, Romain Gary.

Le détecteur d'ondes gravitationnelles Advanced Virgo : Etude de la configuration optique et développement des miroirs.

Résumé français : Les ondes gravitationnelles ont été prédites par Einstein dans sa théorie de la Relativité Générale. Elles sont des perturbations de l'espace-temps que lon essaie de mettre en évidence par interférométrie laser. Plus précisément les détecteurs sont des interféromètres de Michelson de plusieurs km de long combinés avec des cavités Fabry-Perot afin daugmenter la sensibilité de linstrument. La première génération de détecteurs (Virgo, LIGO, GEO) n'a pas permis d'obtenir une détection directe malgré plusieurs phases d'observations en coïncidence à la sensibilité prévue. Une seconde génération de détecteurs est actuellement en préparation avec notamment le projet européen Advanced Virgo. Ce détecteur devrait avoir une sensibilité améliorée d'un ordre de grandeur par rapport à linterféromètre Virgo. Les miroirs de l'interféromètre jouent un rôle primordial dans la sensibilité d'Advanced Virgo puisque celle-ci est limitée à dans les fréquences médianes par le bruit thermique des miroirs et aux hautes fréquences par la quantité de photons que lon arrive à collecter dans les cavités de linterféromètre. La haute puissance contenue dans les cavités Fabry-Perot induit des effets de lentille thermique importants. Cette thèse s'intéresse dans un premier temps aux effets de lentille thermique dans linterféromètre pour différentes configurations optiques. Par la suite, nous nous intéresserons aux miroirs qui composent les cavités Fabry-Perot depuis la définition des besoins en termes de planéité à la réalisation de cette planéité et à sa mesure. La planéité de ces miroirs doit être sub-nanométrique de faon à limiter les pertes optiques dans les cavités Fabry-Perot et ainsi réduire les effets du bruit de photons et de la lumière diffusée. Nous verrons la réalisation de la correction de la planéité des substrats par la technique dite du traitement correctif. Nous étudierons aussi l'uniformité du dépôt des couches minces diélectriques nécessaires à l'obtention de surface hautement réfléchissante avec en particulier l'étude du mouvement planétaire des substrats dans la machine de dépôts.

Mots Clés : ondes gravitationnelles, interférométrie, Advanced Virgo, couches minces, cavité Fabry-Perot, traitement correctif, simulation, métrologie.

The Advanced Virgo Gravitational wave detector: Study of the optical design and development of the mirrors.

Abstract: Gravitational waves have been predicted by Einstein in his General Relativity theory. They are perturbation of the space-time metric and we try to reveal them by laser interferometry. More precisely, gravitational wave detectors are km long Michelson interferometers combined with Fabry-Perot cavities. The network of first generation detectors (Virgo, LIGO, GEO) did not permit a direct detection after several observational runs in coincidence at the nominal sensitivity. A second generation of detectors is in preparation with in particular the European project Advanced Virgo. This detector should have a sensitivity increased by an order of magnitude compared to Virgo. The interferometer mirrors play a crucial role in the Advanced Virgo sensitivity as it is limited by the mirror thermal noise in the mid-frequency region and by the amount of photons collected in the interferometer cavities at high frequencies. The high power circulating in the Fabry-Perot cavities induces important thermal lensing effect. This thesis is interested first in the thermal lensing effect in the interferometer for different optical configurations. Then we are interested in the mirrors composing the Fabry-Perot arm cavity from the calculation of the requirements in terms of flatness to the realization of the mirrors flatness and its measurement. The mirror flatness should be sub-nanometric in order to limit the optical losses in the Fabry-Perot cavities to reduce the effect of the shot noise and of the diffused light. We will see the correction of the substrates flatness by the so-called corrective coating technique. Finally, we study the uniformity of the dielectric multilayer coating deposition necessary to obtained high-reflective mirrors. We study in particular the planetary motion of the substrates in the coating machine.

Key words: gravitational waves, interferometry, Advanced Virgo, thin films, Fabry-Perot cavity, corrective coating, simulation, metrology.

INTITULE ET ADRESSE DE L'U.F.R. OU DU LABORATOIRE :

Laboratoire des Matériaux Avancés (LMA), USR 3264.

7 avenue Pierre de Coubertin

69622 Villeurbanne Cedex

Remerciements

Je tiens tout d'abord à remercier M. Flaminio, directeur du Laboratoire des Matériaux Avancés qui a dirigé cette thèse, ces conseils mon été précieux dans l'élaboration de celle-ci. Je tiens aussi à remercier Laurent Pinard mon co-directeur de thèse. Je le remercie pour ses conseils qui m'ont accompagnés tout au long de cette thèse et pour sa sympathie.

Je remercie Mme Edwige Tournefier (LAPP, Annecy-le-vieux) et M. Fabian Zomer (LAL Orsay, Université Paris Sud 11) d'avoir eu la gentillesse d'accepter la tâche de rapporteur pour cette thèse. Merci aussi à M. Francesco Fidecaro (Università di Pisa) et M. André Rinchet (Sagem) pour avoir acceptés de faire parti du jury de thèse. Enfin, je remercie M. Jean-Claude Plénet (LPMCN, Université Claude Bernard Lyon 1) pour avoir bien voulu présider mon jury de thèe.

Je tiens ensuite à remercier mes collègues de bureaux Bernard et Janyce. C'était un véritable plaisir de partager ce bureau avec vous. Je ne remercierai jamais assez Janyce pour m'avoir fait sentir à l'aise dès mon arrivé et pour m'avoir soutenue dans les moments difficiles. Ton rire et ton sourire nous ont manqués après ton départ. Merci à Bernard aussi pour l'accueil dans le bureau, j'ai apprécié les discussions toujours franches et parfois un peu mouvementées quelle soit d'ordre professionnelle ou non. Travailler avec toi sur le traitement correctif a été un véritable plaisir.

Un merci aussi à toute celles et tous ceux que j'ai pu croiser au laboratoire: À Massimo (Galimberti) pour tout ce que tu m'a appris sur les simulations FFT notamment et pour la patience dont tu as su faire preuve. Nos échanges ont été indispensables pour moi. À Jérôme pour ta bonne humeur, ton humour et ta disponibilité, merci d'avoir rigolé à mes blagues. Merci aussi pour tes nombreux conseils "simulation" et lors de la rédaction de cette thèse. À Nazario pour les discussions boulot, foot ou autres toujours intéressantes. À Benoit pour ne m'avoir pas trop chambrés lors des défaites des verts dans les derbys et pour le travail effectué ensemble. À Danièle pour avoir supportée et parfois rigolée à mes blagues pas toujours drôles lors de mes venues dans le bureau du fond . Merci aussi pour la chaise. À Massimo (Granata), je suis content que tu soit arrivé au labo et que tu ait intégré le groupe midiset. Merci pour les vacances romaines, je ne les oublierai pas...

Enfin un merci général à Christophe, Renée, Willy, Jean-Luc (l'homme de la salle blanche), Ilyass, Nicolas, Quentin, Yvan, Émeline, Guillaume, Vincent (toujours prêt à chambrer) et Geppo (un nouveau rire au labo). Un mot aussi pour les stagiaires qui se sont succédés au Labo, Kévin, Salim, Cécile, Alix et Rafael ("tu tombes bien").

Un merci aussi à toutes les personnes de la collaboration Virgo et en particulier au personnel d'EGO pour leur gentillesse à mon égard et pour m'avoir donné envie de rejoindre la quête des ondes gravitationnelles.

Ces remerciements ne seraient pas complets sans évoquer ceux qui m'ont accompagnés durant cette thèse ou avant. Tout d'abord j'aimerais remercier mes parents, je leur dois beaucoup et je les remercie pour tout du fond du coeur. Merci à ma soeur Jasmine et à mon frère Mathieu qui sont toujours sources d'inspirations. Je suis heureux d'être votre petit frère. Merci à Justine pour les soirées toujours sympa, bon courage pour la fin de ta thèse.

Je remercie aussi mes oncles, mes tantes et mes cousins dont j'apprécie toujours la compagnie. Merci à Maxime en particulier. Une pensée aussi pour les petits Gourdin, je vous souhaite le meilleur. Enfin, un mot pour mes grands parents, je vous embrasse fort.

Merci à tout les copains midiset (comprend qui peut). Je n'oublierai pas tout ces repas de midi et les thés à la menthe à CPE. Je n'oublierai pas non plus les discussions enflammées, souvent incongrues et les réflexions toujours poussées à fond quelque soit le sujet...

Un grand merci tout d'abord aux historiques:

À David pour se poser toujours des tonnes de questions et pour être toujours là que ce soit pour une manif, un concert ou juste une bière. T'es un sacré keupin!

À papa Sam pour les "connways" et tout le reste. J'aurais jamais passé autant de temps sur un quai sans prendre de train... C'était un vrai plaisir de passer ces trois années avec toi.

À Arnaud "le blond" pour "être drôle" et pour ne pas savoir s'arrêter. On se sera bien marré quand même et j'éspère qu'on continuera encore...

À Yoan pour les soirées mémorables passées ensemble et pour avoir été là dans les moments difficiles.

Au reste de la bande midiset: Clément "binbin" (pour les soires fléchettes-mojito), Lucas, Dimitri (fais gaffe quand même), Imane (merci pour les pauses orangina), Massimo ("ascolta il cretino"), José (la macchina grande), Max (ah les JRJC...), Julien, Marie-Anne, Romaing, Claire, Marion, Ludo, Simon, Caroline (ma porte-bonheur), Audrey, Alexia. Merci pour les pétanques, les barbeuks, les apéros au toï toï ou au red-house et pour tout le reste... Vous êtes bien cool!

Une pensée aussi pour celles qui ont accompagnées (un petit peu) mes années de thèse, particulièrement Anaïs et Céline.

Une bise à Lucie, la meilleure des féministes (après ma soeur quand même), je te souhaite plein de bonheur avec ton petit bout de choux, il aura une super maman à n'en pas douter.

Merci à Anna, c'était toujours un plaisir de partager un café, une bière ou un ciné avec toi.

Merci aux copains de sup'recherche, Fabien ("chef"), Éric (Allez Sainté), Alexia et les petits jeunes Olivier et Arthur ("chef 2"), j'ai pas été très actif mais c'était toujours cool de vous voir en manifs, en réunion ou autour d'une bière.

Un merci enfin à cell-eux croisés ici ou là et qui n'entre dans aucun des groupes cités: Nano, Julien, Marie, Camille, Éric et tout les chimistes sympa, les stéphanois (Alexis, Clément, etc..), les ripagériens et tous les autres...

Merci à tout les rades où j'ai trainé mes guêtres: le toï toï et sa terasse, le connways, le red-house, le James Joyce, le bec de jazz, le métronome et autres lieux de vie lyonnais. Un merci aussi à tout les lieux de cultures lyonnais, ripagériens (vive ERL), stéphanois ou burgiens. Que vive les petits cinés et toutes les salles de concert qu'il passe du rock, du rap, du dub-step ou du punk...

Enfin je terminerai sur ces mots une fois prononcés:

Punk une fois, punk toujours!
Vive Midiset!

Contents

Introduction

In 1916, Einstein published its General Relativity theory in which he predicts the existence of gravitational waves and describes them as a ripple in the space-time metric. They are emitted by accelerating massive bodies and travel at the speed of light. So far the only evidence to the existence of gravitational radiations is indirect. It is due to the discovery of the binary pulsar PSR1916+13 by Taylor and Hulse in 1974 and the observation of the decrease of its orbital period which is in agreement with the emission of gravitational waves as predicted by the General Relativity theory. Gravitational waves coming from nearby astrophysical sources are expected to be detectable on earth but a direct detection is still missing.

The strain amplitude of gravitational waves is very weak because of their very weak interaction with matter. The differential nature of the space-time ripple due to the gravitational radiation can be detectable by laser interferometry. The principle of the gravitational waves detection is based on a Michelson interferometer with suspended mirrors. In the Michelson interferometer two beams propagate orthogonally in two orthogonal arms and the passage of a gravitational waves will induce a contraction and relaxation of the arms. This variation in the arm lengths is the signature of the gravitational waves and should be detectable at the output of the interferometer.

The phase deviation induced by the gravitational radiation is detectable by counting the photons at the interferometer output. The shot noise due to the process of photons counting by a photo-diode limits the sensitivity of the interferometer. In order to reduce this limitation the arms of the Michelson interferometer are replaced by Fabry-Perot cavities and the power in the interferometer is recycled by the addition of a mirror between the laser source and the beam splitter that splits the light in the two orthogonal arms. These two techniques of power recycling and Fabry-Perot cavities allow increasing the light power in the interferometer and thus improving the signal to shot noise ratio.

A first generation of detectors has been built in the 2000s and have been operating for several years. The Virgo, LIGO and GEO interferometers form a network of detectors and they have taken observational runs in coincidence. Even though they have reached their design sensitivity, the observational phases did not permit to provide a first direct detection

of a gravitational wave. Anyhow, they have shown the feasibility and ability of the detectors to reach their design sensitivity. The observational runs took place between 2007 and 2011 and the analysis of the collected data allows placing constraints on several astrophysical sources such as binary neutron stars, pulsars and burst sources.

Now that the first generation detectors are being decommissioned, the preparation and installation of the *second generation* interferometric gravitational wave detectors is on going with Advanced Virgo, Advanced LIGO and KAGRA. They are planned to reach a sensitivity an order of magnitude better than the first generation detectors. The first direct detection is foreseen to happen with the second generation interferometers and a first observational run is foreseen coincidently with Advanced LIGO, GEO-HF and Advanced Virgo for the century of the General Relativity theory in 2016.

The sensitivity range of the detectors is between a few Hz and 10 kHZ and three fundamental noises are limiting the detector sensitivity. At low frequency the limit is due to the suspension thermal noise while the mirror thermal noise limits the mid-frequency region. Finally the high frequency is limited by the shot noise. The shot noise being directly related to the amount of power circulating in the interferometer, the mirrors should induced very low losses. In the context of this thesis, we will be interested principally in the loss inside the Fabry-Perot arm cavities and in the thermal lensing effect in the recycling cavities induced by the high power circulating in the cavity.

The requirement on the round-trip losses in the arm cavity is very stringent as they should be smaller than 75 part per million (ppm). The losses in the 3 km cavity are induced by the scattering due to the micro-roughness, the scattering due to the punctual defects on the mirror surface, the coating absorption and the scattering due to the surface figure error. We will focus especially on this last source of losses and will show that the mirrors should have a sub-nanometric flatness to comply with the arm losses requirement.

Thus we will present the development of the mirrors from the calculation of the flatness specification to the dielectric coating deposition required to obtain high-reflective mirror. The mirrors are constituted of a substrate on which we deposit a multilayer dielectric coating having the required reflectivity. We will especially present the corrective coating technique developed to obtain substrates with the required flatness. We will see that the measurement of the substrate surface is crucial for the corrective coating and the measurement of the mirror surface with phase-shifting interferometry is presented along with the actual limitations encountered at LMA. The uniformity of the coating deposition plays also a role in the final flatness of the mirror and we will present the technique developed to improve the deposition uniformity. We study especially the implementation of a system of planetary motion of the substrates necessary to reach a mirror flatness compliant with required losses in the Fabry-Perot arm cavities.

Outline of the thesis:

- **Chapter 1** is introductory as it presents the context of the thesis, that is to say the detection of gravitational waves by laser interferometry. We introduce briefly the gravitational waves and present the principle of their detection by interferometry. The Virgo and Advanced Virgo detectors are described in more details.

- In the **chapter 2** we study the thermal lensing effect for different optical configurations of the Advanced Virgo detector. We show that non degenerate recycling cavities are much more immune to thermal lensing than marginally stable recycling cavities.

- **Chapter 3** presents the calculation of the flatness specification for the arm mirror cavities. The requirements on the mirror flatness are derived by simulating the Advanced Virgo arm cavities with simulated surface maps characteristic of different polishing techniques.

- In the **chapter 4** we describe the measurement of the mirror surface figure by phase-shifting interferometry. We present the performance of the repeatability and reproducibility of the measurement with the present apparatus at LMA as well as the limitations encountered.

- The corrective coating technique used for the correction of the substrates flatness is presented in the **chapter 5**. We especially show the result of a full size test done on an initial Virgo substrate.

- Finally, the uniformity of the coating deposition is discussed in the **chapter 6**. We present the results obtained on the aLIGO mirrors and discuss the implementation of the planetary motion of the substrates in the coating machine.

Chapter 1

The gravitational waves and the Advanced Virgo detector

1.1 Introduction

The gravitational waves existence has been predicted by Einstein as a consequence of his General Relativity theory in 1916 [1]. Almost 100 years after their predictions, a direct detection of the gravitational waves is still missing and only an indirect measurement of the gravitational radiation has been performed [2]. First attempts of detecting gravitational waves have been done in the 1960s with the help of resonant bars but they have been unable to provide a direct detection of the gravitational radiation [3]. During the 1960s the idea of detecting the space time ripple induced by the gravitational radiation with laser interferometry aroused [4]. It has been followed by the construction of a network of laser interferometric gravitational wave detectors in the 2000s among which the French-Italian project Virgo. But after several observational runs this first generation of detectors did not permit to provide a direct detection neither.

Nowadays a second generation of laser interferometric detectors is in preparation, that should provide a factor 10 increase in the detector sensitivities with respect to the first generation and hopefully lead to the first direct detection.

In this chapter, we will describe briefly the gravitational waves as predicted by the General Relativity. We present the basic principles of detection by laser interferometry and the fundamental noises limiting the sensitivity of the detectors. The Virgo interferometer will be described in more details along with a presentation of the ground-based detectors network.

Finally, we will present the second generation gravitational wave detector Advanced Virgo. We focus especially on interferometer optics and on the mirrors used in such gravitational wave detector as they are the topic of interest of the thesis.

1.2 The gravitational waves

1.2.1 Gravitational waves and general relativity

The concept of gravitational waves are derived from the General Relativity theory published by Einstein in 1916 in [1]. In the theory of general relativity, Einstein describes the space-time geometry as being determined by the energy-matter distribution of a system of massive body. The curvature of the space-time metric is linked to the energy content of the universe by the equation:

$$G_{\mu\nu} \;=\; R_{\mu\nu} - \frac{1}{2} g_{\mu\nu} R \;=\; -\frac{8\pi G}{c^4} T_{\mu\nu} \tag{1.1}$$

where $G_{\mu\nu}$ is the Einstein tensor describing the space-time geometry as the sum of the Ricci tensor $R_{\mu\nu}$ and of the metric tensor $g_{\mu\nu}$. G is the gravitation constant defined by Newton and $T_{\mu\nu}$ is the stress-energy tensor. It represents the source of the gravitational waves.

The Einstein's equation can be linearized in the case of small perturbations so that we have:

$$g_{\mu\nu} \;=\; n_{\mu\nu} + h_{\mu\nu} \tag{1.2}$$

with $h_{\mu\nu} << 1$ being the small perturbations induced by the gravitational waves and $n_{\mu\nu}$ being the flat space Minkowski metric. It has been shown ([5, 6]) that using an appropriate choice of coordinate, a solution of the equation 1.1 can be reduced to:

$$\left(\Delta^2 - \frac{1}{c^2}\frac{\partial^2}{\partial t^2}\right) h_{\mu\nu} \;=\; 0 \tag{1.3}$$

The general solution of the equation 1.3 is a superposition of monochromatic plane waves, a single monochromatic plane wave can be written as:

$$h_{\mu\nu} \;=\; (h_+ \epsilon^+_{\mu\nu} + h_\times \epsilon^\times_{\mu\nu}) \cdot \exp\left[i(\Omega_{GW} t - k_{GW} z)\right] \tag{1.4}$$

with Ω_{GW} and k_{GW} being respectively the angular frequency and the wave vector of the gravitational waves. $\epsilon^+_{\mu\nu}$ and $\epsilon^\times_{\mu\nu}$ are the polarization tensors of the wave supposed propagating along the z axis. The two polarization tensors plus (+) and cross (×) are defined as:

$$\epsilon^+_{\mu\nu} \;=\; \begin{pmatrix} 0 & 0 & 0 & 0 \\ 0 & 1 & 0 & 0 \\ 0 & 0 & -1 & 0 \\ 0 & 0 & 0 & 0 \end{pmatrix} \quad \text{and} \quad \epsilon^\times_{\mu\nu} \;=\; \begin{pmatrix} 0 & 0 & 0 & 0 \\ 0 & 0 & 1 & 0 \\ 0 & 1 & 0 & 0 \\ 0 & 0 & 0 & 0 \end{pmatrix} \tag{1.5}$$

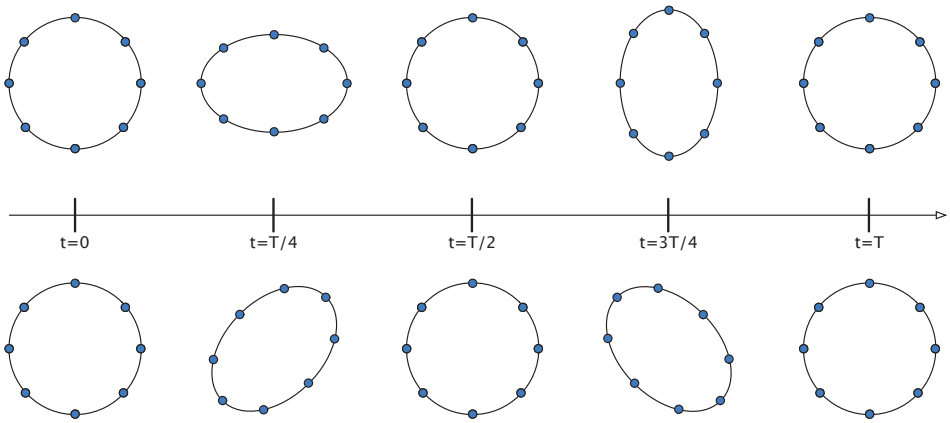

Figure 1.1: Effect of a gravitational waves on a circle of free-falling masses for the plus (+) polarization (top row) and cross (×) polarization (bottom row). The gravitational wave is propagating perpendicularly to the masses.

The effect of a gravitational waves on a circle of free-falling masses laid on the x,y plane is shown in the figure 1.1 for the two states of polarization. Due to the quadrupolar nature of gravitational waves, the relative displacement of the masses along any two orthogonal directions is opposite in sign at all times. This differential effect is exploited in the detection of gravitational waves done with Michelson type interferometry. The amplitude h of the gravitational wave is defined as the strain (relative displacement)of the contraction and dilatation of the space-time in the two directions.

1.2.2 The astrophysical sources

Gravitational waves are emitted by acceleration of quadrupolar mass moment. Considering that gravitational waves are coupled very weakly with matter only astrophysical compact bodies have the necessary high mass and acceleration to emit gravitational waves that can be detectable by ground based detectors on earth [7].

There are different kind of astrophysical sources for gravitational waves and an overview of the gravitational waves sources can be found in [8]. There are four major astrophysical sources that are predicted as being detectable by ground-based detector.

- **Coaleascing Binaries:** They are systems of two massive bodies (neutron stars - neutrons stars, black holes - black holes or neutron stars - black holes) that spiral one around each other with a decreasing orbital period. Such a system is expected to loose energy by emitting a gravitational wave signal with a frequency being twice the one of the binary system. The signal coming from a compact binary coalescence can be predicted with good accuracy [9]. This makes binary coalescence the best target for

the detection of gravitational waves. The expected rate of observable events is of tens per year with advanced detectors [10].

- **Pulsars:** They are neutron stars in rapid rotation emitting an electromagnetic radiation periodically mostly in the radio frequency domain but also in the visible frequency range or at higher frequencies. If a neutron star spins at frequency f around its axis, the quadrupolar mass moment Q and the related gravitational wave change with frequency *2f*. A gravitational radiation is emitted by the pulsar at the condition of a mass asymmetry at its surface. The expected amplitude of the signal is very weak but being virtually periodic it is possible to integrate the signal over a very long time to increase the signal-to-noise ratio. The second Virgo science run allows putting upper limit on the gravitational waves emission from the Vela pulsar [11].

- **Supernovae:** They are the collapse of a stellar objects emitting a high energy. They are thought to emit gravitational waves because of the asymmetry of the collapse. The more asymmetric is the collapse, the more intense the gravitational radiation is. A detailed overview of the expected gravitational waves signals can be found in [12].

- **Stochachstic background:** The stochastic background is believed to have two origins. First the incoherent sum of gravitational wave signals which are too weak or too distant to be resolved individually and secondly a relic stochastic background from the early phase of the universe as predicted by cosmological models. An upper-limit has been set recently on the stochastic gravitational wave background using data from the american detector LIGO [13].

1.2.3 Indirect measurement of gravitational waves

Altough no gravitational waves signal has been detected directly, an indirect measurement of the gravitational radiation has been performed from the observation of the pulsar binary system PSR1913+16. This pulsar has been discovered in 1974 by R. Hulse and J. Taylor [2]. The observation of the orbital decay of the pulsar over more than 30 years provided an indirect evidence of the existence of gravitational waves [14, 15].

The figure 1.2 shows the decay of the orbital period of the pulsar binary system PSR1913+16 over 30 years. The measured decay is in agreement with the decay due to the gravitational waves emission as predicted by the General Relativity. This agreement between the measurement and the General Relativity theory is an indirect demonstration of the existence of the gravitational waves. Taylor and Hulse were granted the physics Nobel Prize for this discovery in 1993.

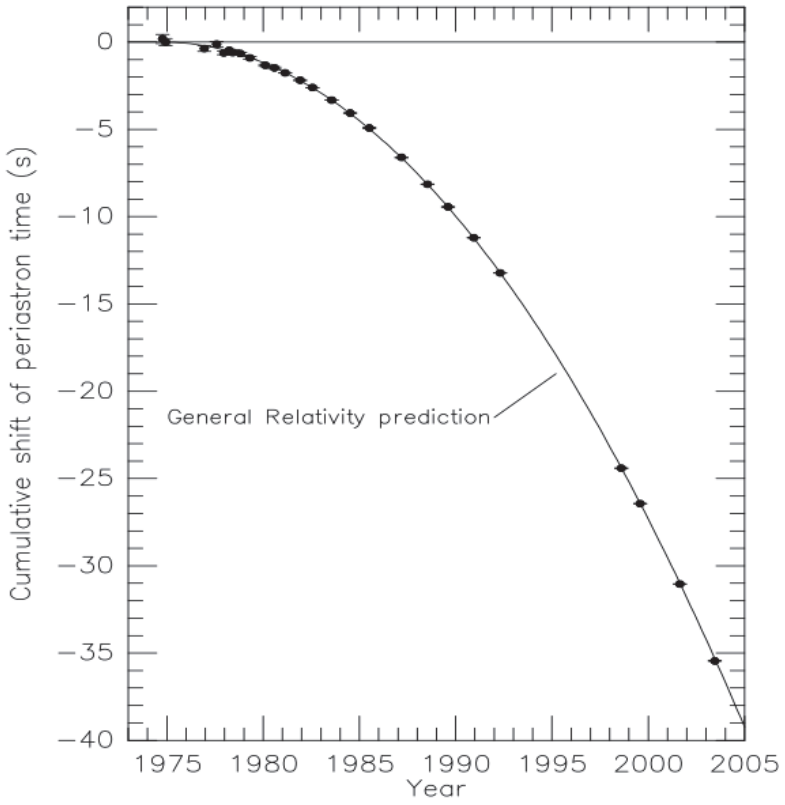

Figure 1.2: Orbital decay of PSR1913+16 binary pulsar system, from [15]. Data points represents the cumulative shift of periastron time measured whereas the parabola curve shows the same quantity predicted by the General Relativity.

1.3 Interferometric detection of gravitational wave

1.3.1 Principles of detection

Even though the existence of gravitational waves have been predicted almost 100 years ago, there never was a direct detection of gravitational radiations. The purpose of gravitational wave detector is to detect directly the gravitational radiation. It is based on laser interferometry, which are extremely sensitive tools to sense a length change. Given the differential nature of the gravitational waves effect on test masses (see paragraph 1.2.1), the Michelson interferometer is the most appropriate optical configuration for the detection of gravitational waves [16, 17].

The principle of the Michelson interferometer is to compare the length of two orthogonal arms composing the interferometer. The Michelson interferometer in its simplest optical configuration is composed of a half reflecting beam splitter and two end mirrors set orthogonally as depicted in figure 1.3. A laser beam impinges on a half reflecting beam splitter. Then the

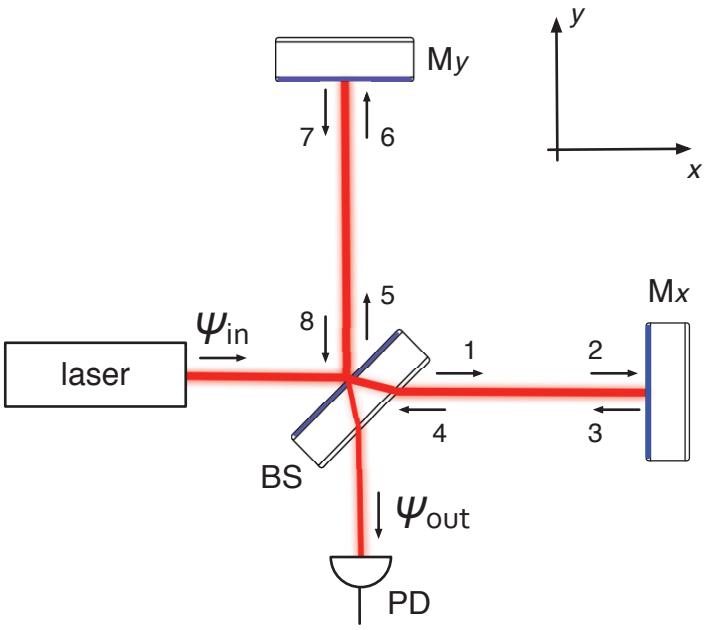

Figure 1.3: Optical scheme of the Michelson interferometer. The light field notation are reported as well as the different elements: the laser source, the beam splitter (BS), the two end mirrors (Mx and My) and the ouput photodiode (PD).

light splits and propagates in the two arms composing the interferometer, is then reflected at the end of the arm by a mirror and propagates back towards the beam splitter. At the beam splitter, the beams coming from the two arms interfere destructively or constructively depending on the length of the two arms.

The light travelling over a distance of length l experiences a fixed-time phase shift such that the amplitude of the field is:

$$\psi \;=\; \psi_0 \exp\left[-ikl\right] \tag{1.6}$$

with $k = \frac{2\pi}{\lambda} = \frac{\omega}{c}$ is the wave number of the light with λ light wavelength, ω the angular frequency and c the speed of light; Ψ_0 is the amplitude at $l = 0$.
The phase relations between incident, transmitted and reflected waves are:

$$\psi_r \;=\; ir\psi_{in} \tag{1.7}$$

$$\psi_t \;=\; \quad t\psi_{in} \tag{1.8}$$

with r and t being the reflection and transmission coefficients of the mirror and ψ_{in} the incident field amplitude.

Finally the principle of energy conservation gives the following condition:

$$r^2 + t^2 \;=\; R + T = 1 - Loss \tag{1.9}$$

where R and T are the reflectivity and transmissivity of the mirror and $Loss$ is the fraction of energy that is lost.

The different light fields shown in the figure 1.3 can be written as:

$$\begin{array}{ll} \psi_1 = t_{BS}\psi_{in} & \psi_2 = \psi_1 \exp\left[-ikL_x\right] \\ \psi_3 = ir_x\psi_2 & \psi_4 = \psi_3 \exp\left[-ikL_x\right] \\ \psi_5 = ir_{BS}\psi_{in} & \psi_6 = \psi_5 \exp\left[-ikL_y\right] \\ \psi_7 = ir_y\psi_6 & \psi_8 = \psi_7 \exp\left[-ikL_y\right] \end{array}$$

The light field ψ_4 and ψ_8 recombine at the output port of the interferometer after being respectively reflected and transmitted by the beam splitter. It gives:

$$\psi_{out} \;=\; ir_{BS}\psi_4 + t_{BS}\psi_8 \tag{1.10}$$

$$\psi_{out} \;=\; -r_{BS}t_{BS}r_x\psi_{in}\exp\left[-2ikL_x\right] - r_{BS}t_{BS}r_y\psi_{in}\exp\left[-2ikL_y\right] \tag{1.11}$$

where $L_{x,y}$ are the lengths of the two arms. The amplitude at the output port finally depends on the phase difference $\phi = 2k(L_y - L_x)$ that depends in the lengths of the two arms. The output power detected at the photodiode is then the square of the output field ($P_{out} = |\psi_{out}|^2$), it is given by the following equation:

$$P_{out} \;=\; R_{BS}T_{BS}\left(R_x + R_y + 2r_x r_y \cos\phi\right) P_{in} \tag{1.12}$$

that can be written as:

$$P_{out} \;=\; R_{BS}T_{BS}(R_x + R_y)\left(1 + C\cos\phi\right) P_{in} \tag{1.13}$$

where $C = \frac{2r_x r_y}{R_x + R_y}$ is the contrast of the interferometer. It is clear that the power detected by the output photodiode depends on the difference of lengths between the two arms. The power is maximal when $\phi = 0$ (bright fringe) and minimum when $\phi = \pi$ (dark fringe). For the purpose of the detection of gravitational waves, the interferometer is tuned to be in the dark fringe condition [18].

In the interferometer, the mirrors (also called test masses) are suspended with the so-called *super-attenuators* that are based on a chain of pendulums, each masses being a spring[19]. There are two reasons for suspending the mirrors, one is to isolate them from

the ground seismic motion and the second is that suspended mirrors behave as free-falling masses in the frequency range above the pendulum resonance which is at a few hertz [19].

When a gravitational wave passes through the Michelson interferometer it induces a change in the optical paths of the Michelson interferometer. As a consequence it modulates in time the signal at the output of the interferometer thus changing the interference conditions by an additional phase shift due to the gravitational wave.

$$P_{out} = R_{BS}T_{BS}(R_x + R_y)\left(1 + C\cos(\phi + \delta\Phi_{GW})\right)P_{in} \tag{1.14}$$

The phase difference $\delta\Phi_{GW}$ due to a gravitational wave propagating perpendicularly to the interferometer plane and with a plus polarization can be expressed as [18]:

$$\delta\Phi_{GW} = \frac{4\pi}{\lambda}hL\mathrm{sinc}\left(\frac{\Omega_{GW}L}{c}\right)\cos\left(\Omega_{GW}(t - \frac{L}{c})\right) \tag{1.15}$$

where Ω_{GW} is the gravitational wave frequency. This equation represents the frequency response of the interferometer and we can see that it is proportional to the arms length L. The longer the arms, the largest the phase difference.

This dephasing due to the gravitational radiation induces a deviation on the power measured at the interferometer output which can be expressed at first order as:

$$\begin{aligned} \delta P_{out} &= R_{BS}T_{BS}(R_x + R_y)P_{in}C \cdot \sin(\phi) \cdot \delta\Phi_{GW} \\ \delta P_{out} &= \frac{P_{in}}{2}C\sin(\phi) \cdot \delta\Phi_{GW} \end{aligned} \tag{1.16}$$

assuming that $R_{BS} = T_{BS} = \frac{1}{2}$ and $R_x = R_y \approx 1$.

One of the fundamental noise that limits the accuracy of the power measurements and so the sensitivity is the *photon shot noise*. This is linked to the quantum nature of the light and the power spectral density (PSD) of the detector current is:

$$S_P(f) = \sqrt{2h_p\nu\eta\ P} \tag{1.17}$$

with f the PSD frequency, ν is the frequency of the light, P the power detected by the photo-diode, η the quantum efficiency of the detector and h_p the planck constant.

Considering the shot noise, the best tuning for a Michelson interferometer correspond to maximise the following signal to noise ratio (SNR).

$$SNR(f) = \frac{S_{\delta_P}}{S_P} = \frac{1}{2}\sqrt{\frac{P_{in}}{h_p\nu}}\frac{C\sin(\phi)}{\sqrt{1+\cos(\phi)}}\frac{2\pi L}{\lambda}S_h(f) \tag{1.18}$$

The maximum SNR is found for a tuning of:

$$\cos(\phi) \;=\; \frac{-1+\sqrt{1-C^2}}{C} \tag{1.19}$$

Finally the best signal to noise ratio is found at the dark fringe condition assuming that the contrast C is close to one [18]. This optimum corresponds to a noise spectral density for the interferometer output signal equal to:

$$h_{shot}(f) \;=\; \frac{\lambda}{4\pi L}\sqrt{\frac{2h_p\nu}{\eta P_{in}}} \tag{1.20}$$

In the expression above we have supposed that $\Omega_{GW} << c/L$ so that $\delta\Phi_{GW} = \frac{4\pi hL}{\lambda}$. Thus we see that the shot noise limitation of the sensitivity is dependent on the laser power and on the length of the interferometer arms. It can be lowered by increasing the laser power and the arm length. We also see that it is not frequency dependent.

1.3.2 Sensitivity improvement of the Michelson interferometer

Fabry-Perot cavity

We have seen previously that the shot noise limit can be lowered by increasing the power in the interferometer and the arm length.

As it is not easy to build ground-based interferometer with arms longer than a few kilometres (3 or 4 km for Virgo and LIGO), Fabry-Perot (FP) cavities [20] are used to enhanced the effective length of the arms. The addition of Fabry-Perot cavities in the interferometer arms allows increasing the optical arms lengths. The cavity is tuned at resonance that is to say that the light after one round trip interfere constructively with the incoming beam. As a consequence the power in the arms is increased by a factor that depends on the *finesse* $\mathfrak{F}$ of the cavity:

$$\mathfrak{F} \;=\; \frac{\pi\sqrt{r_I r_E}}{1-r_I r_E} \tag{1.21}$$

with r_I and r_E are the input and end mirror reflectivity of the mirrors composing the FP cavity.

In such a resonant cavity, the light is stored in the cavity and bounces back and forth before leaving the cavity. The number of round-trips of a photon inside the cavity is linked to its *finesse*. The larger the *finesse*, the more round-trips there are. Thus it allows amplifying the dephasing due to the gravitational wave as the effective optical length seen by the light

is enhanced by a factor g:

$$g = \frac{2\mathfrak{F}}{\pi} \tag{1.22}$$

In the first generation Virgo interferometer, the finesse of the arm cavities was designed to be 50 resulting in an effective arm length of about 100 km instead of 3 km. After the Virgo+ upgrade, the finesse of the cavity has been increased to 150.

The enhancement of the finesse causes a reduction on the bandwidth of the cavity response on length changes. It can be shown that the response of the cavity expressed as radians per metre exhibits the characteristic single pole response function as:

$$\delta\phi = \frac{2\pi}{\lambda}\frac{2\mathfrak{F}}{\pi}hL\frac{1}{\sqrt{1+\left(\frac{f_{GW}}{f_c}\right)^2}} \tag{1.23}$$

with $f_c = c/4\mathfrak{F}L$ and f_{GW} the gravitational wave frequency.

The shot noise with optical resonators in the arms can now be expressed as [18]:

$$h_{shot}(f) = \frac{\lambda}{8\mathfrak{F}L}\sqrt{\frac{2h_p\nu}{\eta P_{in}}}\sqrt{1+\left(\frac{f}{f_c}\right)^2} \tag{1.24}$$

We see that the shot noise becomes frequency dependent. For $f > f_c$, the shot noise increases linearly with the frequency of the gravitational wave.

Power recycling cavity

Another way to decrease the limitation due to the shot noise is to increase the laser power. Again it is not easy to build stable laser with a very high power, for example the Virgo laser was a 20 W laser operating at wavelength of 1064 nm [21]. It delivered a power at the interferometer input of about 8 W during the early phase of the Virgo interferometer and about 17 W after the Virgo+ upgrade [22]. The Advanced Virgo laser is designed to deliver a power of about 125 W at the input of the interferometer [23].

To increase the power circulating inside the interferometer a partially-reflective mirror is added at the input of the interferometer between the laser source and the beam splitter. This mirror is called *power recycling mirror* and the technique is known as power recycling.

Since the interferometer is tuned on the dark fringe condition, all the power is reflected back to the laser source. The mirror placed at the interferometer input allows recycling the power circulating back to the laser source. The power recycling mirror forms a Fabry-Perot cavity with the Michelson interferometer being the second mirrors with a reflectivity r_{mich} close to one as the interferometer is tuned in dark fringe. The power recycling gain due to

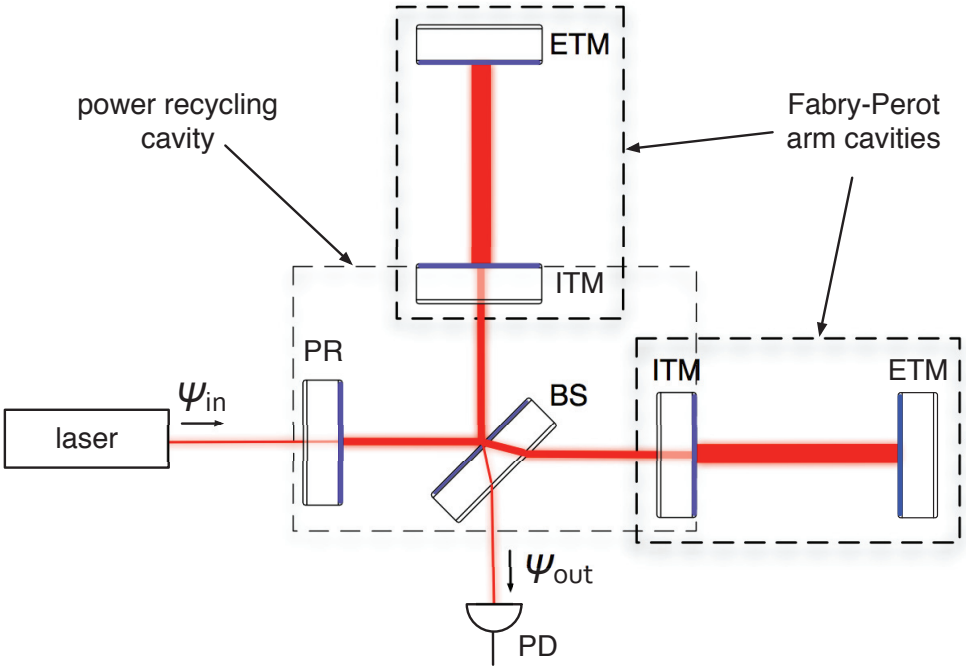

Figure 1.4: Simplified optical scheme of the Virgo interferometer. It is a power recycling Michelson interferometer with Fabry-Perot arm cavities.

the recycling mirror is defined as the ratio of the power circulating inside the recycling cavity (P_{PR}) and the input power (P_{in}).

$$G_{PR} = \frac{P_{PR}}{P_{in}} = \left(\frac{t_{PR}}{1 - r_{PR} r_{mich}}\right)^2 \tag{1.25}$$

The figure 1.4 shows the optical configuration of a Michelson interferometer with Fabry-Perot cavities and power recycling cavity. This is the optical configuration which was used for Virgo.

1.3.3 Noise sources and sensitivity

The sensitivity of Virgo and of any ground based gravitational wave detectors is limited by different kind of noises. Theses noise are random fluctuations in the measured output power that have different origins. We can classify the noises in two classes, the fundamental noises and the technical noises. In the following we will present briefly the fundamental and technical noises as well as the sensitivity design and noise budget of the Virgo interferometer. The sensitivity of the detector can be expressed as a strain equivalent spectral noise amplitude. A review of the different noises limiting the Virgo interferometer sensitivity can

be found in [24]. The sensitivity curve represents the equivalent strain amplitude detectable by the detector and is plotted as the square root of the power spectrum which unit is $\mathrm{Hz}^{-\frac{1}{2}}$. The frequency range of ground-based interferometric detector is typically between a few Hz and 10 kHz. The main fundamental noises that limit the sensitivity of the detectors are the following:

- **Seismic noise:** At very low frequency, the sensitivity is limited by the seismic noise due to the ground motion that couples to the mirrors via the suspension system. The mirrors composing the interferometers are suspended with super attenuators as already explained. This noise is generated by many sources such as the seismic activity, the ocean activity, the wind or the human activity. The suspension system allows to mitigate this noise as it acts as a low-pass filter with a cut-off frequency of a few Hz above which the mirrors are efficiently isolated from the vibrations. It is the dominant noise below 2 Hz according to [24].

- **Suspension thermal noise:** The suspension thermal noise is limiting the sensitivity in the frequency range from 2 Hz to 50 Hz. It is due to relaxation phenomena in the suspension chain of the mirrors that affects the displacement of the test mass. The suspension thermal noise can be thought to have two components: the pendulum noise and the violin modes that induce a longitudinal motion of the test masses and is relevant around the violin resonant mode frequencies. The installation of monolithic suspension with fused silica fibre allows to decrease both these noises [25].

- **Mirror thermal noise:** In the mid frequency region (50 Hz to 100 Hz) the largest contribution of thermal noise comes from relaxation phenomena in the mirror and coatings. In particular, estimations show that the major contributions come from structural relaxation inside the coating layers. The second largest contribution comes from thermoelastic relaxation both in coatings and substrates.

  There are two approaches to reduce the mirror thermal noise. The first one is to average the beam intensity profile on a larger mirror area. This can be done by increasing the beam size or by the use of non-Gaussian beam such as LG33 beam [26]. The second approach is to reduce mechanical loss of the coating materials. As shown by the fluctuation dissipation theorem the power spectral density of the thermal noise is proportional to the dissipative response of the system at all frequencies.

- **Shot Noise:** It is the most important contribution above 100 Hz and as shown by equation 1.24 it scales as the square root of the power at the beam splitter. Thus one can decrease it by increasing the power circulating inside the interferometer. However

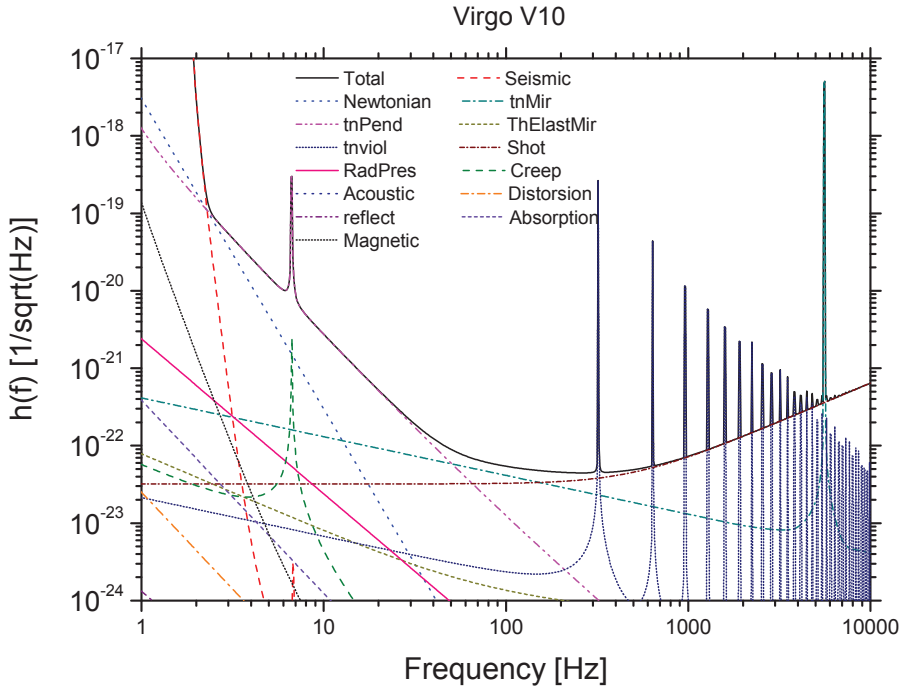

Figure 1.5: The Virgo design noise budget.

the power cannot be increased indefinitely as it would degrade the sensitivity at low frequency because of the radiation pressure noise

- **Radiation pressure noise:** The quantum nature of the light is at the origin of quantum laser power fluctuations that generate the so called radiation pressure noise. The radiation pressure effect is to move the mirrors according to a law in $1/f^2$. And even though this noise is far from being dominant in Virgo, the foreseen increase of power in Advanced Virgo makes it relevant. A trade-off has to be found in the increase of power between the low frequency region limited by the radiation pressure noise and the high frequency region limited by the shot noise. To mitigate this noise one can increase the mass of the mirrors. In the case of Advanced Virgo the mirror mass has been doubled compared to Virgo (from 21 kg to 42 kg) [23].

Figure 1.5 shows as an example the Virgo noise budget available from [27] with the noises presented earlier, the seismic noise is labelled as *Seismic*, the suspension thermal noise as *tnPend*, the mirror thermal noise as *tnMir*, the shot noise as *Shot* and the radiation pressure noise as *RadPres*. The sensitivity of a detector can also be expressed as the maximal distance of a coalescing binary formed by two neutron stars that is detectable with a signal to noise

ratio of 8. It is given in megaparsec (MPc) and it is about 12 MPc for the initial Virgo design.

Apart from these fundamental noises there are other more technical noises that can limit the sensitivity such as the fluctuations of the laser source, the air conditioning system, the electronic noise of the control and read-out system. The fluctuations in the optical path of the laser or the diffused light can also couple to the dark fringe and degrade the sensitivity.

- The laser source must be very stable both in frequency and in power as a change in the frequency or in amplitude of the laser can generate noises at the detector output. The laser beam position must also be very stable as it can generate an additional phase noise called *beam jitter*.

- The whole detector is placed under vacuum in order to avoid fluctuations in the optical path of the laser due to a change of refractive index. It also permits to isolate the interferometer from acoustic noise. The whole detector is placed in pipes and tank which have a residual gas pressure of the order of $10^{-7} - 10^{-8}$ mbar. This level of vacuum allows to reduce theses noises to a negligible level.

- The light scattered by the mirror imperfections can be reflected back to the main beam by the vacuum pipes thus being phase modulated by the pipes vibrations. This diffused light also adds a phase noises and can be a major problem. Light baffles that absorb the spurious light are installed all along the laser path to avoid the coupling of diffused light to the main beam.

An other issue to deal with are the thermal effects due to the high laser power circulating inside the resonant cavities. These thermal effects induce a thermal lens inside the input mirror substrate. The power absorbed in the coating of the input mirror generate a change in the refractive index of the mirror due to the temperature dependence of the refractive index. This change of refractive index induces a thermal lens [28]. To cope with such thermal lensing, a thermal compensating system (TCS) has been developed and built in order to reduce this effect [29]. In the chapter 2 we will study in more details the effect of this thermal lens on the performances of Virgo and Advanced Virgo with different type of power recycling cavities.

Figure 1.6: Aerial view of the gravitational wave detector Virgo.

1.3.4 The Virgo interferometer - a first generation interferometer

The first generation of the Virgo gravitational wave detector has been designed during the 1990s and was finished building in 2003. It is located in Cascina, near Pisa in Italy. The figure 1.6 is an aerial view of the Virgo interferometer, we can see the two long arms oriented towards the north and west.

Between 2003 and 2007, it went through a commissioning phase and the first observational run called Virgo Scientific Run 1 (VSR1) started in May 2007. From 2007 the interferometer underwent several commissioning phases and observational runs. The last run VSR4 ended in November 2011 and the interferometer was decommissioned shortly after.

To reach the design sensitivity limited by fundamental noise, the interferometer must go through a commissioning phase. There are two objectives for this phase, one is to developed a control scheme that allows to reach a stable working configuration, the second is to reach the design sensitivity. The duty cycle is a good tool to assess the stability and performance of the control scheme. The Virgo interferometer has proven to be very robust as it had a duty cycle of about 80 % during the second science run [30]. The commissioning phase is also the phase where the technical noises (laser noises, control noises) are being mitigated to reach the design sensitivity and the fundamental limiting noises. The different commissioning phases allowed reaching the design sensitivity.

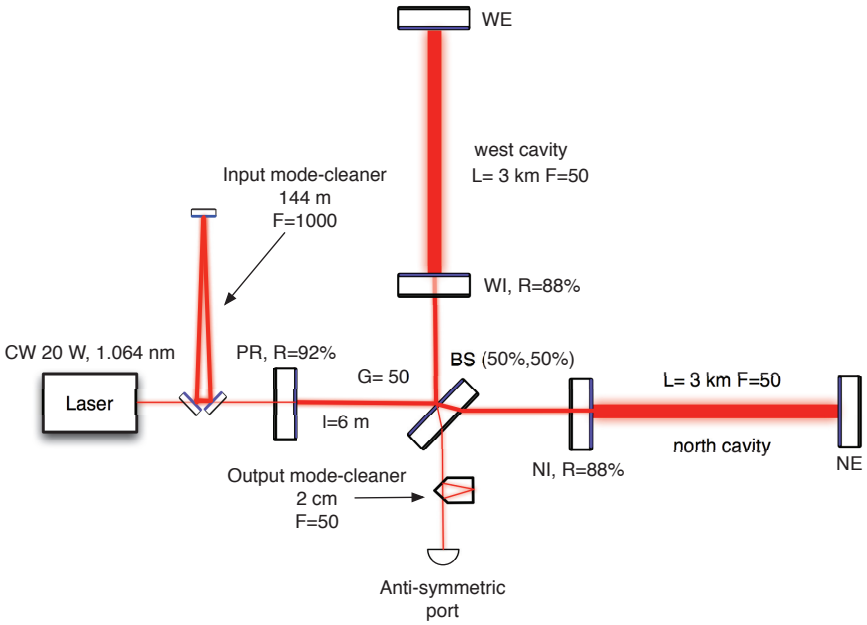

Figure 1.7: Optical layout of the Virgo interferometer.

Virgo optical layout

A simplified optical layout of the Virgo interferometer is depicted in the figure 1.7. It is a power recycling Michelson interferometer with 3 km long Fabry-Perot arm cavities with a power recycling mirror (PR), a beam splitter (BS), two input mirrors (IM) and two end mirrors (EM). The two arms cavities are called north and west because of their geographical orientation.

The FP cavity are composed of an input mirror with a reflectivity of 88% and an end mirror with a transmission of tens of ppm resulting in a finesse of 50. After the Virgo+ upgrade, the reflectivity of the input mirrors was increased to 95.9 % resulting in a finesse of about 150.

The Fabry-Perot cavities are plane-concave cavity, with a flat input mirror and an end mirror with a radius of curvature around 3600 m. The beam sizes on the IM and on the EM are respectively about 2 cm and 5 cm. Every other mirrors of the optical layout are flat mirrors. The mirrors in the interferometers are quite big as they have a diameter of 35 cm and a thickness of 10 cm resulting in a weight of 21 kg. The beam splitter is a bit smaller as it has a diameter of 23 cm and a thickness of 5 cm for a weight of 5 kg.

The distance between the input and end mirrors is about 3 km and the distance between the beam splitter and the input mirrors is approximately 6 m. The power recycling mirror has a reflectivity of about 95 % and is located 6 m from the beam splitter.

The input beam is generated by a laser source with a power of 20 W at a wavelength of

1064 nm. The laser is composed of a high stability solid state Nd:YAG master laser and a high power $Nd : YVO_4$ slave laser. This system allows obtaining an ultra stable beam both in frequency and in amplitude as required for Virgo. Before entering the interferometer, the beam is modulated by two electro-modulators at three different frequencies at about 6 MHz, 8 MHz and 22 MHz. These modulated signals are used to control the interferometer as explained thoroughly in [18]. After being modulated, the beam is sent to the input mode-cleaner (IMC) filter cavity. The main purpose of the IMC is to filter the high order mode content of the beam and to reduce the beam jitter. It is also used to stabilise the laser frequency and amplitude. The input-mode cleaner is triangular cavity with a length of 144 m and a finesse of 1000 resonant on the TEM_{00} mode. A Faraday isolator has been implemented to avoid the backscattering of the light towards the laser. The injection system also includes a telescope to allow controlling the position and the size of the beam.

After passing through the injection system, the beam is directed towards the interferometer output. In Virgo, the power of the beam entering the interferometer is about 8 W (17 W for Virgo+). By means of the recycling and arm cavities the power of the beam in the interferometer increases to about 500 W on the beam splitter and to 7 kW in the FP cavities.

At the output of the interferometer, the beam passes through an ouput mode-cleaner (OMC) and is sent to the photo-diodes. The OMC is a monolithic fused-silica cavity of 2 cm. As for the IMC, the output mode-cleaner role is to filter the high-order mode content of the beam generated in the interferometer thus increasing the fringe contrast.

The mirrors composing the interferometer are suspended with super-attenuators [19] that provide the attenuation of the ground motion. The super attenuators are equipped with actuators that allows controlling the mirrors positions. The control of the mirrors is essential to keep the interferometer in the required interference conditions with all the cavities at resonance and the fringe locked on the dark. The details of the control scheme for Virgo can be found in [18]. It is important to note that the performances of the super-attenuators are within the requirements for Advanced Virgo [31].

1.3.5 A network of detectors

Apart from the French-Italian gravitational wave detector Virgo there are four others ground-based detectors with the two LIGO interferometers, GEO600 and TAMA300. They have shown the feasibility of laser interferometers gravitational wave detectors by operating approximately at their design sensitivity. Several observational runs have been done by LIGO, GEO600 and Virgo for months. Even though no detection has been reported, these scientific runs have permitted to demonstrate that these detectors are capable of working on a

Figure 1.8: The first generation gravitational wave detector network with from top right and clockwise TAMA300, LIGO Hanford, LIGO Livingston and GEO600.

long term basis. The figure 1.8 shows the network of the first generation gravitational wave detector on earth with the two LIGO interferometers, GEO600 and TAMA300.

The LIGO project in the USA has two interferometers, one based at Hanford in the state of Washington and one in Livingston in the state of Louisiana [32, 33]. The two detectors are 3000 kilometres apart. They are both power recycling interferometers with 4 km long FP arm cavities. They have been decommissioned after a last scientific run of about one year (S6) and will undergo a complete upgrade with the Advandced LIGO (aLIGO) project [34].

An other interferometer called GEO600 is located in Germany in the region of Hannover [35]. GEO600 is a British-German collaboration which is part of the LIGO Scientific Collaboration (LSC) [36]. This interferometer has a different optical configuration, it is also a power recycling Michelson interferometer but with 600 m long arms without FP cavities. The GEO600 interferometer already underwent a major upgrade (GEO HF) and it is now a dual-recycling Michelson interferometer with both a power recycling mirrors and a signal recycling mirrors [37]. The signal recycling mirrors allows to enhance the gravitational wave signal. We will explain the principle of the dual-recycling cavities in the paragraph 1.4.

Finally, there is also a Japanese collaboration that has built a gravitational wave detector with the TAMA300 interferometer that features 300 m long FP arm cavities. Japan is now starting to build and design a second generation detector called KAGRA. It is a very challenging detector as the KAGRA interferometer will be cryogenic and underground [38, 39].

A network of second generation ground-based detectors is in preparation and should be in operation in the second half of the 2010s. In the following, we will concentrate on the Advanced Virgo detector and present the major features that makes it a second generation detectors. We will show its design sensitivity and focus on the interferometer optical configuration and on the mirrors which are the main subject of this thesis.

1.4 Advanced Virgo: a second generation detector

The Virgo interferometer is now being decommissioned and the preparation of the Advanced Virgo interferometer is ongoing. The Advanced Virgo project has been funded in 2009 and the technical design report has been released in April 2012 by the Virgo Collaboration. It presents the technical design of the interferometers in details [23].

Advanced Virgo will be a dual recycling Michelson interferometer with Fabry-Perot arm cavities like the American aLIGO and the Japanese KAGRA. It is the same as a power recycling Michelson interferometer but with an additional mirror at the output port of the interferometer. This mirror called *signal recycling* (SR) and shown in figure 1.11, forms an optical cavity with the Michelson interferometer. This cavity is made resonant for the gravitational wave signal thus increasing the gravitational wave signal. A dual recycling interferometer can be tuned either for a broadband configuration or detuned for optimization of the BNS (binary neutron-star) detection [40]. Advanced Virgo can be seen as a tunable interferometer, however the Advanced Virgo strategy implies a two steps strategy as the signal recycling mirrors will be installed in a second step because of time and money constraints. In the first step the interferometer will have a limited configuration without SR and will work at low power (25 W).

In this section, we will describe the sensitivity of the Advanced Virgo interferometer, its optical layout, review the major upgrades on the optic side and then focus on the mirrors and especially the ones composing the Advanced Virgo arm cavities.

1.4.1 The Advanced Virgo design sensitivity

As for Virgo, the reference sensitivity of Advanced Virgo is limited by fundamental noises (thermal noises, shot noise, radiation pressure noise) [41]. The reference sensitivity curve is plotted in the figure 1.9 along with the limiting fundamental noises. The black curve represents the design sensitivity for Advanced Virgo with signal recycling cavity (SRC) and 125 W input power in detuned configuration. That is to say optimized for the detection of coalescing binary neutron star, the corresponding inspiral range is about 135 MPc. It corresponds to an increase of more than a factor 10 compared to Virgo as the same binary

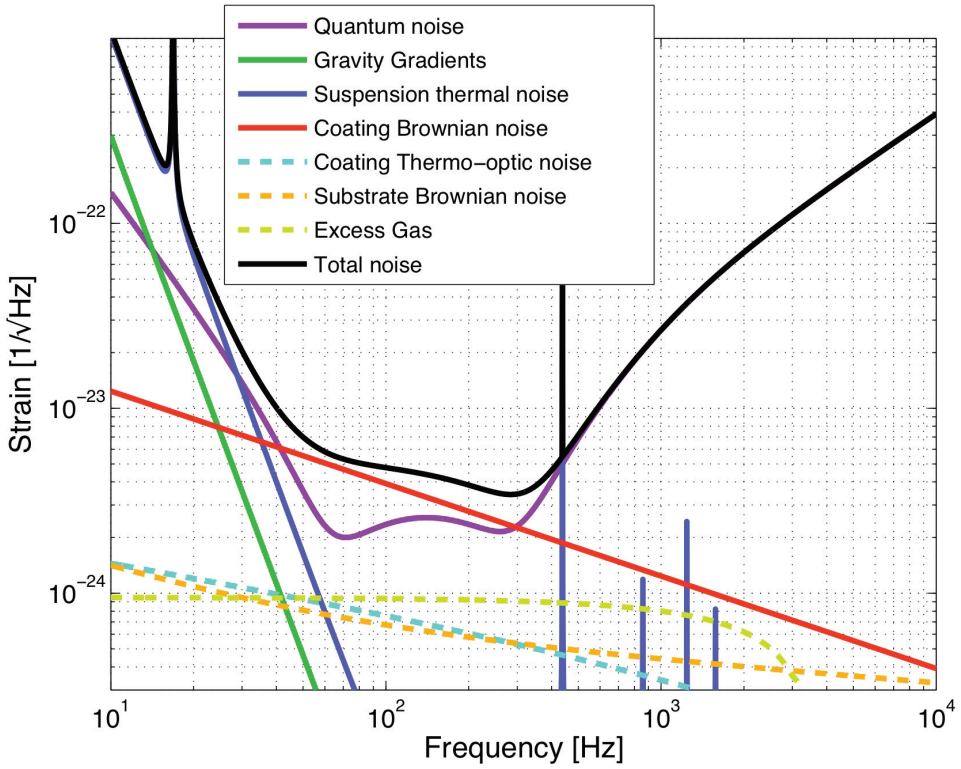

Figure 1.9: Advanced Virgo sensitivity with dual-recycling cavities and expected noise. The SR tuning optimizes the inspiral range for coalescing binary neutron stars, from [23].

neutron stars inspiral range was of only 12 MPc in Virgo. An increase of a factor 10 in the sensitivity leads to an increase of 10^3 in the volume of universe visible by the detector and so in the detectable events assuming an homogeneous and isotropic distribution of the astrophysical sources. The expected detection rate for Advanced Virgo reference design (with SRC and 125 W input power) is of 17 events per year for the binary neutron star [22].

We see in the figure 1.9 that the maximum strain sensitivity in this configuration is $4 \cdot 10^{-24}$ $\mathrm{Hz}^{-\frac{1}{2}}$ at a frequency of 300 Hz. As a comparison it was $4 \cdot 10^{-23}$ $\mathrm{Hz}^{-\frac{1}{2}}$ in Virgo. The reference sensitivity is limited below 20 Hz by the suspension thermal noise. Between 20 Hz and 40 Hz, the sensitivity is dominated by a superposition of the suspension thermal noise and by the quantum noise. The quantum noise plotted here is the sum of the radiation pressure noise (contributing principally at low frequencies) and of the shot noise (contributing principally at high frequencies). In the mid-frequency region (40 Hz - 300 Hz), the mirror thermal noise principally due to the coating brownian noise is dominating. Above 300 Hz, the shot noise contribution in the quantum noise is limiting the Advanced Virgo sensitivity.

The Advanced Virgo interferometer will start at low power (25 W) and without SR mirror. The figure 1.10 shows the sensitivity for different configurations:

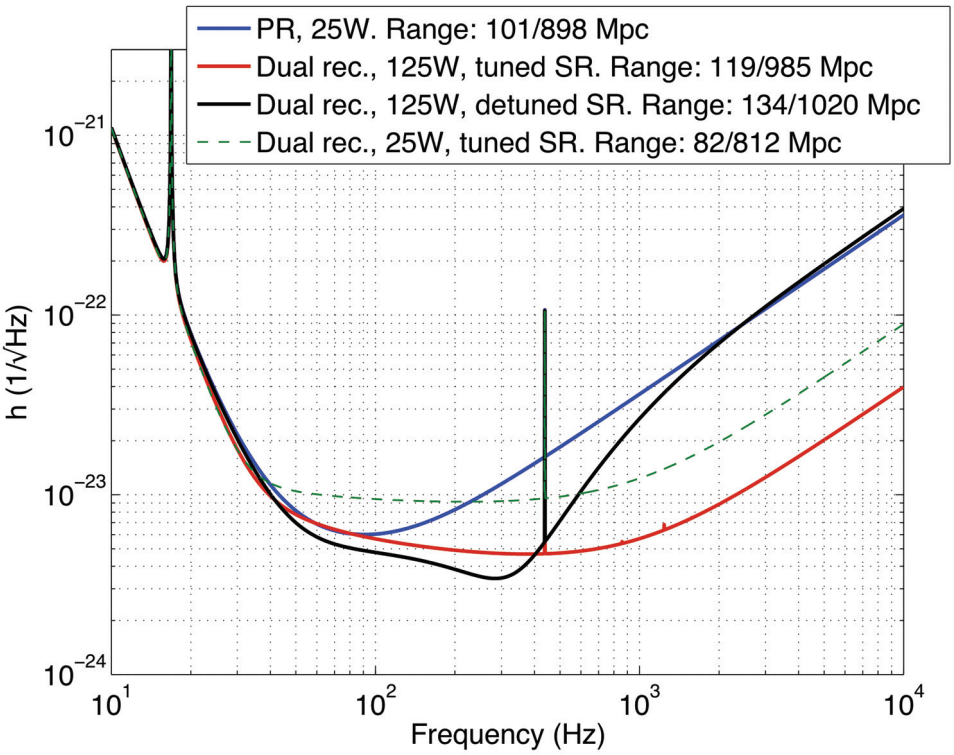

Figure 1.10: Advanced Virgo sensitivity for the different possible scenario in the Advanced Virgo configuration. In the legend, the inspiral ranges for BNS and BBH (each BH of 30 $M_{\odot}$) in Mpc are reported, from [23].

- Power recycling Michelson interferometer with 25 W input power (blue curve).
- Dual-recycling Michelson interferometer with 25 W input power and tuned SR (green dotted curve).
- Dual-recycling Michelson interferometer with 125 W input power and tuned SR (red curve).
- Dual-recycling Michelson interferometer with 125 W input power and detuned SR, the AdV reference sensitivity (black curve).

We see that the PR configuration at low power has a lower sensitivity at frequencies above 100 Hz than the reference sensitivity. The reason to that is essentially the low input power. We see that adding the signal recycling cavity allows to decrease the limitation due to the shot noise above 200 Hz for the same laser power but at the price of a lower sensitivity at low frequency. Working at full power (125 W) and with tuned SR allows to improve the sensitivity on a the whole band above 30 Hz.

The sensitivity red and black curve for Advanced Virgo with SR and at full power allows to see the effect of the SR tuning. Indeed the black curve is the detuned configuration (the reference one) and the red curve is the wide band configuration. In the wide band configuration we gain in sensitivity at high frequencies (> 300 Hz), it is the tuning for the burst search. On the contrary the detuned configuration has an increased sensitivity in the mid-frequency region optimizing the search for coalescing binary neutron stars.

It is important to note that a dual-recycled Michelson interferometer is tunable for the search of the different astrophysical sources.

1.4.2 Optical layout

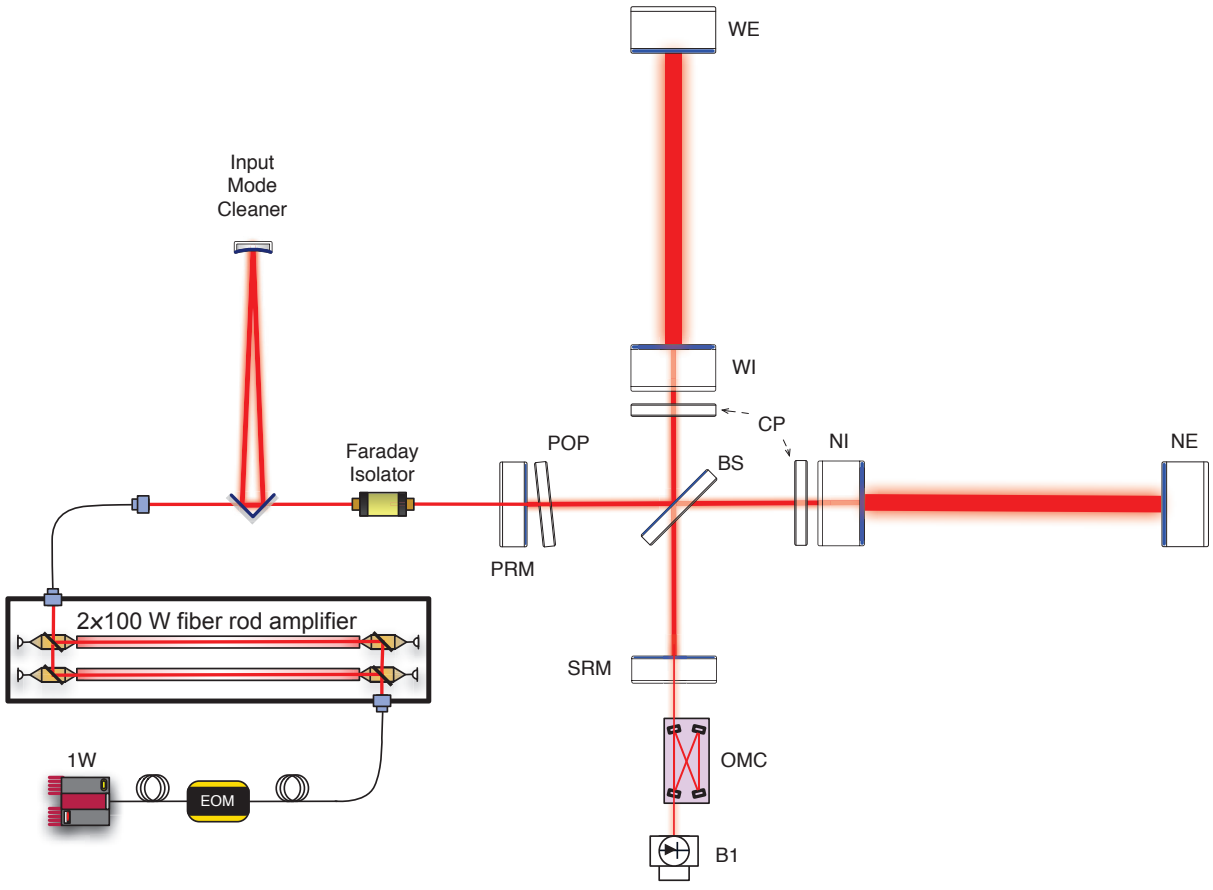

Figure 1.11: Advanced Virgo optical layout from [23].

To achieve the sensitivity described in the previous paragraph, a new optical layout has been designed for Advanced Virgo. The figure 1.11 presents the optical layout of Advanced Virgo with both power and signal recycling. The reference configuration exhibits the same mirrors as Virgo with the power recycling mirror (PRM), the beam splitter (BS), the north

and west input mirrors (NI and WI) and the end mirrors (NE and WE). Four additional optics can be seen on the optical layout, the signal recycling mirror (SRM), 2 compensating plates (CP) and one pick-off plate (POP). The signal recycling mirror will be installed in a second step as already explained. The CP are transmissive optics coated with anti-reflective (AR) coating on both sides, they are used in the thermal compensation system to compensate the wave-front distortion of the beam inside the recycling cavities. A pick-off plate (POP) is put in front of the PRM. It is tilted by 6 degrees in order to extract the necessary beams for the longitudinal control of the interferometer.

The Advanced Virgo baseline design foresaw the installation of long-recycling cavities ([42]) which are non-degenerate and so more immune to thermal effects as we will see in the chapter 2. Different configurations of the recycling cavities have been studied ([26]) and finally the short-recycling cavities solution has been chosen [23]. The choice of the short-recycling cavities has been driven principally by the constraints on the suspension and payload systems. But even though the optical configuration of Advanced Virgo seems to be the same as Virgo there are some major upgrades in the optical configuration itself:

- The Fabry-Perot cavity geometry has been changed from plano-concave to bi-concave with the input and end mirrors having respectively a radius of curvature of 1420 m and 1683 m. In this configuration, the cavity waist is located near the center of the cavity with a waist of 9.7 mm and consequently the beam size on the input mirror is of 48.7 mm and 58.0 mm on the end mirror. This change of configuration is driven principally by the mirror thermal noise issue that requires larger beam.

- The Fabry-Perot cavity finesse has also been increased to 443 with a transmissivity of 1.4 % for the input mirror and of 1 ppm for the end mirror. This larger finesse allows decreasing the effect of the photon shot noise on the interferometer sensitivity. Moreover it helps reducing the effect of the noise coming from the control of the other interferometer mirrors, such as the position control of the beam splitter and of the recyling mirrors.

- The signal recycling mirror with a reflectivity of 80 % is forming a signal recycling cavity with the central Michelson interferometer as end mirror, it has a finesse of 26. At the passage of a gravitational wave of frequency $\Omega_{GW}/2\pi$ the carrier beam modulated at that frequency and a set of carrier sidebands is generated at the frequencies $\omega_0 \pm \Omega_{GW}/2\pi$. These sidebands are the gravitational waves signal and are usually called audio sidebands because of their frequency range. The audio sidebands are resonant in the signal recycling cavity (SRC) whereas the carrier is not, separating then the two audio sidebands from the carrier beam. The audio sidebands being resonant in

the SRC, the signal is amplified depending on the finesse of the cavity. The tuning of signal recycling cavity permits to change the detector sensitivity curve and so to optimize the detector from a broadband configuration to an optimized tuning for a given astrophysical source.

- The laser power has been increased by about a factor 15 with a power of 125 W at the interferometer input in order to reduce the shot noise limit. There is a change of technology in the laser source with a completely new technology. The high power laser will be a system with a 1 W Nd:YAG seed laser amplified by two rod amplifiers developed by the company Eolite. The two rod amplifiers will provide a power of 100 W and the two beams will be added coherently to obtained a single 200 W beam with more than 175 W in the TEM_{00} mode. At the input of the interferometer, the laser should provide a 125 W beam considering the losses in the whole injection system. As in Virgo, the injection system is composed of an electro-optical modulators (EOM), a Faraday isolator, a pre mode-cleaner and an input mode-cleaner. The EOM provides the radio frequency modulation signals used for the interferometer sensing and control. A Faraday isolator place after the IMC avoids the backscattering of light to the laser source and to the IMC. The pre mode-cleaner is a monolithic cavity used to control the beam geometry and the positioning of the beam whereas the IMC provides the amplitude control and the beam jitter filtering. The IMC is as in Virgo a 144 m triangular cavity with a finesse of about 1200 (slightly larger than in Virgo).

- The high power laser source and increased finesse of the arm and recycling cavities will provide an increased optical power in the interferometer. Indeed the optical power on the beam splitter is foreseen to be 4.9 kW in Advanced Virgo instead of 0.3 kW in Virgo. The power circulating in the cavity will be about 650 kW in the final design of Advanced Virgo instead of 6 kW in Virgo. This is a major change compared to Virgo.

- This high power in the interferometer implies larger thermal effects in Advanced Virgo compared to Virgo. Thermal effects are induced by the absorption of laser power in the optics and the thermal compensation sytem (TCS) will have to mitigate those effects [29]. The choice of the marginally stable recycling cavities also means that the TCS will have to correct beam aberrations of the "cold" interferometer (at very low power). The "cold" defects are the ones induced in the recycling cavities by the surface figure of the mirrors or by the inhomogeneity in the refractive index of the input test masses and beam splitter. The TCS should compensate these defects down to a total aberration level of 2 nm RMS [43]. As a results much larger defects have to

be corrected by the TCS and major upgrades have been foreseen both in the sensing and actuation systems.

The sensing system of the TCS in Advanced Virgo will be composed of an Hartmann wave-front sensor, a phase camera and will also used some of the interferometer channels [44]. The Hartmann wave-front sensor will monitor the optics with a significant thermal load such as the input test masses.

On the actuation side, ring heaters will be installed around the arm mirrors to mitigate the thermo-elastic deformation and correct the radius of curvature errors. A CO_2 laser is the baseline solution for the correction of axisymmetric defects. On the contrary of Virgo TCS, the CO_2 laser shines on the compensating plate and not directly on the test mass to avoid a residual motion of the test mass because of power fluctuation of the CO_2 laser. A scanning system is also foreseen to correct the non-axisymmetric system.

The optical parameters of the Advanced Virgo interferometer are reported in 1.1.
Many other systems have been upgraded for Advanced Virgo, such as the detection system which will now be entirely suspended and under vacuum. A new output mode-cleaner is also developed to allow RF sidebands filtering. The vacuum system will also be improved by a factor 100 installing large cryotraps to provide a residual gas pressure of 10^{-9} mbar. The vacuum links have also to be re-designed in the central area to comply with the larger beam.

1.4.3 The Advanced Virgo mirrors

In interferometric gravitational wave detectors the mirrors play a crucial role in the sensitivity of the detectors as we can see from the sensitivity curve (fig. 1.9). Indeed the sensitivity is limited in the mid-frequency region by the coating Brownian noise due to the mechanical losses of the coating. On the high frequency part of the sensitivity curve the limitation is the shot noise which is directly linked to the power circulating inside the cavity. The mirrors should then have very low optical losses such as absorption, scattering due to punctual defects, roughness (defects smaller than $<$ 1 mm) or due to the mirror surface figure. The optical losses due to the mirrors will result in a reduced power and so in an increase of the shot noise level. The scattering due to the roughness and the punctual defects should be less than 10 ppm for each optics. The coating absorption should be less than 1 ppm for the input mirrors, less than 0.5 ppm for the end mirrors and less than 2 ppm for the BS, and recycling mirrors [23].

The Advanced Virgo mirrors are made of high quality fused-silica substrates and of a multilayer coating deposited on the surfaces of the substrates. The multilayer coating is

Table 1.1: Main optical parameters of the Advanced Virgo interferometer.

Laser and optical power	
Laser wavelength	1064 nm
Laser power at input	125 W
Arm cavity power	650 kW
Power on beam splitter	4.9 kW
Fabry-Perot arm cavity geometry	
Length	2999.8 m
Input mirror RoC	1420 m
End mirror RoC	1683 m
Beam size on IM	48.7 mm
Beam size on EM	58.0 mm
Cavity waist	9.69 mm
Waist position	1363 m
Fabry-Perot arm cavity finesse	
Finesse	443
Input mirror transmission	1.4%
End mirror transmission	1 ppm
Round-trip losses	75 ppm
Power recyling cavity	
Length	11.952 m
PR mirror RoC	1430 m
PR transmission	3.5%
Recycling gain	40
Signal recyling cavity	
Length	11.952 m
SR mirror RoC	1430 m
SR transmission	20%
finesse	26
SR tuning	0.35 rad

Figure 1.12: Input mirror blank (35 cm diameter, 20 cm thickness).

an alternate of silica and titanium doped tantala materials (the coating deposition will be discussed in the chapter 6).

The substrates of the IM and EM have a diameter of 35 cm, a thickness of 20 cm and a weight of 42 kg (see figure 1.12). The mirror weight has been increased in comparison to Virgo to reduce the radiation pressure noise which starts to be important even though not dominant at low frequencies. The PR and SR mirrors have also a large diameter of 35 cm but with a thickness of 10 cm and the beam splitter has a diameter of 55 cm with a thickness of 6.5 cm. The specification on the substrate index homogeneity is either $< 5 \cdot 10^{-7}$ m peak to valley in the central 100 mm (IM and BS) or $< 3 \cdot 10^{-6}$ m peak to valley in the central 200 mm (PR, SR, CP, POP and EM). The bulk absorption requirement should be smaller than 0.3 ppm/cm for the input mirror and beam splitter, smaller than 1 ppm/cm for the POP and CP and smaller than 5 ppm/cm for the PR, SR and EM. The complete specifications on the mirror substrates can be found in [23]. The input mirrors and beam splitter have more stringent requirements as a lot of power is passing through them and because of their thickness. Indeed they are thicker than the POP and CP plates which are only 35 mm thick.

The losses due to the mirrors should be very low in order to have the minimum power loss in the interferometer and especially in the Fabry-Perot arm cavity. The specification on the round-trip losses in the Fabry-Perot arm cavity is then < 75 ppm. To achieve such low loss in the 3 km long arm, the surface figure error of the mirror should be very small. In this thesis, we will focus on the surface figure of the arm cavity mirrors and define the specifications on the mirror flatness. Then we will present the strategy to obtain mirrors with

such low flatness, from the specification of substrate flatness, the correction of the surface figure to the coating deposition.

1.5 Conclusion

Gravitational waves detection is a very challenging enterprise as no direct detection ever happened at the time of writing of this thesis. The strain amplitude of the radiation being very tenuous, the length variation to be measured by the interferometer is of the order of 10^{-18} m. Thus gravitational wave detectors require technologies which are on the cutting edge of the technology or above in many domains and in optics especially.

The second generation detectors are foreseen to have a sensitivity improved by an order of magnitude in comparison to first generation detectors. The Advanced Virgo sensitivity curve shows us that the mirrors play a crucial role in the final sensitivity with the coating thermal noise and the shot noise being the limiting factor in the mid-frequency and high-frequency regions.

Chapter 2

Study of the thermal lensing in the Advanced Virgo interferometer

2.1 Introduction

In this chapter, we study the behaviour of the interferometer (ITF) against the thermal lensing induced in the input test masses (ITM). It has been study for Virgo in [45]. We will first describe briefly the thermal lensing effect. Then we will discuss two models to describe its effect in the interferometer. In the first model we study only a recycled Fabry-Perot (FP) cavity and the coupling efficiency between the beam coming from the arm and the beam inside the recycling cavity is computed. The thermal lensing is modelled as a thin lens located inside the recycling cavity in front of the ITM. This coupling allows us to assess the effect of the thermal lensing in a simple way. The second model used to study this thermal lensing effect is more complete as we study the whole interferometer. A modal simulation code of the interferometer has been developed. It expands the fields at different point of the interferometer in Laguerre-Gauss modes. The thermal lensing is again modelled as a thin lens in front of the ITM. A mode coupling matrix is computed to simulate the thermal lensing. The number of modes used in the simulation is also discussed because of its importance in the accuracy of the simulation output.

In both cases, many configurations of the ITF have been studied including a Virgo like configuration and Advanced Virgo configurations both in the marginally stable recycling cavity (MSRC) and in the non degenerate recycling cavity (NDRC) cases. The different configurations are compared in a first section. After that the choice of the MSRC configuration has been decided for Advanced Virgo and we studied different configurations until a final design is reached. We finally study the effect of the thermal lensing for this design.

2.2 The thermal lensing effect at the input test mass

In advanced interferometric detectors it is foreseen to have a very large amount of power stored in the FP arm cavities. In the Advanced Virgo final design the finesse of such cavities will be of about 450 [23], it was around 150 in Virgo+ and it was foressen to be 900 in the Advanced Virgo Baseline [42]. Also the power at the input of the interferometer will be of 125 W instead of 20 W in Virgo+. This high power at the input of the interferometer, the high finesse of the arm cavities and a power recycling gain (PRG) of about 37 will make the power stored in the arm cavities to be of 650 kW. This large power in the arm cavities makes the power absorbed in the mirror not negligible even though their absorption is very small [23]. The laser power absorption in the mirrors causes the substrate to have a thermal gradient.

This thermal gradient induces a deformation of the substrate and even more important a gradient in the index of refraction of the substrate. The very high power stored in the arm cavity makes the power absorbed in the coating dominant even though the coating absorption is smaller than the substrate absorption. This thermal gradient can be modelled at first order as a thin lens [28]. This effect is called thermal lensing. The equivalent focal thermal length due to the absorption of light in the mirrors is [46]:

$$f = \frac{2\pi\ \kappa\ w^2}{Pabs\ \ \frac{dn}{dT}} \tag{2.1}$$

where w is the beam width on the input mirror, κ the thermal conductivity of the material, $\frac{dn}{dT}$ is the thermo-optic coefficient that is to say the dependence in temperature of the refractive index and $Pabs$ is the power absorbed in the mirror. According to the substrate manufacturer, Heraeus, $\kappa = 1.38\ W \cdot m^{-1} \cdot K^{-1}$ and $\frac{dn}{dT} = 8.7 \cdot 10^{-6}\ K^{-1}$ [46]. For example the thermal lensing will make a flat-flat mirror appears as a converging lens and an absorbed power of 100 mW will give a thermal lens with a focal length of about 24 km.

Thermal lensing mostly happens in laser interferometric detector at the ITM where a lot of power is on the coating Its effect is to change the recycling cavity geometry. The thermally induced lens makes the beam circulating inside the recycling cavity to converge and so it changes its beam width. Thus the beam circulating inside the cavity will no longer have the wanted width and the matching condition will not be optimal between the recycling and FP cavities. It lowers the recycling gain of the carrier beam and so reduces the power circulating in the interferometer. Thereby it has an effect on the shot noise limitation on the detector sensitivity at high frequencies.

Another effect of the thermal lensing is to degrade the 6 MHz sidebands power recycling

gain. These 6 MHz sidebands (also called RF sidebands) are used to control the interferometer [18]. It is important to have control signals of good quality to control efficiently the interferometer. That is why we use principally the 6 MHz sidebands power recycling gain as a figure of merit of the interferometer behaviour.

To correct this effect a Thermal Compensating System (TCS) has been developed [29]. The principle of the TCS is to heat the external radius of the mirror by an external CO2 laser in order to compensate the heating of the substrate at its center by the laser beam going through it. The TCS will also be designed to compensate more complex deformation due in particular to the refractive index inhomogeneity of the substrate [47].

2.3 The coupling efficiency approach

In this section, we describe the double cavity configurations that have been studied. Then we present the simulation code used to study the thermal lensing and finally we present the results obtained with the different configurations depicted in 2.3.1.

2.3.1 The different double cavity configuration

In this section we will present the different configurations of the power recycling cavity and Fabry-Perot arm cavity studied. There are three configurations for Advanced Virgo simulations and one configuration for Virgo (figure 2.1).

1. Marginally stable recycling cavity (MSRC) with a curved PR mirror and a bi-concave arm cavity. We will refer to it as MSRC n°1.

2. Marginally stable recycling cavity (MSRC) with a flat PR mirror and a plane-concave arm cavity (described in [48]). We will refer to it as Virgo-like MSRC.

3. A Virgo like configuration (Plane concave arm cavity and a plane PR mirror). We will refer to it as the Virgo configuration.

4. Non degenerate recycling cavity (NDRC) configuration 2 described in the note [49] with a bi-concave arm cavity (as described in [42]), we will refer to it as the Advanced Virgo baseline configuration.

There are two kinds of recycling cavity, one is non degenerate and the other one is marginally stable. The difference between the two kinds of cavity is that only modes of the same order resonate in the non-degenerate cavity whereas every mode can resonate in a marginally stable cavity. The arm cavity is either bi-concave or plane concave. The table 2.1

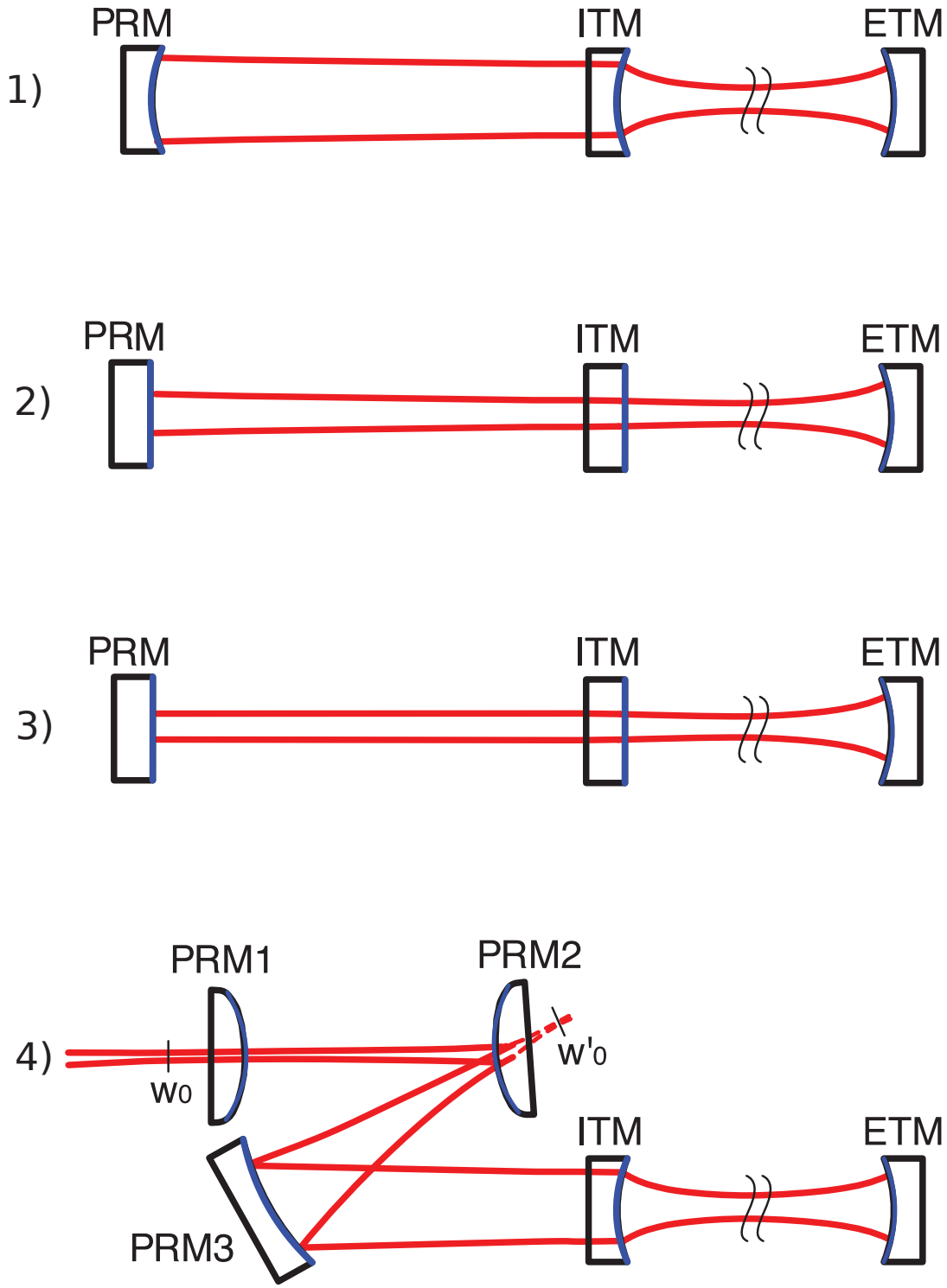

Figure 2.1: The four double cavity configuration studied.

summarises the different parameters for the arm cavity and the figure 2.1 shows a scheme of the configurations.

Table 2.1: Parameters of the arm cavities

Cavity	**RoC ITM**	**RoC ETM**	**Arm Length**
Bi-Concave Arm Cavity	1416 m	1646 m	3000 m
Plane-Concave Arm Cavity	inf	21 km	3000 m
Virgo Arm Cavity	inf	3580 m	3000 m

The MSRC are 12.28 m long and the PR radius of curvature (RoC) is either infinite if coupled with a Plane-Concave cavity or is of 990.92 m if coupled with a bi-concave cavity. The NDRC is a folded cavity with three mirrors that allows to increase the cavity length and curving the wavefront thus the making the cavity stable. The different parameters (RoC, lengths...) are presented in the table 2.2. The parameters used are the one of the configuration 2 in the note [49].

Table 2.2: Parameters of the NDRC

	PRM1	**PRM2**	**PRM3**
RoC (m)	-2.03	-2.04	12.80
	PRM1-PRM2	**PRM2-PRM3**	**PRM3-ITM**
Length (m)	10.5	5.5	11.5

2.3.2 Simulation code

The simulation code is based on ABCD matrices formalism and complex beam parameter (q) propagation [50]. We use the convention given in [51]. The complex beam parameter is defined as follows:

$$\frac{1}{q} = \frac{1}{R} - i\frac{\lambda}{\pi w^2} \tag{2.2}$$

After passing through an element (e.g a lens) described by its matrix $\begin{pmatrix} A & B \\ C & D \end{pmatrix}$, the beam parameter ($q2$) is given by the equation:

$$q2 = \frac{Aq1 + B}{Cq1 + D} \tag{2.3}$$

with $q1$ being the input beam parameter.

A FP cavity can be described as a sequence of elements. From the field leaving the input mirror we have: a free space propagation, a reflection on the end mirror, a free space propagation and to finish a reflection on the input mirror. To compute the equivalent matrix, we multiply each element matrices.

$$M_{FP} = M_{IM} * M_L * M_{EM} * M_L \tag{2.4}$$

where M_L is the free space propagation matrix over the length of the cavity, M_{IM} and M_{EM} are the reflection matrices on the input and end mirror. This kind of periodic sequences are stable when the following condition is obtained:

$$-1 < \frac{1}{2}(A + D) < 1 \tag{2.5}$$

This stability condition of the FP cavity can be written as shown in [50] as:

$$0 < \left(1 - \frac{d}{R1}\right)\left(1 - \frac{d}{R2}\right) < 1 \tag{2.6}$$

where d is the distance between the two mirrors and $R1$,$R2$ are the mirrors radius of curvature (RoC).

The cavity eigenmode is such that the beam after a round-trip in a resonant cavity remains the same. So to compute the beam parameter inside the cavity we solve the equation 2.3 with $q2 = q1 = q$, we get:

$$Cq^2 + (D - A)q - B = 0 \tag{2.7}$$

Solving the equation 2.7 gives:

$$q = \frac{(A - D)}{2C} \pm i\frac{\sqrt{(D - A)^2 + 4BC}}{2C} \tag{2.8}$$

To simulate the thermal lensing effect we add a simple lens in front of the ITM as shown in fig 2.2.

Based on this formalism, the eigenmode of the recycling cavity is computed for different focal length. This beam represents the sidebands at 6 MHz which is anti-resonant in the arm cavity. Then we compute the eigenmode of the arm cavity and we propagate it toward the power recycling (PR) mirror for different focal length.

We estimate the coupling between the two cavities by the mean of the overlap integral between the two beams as shown in [52]. The overlap integral of two beams is simply the

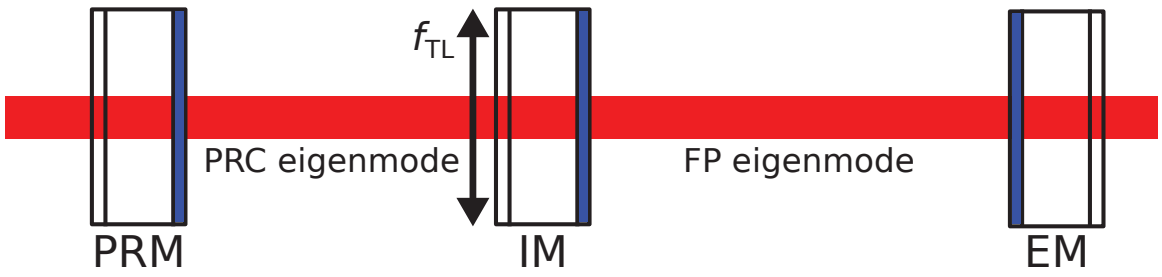

Figure 2.2: Simulation of the thermal lensing effect in a recyled FP cavity.

scalar product of the two normalised beams.

$$\gamma(q1, q2) =< E(q1)|E(q2) > \tag{2.9}$$

Considering that the two beams are TEM00 modes, the overlap integral can be written as:

$$\gamma = \frac{2}{\pi}\sqrt{\frac{1}{w_1^2 w_2^2}}\int_0^{+\inf} re^{-r^2\left[\left(\frac{1}{w_1^2}+\frac{1}{w_2^2}\right)-i\frac{k}{2}\left(\frac{1}{R_1}-\frac{1}{R_2}\right)\right]}dr\int_0^{2\pi} d\theta \tag{2.10}$$

Then we compute the overlap integral between the FP cavity beam propagated toward the PR mirror and the beam circulating in the recycling cavity at the PR mirror. These two beams are dependent on the thermal focal length.

$$\gamma_{FP} =< E(q_{FPprop}(f_{TL}))|E(q_{PR}(f_{TL})) > \tag{2.11}$$

We compute the overlap integral between the beam inside the recycling cavity as a function of the thermal lens and the same beam with no thermal effect, that is to say the beam in the cold state of the interferometer. It represents the coupling between the injection and the recycling cavity.

$$\gamma_{PR} =< E(q_{PR}(f_{TL}))|E(q_{PR}(0)) > \tag{2.12}$$

Finally, the overall coupling between the two cavities is given by:

$$c = \gamma_{FP}^2\gamma_{PR}^2 \tag{2.13}$$

This coupling is normalised to 1 in absence of thermal lensing effect. Please note that the two cavities are taken as if totally independent i.e. what happens in the recycling cavity does not affect the Fabry-Perot arm cavity.

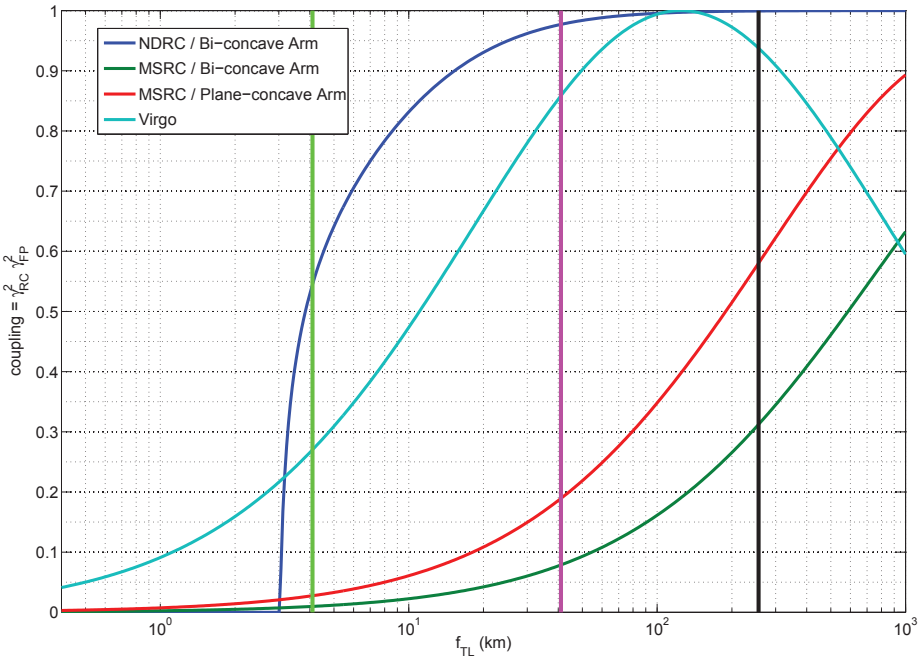

Figure 2.3: Coupling between the recycling and arm cavities as a function of the equivalent thermal focal length. The green vertical line shows the focal length with no compensation, the pink one marks the thermal lensing reduced by a factor 10 (i.e. $f_{TL} = 41\ km$) and the black one marks a thermal lensing of 256 km.

2.3.3 Results of the simulation

The simulations are performed in a range of thermal focal lenght going from 400 m to 1000 km. Figure 2.3 shows the coupling between the arm cavity and the recycling cavity for the four configurations studied. The green vertical lines represents the thermal focal length in absence of correction, the pink line is the thermal lensing reduced by a factor 10 and the black one shows a thermal lensing of 256 km which can be achieved by the TCS correction according to the TCS group [53].

We see that the thermal lensing affects more the configuration with marginally stable recycling cavity. The NDRC configuration is much more immune to thermal lensing as we can see that the coupling is higher than 90 % for a thermal focal length above 15 km and is larger than 99 % above 61.5 km. This configuration is unstable for thermal focal lengths smaller than 3 km. The Advanced Virgo configurations with MSRC configurations are more affected by thermal lensing, we see that for both configurations the coupling do not reach 1 even with thermal focal length of 1000 km, it reaches about 90 % with plane-concave arm and 63 % with bi-concave arm. In the Virgo configuration (North Arm), the coupling reaches 90 % in the range 50 km − 315 km. It drops after a maximum at a thermal focal length of 126 km.

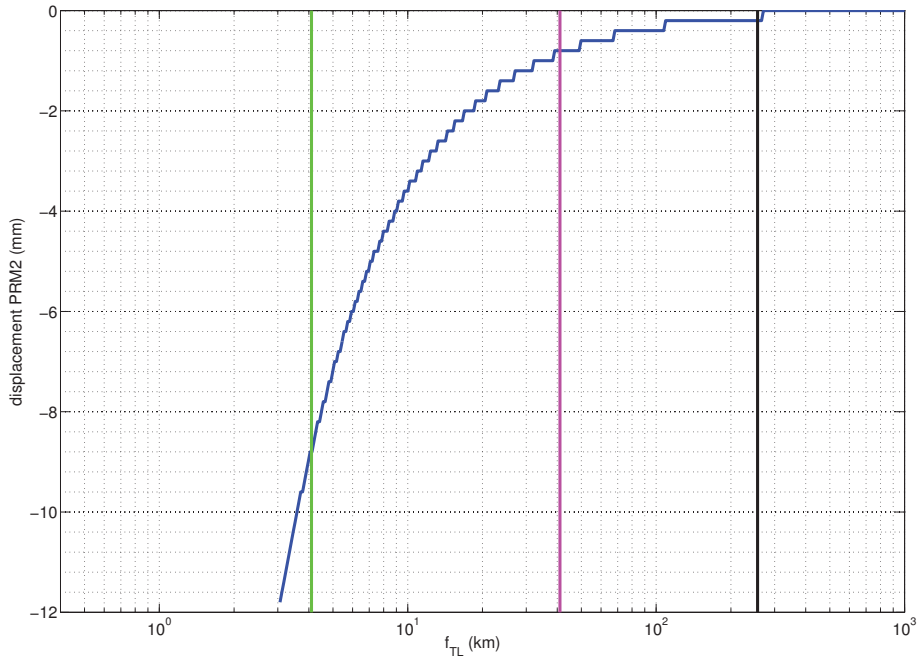

Figure 2.4: Required displacement of the PRM2 mirror to get a maximum coupling as a function of the equivalent thermal focal length. The green vertical line shows the focal length with no compensation, the pink one marks the thermal lensing reduced by a factor 10 (i.e. $f_{TL} = 41\ km$) and the black one marks a thermal lensing of 256 km.

This coupling computation via the overlap integral depends on the size and the radius of curvature of the two beams. And the more the two beams have the same size and RoC, the more the overlap integral approaches 1. In the Virgo case, the coupling drops after a certain thermal lens because of the degeneracy of the plano-plano recycling cavity that makes the beam size tends to the infinite.

The Advanced Virgo configuration with MSRC and Virgo configuration are similar. The major difference is the beam size in the cavities. In Advanced Virgo the beam size in the arm at the ITM is about 5.6 cm, it is about 2.1 cm in the Virgo configuration.

Furthermore in the NDRC configuration, moving the mirror PRM2 from a few millimetres allows to recover a maximum coupling between the two cavities. Figure 2.4 shows the required displacement to obtain a coupling bigger than 99.9%.

From this first basic approach, we see that the configuration with marginally stable recycling cavity are much more sensitive to thermal effects. Moreover the non degenerate recycling cavity offers the possibility to recover the maximum coupling moving the PRM2 mirror of a few millimetres depending on the thermal lensing. In the next paragraph we will present the same study of the thermal effects in the interferometer with a Laguerre-Gauss modal code.

2.4 The Laguerre-Gauss modal code approach

In this section, we describe the study on the thermal lensing in the interferometer using a model based on Laguerre-Gauss mode [51] with a code developed at LMA. The simulation code is presented along with a study on the convergence of the simulation. Then we show the results of the simulation for the baseline design configuration and we compare it with marginally stable recycling cavity configurations. Finally we study different MSRC configurations towards a final design both for common and differential thermal lensing.

2.4.1 Simulation code

The simulation code developed at LMA is a modal code that expands the field inside the interferometer in terms of Laguerre-Gauss mode at different locations of the interferometer. The code is written on GNU Octave (a matlab-like software) and can be run on Matlab. The choice of Laguerre-Gauss mode to simulate thermal lensing is pertinent because of the cylindrical symmetry of the lens. It allows using only the mode LG_p^l with $l = 0$. As a consequence the simulation allows having a smaller number of modes compared to modal code in Hermite-Gauss modes basis. So we use Laguerre-Gauss mode $\mathrm{LG}_{\mathrm{p}}^{\mathrm{l}}$ with $l = 0$ and $p < N_m$ where N_m is the number of modes. The correspondence between Laguerre-Gauss mode and Hermite-Gauss mode is given by $n + m \leq 2 \times (N_m - 1)$, $n + m$ being the mode number of the HG mode simulation. For example $N_m = 5$ corresponds to $n + m = 8$ in terms of Hermite-Gauss modes. A Hermite-Gauss mode based simulation code will use 45 modes for $n + m = 8$ whereas it will only use 5 modes in the Laguerre-Gauss base with $l = 0$. This reduced number of modes fasten the computation with respect to Hermite-Gauss modal code. The complex amplitude of the Laguerre Gauss mode is given by [51], expressed in cylindrical coordinate (r, θ, z, with z being the propagation axis) it is:

$$u_p^l(r,\theta,z) = \sqrt{\frac{2P}{\pi}}\frac{1}{w(z)}\sqrt{\frac{p!}{(p+l)!}}\times\left(\frac{\sqrt{2}r}{w(z)}\right)^l L_p^l\left(\frac{2r^2}{w^2(z)}\right) e^{\left[-i\left(k\left(z+\frac{r^2}{2R(z)}\right)-(2p+l+1)\Phi_G(z)-l\theta\right)\right]} e^{\frac{-r^2}{w^2(z)}} \tag{2.14}$$

where $L_p^l(x)$ is the Laguerre generalized polynomial with p the radial index and l the azimuthal one, w and R are respectively the width and RoC of the beam, P is the beam power and $\Phi_G(z)$ is the Gouy Phase expressed as

$$\Phi_G(z) = \arctan\left(\frac{z}{z_R}\right) \tag{2.15}$$

where Z_R is the Rayleigh range. Assuming $l = 0$ we can write:

$$u_p^l(r,\theta,z) = \sqrt{\frac{2P}{\pi}}\frac{1}{w(z)}\ L_p^l(\frac{2r^2}{w^2(z)})\ e^{\left[-i\left(k\left(z+\frac{r^2}{2R(z)}\right)-(2p+1)\Phi_G(z)\right)\right]}\ e^{\frac{-r^2}{w^2(z)}} \tag{2.16}$$

The fields inside the interferometer are computed at different locations of the interferometer; the simulation provides five of these fields as output:

- Inside the power recycling cavity (PRC), the field on the PR mirror surface which propagates towards BS (Ψ_{RC}).
- Inside the two Fabry-Perot arm cavities, the field on the ITM mirror surface which propagates towards ETM (Ψ_{fp1} (north arm) and Ψ_{fp2} (west arm)).
- Inside the signal recycling cavity (SRC), the field on the SR mirror surface which propagates towards BS (Ψ_{SC}).
- At the Dark Port (Ψ_{DF}).

The fields are expressed in the basis of the long arm cavities mode. The carrier as well as the 6 MHz and 55 MHz sidebands fields are computed. As before, thermal effects are modelled as simple thin lens. The power absorbed in the ITM substrate is high because of the high power circulating inside the FP arms. It causes a transverse gradient of refractive index that can be modelled as a thermal lens under certain assumption [28]. This thermal lens is simulated inserting a lens inside the ITM during the simulation.

The thermal lensing in the modal simulation is modelled as a mode coupling matrix M_{mn} which couples LG modes as the beam passes through it. The coupling matrix is dependent on the beam size as it is computed as the scalar product of the deformed field with the initial one.

$$M_{mn} = \int\int \Psi_n^*\ \exp^{\frac{kr^2}{2f_{TL}}}\ \Psi_m dr \tag{2.17}$$

where m is the index of the output mode (i.e. LG_{m0}), n is the index of the input mode and f_{TL} is the thermal focal length.

The code allows us to set the thermal focal length at each input mirror independently so that we can study the response of the interferometer in differential mode as well as in common mode (same thermal lensing in both arms). The lens matrices are normalised so that the carrier is always resonant inside the power recycling cavity and the arms. However the interferometer is tuned by the mean of microscopic tuning of the various mirror positions so that the resonant conditions are found both for carrier and sidebands. For a given thermal lensing the simulation code tunes the interferometer and gives in output the

five fields described earlier. We applied a tuning to find the desired resonant condition [18] inside the interferometer. Doing so we simulate the locking of the real interferometer. The tuning algorithm is the following:

- PRCL (l_{pr}): It adjusts the PRC length in order to maximize and equalise the lower and upper 6 MHz sidebands inside the PRC.
- CARM ($L_1 + L_2$): It adjusts the arm cavity lengths in order to maximize the carrier inside the PRC. It is equivalent to maximize the mean power of the two FP arms.
- MICH ($l_1 - l_2$): It adjusts the central Michelson lengths, it balances the upper and lower 55 MHz sidebands inside the PRC. We want to have the same power in both 55 MHz sidebands in order to avoid having one sideband resonating more than the other in one recycling cavity and the other one in the other recycling cavity.
- DARM ($L_1 - L_2$): It adjusts the arm cavity lengths to recover the dark fringe condition for the carrier.
- SRCL (l_{sr}): It adjusts the signal recycling cavity length in order to minimize the 55 MHz sidebands inside the PRC and so maximise it in the SRC. This last tuning has no effects on the 6 MHz sidebands and carrier resonant condition as they are not resonant in the SRC.

The main effect of the thermal lens inside the ITM is to degrade the 6 MHz sidebands power recycling gain. Then as a figure of merit of the interferometer behaviour we use the 6 MHz sidebands power recycling gain as a function of the thermal lensing.

2.4.2 Convergence of the simulations

Modal code is quite a versatile tool as the number of modes to be used depends on the parameters of the simulation that is to say the thermal lensing, the geometrical and optical parameters of the interferometer. The convergence of the output should be studied and the number of modes used must be chosen carefully in order to obtain trustworthy results.

The effect of the thermal lensing is to excite the high order modes in the recycling cavity as the light passes through the ITM. These high order modes resonate freely in the marginally stable recycling cavity. It is not the case in the non-degenerate recycling cavity.

A study on the convergence of modal simulations of MSRC in the Virgo and Advanced Virgo configurations has been carried out. There are two main differences between the two MSRC configurations. One is the beam size at the input test mass and the other one is the Gouy phase inside the recycling cavity (the two being linked).

In the Advanced Virgo baseline configuration the beam size at the ITM is about 5.6 cm whereas it is about 2.1 cm in the Virgo case. After the revision of the arm cavity geometry proposed in [54], the beam size on the input mirror is about 4.9 cm. This beam size plays an important role in the number of mode to be used. In the Advanced Virgo case, the beam is larger and thus the thermally induced lens can excite modes of higher order than the thermal lens induced by the 2.1 cm Virgo beam.

In the Virgo configuration the Gouy phase inside the recycling cavity is 0.5 degree whereas it is 0.08 degree in Advanced Virgo. This larger Gouy phase is enough to put very high order mode out of resonance in the recycling cavity. To study the convergence of the simulations we simulate the whole interferometer with common thermal lensing (same thermal lens on both arms) in the range $f_{TL} = \infty - 20$ km and we look at how much the 6 MHz sideband are affected. It has been done on the baseline version of the arm cavity but the conclusion remains true after its revision considering the smaller beam size.

Figure 2.5 shows the 6 MHz sideband recycling gain in the MSRC configurations both for Advanced Virgo and Virgo configurations. We can see that in the Advanced Virgo configuration we need 20 modes to reach a suitable convergence for large thermal lensing (i.e $f_{TL} = 20$ km). 20 modes in LG basis are equivalent in the HG basis to $n + m = 38$ modes that is to say 780 modes. It explains the gain in time while using LG modes in this kind of simulation. The convergence number of modes is reduced to 12 for the Virgo configuration. The red cross and plus shows the coupling between a recycling cavity and a Fabry-Perot cavity computed by the mean of the overlap integral as explained in 2.3. It is interesting to see that the values given by the overlap integral are quite close to the ones given by the modal simulation.

The same simulation has been performed on SIS (Static Interferometer Simulation [55]) on a double cavity in [56]. For a thermal focal length of 70 km, the 6 MHz sidebands recycling gain is 11.1 % whereas it is 17.2 % in the modal simulation and 12.1 % in the coupling computation. The modal simulation seems to overestimate the recycling gain. It can be explained by the effect of the clipping losses due to the finite size of the mirror which is not taken into account in the modal simulation.

A similar study has been done in [57] on the Hermite-Gauss modal code MIST [58]. It shares the same conclusion on the high number of modes to be used when simulating marginally stable recycling cavities especially in Advanced Virgo.

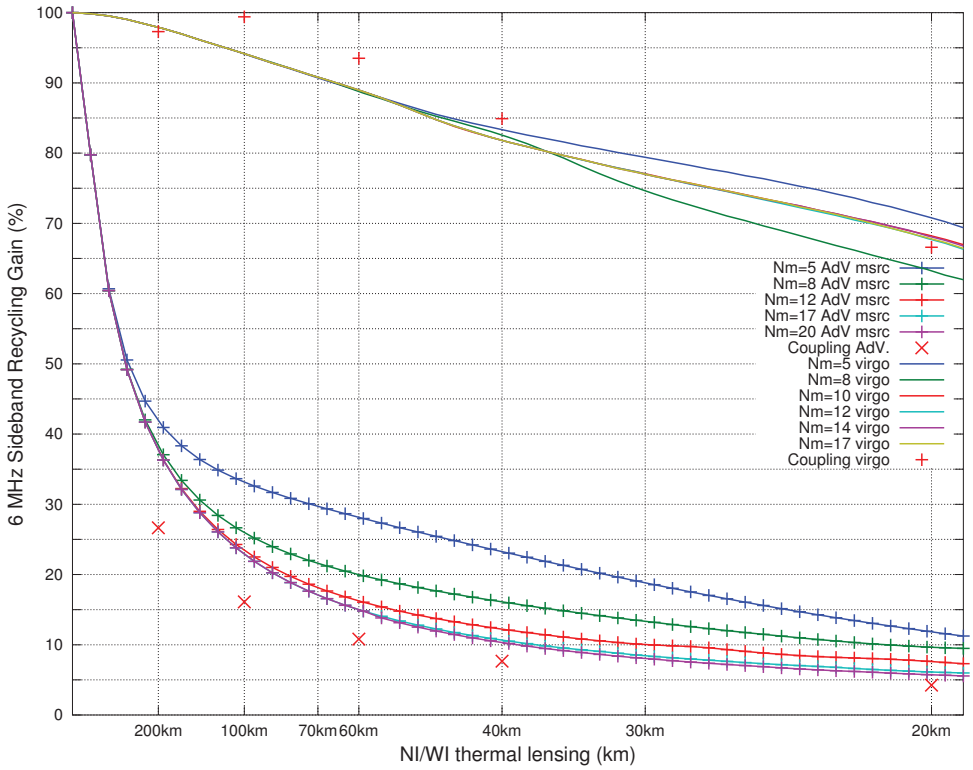

Figure 2.5: 6 MHz Sidebands Power Recycling Gain (%), Adv. MSRC and Virgo cases for different numbers of modes.

2.4.3 The baseline design

Here we study the baseline design [42] as presented in the paragraph 2.3.1. We remind the reader that the baseline design features non-degenerate recycling cavities. The parameters used in the simulations are listed in the table 2.3. First we study the choices of the Gouy phases in the power and signal recycling cavities. To do so we study the effect of the differential thermal lensing that is to say the thermal lensing is set independently in the north and west arm in the range $f_{TL} = \infty$ to $f_{TL} = 20\ km$. Then we will show the effect of differential thermal lensing with the chosen Gouy phases. Finally we compare the effect of the common thermal lensing (i.e. equal thermal lensing in both arms) on the 6 MHz sideband recycling gain between the baseline design, the MSRC n°1 proposed in [48] (configuration 1 in figure 2.1) and the Virgo configuration (configuration 3 in figure 2.1). The MSRC configuration has been proposed to overcome the problem of controlling the double payload. Indeed the baseline configuration implied to have multiple mirrors on the same payload increasing a lot the complexity of the mirrors control [59].

2.4.3.1 Parameters

The parameters of the arm cavities are the same in the MSRC and NDRC configuration for Advanced Virgo. They are listed in table 2.3.

Table 2.3: Advanced Virgo Arm parameters before revision

Mirror	**Power Transmission**	**Losses**	**Radius of Curvature**
ITM (North and West)	0.0069	37 ppm	1416 m
ETM (North and West)	0	37 ppm	1646 m

The other parameters, i.e. the distances between mirrors, the radii of curvature and the mirrors transmission and losses are listed below.

NDRC parameters(from [60])

Distances beetween mirrors	PRC	
	lr1 (PRM1-PRM2)	10.027 m
	lr2 (PRM2-PRM3)	10.123 m
	lr3 (PRM3-BS)	10.450 m
Distances beetween mirrors	SRC	
	ls1 (SRM1-SRM2)	9.556 m
	ls2 (SRM2-SRM3)	9.652 m
	ls3 (SRM3-BS)	9.952 m
Distances between mirrors	Central Part	
	lx (BS-IMX)	5.789 m
	ly (BS-IMY)	5.889 m
Distances between mirrors	Arm Cavities Distances	
	Larm North	3000.55 m
	Larm West	2999.8 m

Radius of Curvature	PRC	
	PRM1	-2.853 m
	PRM2	-2.853 m
	PRM3	22.543 m
Radius of Curvature	SRC	
	SRM1	-2.866 m
	SRM2	-2.866 m
	SRM3	21.626 m

First modulation frequency	6170368 Hz
Second modulation frequency	55533313 Hz

Gouy Phases (PRC)	25 °
Gouy Phases (SRC)	20 °

2.4.3.2 Choice of the Gouy phase

The Gouy phase can be described as the longitudinal delay due to the propagation of the field inside the cavity. In the case of a folded cavity as in the NDRC version of Advanced Virgo, one can adjust the parameters in order to choose the Gouy phase inside the recycling cavities. The Gouy phase plays a role in the resonance of high order modes in a cavity. So, the choice of the Gouy phases in the PRC and SRC can affect the behaviour of the interferometer and causes the carrier or the RF sidebands gains to drop.

To study how the PRC and SRC Gouy phases impact the response of the interferometer to thermal lensing, we run the simulation changing the Gouy phases in the recycling cavities between 5 degree and 25 degree with a 5 degree step. Figure 2.6 shows the carrier recycling gain response to differential thermal lensing for different Gouy phases in PRC and SRC. From the left to the right, the power recycling Gouy phase goes from 5 degree to 25 degree. From bottom to top the signal recycling Gouy phase goes between 5 and 25 degree. Each map represents the carrier power recycling gain as a function of the thermal focal length in the north and west arm respectively for the horizontal and vertical axis. The axis scale in $\frac{1}{f_{TL}}$ with the thermal focal length going from 10000 km to about 20 km. We can see that in the case of a Gouy phase of 15 degree in the power recycling cavity, it causes the carrier power recycling gain to drop below 5 (the maximal carrier recycling gain being around 26) in a large stripe. This drop is due to the LG_2^0 mode that resonates inside the PRC.

Concerning the RF sidebands, we can see in figure 2.7 that the 6 MHz upper sideband power recycling gain drops in two thermal lensing regions for $\Phi_G(PRC) = 5°$ and $\Phi_G(SRC) = 20°$. The LG_2^0 mode is resonating inside the signal recycling cavity in these two regions causing thus a drop of the 6 MHz upper sideband power recycling gain in the PRC. In the same regions of thermal lensing the 6 MHz lower sideband is affected for $\Phi_G(PRC) = 5°$ and $\Phi_G(SRC) = 15°$, see figure 2.8. Again we see that this is due to the LG_2^0 mode resonating inside SRC as well as the LG_3^0 mode.

To conclude, the Gouy phases in the two recycling cavities should be chosen carefully in order to avoid unwanted resonances of high order modes. We see that the RF sidebands (upper and lower) are quite resistant to thermal lensing with non-degenerate recycling cavity.

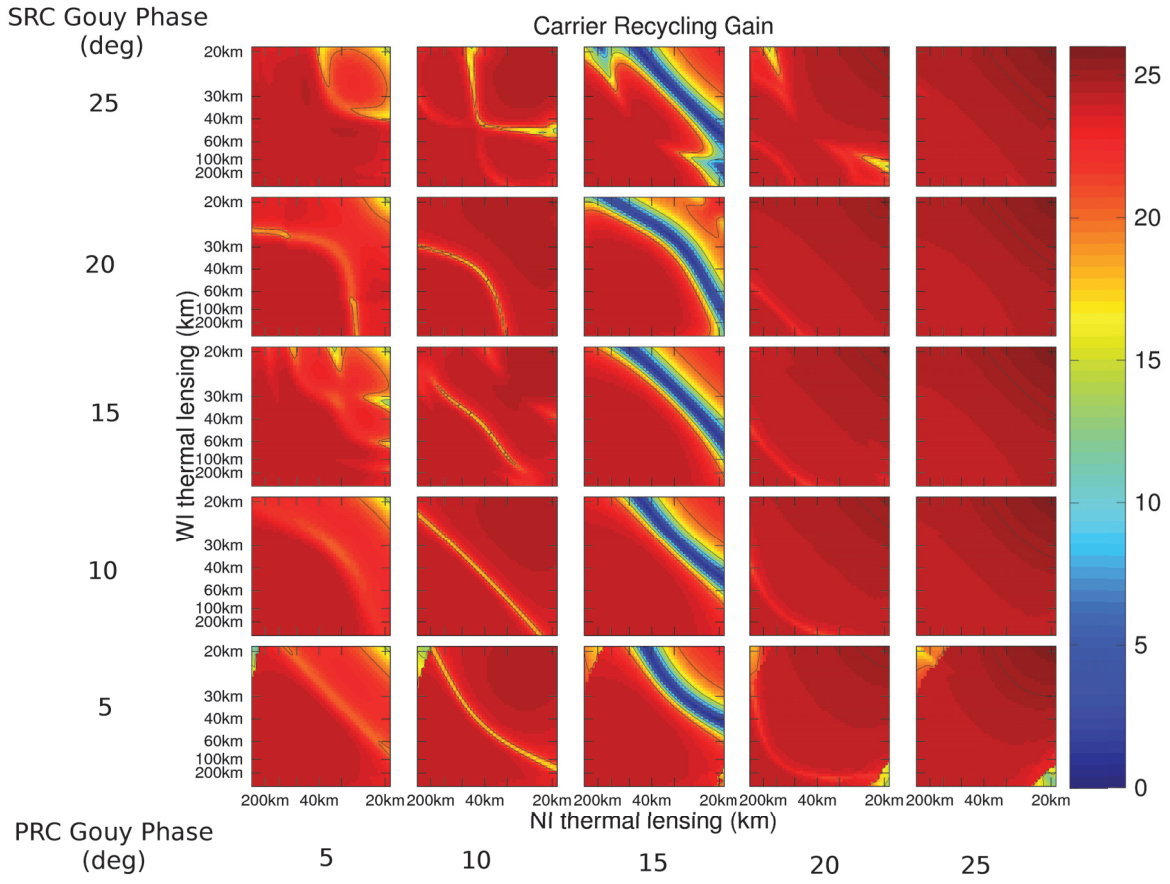

Figure 2.6: Carrier Power Recycling Gain for differential thermal lensing for different PRC and SRC Gouy phases. Sub-plots have the same color axis.

This good response to thermal lensing is intrinsic to the nature of NDRC. Indeed only the TEM_{00} is resonant in those cavities and so even if higher order modes are coupled in the power recycling cavity by thermal lensing they are rapidly extinguished.

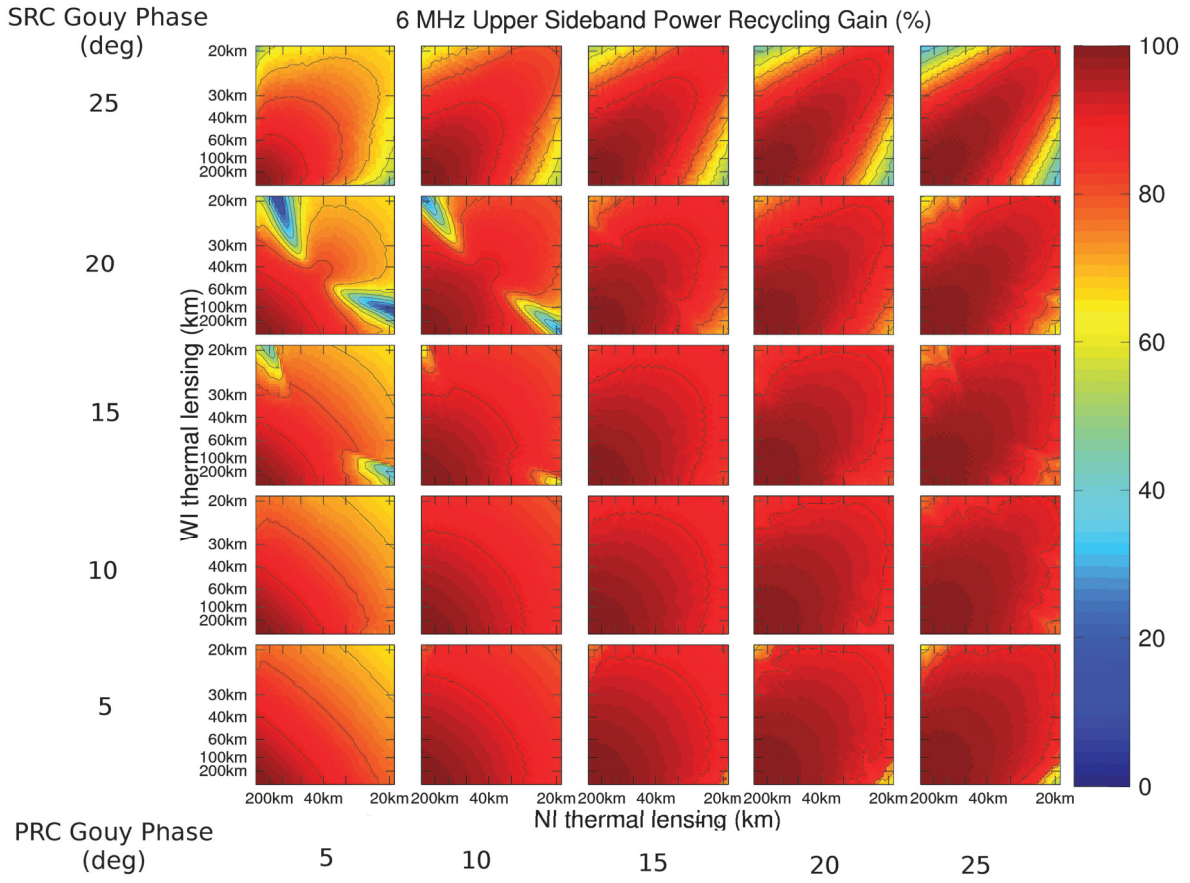

Figure 2.7: 6MHz Upper Sideband Recycling Gain for differential thermal lensing for different PRC and SRC Gouy phases. Sub-plots have the same colar axis.

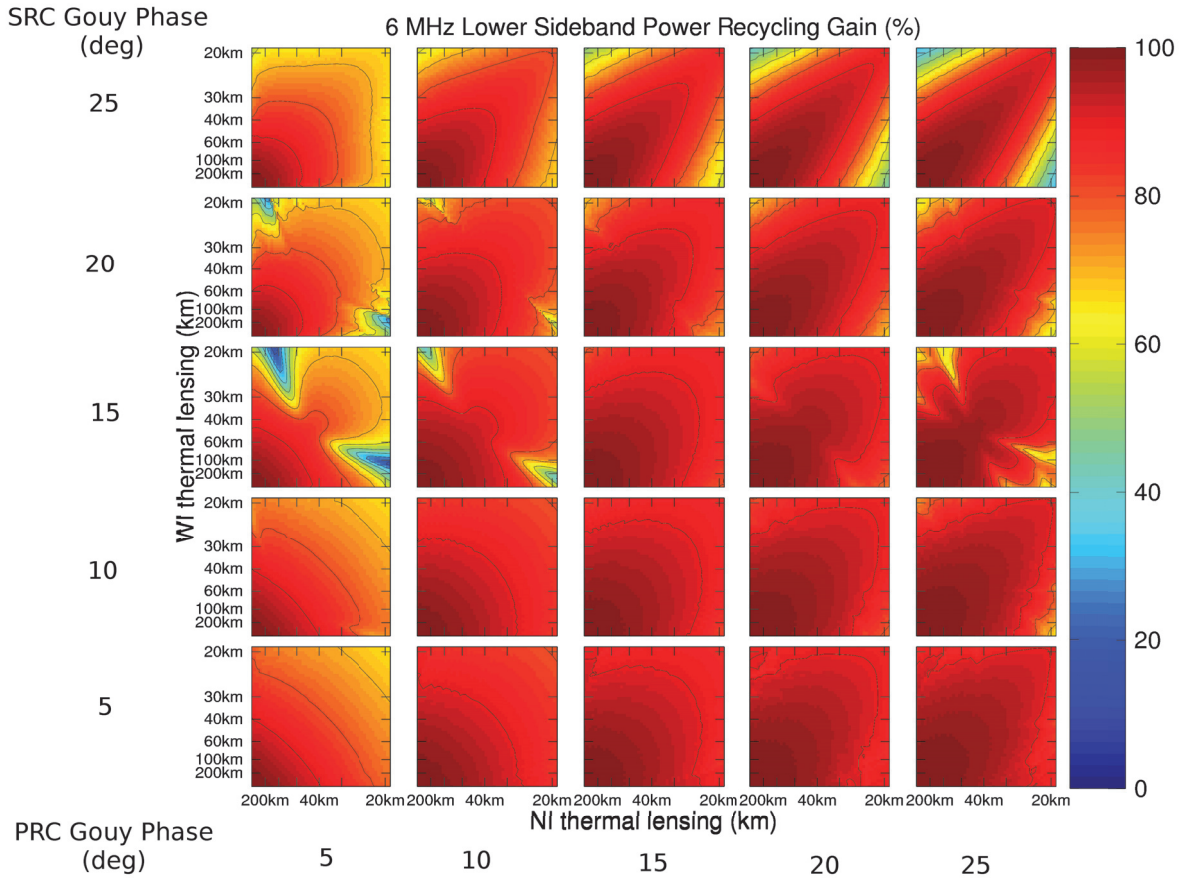

Figure 2.8: 6 MHz Lower Sideband Recycling Gain for differential thermal lensing for different PRC and SRC Gouy phases. Sub-plots have the same colar axis.

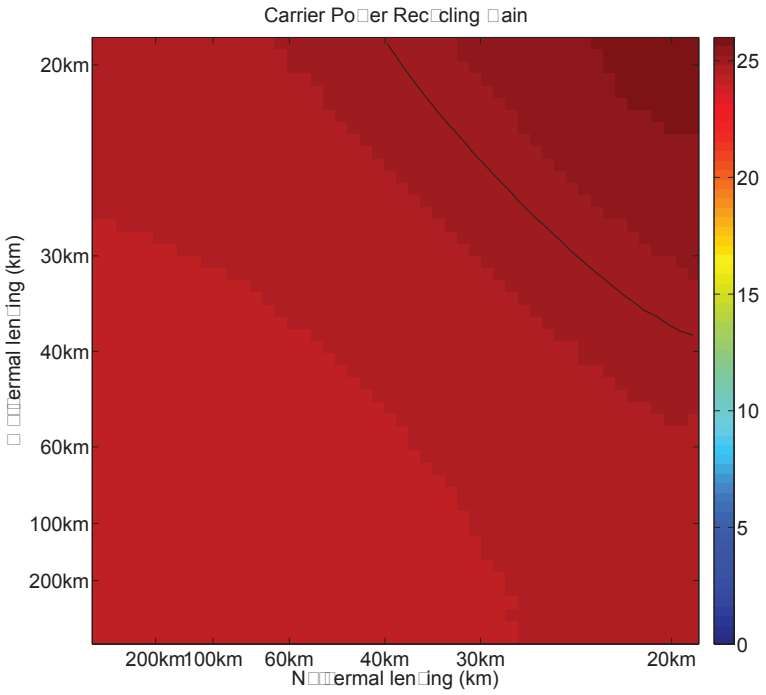

Figure 2.9: Carrier Power Recycling Gain for AdV. baseline configuration (NDRC) as a function of the thermal lensing in NI and WI. The Gouy Phases are 25 degrees for PRC and 20 degrees for SRC.

2.4.3.3 Simulations with the chosen Gouy phases

Finally a PRC and SRC Gouy phases of respectively 25 degrees and 20 degrees seems to be a good choice. In the following we show in details the results of the simulations for such a choice. Figure 2.9 shows the carrier recycling gain as a function of the thermal lens in the NI and WI mirrors respectively on the horizontal and vertical axis. We see that the carrier gain remains high for every thermal lens even with very high differential thermal lensing.

The behaviour of the 6 MHz sidebands is good even for very high differential thermal lensing, see figure 2.10. It is in the worst case around 60% of the maximal gain for a thermal focal length of 20 km in NI and no thermal lens in WI. In most cases the RF sidebands gain remains higher than 80%.

2.4.3.4 Comparison of the baseline configuration with MSRC configuration

The baseline design implies to have multiple mirrors on the same payload [59]. After study some problems arose about the control of such double payload. Consequently a new configu-

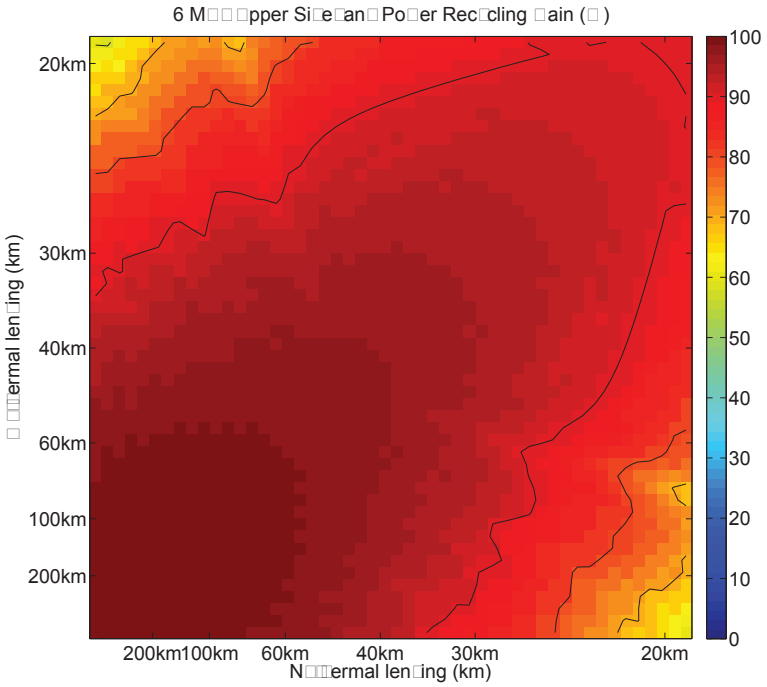

Figure 2.10: 6 MHz Sideband Power Recycling Gain (%) for AdV. baseline configuration (NDRC) as a function of the thermal lensing in NI and WI. The Gouy Phases are 25 degrees for PRC and 20 degrees for SRC.

ration has been proposed with marginally stable recycling cavities for Advanced Virgo [48]. Therefore we study the effect of the common thermal lensing in the proposed configuration. We compare it with the baseline design and with the Virgo configuration. The parameters for the recycling cavities in the MSRC for Advanced Virgo and the Virgo configurations are listed below.

Recycling Cavities Parameters — MSRC

Distances beetween mirrors	l_{PRC}	11.952 m
	l_{SRC}	10.624 m
Distances between mirrors	Arm Cavities Distances	
	Larm North	3000 m
	Larm West	3000 m

Radius of Curvature	PR	988.801 m
	SR	988.801 m

First modulation frequency	6270659 Hz
Second modulation frequency	56435931 Hz

Recycling Cavity Parameters — Virgo

Mirror	Power Transmission	Losses	Radius of Curvature
PR	0.0513	25.54 ppm	inf
NI	0.118	250 ppm	inf
NE	42.9 ppm	250 ppm	3580 m
WI	0.1166	250 ppm	inf
WE	38.3 ppm	250 ppm	3601 m

Distances beetween mirrors	l_{PRC}	11.88 m
	L_N	3000 m
	L_W	3000 m
First modulation frequency	6229653 Hz	

The results shown in figure 2.11 are obtained with a number of modes $Nm = 20$ ($\equiv n + m = 38$, that is to say 780 modes in HG basis) for Advanced Virgo and $Nm = 12$ ($\equiv n + m = 22$, that is to say 276 modes in HG basis) for Virgo (see the discussion in 2.4.2 about the pertinence of the number of modes chosen). It shows that the MSRC configuration is considerably affected by thermal lensing compared to the non-degenerate one. This is due to the fact that the high order modes are not resonant inside the non-degenerate recycling cavities, i.e only the TEM_{00} is resonant. The high order modes excited by the thermal lens are filtered by the cavity.

On the contrary, in the MSRC case, the high order modes excited by the thermal lens are free to resonate inside the power recycling cavity and so they induce a loss of power in the TEM00. For the MSRC case, to get at least 30 % of the 6 MHz sidebands in the power recycling cavity the common thermal lensing should not be smaller than 144 km. For NDRC this condition is always reached in the range of focal length studied. Indeed with a common thermal lensing of 20 km, the 6 MHz sidebands gain inside the PRC is about 90 %.

For the Virgo case the 6 MHz sidebands gain is always higher than 65 % in the same range of thermal focal length, it is 67.8 % at 20 km. The marginally stable configuration case is more affected by thermal lensing in the Advanced Virgo case than in the Virgo case. This is presumably due to the size of the beam at the input mirrors. The beam is bigger in Advanced Virgo and so a given thermal lens excites more modes than with a smaller beam. Another explanation to this difference is the Gouy phase being larger in Virgo than in Advanced Virgo(0.5° compared to 0.08°). This larger Gouy phase causes the higher order mode to be out of resonance in Virgo whereas they are not in Advanced Virgo

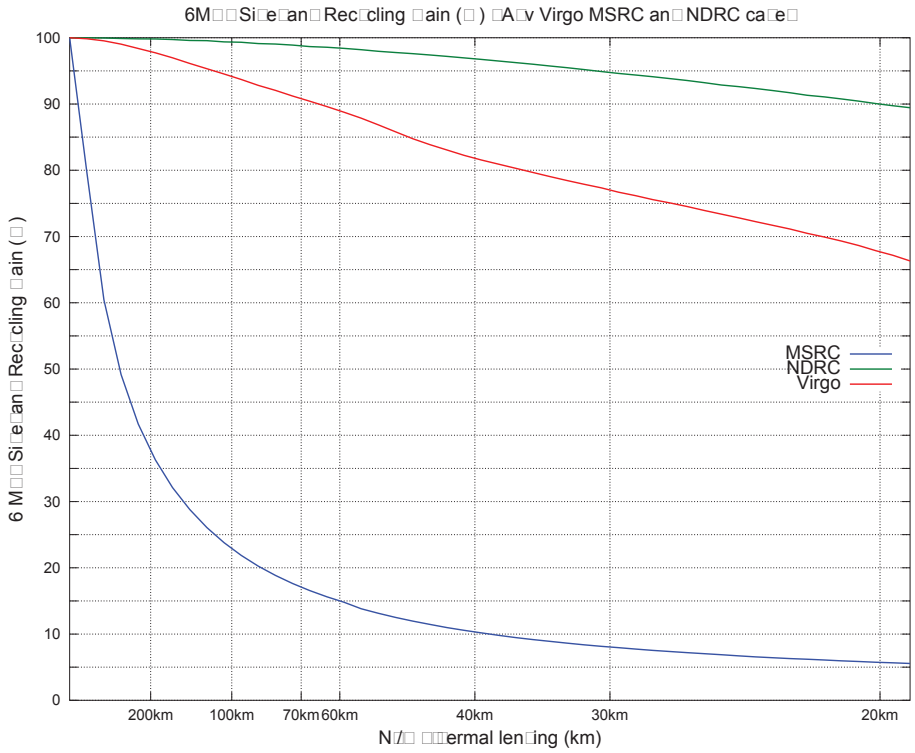

Figure 2.11: 6 MHz Sideband Power Recycling Gain (%) for different configuration, AdV. MSRC and NDRC and a configuration similar to Virgo. The gains are plotted as a function of the thermal lensing.

We also plot the same 6 MHz sidebands power recycling gain but as a function of the absorbed power in the mirror substrates (in ppm) in a range from 0.1 ppm to 3 ppm (figure 2.12). Considering a beam width of 5.6 cm on the ITM that is to say the Advanced Virgo baseline design, the relation between the focal length and the absorbed power is $f \approx \frac{3100}{P_{abs}}$ m where P_{abs} is the laser power absorbed in the input mirror in Watt. For Virgo, the same relation considering a beam width of 2.1 cm becomes $f \approx \frac{440}{P_{abs}}$ m. The range of absorption from 0.1 ppm and 3 ppm corresponds to a range of focal length of about 41 km to 1.4 km for Advanced Virgo with 760 kW impinging on the ITM. The range of focal length becomes 730 km to 24 km for Virgo with 6 kW of laser power on the ITM. We clearly see that for a given coating absorption the induced thermal lensing is smaller (i.e. larger thermal focal length). The Advanced Virgo MSRC configuration is very badly affected by thermal lensing with a 6 MHz sidebands power recycling smaller than 11 % for Advanced Virgo in the range of absorption studied. On the contrary, the Virgo configuration is more robust to thermal lensing with a 6 MHz sidebands power recycling gain always higher than 73 %.

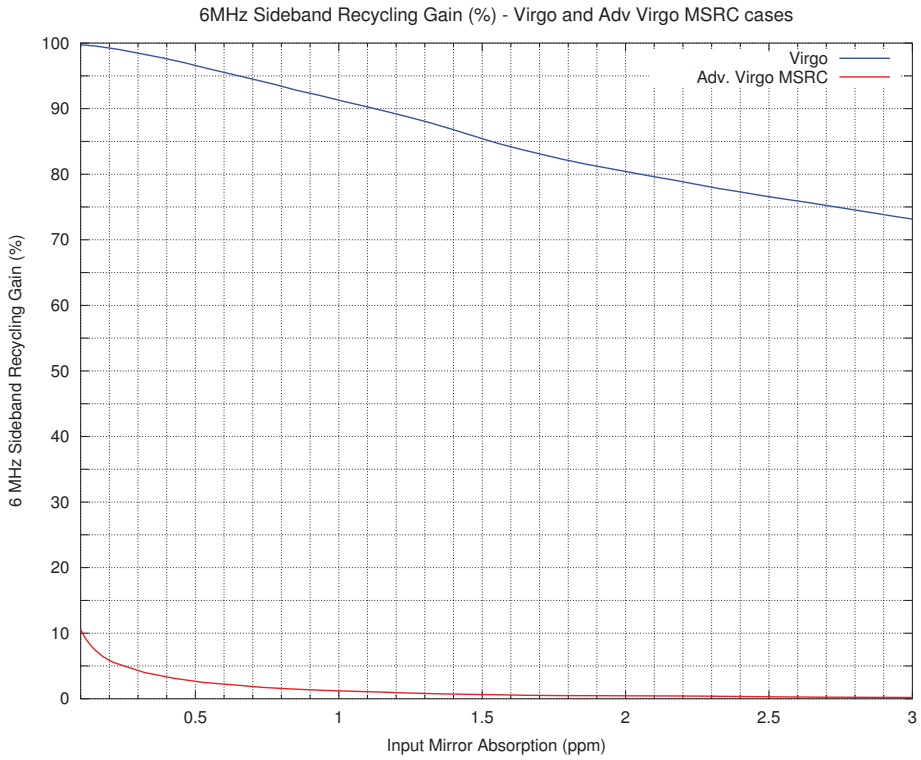

Figure 2.12: 6 MHz Sideband Power Recycling Gain (%) for different configuration, AdV. MSRC and a configuration similar to Virgo. The gains are plotted as a function of the absorption in the input mirror

2.4.4 The Marginally Stable Recycling Cavities configurations

In this section, we study the thermal lensing effect with different configurations proposed before reaching a final design for Advanced Virgo with marginally stable recycling cavities. A study on the differential thermal lensing on this final design is being presented thereafter.

2.4.4.1 Toward a final design

After revision of the arm cavity RoC, a new simulation has been performed with the MSRC configuration. The beam width on the ITM is smaller after revision, it is 4.9 cm instead of 5.6 cm and thus less high order are coupled in the PRC. The simulation results are shown in figure 2.13, we can see that reducing the beam width on the ITM reduces slightly the degradation of the 6 MHz sidebands gain especially for quite high thermal focal length ($f_{TL} < 100\ km$). At most the RF sideband power recycling gain is increased to 7.5 % instead of 5 % for a large thermal lens.

In 2011, a new configuration has been proposed in [61]. It proposed to lower the arm cavity finesse to 180 along with a higher power recycling gain and changes in the geometrical parameters (RoC, lengths, etc...) of the recycling cavity. New simulations have been

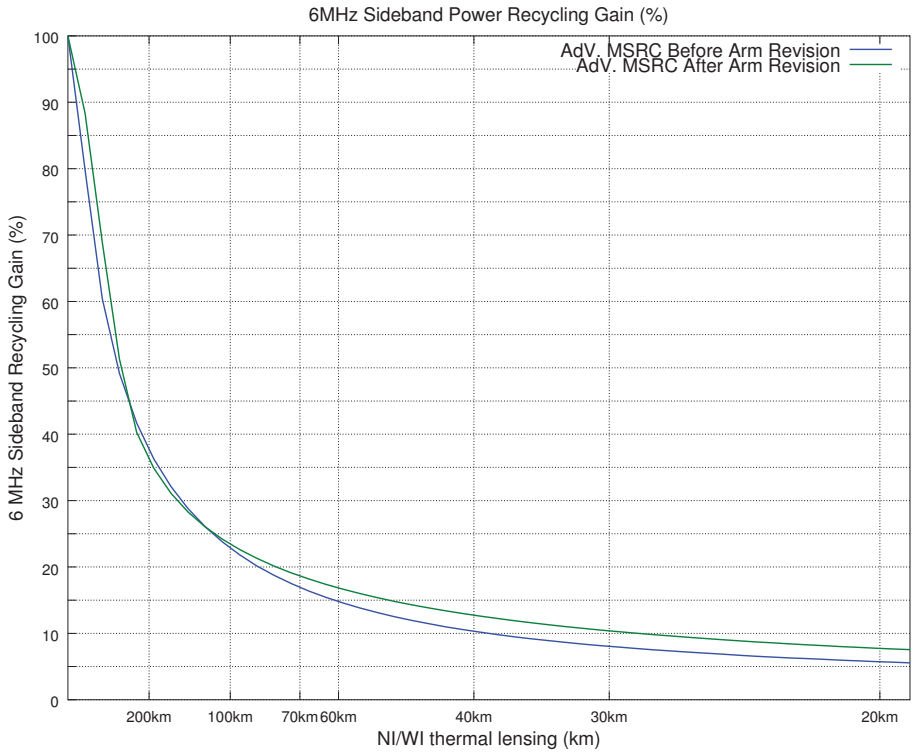

Figure 2.13: 6 MHz Sideband Power Recycling Gain (%) for AdV. MSRC configuration before (blue) and after (red) arm revision. The gains are plotted as a function of the thermal lensing.

performed with these new parameters. The 6 MHz sidebands recycling gain is plotted in the figure 2.14 for different optical and geometrical parameters. We can see that the recycling gain is dropping for a thermal focal length of about 1300 km. This is due to the excitation of the LG_1^0 mode in the PRC. This mode shows a peak of resonance at this thermal focal length (figure 2.15). This drop in the RF sidebands recycling gain is due to the lower finesse of the arm cavities and the higher recycling cavities gain as with the new geometrical parameters, the finesse of 900 and lower recycling gain, this drop disappears. This observation has been confirmed by independent simulation done with the simulation modal code MIST [62].

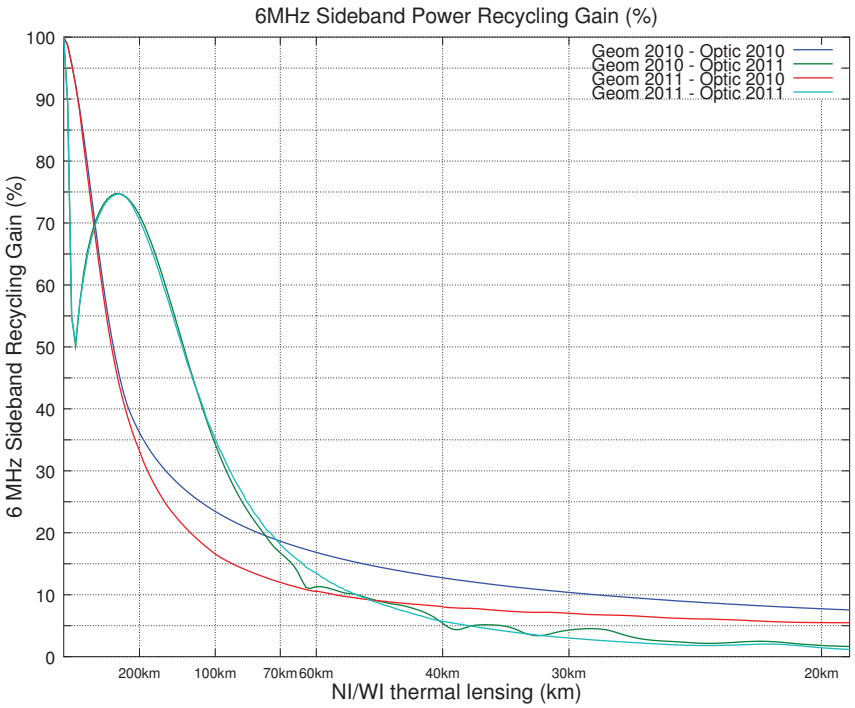

Figure 2.14: 6 MHz Sideband Power Recycling Gain (%) for different optical and geometrical AdV. MSRC configuration. The gains are plotted as a function of the thermal lensing.

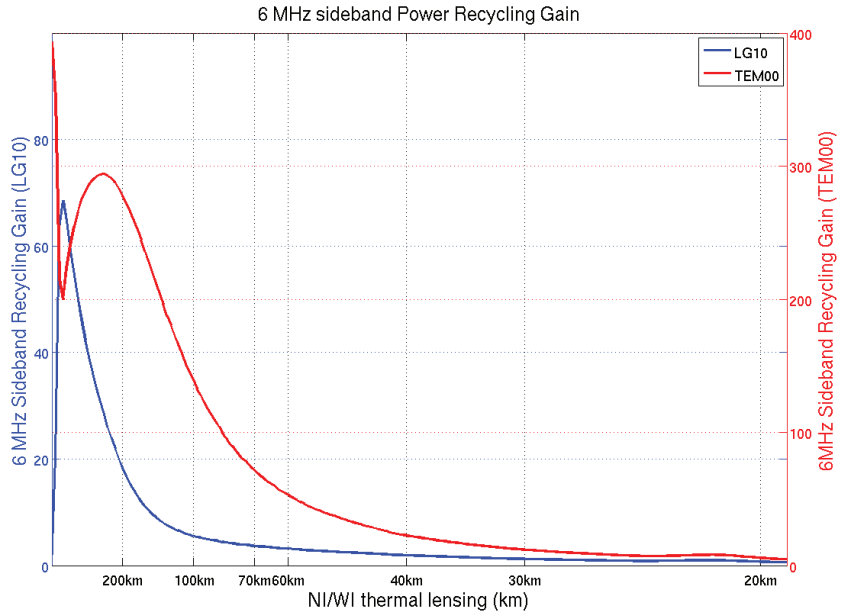

Figure 2.15: 6 MHz Sideband Power Recycling Gain (%) 2011 optical and geometrical AdV. MSRC configuration for TEM00 and LG01 modes. The gains are plotted as a function of the thermal lensing.

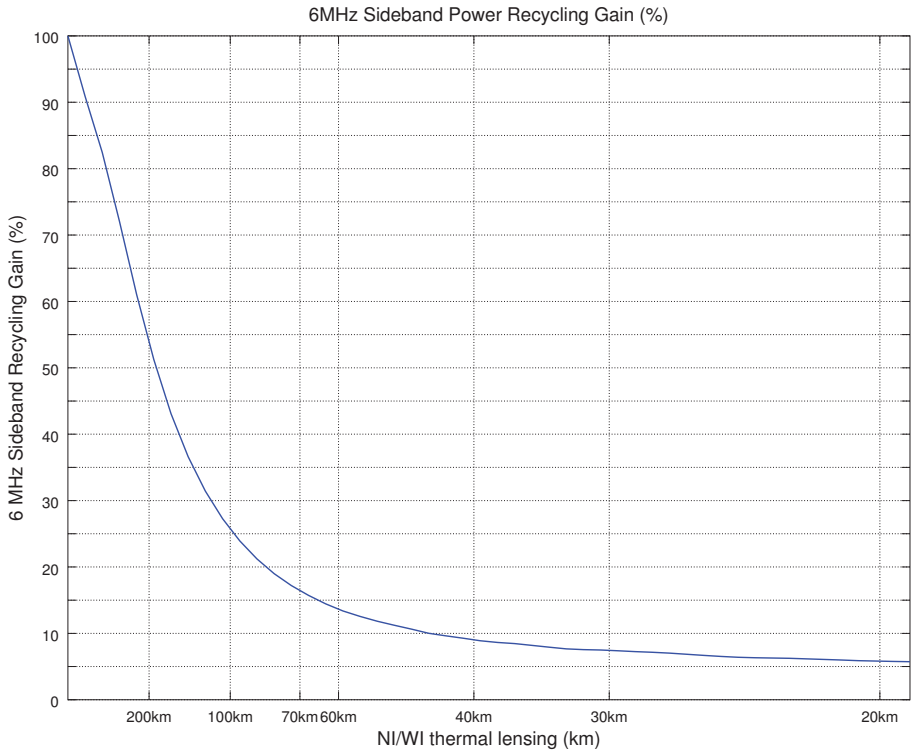

Figure 2.16: 6 MHz Sideband Power Recycling Gain (%) for the final design of Advanced Virgo. The gains are plotted as a function of the thermal lensing.

2.4.4.2 Simulations results - final design

Finally, the final design of the Advanced Virgo project presented in [23] has marginally stable recycling cavities with FP arm cavities having a finesse of 450. Figure 2.16 shows the RF sideband power recycling gain as a function of the thermal lensing. We see that for a thermal lensing of 200 km, which should be reached by the thermal compensating system, the 6 MHz sideband is about 55 % of the maximum gain. It is a bit higher than in the older configurations for high thermal focal length as it was around 35 % at 200 km in the MSRC n°1 configuration.

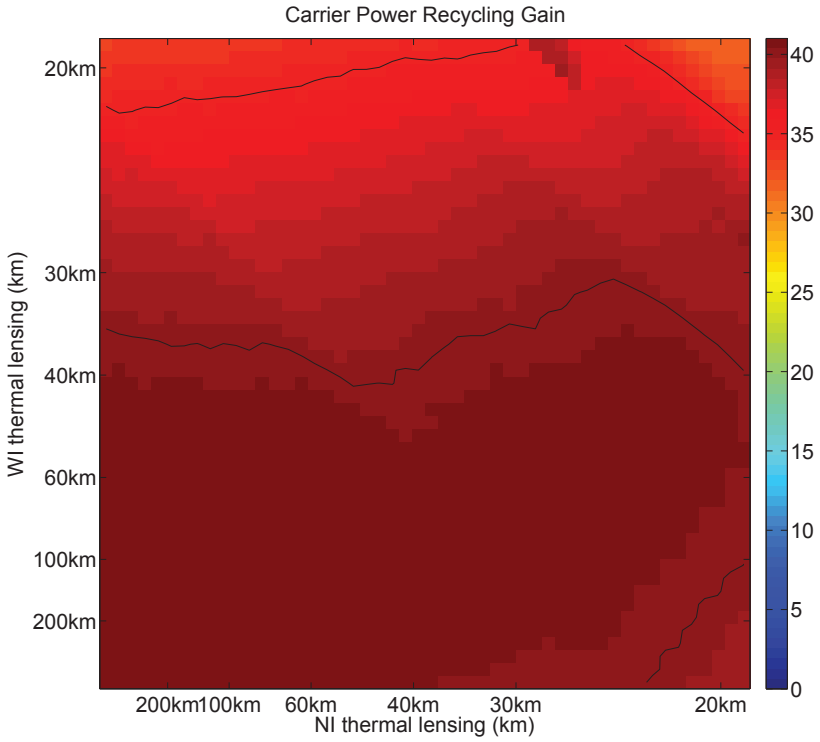

Figure 2.17: Carrier Power Recycling Gain for AdV.final design (MSRC) as a function of the thermal lensing in NI and WI.

2.4.4.3 Differential thermal lensing - final design

We study the differential thermal lensing on the final design of Avanced Virgo. The study has been done as before in the range $f_{TL} = \infty - 20km$ for both the north and west arm thermal lensing. Figure 2.17 exhibits the carrier gain in the PRC. It remains higher than 30 in every case and shows no weaknesses against thermal lensing even for high differential thermal lensing.

As already seen in the study of common thermal lensing in paragraph 2.4.4.2, the 6 MHz sidebands are very sensitive to thermal lensing. Figure 2.18 exhibit the power recycling gain of the RF sidebands. It drops quickly with thermal lensing but does not show a particular weakness to differential thermal lensing. Based on this simulation, we can say that the thermal lensing should be controlled in a very efficient way in order to keep it at an acceptable level. We can see that differential thermal lensing is not a major issue with this final design as the RF sidebands gain does not show a region where it drops critically compared to common thermal lensing. Anyhow we see that for example a thermal focal length of about 30 km in the north input mirror and 80 in the west input mirror induce

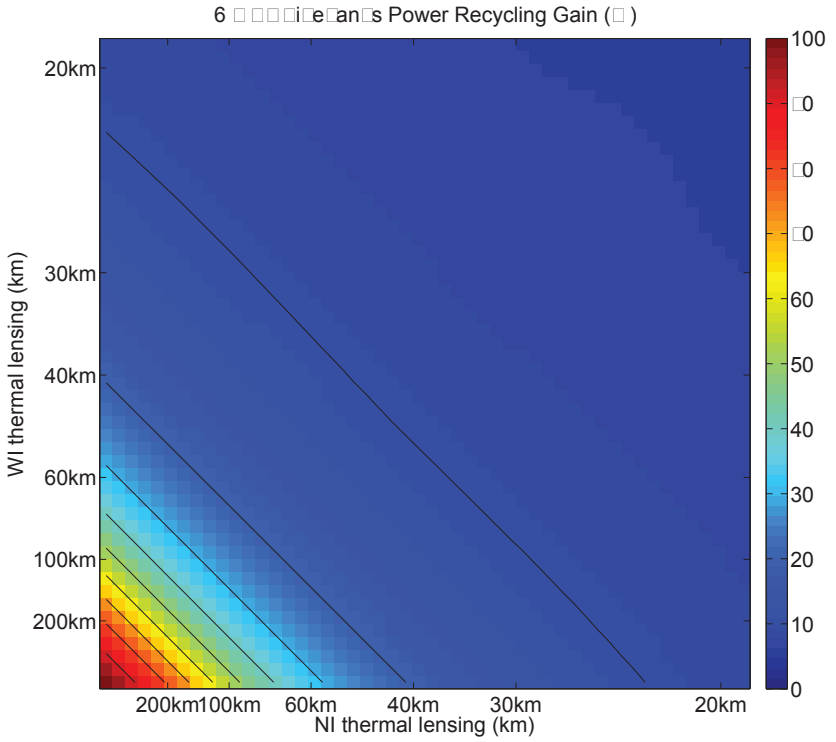

Figure 2.18: 6 MHz Sidebands Power Recycling Gain for AdV.final design (MSRC) as a function of the thermal lensing in NI and WI.

the same 6 MHz power recycling gain as a common thermal lensing of about 45 km. So with a smaller compensation of the thermal lensing effect on the two input mirrors one can obtained the same recycling gain than for a larger compensation on only one input mirror. It seems that it would better to correct the thermal lensing equally in the two arms as it requires a lower level of correction.

To conclude, the thermal lensing should be quite well controlled in order to have enough recycling gain. Indeed, to get more than 50 % of the RF sidebands power recycling gain the thermal lensing should be higher than 200 km in both arms. According to [53] this is achievable by the the TCS using a compensating plate and a ring heater.

2.5 Conclusion

In conclusion, thermal lensing in Advanced detectors is quite a serious problem if not well controlled. The main effect of thermal lensing is to degrade the RF sideband power recycling gain. The effect of thermal lensing on the interferometer has been studied for different configurations and with two different methods. The first method is based on the computation of the coupling between the beams in the recycling and in the arm cavities. The second method uses a Laguerre-Gauss modal code developed at LMA. They both exhibit similar results.

This study on the thermal lensing effect shows that marginally stable cavities are much more sensitive to thermal lensing than non degenerate cavities. This is intrinsic of their nature as in MSRC high order modes are free to resonate in the cavity whereas they are not in stable cavity. Thus a lot of power can be lost in the high order modes. The size of the beam at the ITMs where the thermal lensing occurs is important in the behaviour of the cavity. Indeed we saw that a bigger beam makes the thermal lensing to be more important because higher order modes couple more easily into the recycling cavities. Unfortunately the size of the beam cannot be reduced more because of the mirror thermal noise limitation on the sensitivity detector. Indeed the beam had to be enlarged compared to Virgo to reduce the mirror thermal noise limitation.

Non degenerate recycling cavities are robust to thermal lensing even in case of differential thermal lensing. In spite of their robustness the Gouy phases of the power and signal recycling cavities have to be chosen carefully in order to avoid some of the high order modes to be resonant in the recycling cavity avoiding thus a drop in the RF sidebands gain.

The final design of the Advanced Virgo interferometer has marginally stable recycling cavities. With this design the 6 MHz sidebands are very sensitive to thermal lensing and so it needs to be well controlled by the thermal compensating system.

Chapter 3

Defining the arm cavity mirrors flatness

3.1 Introduction

Interferometric gravitational wave detectors are very sensitive to optical losses indeed they are limited in sensitivity by the shot noise at high frequencies. In the interferometer the power is build up essentially in the Fabry-Perot(FP) arm cavities. Therefore the optical losses in the Fabry-Perot cavities increase the signal to noise ratio of the shot noise degrading thus the detector sensitivity at high frequencies. Consequently, the mirrors composing the arm cavities should induce minimum losses and these mirrors are the core optics of the interferometer. The round-trip losses in the arm cavities should be very small in order to reach a good detector sensitivity. Apart from the shot noise limitation, the contrast defects at the output of the interferometer can also degrade the sensitivity of the interferometer. Having low losses in the two arm cavities will reduce the risk of having large contrast defects coming from the asymmetry of the two arms. Another reason to limit the losses in the arm cavities is the diffused light due to the surface figure error of the mirrors. This diffused light can couple back to the dark fringe after being modulated by the vacuum pipes vibrations. Then minimising the losses in the arms will obviously reduce the diffused light. Finally we present in this chapter the simulations done to define the specifications on the substrates flatness.

First we present the Advanced Virgo specification on the round-trip losses in the Fabry-Perot arm cavities and define the tools used to assess the Fabry-Perot cavity performances in terms of losses. We also present the tools used to assess the mirror qualities in terms of flatness. Then we will describe the simulation protocol and show the results obtained in terms of flatness specifications for the substrate. These flatness specification being very low,

we will present the simulations of the corrective coating technique that will be later used to bring down the mirror flatness to the required level. The corrective coating technique is a technique developed at LMA to flatten the substrate. It will be explained in more details in chapter 5.

3.2 Definitions and specifications

3.2.1 Flatness and Power Spectral Density

The flatness of a mirror surface can be seen as deviations from an ideal surface, either plane or spherical depending on the optics. In the following we focus on the FP arm cavities substrates which are both spherical. They have a radius of curvature (RoC) of 1420 and 1683 m respectively for the input test mass (ITM) and end test mass (ETM) [23]. The parameter commonly used to express the flatness of a surface is the root mean square (RMS) fluctuation in height of the surface. It is computed over a given diameter, the central part of the optics, typically 150 mm for Advanced Virgo. The surface figure of the mirror is typically measured with a phase-shifting interferometer (see chapter 4). Given the surface figure measured and sampled over a discrete grid $h(x, y)$, the RMS flatness is:

$$\sigma_{RMS} = \sqrt{\frac{\sum_x \sum_y [h(x,y) - \overline{h}]^2}{N}} \tag{3.1}$$

where N is the number of pixels in the surface map over which the RMS is computed and $\overline{h}$ is the mean deviation from the ideal surface.

Another useful tool to asses the quality of a surface is the power spectral density (PSD). The PSD describes the surface via the distribution in spatial frequency of the square amplitude of the deformations. Spatial frequencies are linked to the measurement of the surface figure. The highest spatial frequency of the defects one can measure is limited by the pixel size of the measurement (Δx), it is $f_{max} = \frac{1}{2\Delta x}$. The lowest spatial frequency is determined by the size of the map (G), $f_{min} = \frac{1}{G}$.
The two-dimensional PSD is computed as following:

$$\text{PSD2D}(fx, fy) = |\text{FFT2D}\{h(x,y)\}|^2 \times \Delta x \Delta y \tag{3.2}$$

where $FFT2D$ is a two dimensional Fourier transform, Δx and Δy are pixel size of the map in the x and y direction, typically $\Delta x = \Delta y$. We usually apply an hann window to the height map $h(x, y)$ to avoid edge effects.

The two-dimensional PSD is related to the RMS of the mirror as its integration over the whole spatial frequency range yields to the mirror flatness RMS:

$$\sigma_{RMS} = \sqrt{\sum_{f_x} \sum_{f_y} \{\text{PSD2D}\} \times \Delta f_x \Delta f_y} \tag{3.3}$$

where Δf_x and Δf_y are the spatial frequency resolution of the two-dimensional PSD in the x and y direction.

We can also compute the one-dimensional PSD from the two-dimensional PSD to make comparison easier. Assuming the 2D PSD to be rotationally symmetric, one can integrate radially the 2D PSD to get the 1D PSD:

$$\text{PSD1D}(f_r) = \int_0^{2\pi} \text{PSD2D}(f_r, \theta)\, f_r\, d\theta \tag{3.4}$$

where $f_r = \sqrt{f_x^2 + f_y^2}$ is the radial frequency.
Another way to compute the one-dimensional PSD is to integrate along one direction [63]:

$$\text{PSD1D}_\text{X}(f) = \int_{-\infty}^{\infty} \text{PSD2D}(f_x, f_y) df_y \tag{3.5}$$

In this chapter the one-dimensional power spectral densities shown are computed using the radial integration.
The one dimensional PSD is related to the RMS flatness of a surface with the equation:

$$\sigma_{RMS}^2 = \int_0^{\infty} \text{PSD1D}(f_r) df_r \tag{3.6}$$

The spatial frequency of the defects is related to the angle (θ) at which the light is diffracted when impinging on such a defect by the relation:

$$\theta = \lambda \times f \tag{3.7}$$

where f is the spatial frequency of the defects and λ the wavelength of the light.

3.2.2 Advanced Virgo arm cavity specification

The Advanced Virgo baseline [42] specified that the round-trip losses (RTL) in the arm cavities should be smaller than 75 part per million (ppm). To improve the sensitivity by a factor ten, the shot noise should be reduced by a factor ten and thus the power circulating in the arm should be increased by a a factor 100. Part of this factor 100 in the circulating power in the arm cavities is achieved by increasing the laser power at the interferometer input. Then the losses in the arm cavities have to be reduced to achieve the laser power increase and the 75 ppm round-trip losses allow to obtain it combined with a high laser power at the input of the interferometer. The round-trip losses quantify the fraction of light lost after a round-trip in the cavity. The losses in a cavity are due to the diffraction at low and high spatial frequencies (LSF and HSF) as well as the losses due to absorption in the coating, the end mirror transmission and the punctual defects on the mirror surface i.e. the scratches, digs and points. In the following, we focus only on the diffraction due to surface defects at low spatial frequencies.

The low and high spatial frequencies are defined as below or above 1000 $m^{-1}(= 1\ mm^{-1})$. The low surface figure of a substrate is measured typically with a phase-shifting interferometer as will be presented in chapter 4. To measure the high spatial frequency roughness of a sample, we use a commercial optical surface profiler. The diffraction due to high spatial frequencies is due to the micro-roughness of the substrates, they are estimated to be about 2×10 ppm including punctual defects [23]. The losses due to absorption and transmission of the end mirror are estimated to be of 5 ppm. Then the losses due to the low spatial frequencies defects have to be less than 50 ppm.

To quantify the round-trip losses in an optical cavity we use the definition via the energy conservation law, as defined in [64]:

$$RTL = \frac{P_{in} - P_t - P_r}{P_{circ}} \tag{3.8}$$

where $P_{in},\ P_t,\ P_r$ and P_{circ} are the power of the fields depicted in the figure 3.1.
We can also compute the round-trip losses projected on the TEM_{00} mode (RTL_{00})) using the following equation.

$$RTL_{00} = \frac{P_{in} - P_t^{00} - P_r^{00}}{P_{circ}} \tag{3.9}$$

where $P_t^{00},\ P_r^{00}$ are the powers contained in the TEM00 mode of the fields.
This will allow us to assess how the mode in the cavity has been distorted in regards of the theoretical mode that should circulate. Strictly speaking, this RTL_{00} are not pure losses as it accounts both for the fraction of power that leaves the cavity (which is definitely lost) and

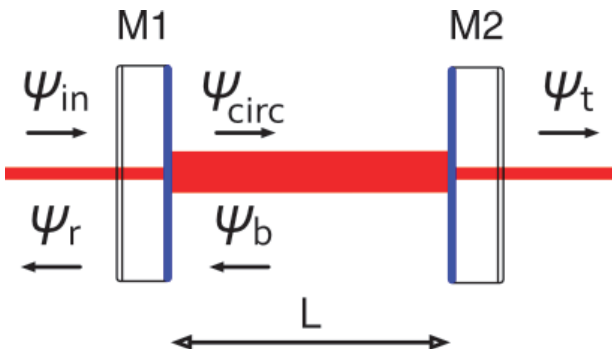

Figure 3.1: Fields in a Fabry-Perot cavity

the high order modes (HOM) excited in the cavity.
In one word, the RTL are the clipping losses due to the finite size of the mirrors whereas the RTL_{00} represents both the clipping losses and part of the coupling losses.

3.3 Simulation protocol

3.3.1 The different PSD shapes

In order to define the required flatness of the surfaces for the arm cavity mirrors, we perform Monte-Carlo simulations with simulated mirrors having a random flatness. To simulate mirrors we measure the flatness of actual mirrors to know what the PSD of the mirror surfaces looks like. The measurement is done with phase-shifting interferometer as already mentioned. Different kind of mirrors polished by different polishers have been measured at LMA or elsewhere. Figure 3.2 shows the PSDs of substrates polished by General Optics, CSIRO and Tinsley [65, 66]. These PSD are computed over a diameter of 150 mm.

The two substrates polished by General Optics (blue and green curves) have been measured at LMA. They are the Virgo+ end mirrors, they have a flatness of 2.9 and 5.1 nm RMS. Their PSDs is falling down quite regularly with a law in f^{-n} where $n = 2.3$. The light blue curve is the PSD of the substrate polished and measured by CSIRO for LIGO pathfinder, it has a flatness of 0.9 nm RMS and its PSD increases slightly above 50 m^{-1}. This is due to the polishing process and they claim that they can reduce this "high" frequency component [67].

Finally the substrates for Advanced LIGO have been polished by Tinsley using the technique of ion beam figuring (IBF). They have a very low flatness of 0.15 and 0.16 nm RMS and their PSDs is starting to bend over below a spatial frequency of approximately 100 m^{-1}. The IBF technique consists of removing material on the substrate surface with a focused ion beam. The spatial frequency at which the IBF acts is linked to the size of the ion beam used

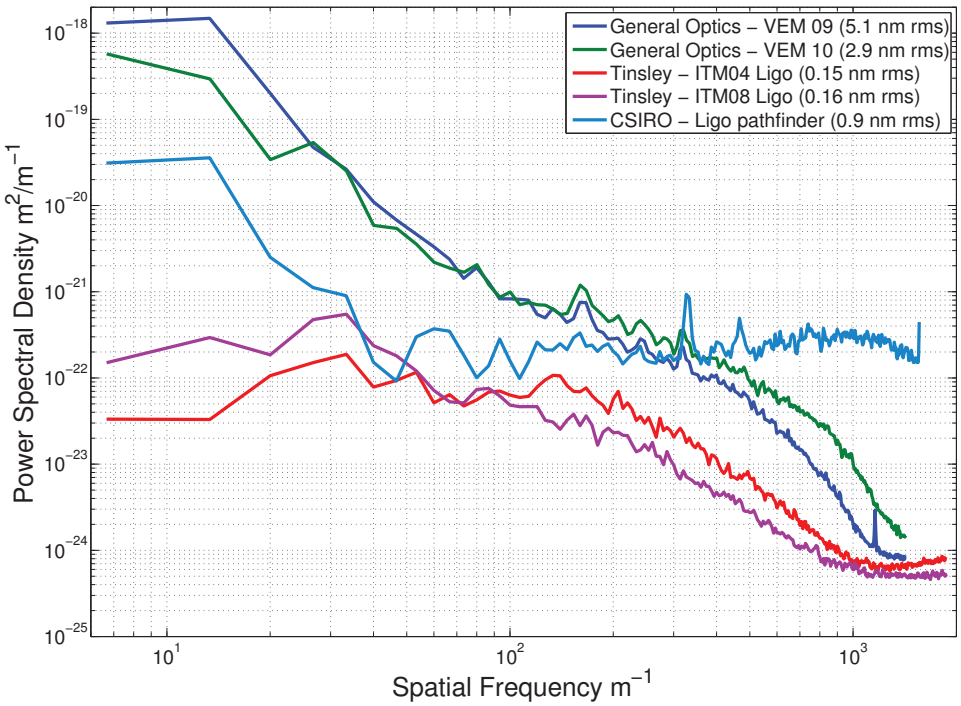

Figure 3.2: PSD of substrates polished by different polishing companies computed over a 150 mm diameter.

to remove materials on the substrate surface. The techniques of IBF and corrective coating work on the same idea of controlling the surface figure of a substrate. The only difference is that IBF removes materials whereas the corrective coating adds materials where it is needed. From those different PSDs, one can see that the shape of the power spectral density is related to the polishing company and the process used to polish the surface.

3.3.2 From actual mirror maps to simulated maps

In order to understand the influence of the PSD shapes on the arm cavity behaviour, we simulate a large amount of mirror surfaces having the same PSD shape as General Optics (GO) and CSIRO substrates in order to have statistics. Then we simulate the Advanced Virgo Fabry-Perot cavity with the simulation software SIESTA [68] with mirrors having surface figures characteristic of the polishing companies. We did not simulate mirrors with Tinsley PSD shape as we already know from Advanced LIGO simulations ([69]) that they induced very small losses, typically around 5 ppm.

To simulate artificial mirror surfaces we modelled the power spectral density of the surfaces by straight lines (in log-log scale). For General optics, the PSD as been modelled in the whole spatial frequency range as PSD1D $\approx f^{-2.3}$ as one can see in figure 3.3.

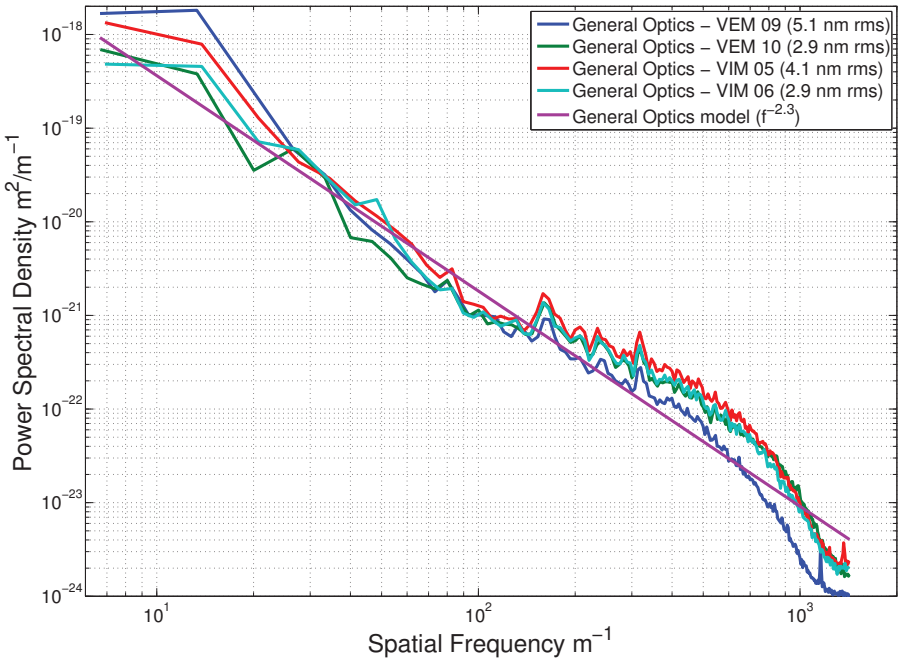

Figure 3.3: PSD of General Optics substrates and modelling computed over a 150 mm diameter.

CSIRO surfaces has been modelled using four segments in the different spatial frequency ranges as shown in figure 3.4. Once the one dimensional PSD is modelled, we create a two dimensional PSD with the desired shape (GO or CSIRO) assuming a circular symmetry. We apply a random phase to this two-dimensional PSD in order to randomize the surface figure. Then we apply an inverse Fourier transform to generate the surface, it is normalized to obtain a map with the wanted flatness RMS. The algorithm used is the one explained in more details in [70]. This algorithm to generate random surfaces has been implemented in SIESTA. The surfaces map are attached to the mirrors to understand how it will affect the losses in the cavity. It is also important to state that the simulated surfaces are essentially free of low-order aberrations such as astigmatism, coma or spherical aberration. Typically the astigmatism of a generated surface is below 0.01 %. Therefore, the simulations results presented in this chapter does not take into account the effect of very low-order aberrations. Those effects will be studied in chapter 6 as low-order aberrations can arise during the process of the coating deposition on the substrate.

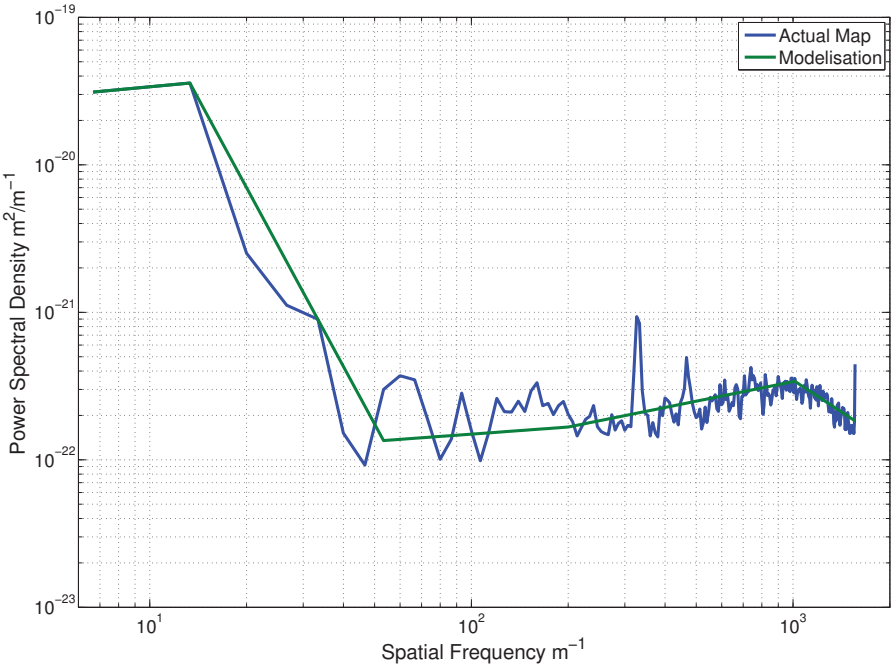

Figure 3.4: PSD of the CSIRO substrate and modelling computed over a 150 mm diameter.

3.3.3 Simulating a Fabry-Perot cavity with FFT code.

The simulation have been performed under SIESTA which is a simulation software developed within the Virgo collaboration [68]. It can work as a modal or as a FFT code. In the following, we use it as a FFT simulation tools. FFT optical simulations are based on Fourier transform [71]. First we decompose the complex amplitude of the electrical field into sum of elementary plane wave. This is done by a two-dimensional Fourier transform. Then the propagation of the field is handled by adding a phase-shift (which depends on the length of propagation and wavelength of the field) to the elementary plane waves that compose the field. Finally, the field is recompose by applying an inverse Fourier transform to the elementary plane waves composing the field. All other operation such as reflection or transmission through an aperture are performed directly on the complex amplitude of the electric field.

So we simulate a FP cavity having the Advanced Virgo parameters as described in [23] and reported in the table 3.1 with mirrors having a simulated surface characteristic of the polishing process.

The simulation gives as an output the power of the light at different locations in the cavity. Then we can compute the RTL using the definition in 3.8 to asses how much light has escaped the cavity because of the imperfect mirror surface figures. Thousands of simulations have been performed with simulated surfaces and the results will be shown in the section 3.4.
We cross-checked the results using two different simulation programs, SIESTA and OSCAR

Table 3.1: Advanced FP Cavity Parameters

Mirror	**Radius of Curvature**
ITM	1420 m
ETM	1683 m
Mirror	**Diameter**
ITM	0.340 m
ETM	0.340 m
Mirror	**Transmission**
ITM	1.4%
ETM	10 ppm
Cavity Length	3000 m

[71]. We found that the results on the losses using the same parameters and maps are compatible within less than 10%.

3.3.3.1 FFT parameters

When performing simulations with FFT codes one should be careful while choosing the grid parameters, i.e. the number of points in the grid (often called resolution) and the grid size. A wrong choice in those parameters could result in aliasing which would seriously affect the simulation output. Aliasing has been thoroughly studied in [72], its effect is to underestimate the losses in a simulation of a Fabry-Perot cavity. An inappropriate choice in the grid parameters could also results in prohibitive demands in terms of computational memory and time. Then the choice of the appropriate grid parameters is a trade-off between correct output and computational resources.
The theoretical grid parameters as defined in [72] are not suitable in regards of the available computational resources and therefore an empirical approach has been adopted to determine the appropriate parameters. These parameters are dependent in the simulation performed and thus the resolution and grid size are different when simulating a cavity with GO like or CSIRO like surface figures.

General Optics In order to choose the grid parameters in the case of GO like mirrors, we perform two set of simulations. First we simulate a surface map and then we increase the grid size by padding the map with zeros, that is to say we extend the grid resolution and add zeros in the extended region. Doing so we keep the pixel size constant so that the spatial frequency content of the map is preserved. The simulation has been run with mirrors having a 1.5 nm RMS flatness with a grid of size 0.4 m with 256x256 pixels, then we increased the resolution and grid size by 2 and 4 (0.8 m/512x512 pixels and 1.6 m/1024x1024 pixels). In

every cases the RTL and RTL_{00} are computed and reported in table 3.2, we can see that the losses do not change significantly with the grid size and therefore we set the grid size to be 0.4 m.

Table 3.2: Losses as a function of the Grid Size, General Optics

Grid Parameters	**RTL**	**RTL_{00}**
256x256 / 0.4 m	34.4 ppm	43.8 ppm
512x512 / 0.8 m	34.2 ppm	43.4 ppm
1024x1024 / 1.6 m	34.0 ppm	43.2 ppm

Then we need to set the number of pixels (i.e the resolution) of the grid and so we run simulations with an other set of mirrors maps having a grid size of 1.6 m and 4096x4096 pixels and then reduced the resolution by 2 and 4 (by down-sampling the map) while keeping the grid size constant. Doing so, we modified the spatial frequencies content of the mirror maps as the high spatial frequencies are cut off as we down-sample the maps. The spatial frequencies content of a map is related to the pixel size of the grid. The maximum frequency contained in the map is $f_{max} = \frac{N}{2 \times G}$ where (G) is the grid size and (N) the resolution. The RTL and RTL_{00} computed from the output of the simulations are reported in the table 3.3. Once again we do not see significant changes in the losses.

Table 3.3: Losses as a function of the Number of Pixels, General Optics

Grid Parameters	**RTL**	**RTL_{00}**
1024x1024 / 1.6 m	33.8 ppm	49.4 ppm
2048x2048 / 1.6 m	33.5 ppm	49.0 ppm
4096x4096 / 1.6 m	34.0 ppm	49.5 ppm

From this second set of simulations, we can say that the highest spatial frequencies of the surface map do not play an important role in the case of General Optics like mirror. Indeed the RTL are the same whether the maximum is frequency is 1280 m^{-1} (1.6m/4096x4096) or 320 m^{-1} (1.6m/1024x1024). This is in accordance with the PSD shape since the overall defects above this spatial frequency of 320 m^{-1} are very low because of the steep decrease in the PSD.

To conclude, it is equivalent to have a grid of 1.6 m with 4096 pixels or a grid of 0.4 m with 256 pixels and thence we will choose these parameters when simulating a FP cavity with GO like mirror surfaces. This choice allows us to save a great amount of CPU time and memory without compromising the accuracy of the simulation output.

CSIRO For the CSIRO like mirrors simulations we need to refine the parameters of the FFT simulation. It is clear looking at the CSIRO PSD that it is not appropriate to use a grid with a resolution of 256x256 pixels for a grid size of 0.4m as the spatial frequencies above 320 m^{-1} which contain a lot of power will not be taken into account. We will use at least a 1024 pixels grid with a 0.4 m grid size in order to keep the spatial frequency content of the map up to 1280 m^{-1}. Thus we perform simulations increasing the grid size by a factor 2 and 4 as before by padding the map with zeros so that the spatial frequency content of the map is preserved. The RTL computed from the output of the simulations is reported in the table 3.4. The losses change at most by about 4%. Therefore we will use a grid of 1024 pixels for 0.4 m. This is still suitable in terms of CPU time but much more slower than for the parameters for GO like mirrors.

Table 3.4: RTL as a function of the Grid Size, CSIRO

Grid Parameters	RTL	RTL_{00}
1024x1024 / 0.4 m	338.7 ppm	361.5 ppm
2048x2048 / 0.8 m	349.9 ppm	366.1 ppm
4096x4096 / 1.6 m	351.8 ppm	360.3 ppm

3.4 Simulations results

In the first set of simulations, we perform thousands of simulations spanning an interval of RMS flatness going from 0 nm to 2.5 nm for both sort of polishing. For GO like mirrors we run 5000 simulations with mirrors having a flatness between 0.5 and 2.5 nm RMS. Figure 3.5 shows the results of the simulations, it plots the round-trip losses against the mirrors surfaces flatness expressed in nm RMS. We can see an important dispersion in the round-trip losses in the Advanced Virgo cavity for a given flatness. This is due to the fact that in some cases the two opposites surfaces can compensate. In the figure 3.5, the limit of acceptable losses is drawn in red. This 50 ppm limit is crossed around 1 nm RMS.

We can compute the fraction of simulations which gives round-trip losses smaller than 50 ppm for a given flatness RMS. It has been computed on the same data set with bins of 0.05 nm RMS. We get that more than 95% of the simulations with mirrors of 1 nm RMS flatness give RTL smaller than 50 ppm. In other words, according to our simulations with mirrors having a flatness of 1 nm RMS and GO like PSD shape the losses due to LSF in the Advanced Virgo arm cavity will be less than 50 ppm with a 95% confidence.

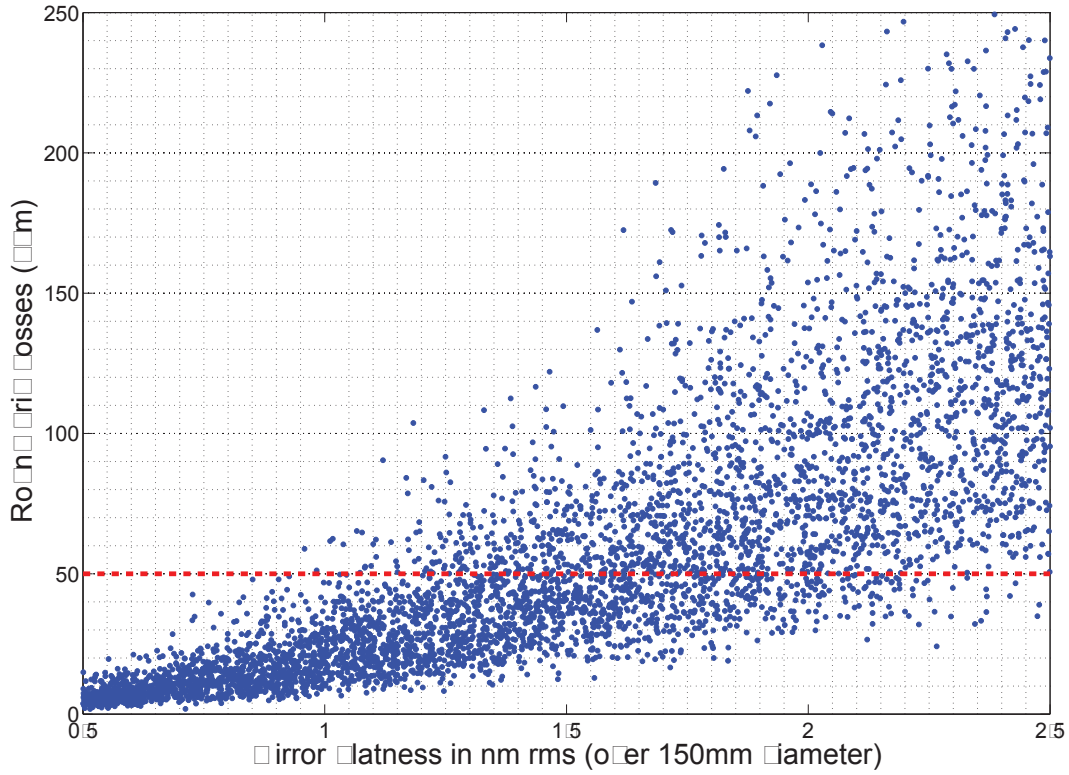

Figure 3.5: Round-Trip Losses for GO-like surfaces

As a reference we compute the losses in the Virgo cavity with the actual Virgo+ surface maps measured at LMA. The fours mirrors of the two arms have a flatness around 4 nm RMS, their flatness is reported in table 3.5 along with the computed RTL and RTL projected on the TEM_{00}. We see that the losses are different for the two cavities, it is 273 ppm in the north arm against 699 ppm in the west arm. This causes the contrast defects to be quite high [73]. Also the RTL projected on the TEM_{00} mode are very high (around 1100 ppm) because of the low order aberrations of the surface figures.

Table 3.5: Virgo+ arm cavity mirrors flatness

Arm	**ITM Flatness**	**ETM Flatness**	**RTL**	**RTL_{00}**
North Arm (VIM05 - VEM10)	4.1 nm rms	3.1 nm rms	273 ppm	1100 ppm
West Arm (VIM06 - VEM09)	4.1 nm rms	5.1 nm rms	699 ppm	1146 ppm

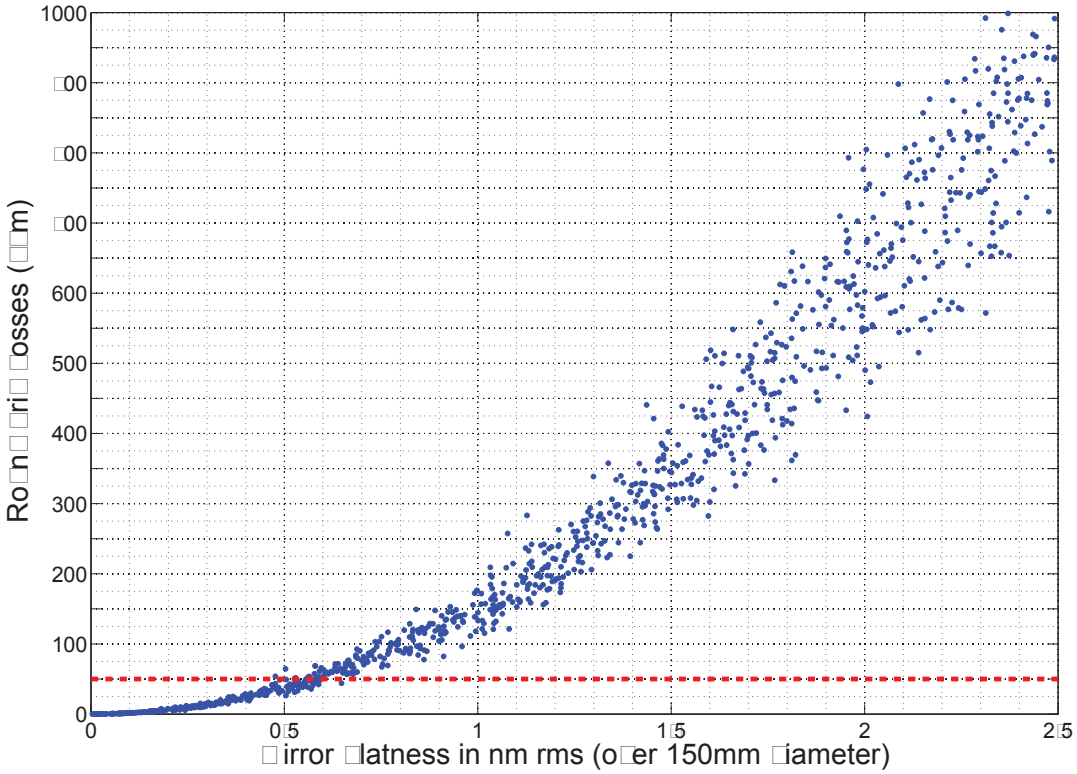

Figure 3.6: Round-Trip Losses for GO-like surfaces

The same kind of simulations have been run with CSIRO like surfaces having a flatness in the interval 0 - 2.5 nm RMS. Only 1000 simulations have been performed due to the longer time needed for one simulation because of the higher resolution of the FFT grid. The results are presented in the figure 3.6 as before. We see that the losses in the Advanced Virgo FP cavity are much more higher with this kind of mirror surfaces. This is due to the fact that the high spatial frequencies have much more power.

We compute as before the fraction of simulations which gives round-trip losses smaller than 50 ppm. In that case, we obtain that to get less than 50 ppm losses in the Advanced Virgo FP cavity with a 95% confidence we need to have mirrors with a flatness of 0.45 nm RMS or less.

With these two set of simulations we see that for a given flatness RMS the losses in a FP cavity are different for different kind of polishing. The flatness expressed in nm RMS is not significant enough in itself and the shape of the PSD should has to be taken into account. In the next paragraph we discuss the issue of the higher part of the low spatial frequencies content of the surface maps.

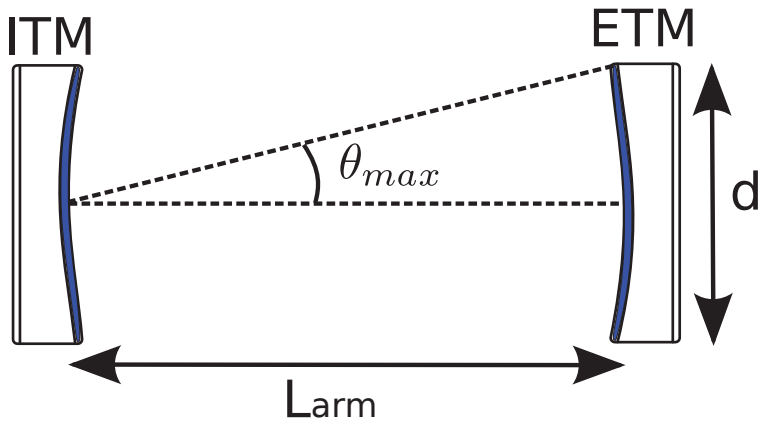

Figure 3.7: Advanced Virgo Fabry-Perot cavity geometry

3.5 The high spatial frequencies

We saw previously that the RMS flatness of a surface is not enough to characterise a surface as it is dominated by the very low spatial frequencies. That is to say that the high spatial frequency content being smaller in amplitude does not appear much in the overall surface flatness. Then the higher spatial frequencies should be controlled in order to avoid extra losses as for CSIRO like mirrors. In this thesis we will talk about high spatial frequencies (HSF) in the range 50 m^{-1} – 1000 m^{-1} as the surface figures are measured with a Phase-Shifting interferometer. It is important not to confuse these HSF with the micro-roughness as measured by profilometer which gives measurements with spatial frequencies above 1000 m^{-1}.

This 50 m^{-1} has been chosen looking at the geometry of the Advanced Virgo cavity. Assuming that most of the power circulating in the cavity is concentrated in the central part of the mirror, the maximum angle at which the diffracted light stay in the cavity is θ_{max} as depicted in figure 3.7. Then we have:

$$\theta_{max} = \frac{d}{2L_{arm}} \tag{3.10}$$

Recalling equation 3.7, the spatial frequency corresponding to the maximum diffraction angle is

$$f_{max} = \frac{\theta_{max}}{\lambda} = \frac{d}{2L_{arm} \times \lambda} \tag{3.11}$$

with L_{arm} the cavity length, d the coating diameter and λ the laser wavelength. Considering that the coating will have a diameter of 33 cm, we find that $f_{max} \approx 52\ m^{-1}$. So the light impinging on defects having a spatial frequency of 50 m^{-1} or higher will be diffracted with such an angle that the light will never reach the opposite mirror of the cavity and thus be

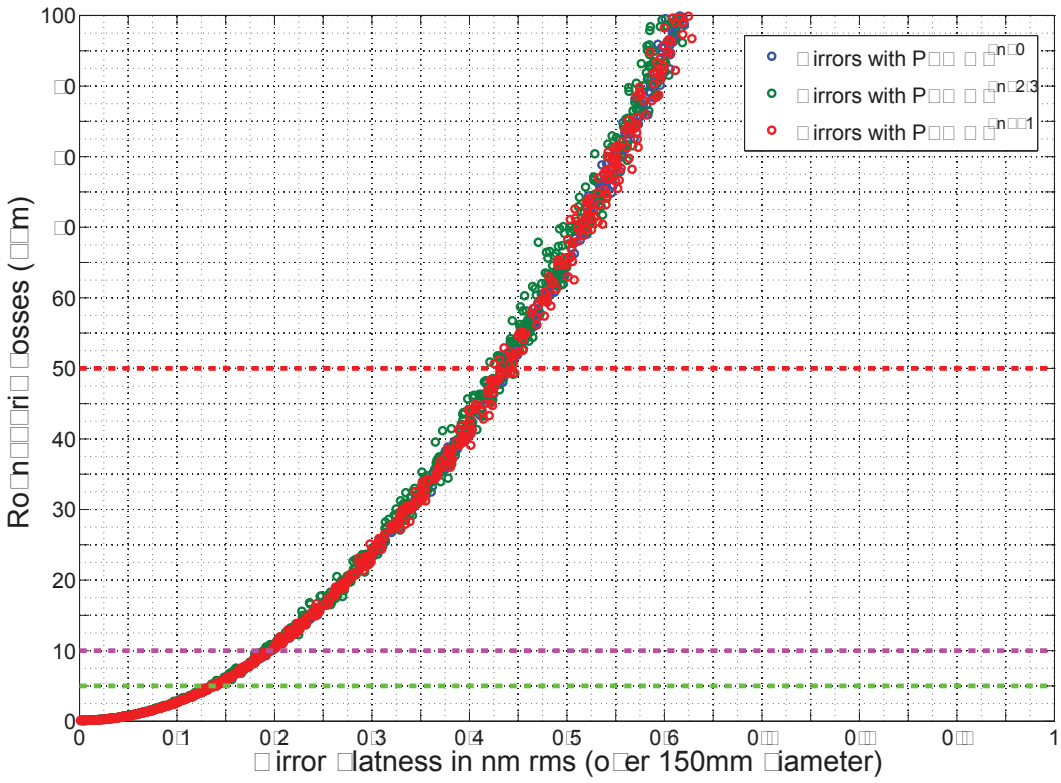

Figure 3.8: Round-Trip Losses for surfaces having only defects above 50 m^{-1} for different PSD shape.

definitely lost.

Then to see the effect of this HSF, we simulate mirrors with defects only above 50 m^{-1} and different PSD shape. The different PSD shape follow a law in $PSD1D = f^{-n}$ with $n = 2.3$ as of GO surfaces, $n = 0$ (no slope) and $n = -1$ a growing PSD. Once more we perform one thousand simulations of the Advanced Virgo FP cavity with such mirror surfaces. The results are displayed in figure 3.8, the red line is the 50 ppm limit while the magenta and green lines are respectively 20% (10 ppm) and 10% (5 ppm) of this limit. Whatever the PSD shape, the round-trip losses are found to be the same. They follow the total integrated scatter (TIS) law (eq. 3.12) with a factor 2 because of the two mirrors composing the cavity. The TIS law gives the overall scattering of a surface as a function of its roughness [74]. In our case the scattered light is equivalent to the losses as the light is diffracted such that it escapes the cavity.

$$Losses = \left(\frac{4 \times \pi \times RMS}{\lambda}\right)^2 \tag{3.12}$$

To conclude on the HSF, it has been decided in Advanced Virgo to give to the polishing

company a specification on the flatness in the range 50 m^{-1} - 1000 m^{-1}. This specification is set to be 0.15 nm RMS so as to limit the losses to 10 ppm because of the HSF. This specification seems to be achievable by classical polishing looking at the aLIGO substrate power spectral densities. Indeed they have been polished by classical technique in a first step and then have been ion beam figured in order to get the very low flatness substrates we know (typically $<$ 0.2 nm RMS on a diameter of 160 mm). We remind the reader that the IBF only improve the low frequencies, the high frequencies remaining constant. In the range 50 m^{-1} - 1000 m^{-1}, the substrates ITM04 and ITM08 whose PSD are shown in the figure 3.2 have a flatness of respectively 0.135 and 0.102 nm RMS.

3.6 Simulation of the corrective coating in the spatial frequency domain

According to manufacturers, the polishing by classical means (i.e. by abrasion) is not efficient enough at low frequencies to reach the requested flatness on large optics for Advanced Virgo. The Advanced Virgo strategy implies two steps to reach the required flatness for the Advanced Virgo arm cavity substrates. The first step will be a classical polishing done by polishers such as Coastline Optics, CSIRO or Zygo. The second step is the corrective coating [75]. The corrective coating is a technique developed at LMA which consists in adding materials on the surface where it is needed to obtain the desired flatness. To understand how much the corrective coating will be able to correct the flatness of a substrate, we simulate the corrective coating technique in the spatial frequency domain. These simulations will allow us to find out the level of flatness required in the first phase (i.e. the classical polishing) that permits the corrective coating to be efficient enough. Indeed if the substrates is not flat enough, it might be difficult to correct the surface to a sub-nanometric level.

To understand how much the corrective coating will be able to correct the flatness of a substrate, we perform simulations of the corrective coating in the spatial frequency domain. The approach used to simulate the action of the corrective coating is the following. From the data of the test done on a 120 mm diameter substrate in the early 2000s, we plot the power spectral density of the substrate surface before and after correction, figure 3.9. We see that the corrective coating acts as a high-pass filter on the power spectral density. That is to say the low frequencies below a given cut-off frequency are reduced whereas the high spatial frequencies remains the same. The frequency cut off the corrective coating is defined by the size of the mask used for the correction. A 2 cm mask will correct defects bigger than 2 cm and so below a spatial frequency of $f = \frac{1}{2}$ cm^{-1} $=$ 50 m^{-1}. We also see a bump in

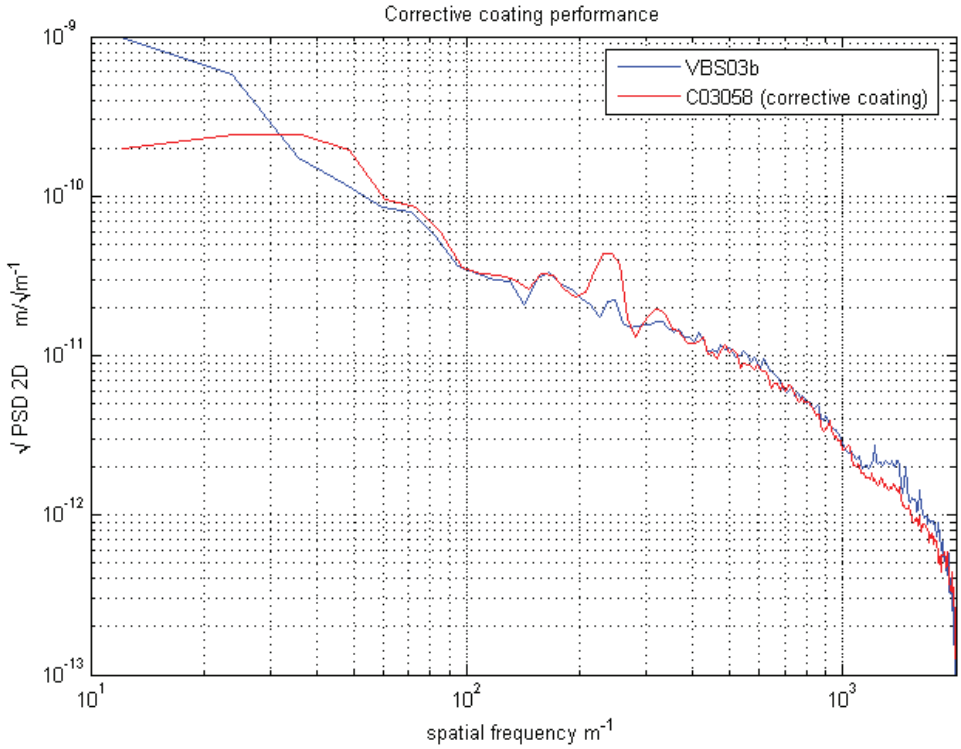

Figure 3.9: PSD of the 120 mm diameter substrate before and after corrective coating from the 2003 test, from [76].

the PSD of the surface after correction. This bump was not taken into account in the spatial frequency domain simulations.

To simulate the corrective coating, we start from virtual map generated as explained earlier in the paragraph 3.3.2. Then we compute the two-dimensional Fourier transform of the map (i.e. the 2D PSD) and we applied a two dimensional filter characteristic of the corrective coating technique. The filter reduces the content of the 2D PSD below the cut-off frequency by multiplying each point of the 2D PSD by a factor depending on the spatial frequency knowing that the one-dimensional PSD of the original surface has a shape in f^{-n}. The filter does nothing above the cut-off frequency. We have:

$$F_{CC} = \begin{cases} f_r^n / f_{cut-off} & \text{for } f_r < f_{cut-off} \\ 1 & \text{for } f_r \geq f_{cut-off} \end{cases} \tag{3.13}$$

with f_r being the radial frequency and $f_{cut-off}$ the cut-off frequency of the corrective coating. Finally we apply an inverse Fourier transform to get the corrected map. Figure 3.10 shows the power spectral density of a simulated surface without correction and corrected for different cut-off frequency of 25 m^{-1}, 50 m^{-1}, 75 m^{-1} and 100 m^{-1}. Figure 3.11 shows a simulated map with an original flatness of 2 nm RMS corrected in the spatial frequency domain method.

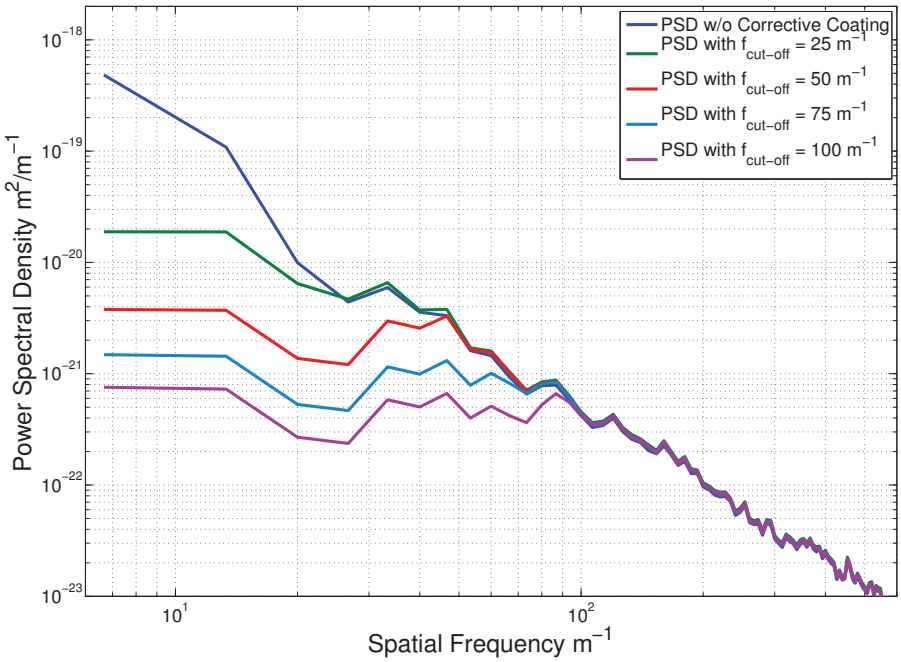

Figure 3.10: PSD of a simulated surface corrected at different cut-off frequencies.

The frequency cut of the corrective coating is 50 m^{-1} in that case. It lowers the flatness to a value of 0.33 nm RMS.

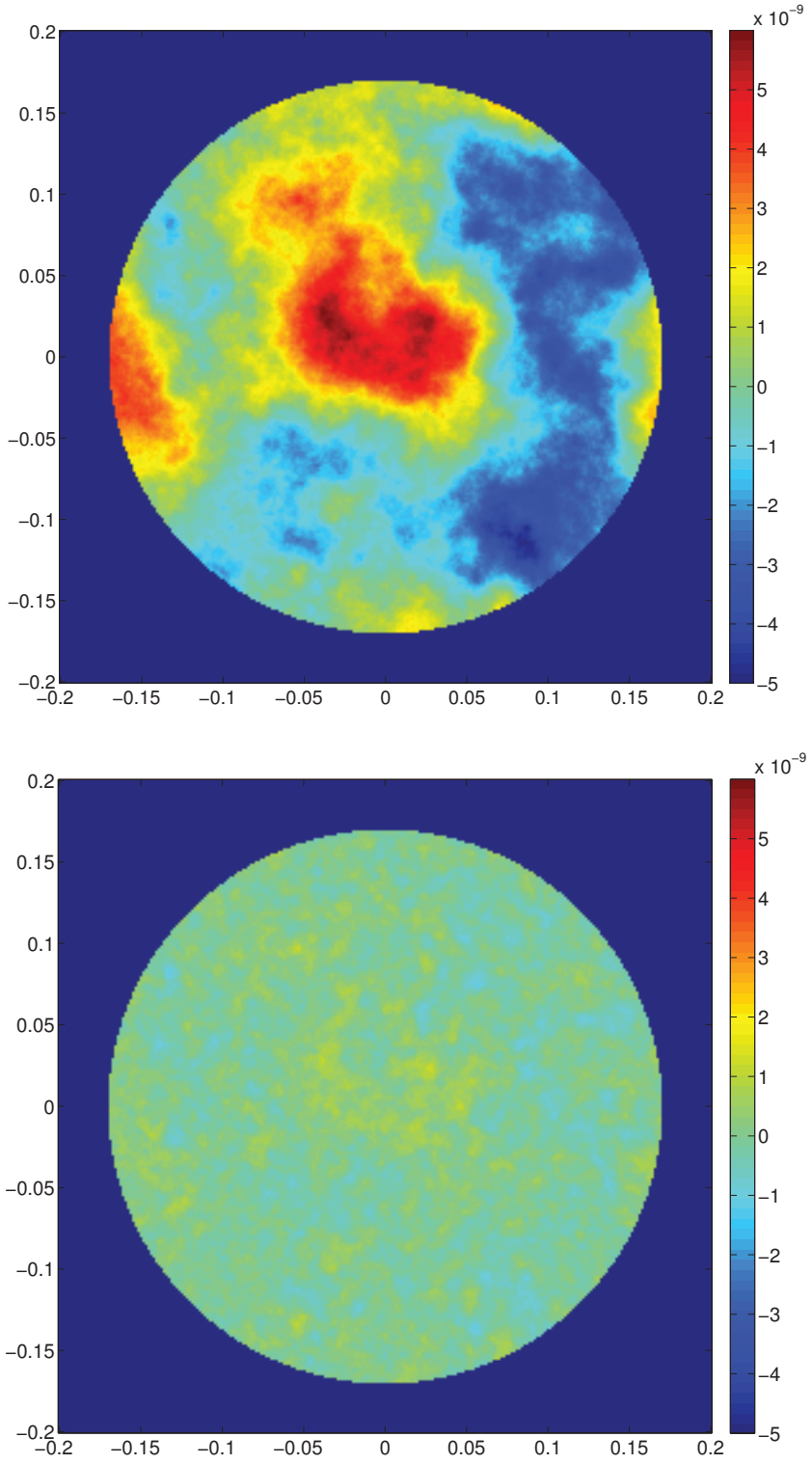

Figure 3.11: A simulated surface map with flatness of 2 nm RMS (top) and the same surface corrected up to 50 m^{-1} (bottom), its flatness is 0.33 nm RMS. The color scale is the same for both maps.

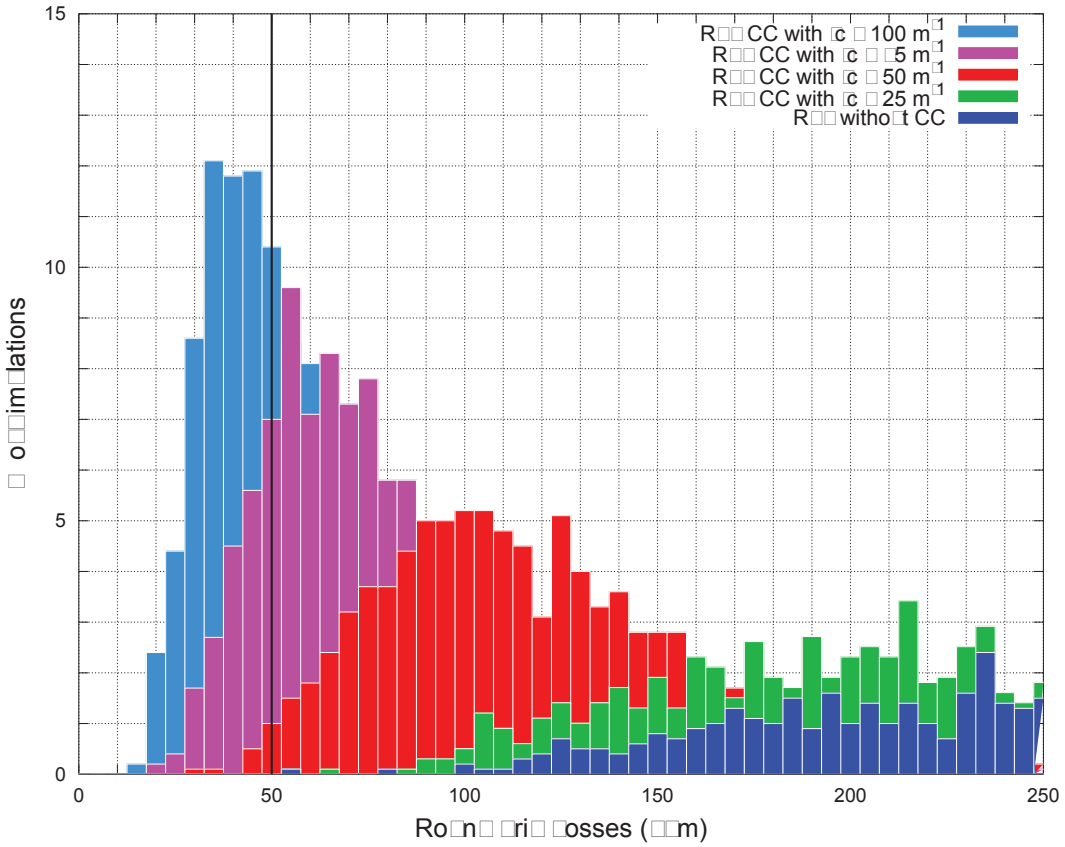

Figure 3.12: Histogram of the RTL in the Advanced Virgo cavity with original mirror surfaces flatness of 4 nm RMS and corrected with a frequency cut of 25 m^{-1}, 50 m^{-1}, 75 m^{-1} and 100 m^{-1}.

So we simulate two thousands of maps that we correct later with the described technique for different cut-off frequency. We start from virtual maps having a PSD characteristic of the General Optics polishing. Then we put those maps in the simulation of the Advanced Virgo cavity (with SIESTA) with the FFT parameters found in 3.3.3.1.

First we simulate mirrors having a flatness of 4 nm RMS as those composing the Virgo+ arm cavity, see table 3.5. We compute the RTL in the cavity for each pairs of mirrors corrected with a cut-off frequency of 25 m^{-1}, 50 m^{-1}, 75 m^{-1} and 100 m^{-1} and without correction. Figure 3.12 displays the round-trip loss computed from the simulations in the form of an histogram. On the horizontal axis we have the RTL in the Advanced Virgo cavity, and on the vertical axis we have the percentage of simulations that gives such RTL. The histogram is computed with bins of 5 ppm.

We see that the increase of frequency cut shifts the histogram to the left, i.e. towards lower round-trip losses in the cavity. This is in agreement with the fact that the HSF defects (above 50 m^{-1}) diffract the light out of the cavity. Thus the more one corrects high spatial frequencies the less the light escapes the cavity. Anyhow as simulated here the correction is

not enough to get the RTL down to 50 ppm. This is true even if it corrects up to 100 m^{-1}, i.e. a mask of 1 cm. Only 1 % of the simulations with mirror surfaces corrected up to 50 m^{-1} gives RTL smaller than 50 ppm. As for a 1 cm mask ($f_c = 100$ m^{-1}), it gives about 57 % only of the simulations with round-trip losses below the 50 ppm limit, that is not enough. Moreover in order to adopt a conservative approach we consider that we will use a 2 cm mask so we will only correct the substrate surface figure up to a frequency of 50 m^{-1}.

Then we perform the same simulations with mirrors having an original flatness of 3, 2, and 1.5 nm RMS, for the same cut-off frequency. Table 3.6 gives the median value of the round-trip losses given in part per million for these simulations. Table 3.7 gives the standard deviation of the RTL for each set of simulations. And finally the table 3.8 gives the percentage of simulations that gives RTL below 50 ppm.

Table 3.6: Median value of the RTL for each set of simulations

	Median(RTL)				
surface quality	**No CC**	**CC with** $f_c = 25$ m^{-1}	**CC with** $f_c = 50$ m^{-1}	**CC with** $f_c = 75$ m^{-1}	**CC with** $f_c = 100$ m^{-1}
Original Flatness = 4 nm RMS	315.0 ppm	241.8 ppm	114.8 ppm	69.1 ppm	46.9 ppm
Original Flatness = 3 nm RMS	181.3 ppm	139.7 ppm	67.0 ppm	40.4 ppm	27.2 ppm
Original Flatness = 2 nm RMS	81.3 ppm	62.5 ppm	29.5 ppm	17.7 ppm	12.0 ppm
Original Flatness = 1.5 nm RMS	44.5 ppm	38.0 ppm	18.4 ppm	11.1 ppm	7.4 ppm

We see that the RTL median value is smaller than 50 ppm for the set of simulations with an original surfaces of 2 nm RMS and a frequency cut of 50 m^{-1} for the corrective coating. It is about 30 ppm but with a dispersion in the data of about 14 ppm. If we take a safety margin of 2 times the dispersion, we find that $\tilde{RTL} + 2\sigma_{RTL} = 57.9\ ppm$. This value is not compliant with the specification on the arm cavity losses.

According to the simulations, the Advanced Virgo cavity with 1.5 nm RMS flatness mirrors has quite low losses. The median value of the RTL for the original surface map is about 45 ppm but once again the dispersion is big for such mirrors ($\sigma_{RTL} == 21.5 ppm$). In order to be safe we need to correct such mirrors with at least a corrective coating frequency cut of 50 m^{-1} so that we meet the round-trip losses specification as we have $\tilde{RTL} + 2\sigma_{RTL} = 42.8\ ppm$.

Table 3.7: Standard deviation value of the RTL for each set of simulations

	STD(RTL)				
surface quality	**No CC**	**CC with** $f_c = 25$ m^{-1}	**CC with** $f_c = 50$ m^{-1}	**CC with** $f_c = 75$ m^{-1}	**CC with** $f_c = 100$ m^{-1}
Original Flatness = 4 nm RMS	168.7 ppm	111.9 ppm	52.0 ppm	30.8 ppm	20.7 ppm
Original Flatness = 3 nm RMS	93.4 ppm	65.0 ppm	29.3 ppm	17.3 ppm	11.6 ppm
Original Flatness = 2 nm RMS	44.0 ppm	31.1 ppm	14.2 ppm	8.4 ppm	5.6 ppm
Original Flatness = 1.5 nm RMS	21.5 ppm	25.4 ppm	12.2 ppm	7.9 ppm	5.4 ppm

Table 3.8: Percentage of simulations giving RTL smaller than 50 ppm

	RTL < 50 ppm				
surface quality	**No CC**	**CC with** $f_c = 25$ m^{-1}	**CC with** $f_c = 50$ m^{-1}	**CC with** $f_c = 75$ m^{-1}	**CC with** $f_c = 100$ m^{-1}
Original Flatness = 4 nm RMS	0 %	0 %	1 %	18.8 %	56.8 %
Original Flatness = 3 nm RMS	0.3 %	0.8 %	23.8 %	69.2 %	94.8 %
Original Flatness = 2 nm RMS	13.9 %	33.2 %	88.4 %	99.3 %	100 %
Original Flatness = 1.5 nm RMS	61.3 %	71.6 %	95.9 %	99.6 %	100 %

When doing this kind of Monte-Carlo simulations, it is also interesting to look at the percentage of simulations compliant with the specification. In order to have a safety margin, we want to have more then 95 % of the simulations with losses smaller than 50 ppm. This condition is reached for mirrors with 2 nm RMS flatness corrected up to a spatial frequency of 75 m^{-1} or more. As we estimate at the time of writing that we will not correct the mirrors up to a spatial frequency higher than 50 m^{-1}, it is not enough to start with 2 nm RMS mirrors. Thus, we need to start from mirrors having a lower flatness. And we see that the 1.5 nm RMS mirrors corrected up to 50 m^{-1} reach the 95 % condition.

Figure 3.13 shows the results of the simulations with mirrors having an original flatness of 1.5 nm RMS. We assume that the corrective coating will work at 50 m^{-1} we have about 96 % of the simulations giving RTL smaller than 50 ppm. The median of the thousand simulations with the maps corrected up to 50 m^{-1} is about 19 ppm. It is smaller than the 50 ppm limit but the dispersion of those results is also quite big, it is about 12 ppm. The histogram of the RTL for the mirrors corrected up to 50 m^{-1} only is shown in figure 3.14.

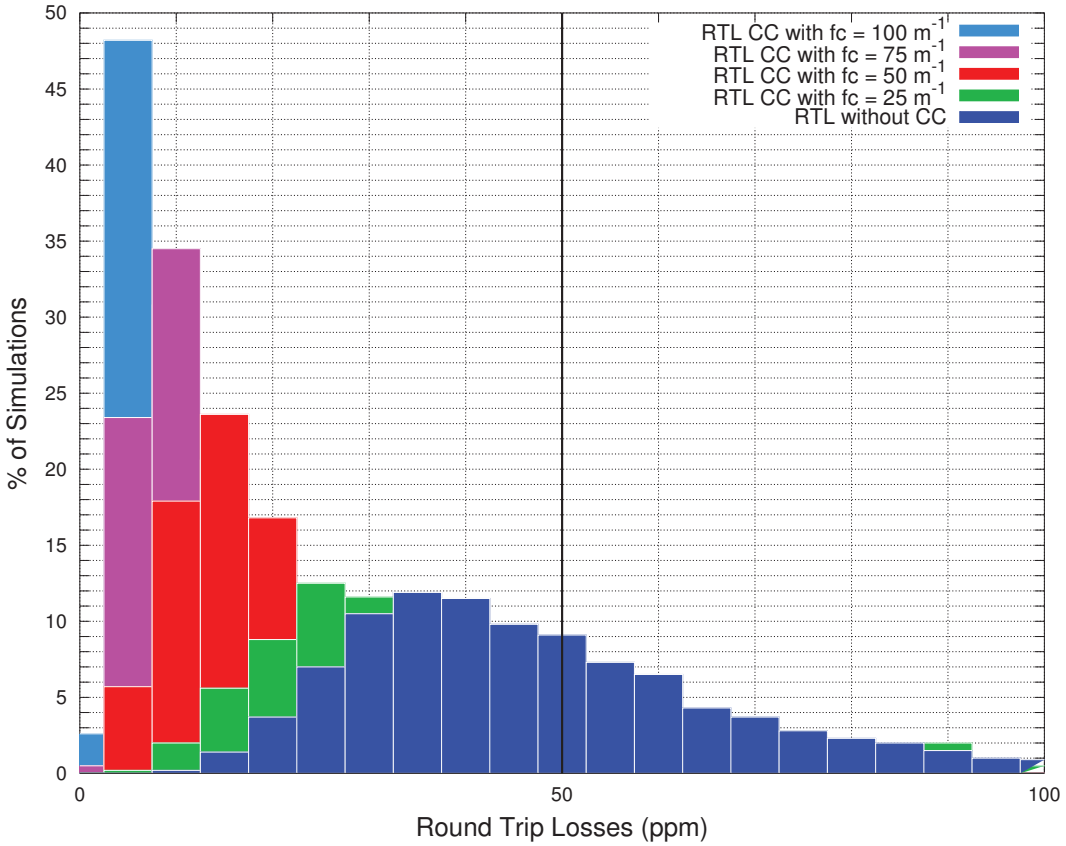

Figure 3.13: Histogram of the RTL in the Advanced Virgo cavity with original mirror surfaces flatness of 1.5 nm RMS and corrected with a frequency cut of 25 m^{-1}, 50 m^{-1}, 75 m^{-1} and 100 m^{-1}.

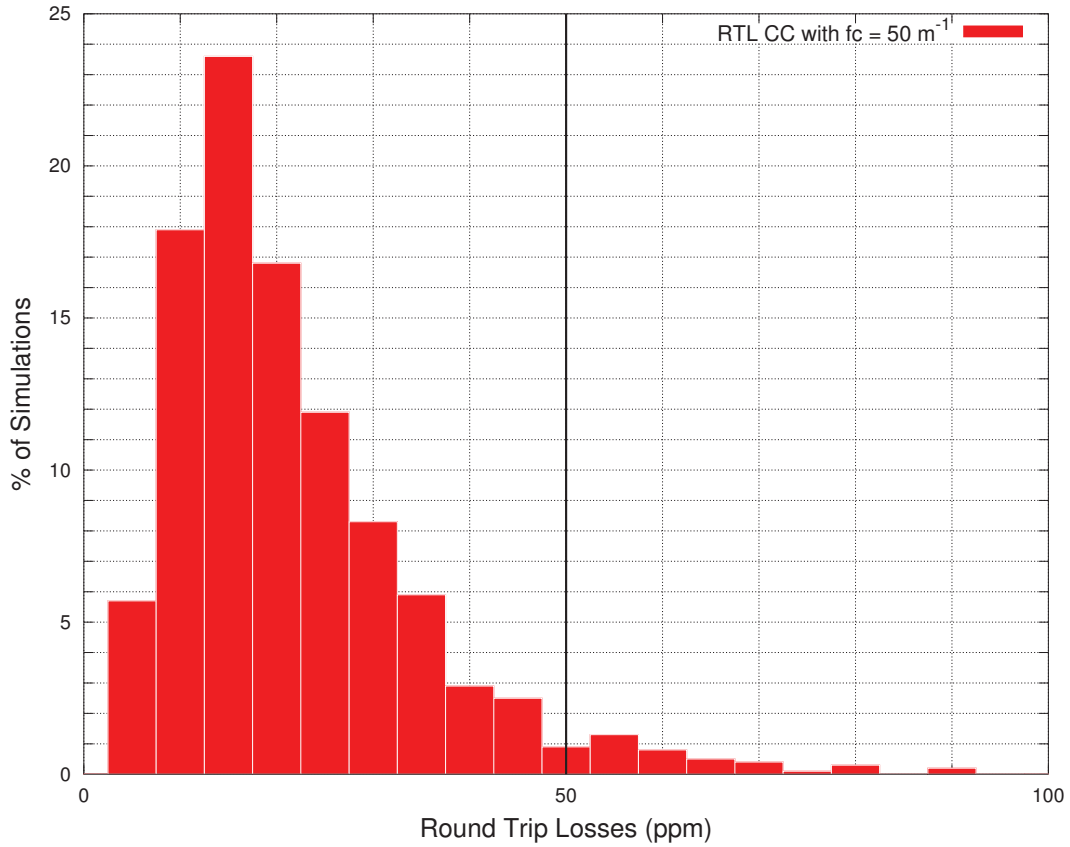

Figure 3.14: Histogram of the RTL in the Advanced Virgo cavity with original mirror surfaces flatness of 1.5 nm RMS and corrected with a frequency cut of 50 m^{-1} only.

From these simulations we can say that we need to correct a 1.5 nm RMS substrate with a corrective coating working up to a spatial frequency of 50 m^{-1}. Whereas if we are able to correct a surface up to a spatial frequency higher than 50 m^{-1}, a surface having a flatness of 2 nm RMS is enough to reach the required flatness for Advanced Virgo. Then the following specifications will be given depending on further experimental tests:

- Flatness = 1.5 nm RMS on a 150 mm diameter, if $f_{cut-off} = 50$ m^{-1}.
- Flatness = 2 nm RMS on a 150 mm diameter, if $f_{cut-off} > 50$ m^{-1}.
- Flatness = 0.15 nm RMS on a 150 mm diameter in the spatial frequency range 50 m^{-1} – 1000 m^{-1} .

3.7 Conclusion

To conclude, in this chapter we show the influence of the mirrors surface flatness on the round-trip losses in a Fabry-Perot cavity. The lower the flatness is, the lower the losses are. The Advanced Virgo baseline [42] specifies that the intra cavity losses in the arm cavity losses should be smaller than 75 ppm. We estimate that the contribution of the mirror surface due to the low spatial frequency (i.e. smaller than 1000 m^{-1}) should not exceed 50 ppm. The losses resulting from this LSF are due to the finite size of the mirrors that makes the light diffracted by the defects when impinging on the mirrors exits the cavity. This kind of losses are called clipping losses. There is another kind of losses in the cavity which is called the coupling losses. The coupling losses are the mismatch between the theoretical beam circulating and the one actually circulating. They can be different because of the mirror surfaces that distorted the beam from the theoretical TEM_{00} mode. High order modes can also be excited by the surface figures and it will be accounted in the RTL_{00}.

Starting from there we derived the specifications on the LSF for the arm cavity mirrors surface. To do so we performed thousands of simulations using a monte-carlo approach. Theses simulations underline that expressing the flatness in terms of RMS is not enough. The PSD shape of the surfaces is important as different PSD shapes gives different losses in a FP cavity for an equal flatness. We also showed that the light diffracted by defects having a spatial frequency above 50 m^{-1} never reach the other end of the cavity and so the shape of the PSD does not matter any more. Then we decided to give a specification in the HSF range (i.e. 50 m^{-1} – 1000 m^{-1}), this specification is set to be 0.15 nm RMS.

We also simulate the corrective coating to understand the effect of the correction on the RTL in the Advanced Virgo cavity. It has been simulated in two ways, the first one is in the spatial frequency domain and the second is in the spatial domain. The effect of the corrective coating is to flatten the power spectral density below a certain frequency cut. The cut-off frequency of the correction is related to the size of the mask used in the deposition of the corrective coating. We found that correcting a 1.5 nm RMS mirror with a frequency cut of 50 m^{-1}, i.e. a 2 cm mask, will allow us to meet the specification required in terms of RTL in Advanced Virgo. Thus we set the specification of the polishing to be of 1.5 nm RMS in the central region (150 mm diameter) plus the specification on the HSF mentioned earlier (i.e. 0.15 nm RMS in the range 50 m^{-1} – 1000 m^{-1}). We will then have to correct the substrate to lower its flatness and so provide substrates that induce round-trip losses smaller than 50 ppm in the Advanced Virgo arm cavity.

Chapter 4

Measurement of a surface flatness: phase-shifting interferometry

4.1 Introduction

In this chapter, we will discuss the measurement of mirror optical surface using the technique of the phase-shifting interferometry (PSI) first described by P. Carré in 1966 [77]. The development of the PSI technique took off in the early 1970 ([78, 79, 80]) and it is still the object of research and development in the domain of metrology. Nowadays the phase-shifting interferometry technique is widely used to test the quality of a surface over a diameter of typically 100 mm or more.

First we will describe the basic principle of phase-shifting interferometry. Then, we will present the actual apparatus at LMA which is composed of a commercial phase-shift interferometer associated with a motorized stage to perform measurement on a diameter larger than the interferometer pupil size. We will then present the main noise sources that limit the accuracy and the precision of the measurement and some methods will be introduced to mitigate their effects. We will also show a study on the repeatability of the measurement which is directly related to the noise sources presented earlier.

Then we will focus on the stitching technique, this technique is used to measure surfaces over a diameter larger than the interferometer pupil size. We will show the reproducibility of the measurement method and introduce the limiting factors for such a measurement.

Finally, we will compare the measurements done at LMA with measurements done at the polishing company in the case of substrates used for the aLIGO project. These substrates have been ion-beam polished and have a very-low flatness below 0.2 nm RMS on a diameter of 160 mm for the front surface and below 1 nm RMS for the back surface on the central part. We will show with the actual set up at LMA, the measurement of curved surface is

limited in the absence of a curved reference surface.

4.2 The Phase-Shifting Interferometry

The goal of the Phase-Shift Interferometry is to measure the surface figure of a substrate or a mirror. Its principles is described in details in [81]. It is based on laser interferometry more precisely the Fizeau interferometer. Figure 4.1 shows a scheme of the phase-shifting technique. The Fizeau interferometer consists of two surfaces, i.e. the reference surface and the surface to be measured (test surface), facing each other. The combination of the two wave-fronts coming from the reference and test surfaces results in an interferogram. This interferogram is related to the change in the optical path difference between the two surfaces and it is directly linked to the height of the tested surface. At each location the height $h(x, y)$ is related to the phase $\phi(x, y)$ by:

$$h(x, y) = \frac{\phi(x, y) \times \lambda}{4\pi} \tag{4.1}$$

where x and y are the spatial coordinates and λ is the wavelength of the laser interferometer.

The PSI technique consists in introducing a time-varying phase shift between the reference and test surfaces by the mean of a piezoelectric actuator that moves the reference surface. This phase-shift changes the interference patterns due to the optical path difference between the two surfaces. A number of interference patterns are acquired at different phase-shifts position differing typically by a multiple of $\frac{\pi}{2}$. Then an appropriate algorithm allows to retrieve the phase-shift between the two surfaces and so we can derive the height of the test surface.

The wave-fronts coming from the reference and test surfaces are expressed as:

$$E_r(x, y, t) = A_r(x, y)e^{i[\phi_r(x,y)-\delta(t)]} \tag{4.2}$$

and

$$E_t(x, y) = A_t(x, y)e^{i\phi_t(x,y)} \tag{4.3}$$

where $A_r(x, y)$, $A_t(x, y)$, $\phi_r(x, y)$ and $\phi_t(x, y)$ are the wave-front amplitudes the phases of the fields coming from the reference and test surfaces. The r and t indices refer to either the reference or test surfaces. $\delta(t)$ is the time dependent phase-shift introduced during the measurement.

The intensity pattern resulting from the interference of the two wave-fronts is:

$$I(x, y, t) = [E_r(x, y, t) + E_t(x, y)]^2 \tag{4.4}$$

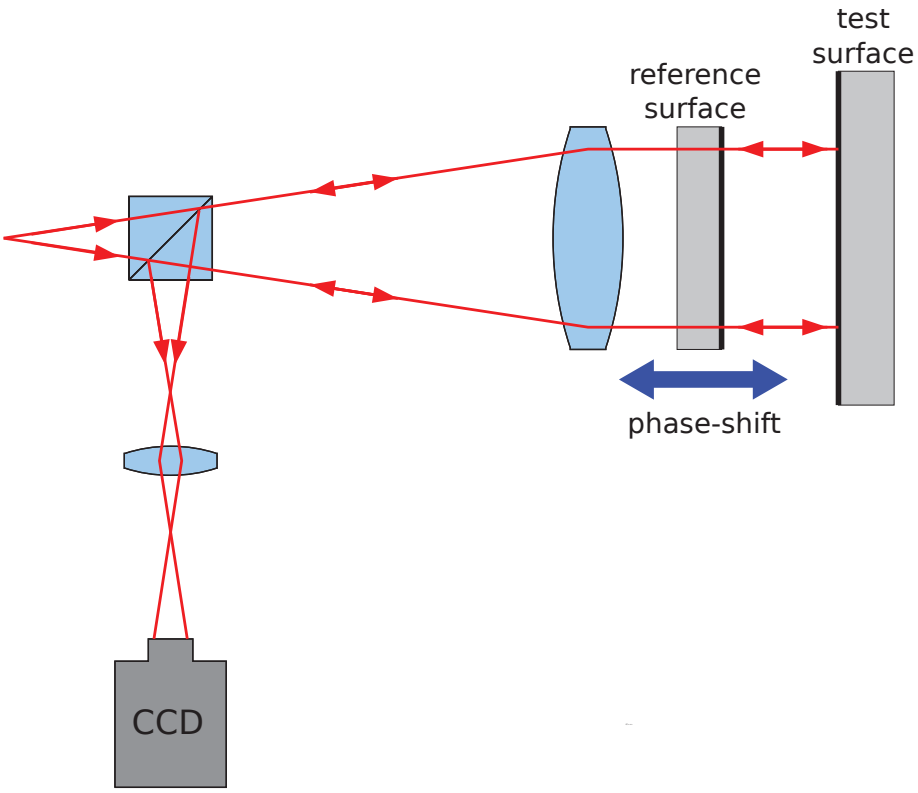

Figure 4.1: Phase-Shifting Interferometry.

which can be derived as following

$$I(x,y,t) = [A_r(x,y)e^{i[\phi_r(x,y)-\delta(t)]} + A_t(x,y)e^{i\phi_t(x,y)}]^2 \tag{4.5}$$

$$I(x,y,t) = A_r^2(x,y) + A_t^2(x,y) + A_t(x,y)A_r(x,y)[e^{i(\phi_t(x,y)-\phi_r(x,y)+\delta(t))} + e^{-i(\phi_t(x,y)-\phi_r(x,y)+\delta(t))}] \tag{4.6}$$

then we have,

$$I(x,y,t) = I'(x,y) + I''(x,y)\cos[\phi_t(x,y) - \phi_r(x,y) + \delta(t)] \tag{4.7}$$

where $I'(x,y) = A_r^2(x,y)+A_t^2(x,y)$ is the average intensity and $I''(x,y) = 2*A_t(x,y)A_r(x,y)$ is the intensity modulation. The fundamental PSI equation is then written as:

$$I(x,y,t) = I'(x,y) + I''(x,y)\cos[\phi(x,y) + \delta(t)] \tag{4.8}$$

where $\phi(x,y) = \phi_t(x,y) - \phi_r(x,y)$ is the phase difference due to the optical path difference between the two surfaces i.e. the quantity one wants to measure to retrieve the surface figure of the sample under test.

From this equation we can extract the unknown phase $\phi(x, y)$ using an appropriate algorithm. PSI algorithms are based on the analysis of the intensity variation.

Many algorithms have been developed in the 1980s which are more or less sensitive to the different noise sources as summarized in [81].

Here for the sake of simplicity, we will present the well-known *four step algorithm*. Four separate interferograms are acquired to compute the phase at each location. In this case the four interferograms are recorded with a phase separation of 90°. The phase-shift $\delta(t)$ have four different values:

$$\delta_i = 0, \pi/2, \pi, 3\pi/2; \qquad i = 1, 2, 3, 4; \tag{4.9}$$

Inserting these values into equation 4.8 we have the four inteferograms described by:

$$\begin{aligned} I_1(x,y) &= I'(x,y) + I''(x,y)\cos[\phi(x,y)] && (4.10)\\ I_2(x,y) &= I'(x,y) + I''(x,y)\cos[\phi(x,y) + \frac{\pi}{2}] && (4.11)\\ I_3(x,y) &= I'(x,y) + I''(x,y)\cos[\phi(x,y) + \pi] && (4.12)\\ I_4(x,y) &= I'(x,y) + I''(x,y)\cos[\phi(x,y) + \frac{3\pi}{2}] && (4.13) \end{aligned}$$

These four equations can be derived by a simple trigonometric identity in:

$$\begin{aligned} I_1(x,y) &= I'(x,y) + I''(x,y)\cos[\phi(x,y)] && (4.14)\\ I_2(x,y) &= I'(x,y) - I''(x,y)\sin[\phi(x,y)] && (4.15)\\ I_3(x,y) &= I'(x,y) - I''(x,y)\cos[\phi(x,y)] && (4.16)\\ I_4(x,y) &= I'(x,y) + I''(x,y)\sin[\phi(x,y)] && (4.17) \end{aligned}$$

We can resolve this system of equation for the phase term $\phi(x, y)$ by subtracting the even and odd terms one to each other:

$$I_4(x,y) - I_2(x,y) = 2I''(x,y)\sin[\phi(x,y)] \tag{4.18}$$

$$I_1(x,y) - I_3(x,y) = 2I''(x,y)\cos[\phi(x,y)] \tag{4.19}$$

Thus the average intensity term is eliminated. Then we divide the equation 4.18 by equation 4.19 to eliminate the modulation intensity term.

$$\frac{I_4(x,y) - I_2(x,y)}{I_1(x,y) - I_3(x,y)} = \frac{\sin(\phi(x,y))}{\cos(\phi(x,y))} = tan[\phi(x,y)] \tag{4.20}$$

Finally, we get the phase at each location (x,y) as a function of the four recorded interferograms.

$$\phi(x,y) = \tan^{-1}\left[\frac{I_4(x,y) - I_2(x,y)}{I_1(x,y) - I_3(x,y)}\right] \tag{4.21}$$

So applying the algorithm we obtain the phase-shift between the two surfaces. Then we can determine the equivalent height using equation 4.1 to which we subtract the contribution of the reference surface, which is known a priori. By subtracting the reference surface we obtain the surface figure of the sample we want to measure.

It also should be noted that when using a phase-shift interferometer the back surface of the tested optics can contribute to the phase measured by the interferometer if there is no wedge between the two surfaces of the optic. In the case of the set up available at LMA the two surfaces should be tilted by an angle of at least 0.8 mrad as shown in [82] in order not to disturb the measurement of the surface under test. The measurement of parallel substrate as foreseen in the Advanced Virgo technical design report [23] is impossible with good accuracy at LMA with the present set up.

The issue of the parallel second face of a substrate can be overcome by the use of a wavelength shifting interferometer. The basic principle of the measurement is the same but instead of having a mechanical phase shifting the phase shifting is provided by the tuning of the wavelength of the laser source. The contribution of the two surfaces and thickness of the sample induce an interferogram with multiple interference. A Fourier analysis of the signal recorded during the wavelength shift combined with controlled acquisition parameters allow to retrieve the contribution of the two surfaces and of the substrate [83]. The technique is also less sensitive to noise sources such as vibrations according to [83].

4.3 The measurement at LMA

In this paragraph we will present the apparatus available at LMA to measure the mirrors surface shape. It is composed of a commercial phase-shifting interferometer with a 6 inches pupil from ADE phase-shift. A stitching software associated with a positioning system to transversally move the substrate allows to measure wave-front over a diameter of 300 mm [84]. We will first present the interferometer in itself and then we will describe the stitching technique.

4.3.1 Description of the phase-shift interferometer

We measure the wave-front surface at LMA using a commercial phase-shifting interferometer from ADE phase-shift called Minifiz [85]. It has a 6 inches (152.4 mm) pupil and works at a

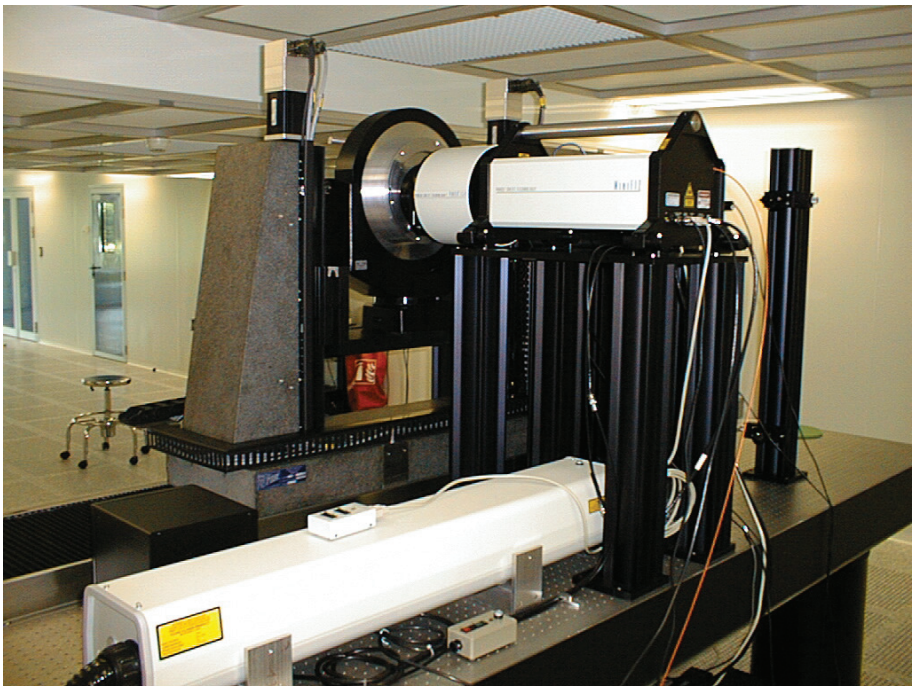

Figure 4.2: The Minifiz phase-shifting interferometer on the metrology bench.

wavelength of 1064 nm. It was designed without any optical zoom so that it is as aberration-free as possible. It provides a surface figure map over a grid of 415×415 pixels. The pixels of the grid are squares with a width of 350 µm.

Figure 4.2 shows a picture of the Minifiz interferometer. It is set up at a height of 60 cm on the table so that the sample can be moved in front of it when measuring wave-front on a diameter larger than 145 mm.

The substrate is mounted into a sample holder. Figure 4.3 shows an exploded view of the sample holder for the aLIGO substrates (340 mm diameter and 200 mm thick). The design of the sample holder is the same as for the initial Virgo mirrors which are a bit larger while 2 times thinner (350 mm diameter and 100 mm thick). They are composed of two circular parts into which the substrates is put and hold. Theses circular part are larger than the mirror diameter by about 1 mm so that the substrate can enter easily in the sample holder. Unfortunately it causes the substrate to rest on a singular line and so it induces deformations of the substrate surface because of the weight of the substrate. Ideally the sample holder should fit perfectly the sample to be measured so that the substrate rest on a large surface reducing consequently the deformation induced on the surface. Practically this is not achievable as the substrates have a variation in dimension at the level of the tenths of mm. We will see later that the mounting of the substrate in the sample holder can induce surface deformation.

Figure 4.3: Exploded view of the sample holder for the measurement of aLIGO mirror surface figures with phase-shifting interferometry. The tested surface is located on the right of the figure. Plexiglass allows to protect the substrate surfaces while being handled.

The substrate is mounted horizontally in the sample holder. Two rings with a plexiglass plate having a smaller diameter than the substrate allows to close the sample holder. The role of that rings is to hold the substrate in the sample holder while being translated from an horizontal to a vertical position for measuring. Once mounted in the sample holder the substrate is put into a gimbals set on a motorized stage in front of the interferometer as one can see in the figure 4.2. The gimbals allows to adjust the vertical and horizontal tilt of the surface to be tested whereas the motorized stage allows to move the surface in front of the interferometer when performing a stitching measurement (see paragraph 4.3.2).

4.3.2 The stitching technique

The PSI available at LMA allows measuring surfaces over a diameter as large as the pupil diameter i.e. 150 mm. To overcome this limitation a numerical method has been developed by a French company (MB Optique) called "stitching interferometry" [84], [86]. It allows to measure larger diameter by taking overlapped measurements as shown in the figure 4.4. Then the measurements are stitched together by adjusting their tilt (the inclination of the surface in the x and y direction) and piston. At LMA, the substrate is mounted in a sample holder which is mounted on a gimbal that can be moved in front of the interferometer. It allows

to take measurements of the surface at different position. Then a software developed by the company MB Optique reconstructs the surface figure of the substrate on a large diameter. Figure 4.4 presents the position of the sub-aperture measurements for a measurement on a diameter of about 310 mm. 8 measurements are performed, one on the center and 7 on the external radius of the measurements.

This stitching technique enables us to measure a substrate on a large diameter but it also adds errors on the measurement. Indeed several sub-aperture measurements are needed to get a full aperture measurement and each one is subjected to the various noise sources that affect the precision and accuracy of the final measurement. Also the sub-aperture measurements should be taken in a row to avoid any drift in the conditions of the measurements. It takes about one minute to take one sub-aperture measurements and we wait around 30 seconds between each sub-aperture measurement to give time for the substrate to move to the new position and to stabilize.

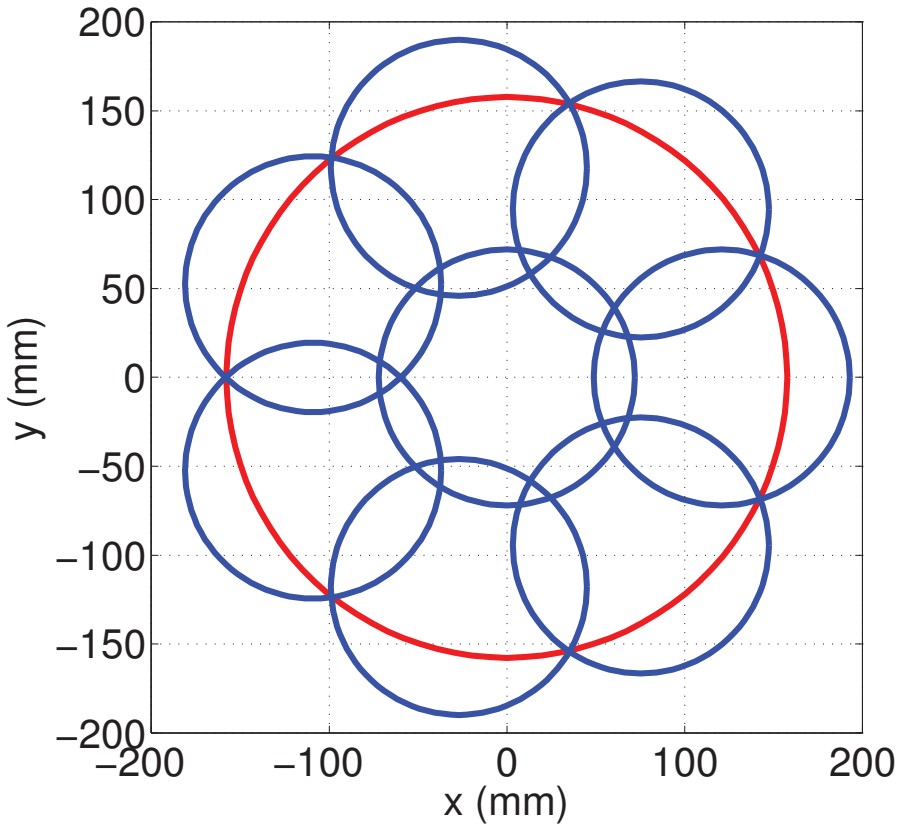

Figure 4.4: The stitching technique. The blue circles represent the different sub-aperture measurement and the red circle represent the overall measurement.

4.4 Main error sources.

Various error sources can affect the accuracy of the phase measurement such as the phase-shift calibration, the detector non linearity or the environmental condition (vibrations and air turbulences) [87]. We can differentiate different kind of errors. First the random errors that are mostly due to the environmental conditions. They principally affect the precision and the repeatability of the measurement. This kind of errors can be mitigated by the averaging of multiple measurements.

These random errors mentioned above are different from the systematic errors which are due to the instrument itself (phase-shift calibration, laser wavelength drift). The systematic errors occurs in any measurements and it affects principally the accuracy of the measurement. Some of the systematic error sources are discussed in [88]. A way to evaluate the accuracy of the measurement is to compare the measurements of the same substrate done by different instruments. In section 4.7 we will show some comparisons of the measurement done on the aLIGO substrate at LMA and at Tinsley[1].

The repeatability and the reproducibility of the measurement will also be studied. In the following we will define the repeatability as the comparison of successive measurements without dismounting the sample from the sample holder whereas the reproducibility of the measurement will be the comparison measurements made at different times with the sample dismounted and remounted from the sample holder. A high repeatability and reproducibility is mandatory to have a high accuracy measurement but a high repeatability does not mean a high accuracy. Indeed a poor accuracy of the measurement caused by a systematic error will appear systematically on the measurement and so will be repeatable. To asses the repeatability and reproducibility of the measurement, we calculate the difference between different measurements and look at the flatness of the subtractions or at their power spectral densities. We will study the repeatability of the measurement in the paragraph 4.5

In the following, we will concentrate on the environmental noises and we will show their effects on the phase map measurement.

4.4.1 Vibrations.

The effect of vibrations have been studied extensively by de Groot in [89]. It shows that the effect of vibrations is to print a ripple on the phase map having twice the spatial frequency of the interference fringes. This error is commonly called ripple noise. It is shown in the same paper that the error induced by the vibrations is dependent on the reconstruction algorithm

[1] the substrate polishing company

used to compute the surface map. A study of the behaviour of the different algorithms developed in the domain on the phase-shifting interferometry can be found in [81].

Unfortunately, in the software that controls the phase-shifting interferometer, the algorithm used is fixed and unknown to us.

4.4.2 Air turbulences.

The air turbulences can have a strong effect on the measurement, indeed when measuring a surface the air circulating between the test and reference surfaces can modify the optical path difference by a change in the index of refraction. This effect is visible even if the surface under test is set up close to the reference surface (typically 5 cm) in order to have the minimum air gap between the two surfaces. The effect of the air turbulences is to add low spatial frequency structures in the phase map. This is not easy to see on the phase map as it could easily be misinterpreted as being part of the tested surface.

A way to highlight the air turbulences effect is to take several measurement in a row with a small time lapse between measurements and to look at them subsequently. Doing this one can easily see a background on the figure that remains constant (being the real surface) and a dynamic components (the random error on the measurement) that moves in front of the background. Another way to see this effect is to subtract several measurements of the same sample one to each other. On these subtractions, one can easily see extra bumps that are due to the air turbulences.

4.5 Repeatability of the measurement.

A study of the repeatability of the measurement has been carried out with the phase-shifting interferometer in different conditions of vibrations and air turbulences. This study has been done in the context of the development of a new metrology bench for the measurement of Advanced Virgo substrates and mirrors. We have studied the repeatability of the measurements in the clean room which has a floating floor and in the plenum, i.e. the room located below the clean room which has a concrete floor. The Minifiz is actually installed in the clean room. A study of the seismic noise was made by I. Fiori and F. Paoletti from the European Gravitational Observatory (EGO) [90]. As expected they have shown in [91] that the seismic conditions are better in the plenum which has a concrete floor than on the floating floor of the clean room. They also show that the noise in the plenum is dominated by structures at 48 Hz which are presumably due to asynchronous motors. Identified vibrations sources (pumps, compressors) have been set on elastomer in order to mitigate those noises.

Typically we take 40 measurements of the same sample in a row with about 1 minute gap between two measurements. Then we subtract the measurements one to each other, it gives 780 new surface maps of the difference that will be called in the following subtraction map. Then we compute the RMS flatness of the difference, it gives a data set of subtractions flatness. Ideally the difference between two consecutive measurements should be null. In these measurements only the tilt and the piston are removed from the surface maps as those have from origin a slow drift in the relative position of the substrate and of the reference. The median value of the RMS flatness of the subtractions data set along with the standard deviation are two essential numbers to characterise the repeatability or the reproducibility of the measurements. A high value for the standard deviation compared to the median value shows that the measurement was not stable over time. For example, the substrate could be not fully stabilized in the sample holder. A slow deformation of the substrate would induce a high difference between the firsts and the lasts measurement but would not be seen in the subtraction of two consecutive measurements.

Another important figure of merit for Virgo is the radius of curvature and so using the same data sets we look at the repeatability of its measurement. To do so we decompose the surface maps in Zernike terms [92, 93] and look at the highest difference in the amplitude of the Zernike polynomials Z_2^0 which characterize the radius of curvature of a surface. See appendix A for more details on the Zernike polynomials. The radius of curvature (RoC) of a surface is linked to the amplitude α_2^0 of the Zernike polynomial Z_2^0 by the following formula:

$$\mathrm{RoC} \;=\; \frac{r^2}{4 \times \alpha_2^0} \tag{4.22}$$

with r being the radius of the measurement.

We will next show a study of the repeatability in the clean room and in the plenum. In the future it is foreseen to move the metrology bench for the measurement of surface figure in the plenum.

4.5.1 Clean room

A lot of series of measurements have been done in the central area (on a diameter of 145 mm) of aLIGO substrates in the clean room under different conditions. First we measured plane surfaces with no fringes on the interference pattern; we will call this condition the flat-tint condition. Then plane surfaces have also been measured with fringes on the interferogram obtained by tilting the tested the surface with respect to the reference surface. And finally concave surfaces with circular fringes in the field of view have been measured.

Table 4.1: Repeatability of the measurement of plane surface in the clean room. The rows highlighted in grey are the one with fringes and the one highlighted in red are the measurement that have been discarded because of their instability.

Measurement Serie	**Number of measurement**	**median RMS (nm)**	**STD RMS (nm)**	**PV Z_2^0 (nm)**
etm02/etm02_s2_serie1/	39	0.12	0.03	0.27
etm02/etm02_s2_serie2/	39	0.15	0.09	0.56
etm02/etm02_s2_serie3/	19	0.13	0.03	0.22
etm02/etm02_s2_serie4/	40	0.11	0.02	0.07
etm02/etm02_s2_serie5/ (w. fringes)	40	0.20	0.04	0.27
etm02/etm02_s2_serie6/ (w. fringes)	40	0.18	0.04	0.26
etm02/etm02_s2_serie7/ (w. fringes)	40	0.22	0.05	0.33
etm01/etm01_s2/	38	0.15	0.38	0.86
etm01/etm01_s2b/ (7 fringes)	39	0.21	0.17	0.40
etm01/etm01_s2c/	40	0.16	0.07	0.54
etm01/etm01_s2d/ (25 fringes)	39	0.32	0.06	0.57
etm01/etm01_s2e/	40	0.12	0.09	0.71
itm04/itm04_s2/	100	0.29	0.11	0.37
itm04/itm04_s2b/	40	0.15	0.03	0.25
itm04/itm04_s2c/	40	0.13	0.02	0.14

Flat surface The series of measurements on a flat surfaces in flat-tint condition show quite a good repeatability. The table 4.1 shows the median value and the standard deviation of the RMS flatness of the data set as defined in the previous section for 10 series of measurement each series being composed of typically 40 measurements. The maximum difference in the amplitude of the Zernike term Z_2^0 is also reported in the table under the column "**PV Z_2^0**" .

The median value of the flatness of the subtraction is between 0.11 nm RMS and 0.16 nm RMS if we exclude the series of the measurements that shows a problem of stability, i.e. the series of measurements with a high standard deviation value of the data set ($>$ 0.1 nm RMS). The series of measurements excluded because of an abnormal instability are highlight in light red in the table 4.1.

Figure 4.5 shows the histogram of the RMS flatness of the data set of measurement subtractions in the case of a plane surface in flat-tint condition. It includes all the differences from all series of measurements with the exception of series etm01_s2 and itm04_s2 The red line shows the median value of the overall data set, it is 0.13 nm RMS. The measurement

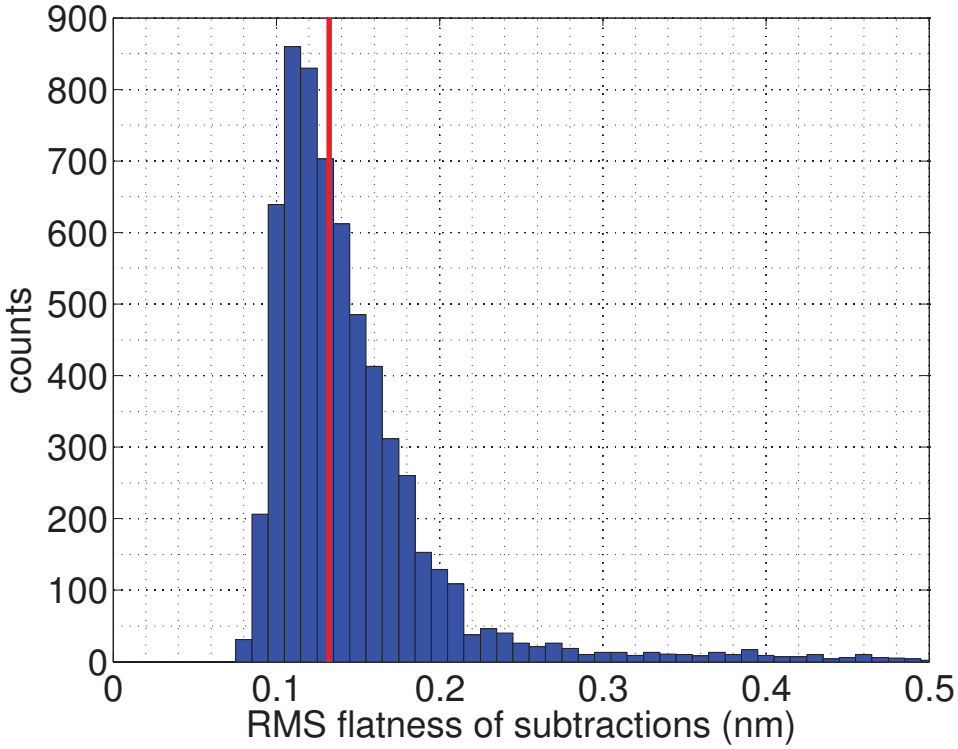

Figure 4.5: Repeatability of the measurements in flat-tint condition for a plane surface in the clean room. The red line is the median value of the data set.

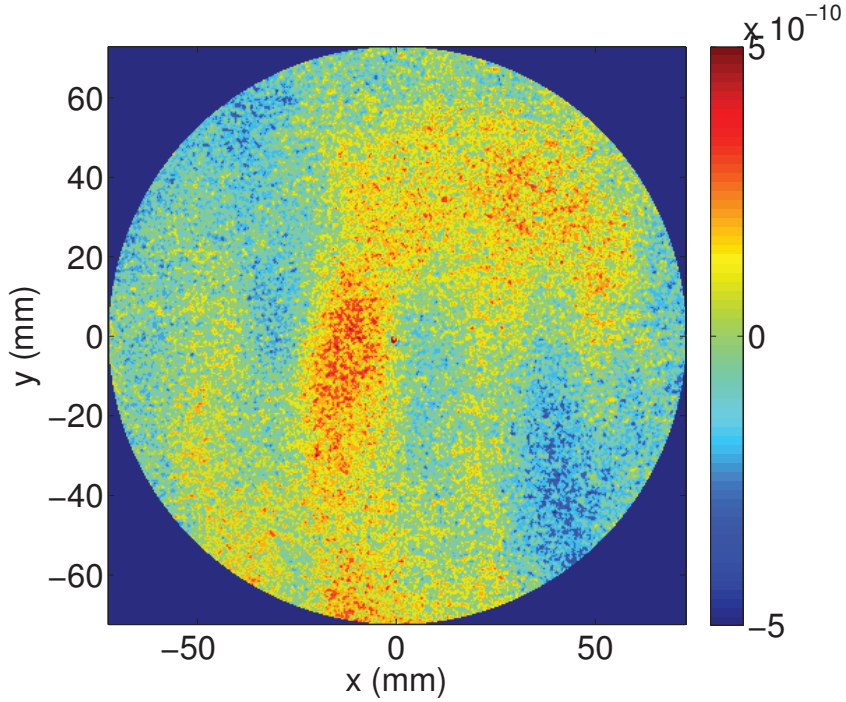

Figure 4.6: Subtraction of two successive measurements of a plane surface in flat-tint condition.

error is mainly due to the laminar air flux in the clean room. Figure 4.6 displays the subtraction of two successive measurements. We can see the effect of the laminar air flux that appears as vertical stripes in the figure. The difference of astigmatism measured limits also the repeatability. It is due to the mounting of the substrate in the sample holder that can induce deformations on the substrate surface. These deformations can change if the substrate is not well stabilized in the sample holder. The effect of the vibrations is negligible in this measurement because of the flat-tint condition. As there are no fringes in the field of view the ripple noise due to the vibrations cannot print on the phase map.

We also see that the repeatability of the amplitude of Z_2^0 Zernike polynomials amplitude is quite good as the maximum differences is at most 0.86 nm which would correspond to a difference of RoC of only 1.3 m on the radius of curvature of an ITM (nominal RoC = 1420 m) and 1.9 m on the radius of curvature of an ETM (nominal RoC = 1683 m).

In the table 4.1, some of the series of measurements (highlight in grey in the table) have been done with fringes in the field of view. Then the effects of the vibrations now dominates on the repeatability error. The median value of the flatness of the differences is now between 0.18 nm RMS and 0.32 nm RMS. The error due to vibrations prints on the surface map with two times the spatial frequency of the fringes pattern as mentioned in 4.4.1. Figure 4.8 shows the subtractions of two of the measurements, it has a flatness of 0.16 nm RMS. We see that the figure is dominated by the effect of vibrations with the fringes caused by the ripple noise.

Figure 4.7 shows the histogram of the RMS flatness of the differences between the measurements with fringes. It includes all the differences of the series of measurements highlight in grey in table 4.1. The median value of the data set is now 0.22 nm RMS. Comparing the two data sets of the flatness of the differences of the measurements with or without fringes highlights the effect of having fringes in the interference pattern. Indeed, in the same conditions the repeatability error is higher with fringes in the interferogram than in the flat-tint condition.

Concerning the radius of curvature measurement, having fringes in the interference pattern does not change the repeatability of its measurement. Indeed the maximal difference in the amplitude on the Zernike polynomial Z_2^0 in a series of measurements remains in the same range as before without fringes.

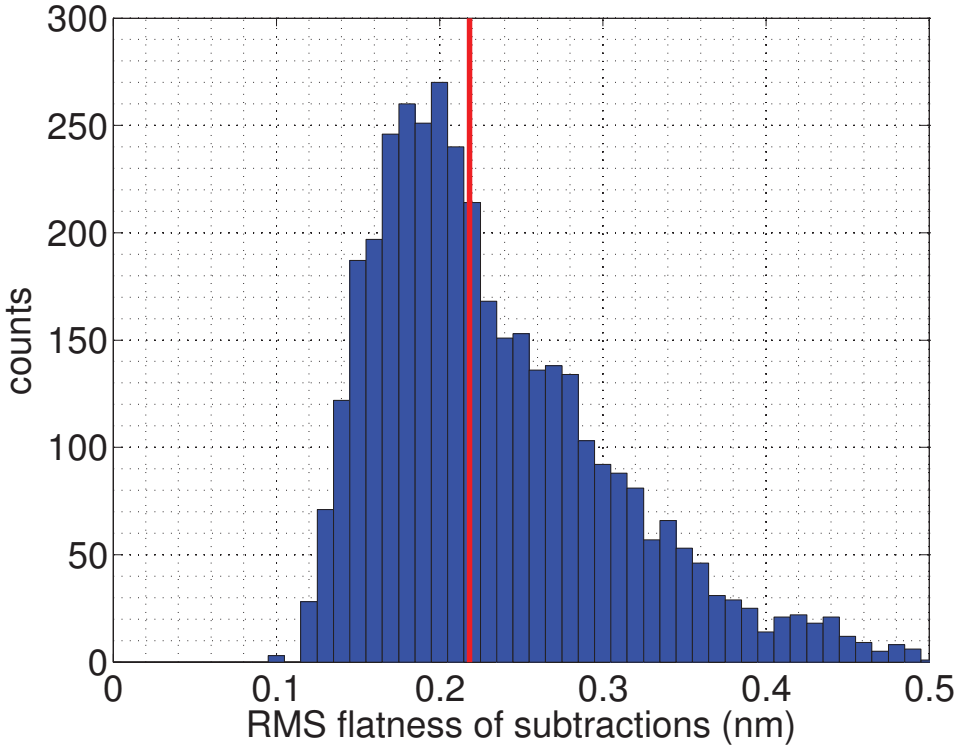

Figure 4.7: Histogram of the repeatability of the measurements with fringes in the interference pattern for a plane surface in the clean room. The red line represents the median value.

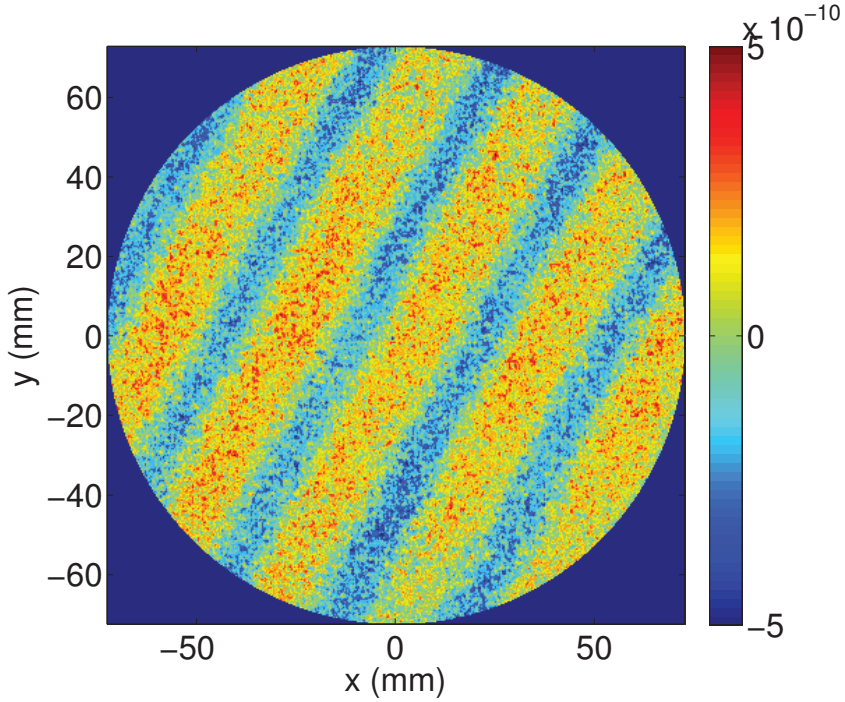

Figure 4.8: Subtractions of two successive measurements of a plane surface done with fringes on the interference pattern.

Table 4.2: Repeatability of the measurement of concave surface in the clean room. The rows highlighted in red are the measurement that have been discarded because of their instability.

Measurement Serie	**Number of measurement**	**median RMS (nm)**	**STD RMS (nm)**	**PV Z_2^0 (nm)**
itm04/Itm04_s1_centre1/	40	0.18	0.03	0.37
itm04/Itm04_s1_centre2/	40	0.23	0.09	0.58
itm04/Itm04_s1_centre3/	40	0.18	0.03	0.20
etm02/etm02_s1/	40	0.20	0.05	0.16
etm02/etm02_s1b/	40	0.16	0.03	0.20
etm02/etm02_s1c/	40	0.29	0.14	0.71
etm02/etm02_s1d/	40	0.20	0.04	0.30
etm02/etm02_s1e/	40	0.23	0.04	0.34
etm02/etm02_s1f/	40	0.21	0.03	0.34
etm01/etm01_s1_serie1/	34	0.31	0.09	0.55
etm01/etm01_s1_serie2/	37	0.19	0.05	0.28
etm01/etm01_s1_serie3/	37	0.29	0.13	0.76
etm01/etm01_s1_serie4/	37	0.28	0.14	0.77
etm01/etm01_s1_serie5/	39	0.20	0.06	0.46

Concave surface We have also studied the repeatability of the measurement of concave surfaces with the aLIGO substrates named ITM04, ETM02 and ETM01. The end test mass (ETM) have a radius of curvature of about 2250 m while the input test mass (ITM) have a radius of curvature of about 1940 m. The optical path difference between a flat and a spherical surface induces circular fringes in the field of view. In those cases there are between 2 and 3 circular fringes in the interference pattern as we only have flat reference surfaces. Here we only studied the repeatability of the measurement without looking at the systematic errors that occur. The latter will be studied in paragraph 4.7.2.

Table 4.2 shows as before the median value and standard deviation value of the flatness of the subtractions of the measurements one to each other for different series of measurements. As before, the last column shows the highest difference between the amplitude of the Zernike term Z_2^0. We see that the median value for the different data set is between 0.18 and 0.31 nm RMS. Once again the repeatability error is dominated by the effect of the vibrations.

Figure 4.9 shows the histogram of the overall data presented in the table 4.2. The series of measurement with standard deviation higher than 0.1 nm RMS have been discarded because of their instability. They have been highlighted in red in the table 4.2. It has the same shape as the figure 4.7 with a long tail and with the maximum below the median value. The median value of the data set is 0.21 nm RMS.

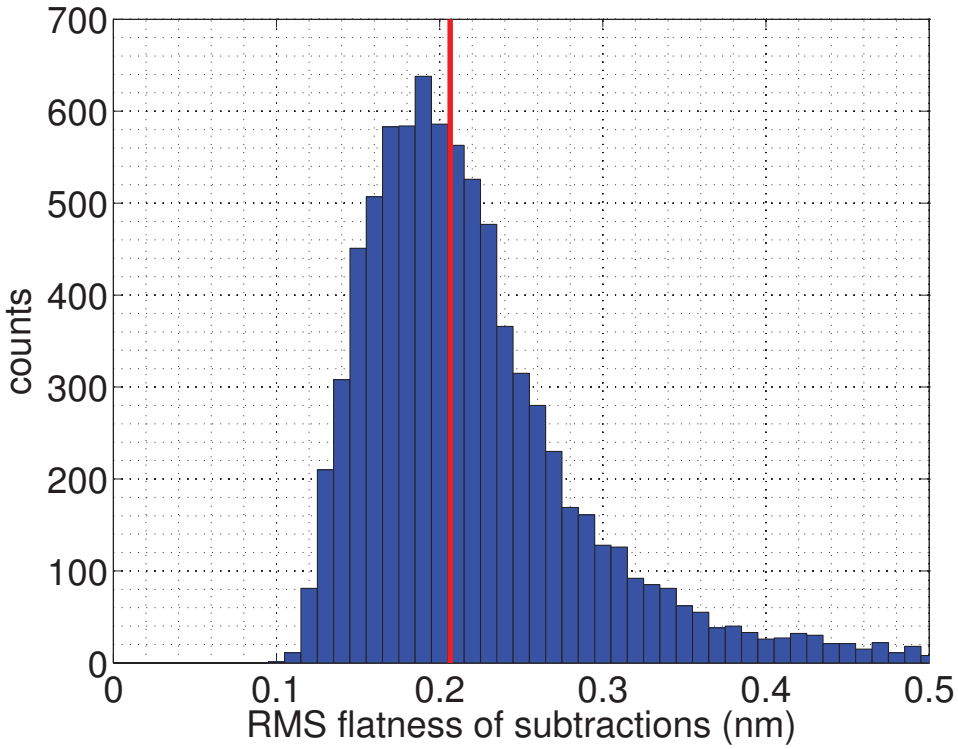

Figure 4.9: Histogram of the repeatability of the measurements with fringes in the interference pattern for a concave surface in the clean room. The red line represents the median value.

As before the repeatability of the measurement of the RoC is quite good even for the measurement that shows an instability. Indeed the largest difference between two measurements on the amplitude of the Z_2^0 term is 0.77 nm. It corresponds to a change of curvature of $\pm$ 1.5 m on a radius of curvature of 2257.5 m, the mean value of the RoC of the 37 measurements in the series etm01_s1_serie4

To conclude, we can say that the repeatability of the measurement in the clean room is limited to a level of about 0.21 nm RMS in the case where we have fringes in the interference pattern. It is dominated by the errors due to the vibrations that occur during the measurement. The fact that the clean room is on a floating floor and that the interferometer is set up at 60 cm of the table does not help reducing the error due to vibrations. It has to be noted that being in the flat-tint condition reduces the repeatability to a level of 0.13 nm RMS. It is a strong argument to foresee the purchase of a concave reference surface with a radius of curvature close to the one of the substrate surfaces that we want to measure.

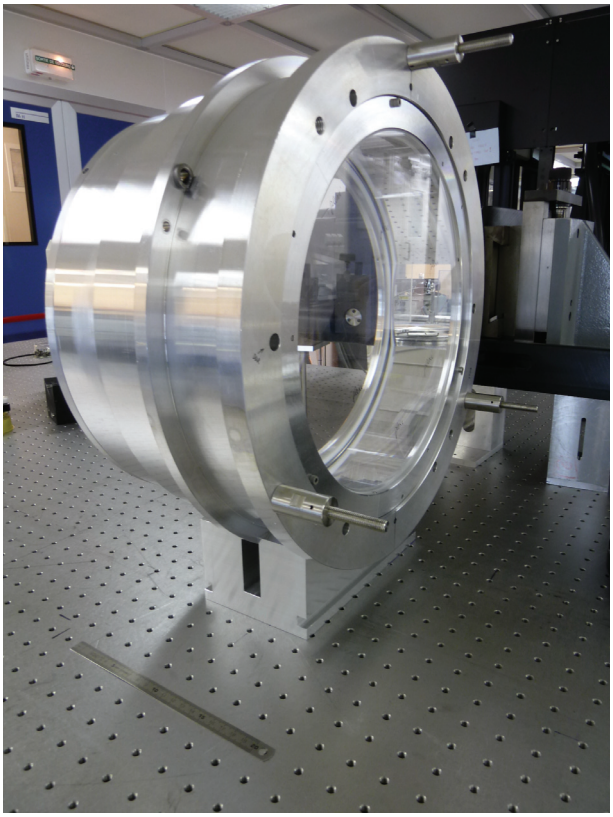

Figure 4.10: aLIGO substrates in the sample holder set up on a V-mount.

4.5.2 Plenum

One of the foreseen change to improve the repeatability of the measurement is to move the metrology bench in the plenum (below the clean room) where the seismic vibrations have been measured to be lower [91]. We have tested the repeatability of the measurement in the plenum. For these tests we moved the MiniFiz interferometer to another optical bench located in the plenum. And we measure the surface of aLIGO substrates. The substrates are mounted in the same sample holder as before and this sample holder is put on a V-mount as shown in the figure 4.10. In order to measure the center of the large substrates, the instrument is set up a few cm above the table.

Table 4.3 shows some series of measurements in the plenum. These measurements have been done on a plane surface (itm04_s2_xxx) and on a spherical surface (etm02_s1_xxx).

From theses series of measurements we can exclude the series "etm02/etm02_s1_plenum3/" as it shows a clear instability on the RoC measurement probably due to the fact that the substrate was not fully stabilized in the sample holder. Indeed the radius of curvature on this series of measurements goes from 2253.7 m to 2261.4 m. The high standard deviation value confirm the instability of this measurement.

Table 4.3: Repeatability of the measurement in the plenum. The row highlighted in red has been discarded because of its instability.

Measurement Serie	**Number of measurement**	**median RMS (nm)**	**STD RMS (nm)**	**PV Z_2^0 (nm)**
etm02/etm02_s1_plenum1/	40	0.37	0.07	0.81
etm02/etm02_s1_plenum2/	40	0.37	0.06	0.78
etm02/etm02_s1_plenum3/	40	0.80	0.21	2.0
etm02/etm02_s1_plenum4/	40	0.22	0.03	0.27
etm02/etm02_s1_plenum5/	40	0.28	0.06	0.74
etm02/etm02_s1_plenum6/	40	0.26	0.06	0.47
etm02/etm02_s1_plenum7/	40	0.30	0.09	0.59
etm02/etm02_s1_plenum8/	40	0.24	0.04	0.51
etm02/etm02_s1_plenum9/	40	0.24	0.04	0.39
itm04/itm04_s2_plenum1/	40	0.28	0.06	0.66
itm04/itm04_s2_plenum2/	40	0.28	0.05	0.46
itm04/itm04_s2_plenum3/	40	0.27	0.05	0.60
itm04/itm04_s2_plenum4/	40	0.34	0.06	0.76
itm04/itm04_s2_plenum5/	40	0.35	0.04	0.42

The median value of the flatness of the differences of the measurements is between 0.22 nm RMS and 0.37 nm RMS both for the measurement of plane or spherical surface. The median RMS flatness value is the same both for the cases where there are fringes in the field of view or in flat-tint condition. It means that the repeatability is not limited by the vibrations. Indeed if we look at the measurements subtractions we clearly see that it is limited by a random error. This random error is due to the air flux which is not controlled as it is in the clean room. The subtractions of two successive measurements of a plane surface in flat-tint condition in the plenum is shown in figure 4.11. We see on that figure that the error is dominated by the effect of the air turbulences that shows as bumps and holes on the image.

We can look at the subtractions of two successive measurements done on a spherical surface so with circular fringes as shown in figure 4.12. The subtraction map in the figure has a flatness of 0.34 nm RMS. We see in that figure both the effect of the vibrations with the imprints of the circular fringes and the effect of the air turbulence with the random noise. Anyhow the effect of the air turbulences is dominating even though the effect of the vibration is visible. Finally the figure 4.13 shows the distribution of the flatness of all the measurements subtractions done in the plenum. It has an overall median value of 0.29 nm RMS.

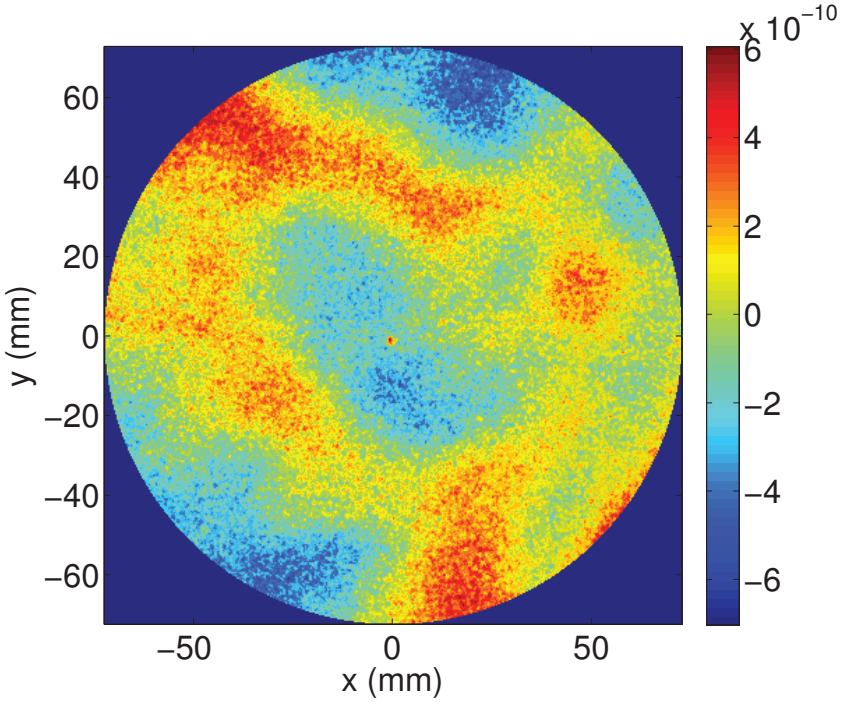

Figure 4.11: Subtraction of two successive measurements in the plenum in flat-tint condition. It has a flatness of 0.19 nm RMS.

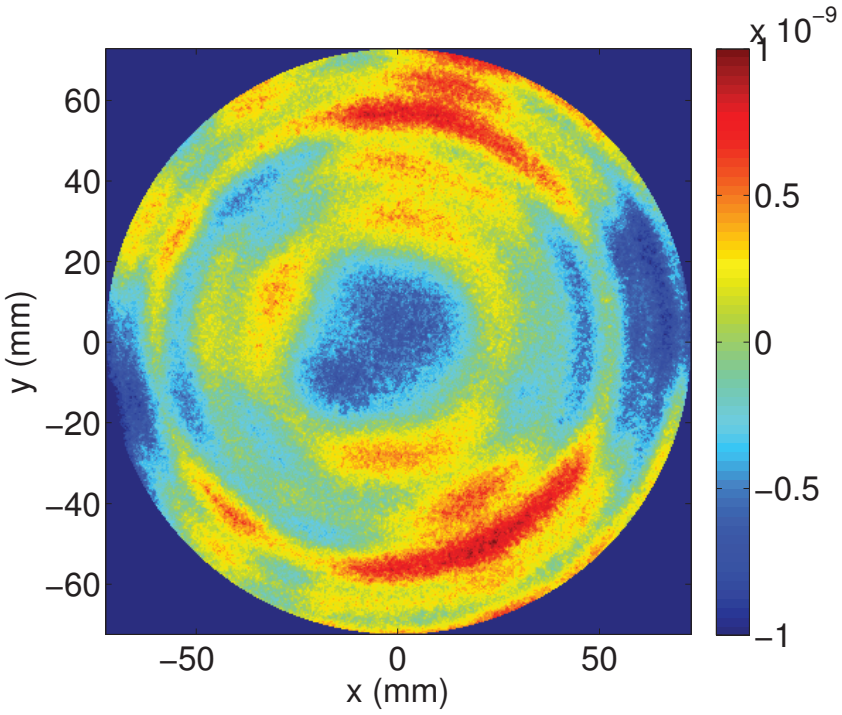

Figure 4.12: Subtraction of two successive measurements in the plenum with circular fringes in the interference pattern.

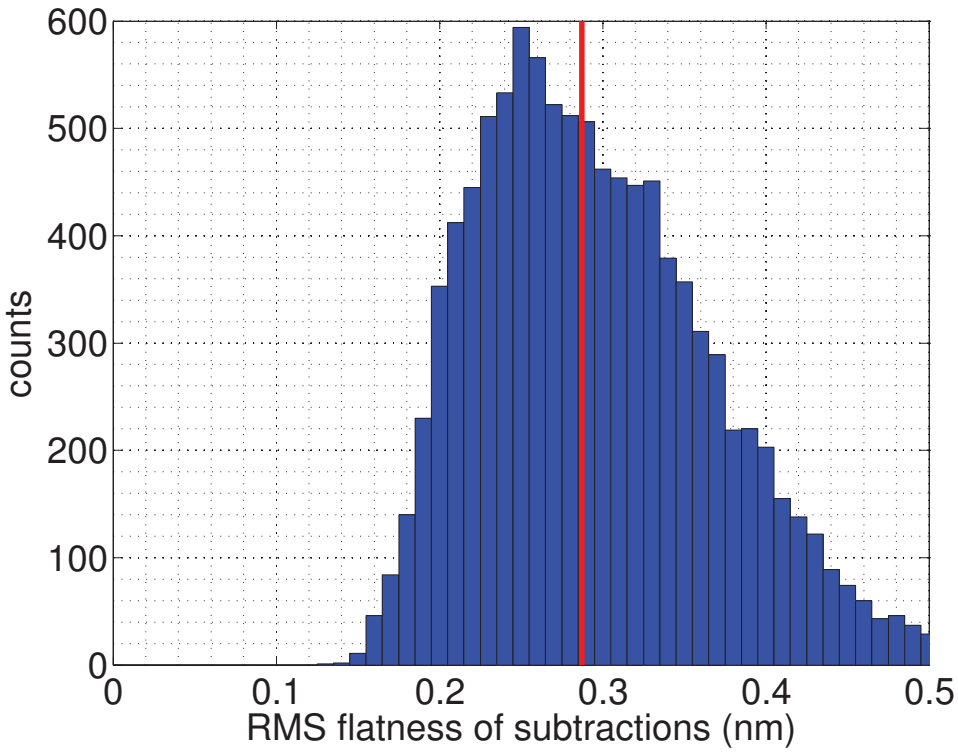

Figure 4.13: Histogram of the repeatability of the measurements in the plenum. The red line represents the median value.

In light of those tests, it is clear that a solution has to be found to cope with the problem of the air turbulence in the clean room. Many tests have been done to mitigate the effect of the air turbulences, they have been presented in [94]. A solution to avoid the air turbulences is to set up at local laminar air flux above the measurement set up. It allows to control the air flux circulating between the reference surface and the tested surface. The figure 4.14 shows the flatness of the differences of 255 measurements taken in a row and subtracted one to each other. The measurements have been done on a curved Virgo substrate in the plenum. It has to be underlined that the measurement has been taken with fringes in the field of view. The median value of the difference flatness data set is 0.13 nm RMS and the standard deviation of is 0.03 nm. The measurement repeatability is limited by the ripple noise due to the vibrations but at a much lower level than in the clean room. Indeed considering that there are fringes in the field of view, it has to be compared with the set of measurements done with fringes in the clean room that showed a median value of 0.21 nm RMS. Thus measuring the substrates in the plenum with a local laminar flux allows to lower the vibrations effect by a factor 1.7 without being limited by the air turbulences. Another well-know solution would be to have an enclosure that cover the reference and tested surface but this solution is not compatible with the stitching technique (paragraph 4.6).

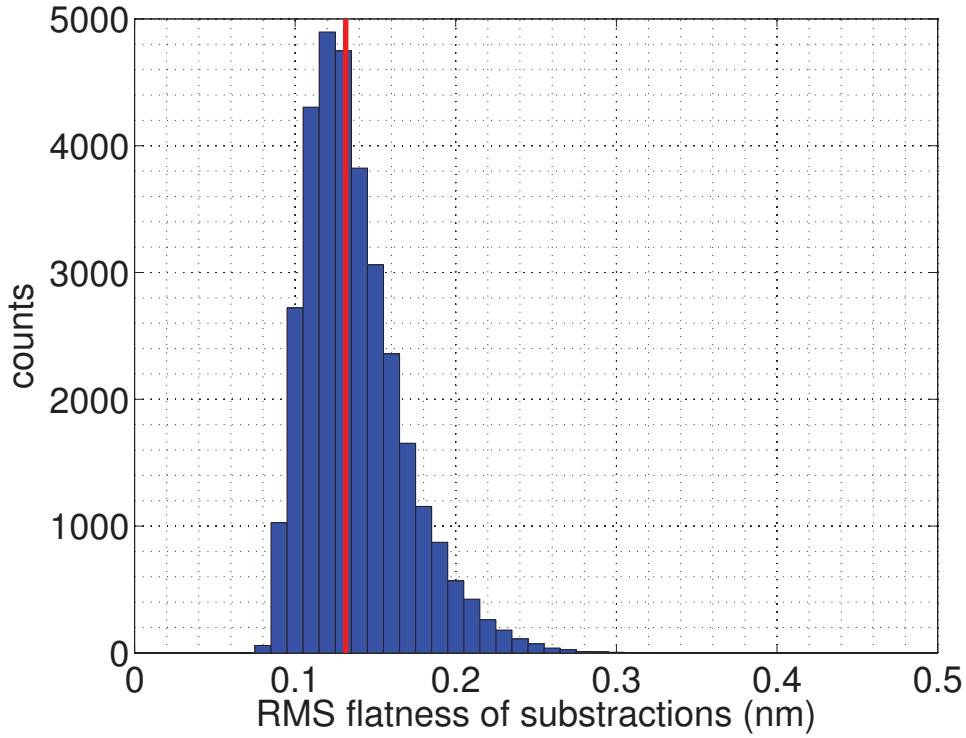

Figure 4.14: Histogram of the repeatability of the measurements in the plenum with a local laminar air flux. The red line represents the median value.

4.5.3 Conclusion

Considering all those tests on the repeatability of the measurement, we can draw two major conclusions.

The first one is that the repeatability of the measurement can be limited by the mechanical vibrations that occur during the measurement. The effect of the vibrations is called ripple noise and is related to the fringes pattern on the interferogram. The solution to mitigate the effect of this noise is to set the interference pattern in the flat-tint condition. Indeed the ripple noise is minimized when no fringes are present. The flat-tint condition is achievable by having the reference and test surfaces with the same curvature or a very close one. The second conclusion is that the effect of the air turbulences should be controlled to ensure a measurement with a good repeatability. The solution of a local laminar air flux allows to cope with the issue of the air turbulences as it has been shown with the test in the plenum.

Finally it appears that once the issue of air turbulences is under control, the effect of vibrations is lower in the plenum mainly because of its concrete floor. So it would be preferable to move the metrology bench in that room.

4.6 Measurement with the stitching technique.

The measurement of the substrate on a large diameter of 300 mm with the present apparatus implies the use of the stitching technique as explained in 4.3.2. This technique is much more complex than a single measurement as it requires at least 8 measurements to be combined together. The combination of several samples of data results in an increase of the errors. The measurement with the stitching technique takes long time as the substrate has to be moved in front of the interferometer and then the surface figure is reconstructed a posteriori. It becomes more difficult to average a high number of measurements. So the random errors due to the environment (vibrations and air turbulences) cannot be averaged as efficiently as for the measurement on the central area only. We will see in this section, a study of the reproducibility of the measurement using the stitching technique. We will also show an improvement made on the sample holder to improve this reproducibility.

4.6.1 Reproducibility of the stitching measurement.

The reproducibility of a measurement is evaluated by dismounting and remounting the optics under test in its mount between each measurement. The reproducibility takes into account the overall process of the measurement including the error that can arise from the mirror mount and not only the repeatability error due to the measurement in itself.

Two series of 5 measurements numbered from 1 to 5 and 6 to 10 have been performed on the plane surface (surface a) of the Virgo substrate called VEM02. The substrate has been dismounted and remounted on the metrology bench between each measurement except between the measurement 1 and 2. In the following we will then not take into account the measurement number 2. This substrate is a spare substrate for the Virgo end mirrors. The radius of curvature measured changes quite a lot from one series of measurement to the other as we can see in table 4.4. We see it is changing from -70.4 km to -73.1 km, which corresponds to a difference in the Z_2^0 polynomial amplitude of 3.0 nm on a 300 mm diameter.

In the same table, we also report the astigmatism measured expressed with its amplitude $amplitude = \sqrt{(\alpha_2^{-2})^2 + (\alpha_2^2)^2}$ and its orientation that is $angle = atan(\frac{\alpha_2^{-2}}{\alpha_2^2})$ where α_2^{-2} and α_2^2 are the astigmatism at 45°and 0°as defined by Zernike [92]. We see that the orientation of the astigmatism change also quite a lot between the different measurements with the extreme values being -11.8°and -73.8°. The amplitude of the astigmatism measured also varies from 1.7 nm to 3.3 nm. The fact that the measured astigmatism changes in amplitude and orientation means that it is not intrinsic to the mirror surface. This astigmatism is presumably induced by the mounting of the substrate in the sample holder. Indeed, depending on the way the substrate is mounted the substrate can rest in different positions that

Table 4.4: RoC and astigmatism of the vem02a surface on 300 mm.

Measurement number	**RoC (km)**	**Astigmatism amplitude (nm)**	**Astigmatism angle (°)**
1	-70.717	2.1	-14.5
2	-71.172	2.7	-16.2
3	-71.432	1.7	-17.0
4	-70.406	1.8	-11.8
5	-72.420	3.3	-65.8
6	-73.144	2.7	-70.9
7	-73.076	1.9	-73.8
8	-72.593	2.6	-67.2
9	-72.713	2.5	-65.7
10	-72.793	2.1	-58.2

can induce different kind of deformations. In the present sample holder, the substrate can rest on the front of the sample holder. And so it will induced a deformation which is not reproducible. This irreproducibility in the way the substrate rest on the sample holder is responsible for the change of amplitude and of orientation of the astigmatism measured.

The radius of curvature and astigmatism of these measurements on the central 150 mm are also reported in the table 4.5. It shows again an uncertainty on the measurement of the astigmatism and radius of curvature with a difference on the Z_2^0 polynomial amplitude of 0.69 nm. This value is in the range of the RoC measurement repeatability. Concerning the astigmatism, its amplitude goes from 0.57 nm to 1.19 nm and its orientation varies from -31.8°to -63.9°. We can explain this discrepancy in the measured astigmatism as before by the mounting of the substrate in the sample holder used for the stitching technique.

Again we can subtract the 9 measurements one to each other, it gives 36 subtractions. For each of these measurements we look at the power spectral densities and plot the mean power spectral densities as well as the upper and lower envelope of theses PSDs. The figure 4.15 shows these reproducibility curves along with the average of the measurements 2 to 5 computed on a diameter of 150 mm. We see that the power spectral densities of the measurements (blue curve) is lower than the mean reproducibility curves above a spatial frequency of about 250 $m^{-}1$. This is due to the averaging of several measurements that increases the signal to noise ratio resulting in the reduction of the content at high spatial frequencies.

Table 4.5: RoC and astigmatism of the VEM02a surface on 150 mm.

Measurement number	RoC (km)	Astigmatism amplitude (nm)	Astigmatism angle (°)
1	-98.492	0.57	-35.2
2	-100.930	0.77	-30.3
3	-99.007	0.63	-41.6
4	-98.768	0.76	-31.8
5	-103.450	1.19	-64.1
6	-102.770	0.84	-60.0
7	-103.160	0.58	-59.3
8	-103.010	0.92	-61.8
9	-102.620	0.69	-63.9
10	-102.520	0.82	-57.8

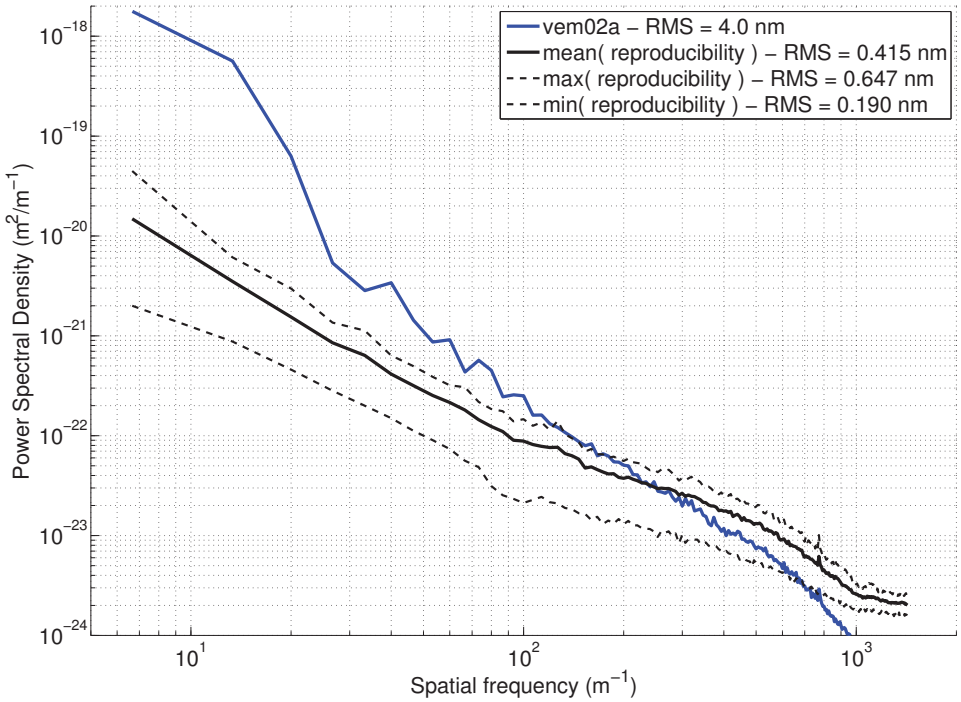

Figure 4.15: Power spectral densities of the VEM02a surface and the reproducibility measurement on 150 mm.

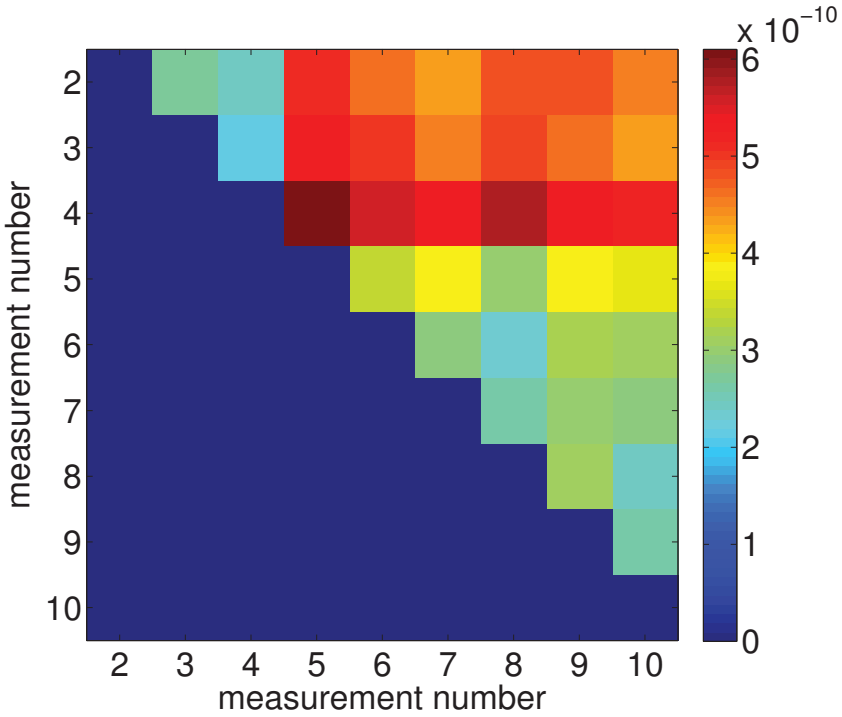

Figure 4.16: Flatness of the subtractions of the 9 measurements with stitching one to each other on 150 mm.

We can also look at the flatness of the different subtractions. The figure 4.16 shows the flatness of the 36 subtractions obtained from the 9 measurements done with stitching one to each other on a diameter of 150 mm. We see that the flatness of the subtractions goes from 0.21 nm RMS to 0.61 nm RMS with a median value of 0.41 nm RMS.

On 300 mm, the reproducibility of the measurement is higher as one can see in the figure 4.17. The flatness of the subtractions on 300 mm varies from 0.52 nm RMS to 2.6 nm RMS with a median value of 1.6 nm RMS. The reproducibility of the measurement is limited both by the stitching technique and the sample holder. The sample holder induces deformations on the tested surface that are not reproducible. Also the measurement at LMA with stitching in itself adds some errors because the surface is not in flat-tint condition even if it was set up in flat tint condition at the beginning of the measurement. The ripple noise due to the fringes is now visible on the subtraction of two measurement. For example, the figure 4.18 shows the subtractions of the measurement number 9 with the measurement number 8 on a diameter of 300 mm. The different sub-aperture measurements are represented by white dotted circle on the figure. These two measurements have about the same astigmatism and radius of curvature. So on the subtraction shown on figure 4.18, we only see the effect of the stitching. We can see the different zones of the stitching measurements with fringes having different orientations and spatial frequency in the different zones. A system that allows to

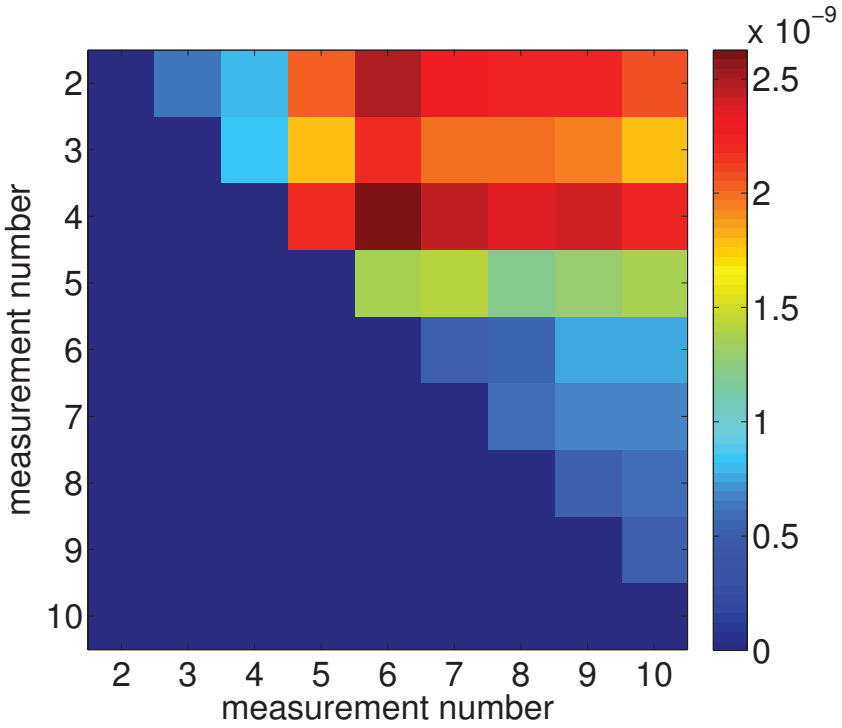

Figure 4.17: Flatness of the subtractions of the 9 measurements with stitching one to each other on 300 mm.

recover the flat-tint condition automatically would also improve the reproducibility of the measurement with the stitching technique.

We can remove from the surface the contribution of the radius of curvature and astigmatism as they are strongly related to the sample holder. If we do so, the median value of the subtractions flatness becomes 1.2 nm RMS on a diameter of 300 mm and 0.36 nm RMS on a diameter of 150 mm. This values can be seen as a limit on the reproducibility of the measurement with stitching as removing the curvature and astigmatism from the measurements exclude the role of the sample holder on the reproducibility of the measurement.

4.6.2 Improvement of the sample holder.

The reproducibility of the measurement is limited by the deformations induced by the sample holder that are random as the mirror is never resting the same way in its mount. It appears that in the sample holder the tested surface rests on the front ring of the sample holder (see figure 4.10). This yields to non reproducible deformations. To avoid theses deformations, we tried to push back the tested surface from the front ring of the sample holder so that they are not in contact any more.

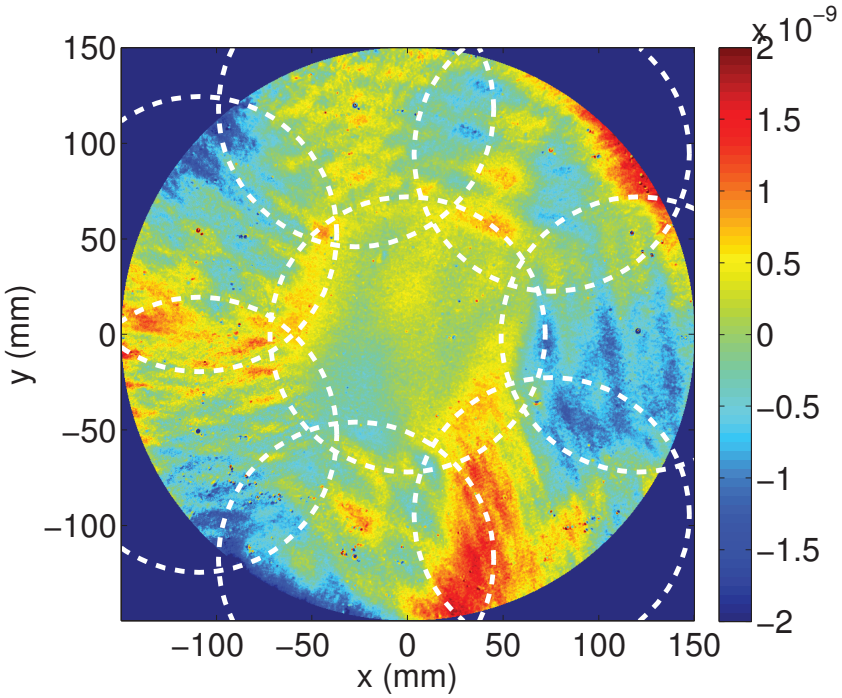

Figure 4.18: Subtractions of the measurement number 9 with the measurement number 8 on 300 mm. It has a flatness of 0.53 nm RMS. The dotted white circle represents the 8 sub-aperture measurements.

To do so we add a screw on the front ring that allows to push back the substrate from the front ring. There is a Teflon ring between the substrate surface and the screw so that it does not damage the surface. Doing so the deformations induced on the substrate surface are more reproducible from one measurement to another as we will see.

Seven measurements of the substrate vem02a after correction by the corrective coating technique (see chapter 5) with stitching have been performed with the substrate being dismounted and remounted on the metrology bench between each measurements. The table 4.6 reports the radius of curvature and astigmatism for the seven measurements. We see that the values of the RoC changes from -67.1 km to -69.8 km on 300 mm. It corresponds to a change of amplitude in the Zernike term Z_2^0 of 3.2 nm. It is in the same range as for the measurement before the addition of the screw on the sample holder. The measurements 1 and 7 show the smaller curvature. These measurements have been done more than a night after the mounting of the substrate in the sample holder and on the metrology bench. An explanation to their smaller RoC could be the relaxation of the substrate in the sample holder.

Concerning the astigmatism, we see that for the seven measurements the orientation of the astigmatism measured remains constant with an average value of 85.4 $\pm$ 2.25°. It is a

Table 4.6: RoC and astigmatism of the vem02a surface on 300 mm.

Measurement number	**RoC (km)**	**Astigmatism amplitude (nm)**	**Astigmatism angle (°)**
1	-67.110	3.70	83.1
2	-68.380	4.44	87.6
3	-68.258	5.42	84.6
4	-68.536	3.78	86.6
5	-68.306	5.84	85.9
6	-69.818	3.87	86.3
7	-67.532	4.03	83.4

major improvement as the astigmatism measured is now reproducible in its orientation. The astigmatism due to the deformation is now measured with a good reproducibility. About the amplitude of the astigmatism, one should not compare with the values of the previous paragraph 4.6.1 as a different surface has been measured for the two sets of measurement. We should only compare the maximum difference of the astigmatism amplitude between the two sets of measurement. It is 2.1 nm on 300 mm with the improved sample holder whereas it was 1.6 nm before. This difference in the amplitude of the astigmatism measured between different measurements is a bit higher than before the change in the sample holder.

Then we can look at the flatness of the subtractions of the 7 measurements on a diameter of 300 mm and on a diameter of 150 mm. The table 4.7 presents the RMS flatness of the 21 subtractions of the 7 measurements one to each other. The median value of the flatness of the difference is 1.3 nm RMS. It is a bit better than before as the median value of the flatness subtractions was 1.6 nm RMS on a diameter of 300 mm. This improvement is due mainly to the astigmatism which is now measured in a more reproducible way.

On a diameter of 150 mm, the median value of the subtractions flatness is 0.38 nm RMS. The flatness of the subtractions of the 7 measurements one to each other are reported in the table 4.8. Again we see a small improvement as the median value is now 0.38 nm RMS compared to 0.41 nm RMS. On 150 mm the improvement is less visible than on 300 mm.

To conclude, using a screw to push back the surface of the substrate from the front disk of the sample holder allows to measure the astigmatism in a more reproducible way. Indeed now the astigmatism present on the surface has always the same orientation. The median value of the subtractions flatness tends to approach the value obtained when removing the curvature and astigmatism in the measurements with the old sample holder. We have a median value on the subtractions flatness of 0.38 nm RMS against 0.36 nm RMS on a diameter 150 mm and of 1.3 nm RMS against 1.2 nm RMS on a diameter of 300 mm.

Table 4.7: Flatness of the subtractions of the 7 measurements with stitching one to each other on 300 mm with the improved sample holder (in nm RMS).

Measurement number	2	3	4	5	6	7
1	1.3	1.2	1.4	1.6	2.0	0.62
2	0	1.2	1.4	1.5	1.4	1.2
3	-	0	1.0	0.84	1.4	1.0
4	-	-	0	1.0	1.2	1.1
5	-	-	-	0	1.6	1.4
6	-	-	-	-	0	1.6

Table 4.8: Flatness of the subtractions of the 7 measurements with stitching one to each other on 150 mm with the improved sample holder (in nm RMS).

Measurement number	2	3	4	5	6	7
1	0.33	0.49	0.38	0.57	0.50	0.28
2	0	0.36	0.25	0.46	0.28	0.22
3	-	0	0.39	0.27	0.42	0.44
4	-	-	0	0.51	0.23	0.30
5	-	-	-	0	0.53	0.53
6	-	-	-	-	0	0.37

This astigmatism seems strongly related to the sample holder. The radius of curvature of a surface seems also to be dependent on the time it stays on the sample holder. The substrate is relaxing long after it has been mounted in the sample holder In the future a new sample holder has to be developed in order to have the smallest deformations possible on the substrate surface. The new sample holder should be designed in a way that minimise the constraints due to the weight of the substrate.

4.7 Measurement of very low flatness surfaces.

With the aLIGO substrates that have to be coated at LMA we have been able to compare the measurement of their surfaces done at LMA with the measurement done at Tinsley ([66]) the polishing company of the Advanced LIGO arm mirror substrates. It gives us an idea on the accuracy of the measurement and it brought to light some systematic errors of our actual phase-shifting interferometer. The aLIGO substrate have been polished using the technique of the ion beam polishing. They show a very low flatness down to 0.1 nm RMS on a diameter of 160 mm [95]. This kind of sub-nanometric surfaces are a very good tool to estimate the accuracy of the measurement as we can test our ability to measure such surfaces.

In this section we will show the result of the measurements done on the aLIGO substrate, we will distinguish two kinds of measurements. The measurement of a flat surface, i.e. the measurement of the back surface of the substrate and the measurement of a curved surface, i.e. the measurement of front surfaces which have a radius of curvature of about 1940 m for the input test masses and 2250 m for the end test masses.

4.7.1 Measurement of a flat surface.

In this paragraph, we show the measurement done on the back surface of the aLIGO ITM substrate number four (ITM04 surface 2) which is flat. We compare this measurement with the one done by the polishing company, Tinsley.

The measurement we show here has been done on the central part of the optics, that is to say a measurement without stitching. To mitigate the random noise due to the environmental errors we perform 40 measurements successively and we average those measurements to obtain the final measurement. There is a time lapse of about 1 minute between each measurement. Averaging the measurements allows to increase the signal to noise ratio of the measurement and so it minimises the random errors.

The figure 4.19 shows the surface figure of the measurement at LMA with the piston, tilt, RoC and astigmatism removed. It has a flatness of 0.65 nm RMS on a diameter of 145 mm. It can be compared with the measurement of the same part at Tinsley, see figure 4.20. The latter has a flatness of 0.60 nm RMS. The two measurements are very close one to each other. The similarity of these two independents measurement is very good, one can observe the same scratches in both figures. This proves the accuracy of the measurement of flat surface at LMA.

We can also decompose the surfaces in terms of Zernike polynomials [92]. This decomposition allows to asses the amplitude of different low-order aberrations such as the radius of curvature or the astigmatism. The measurement at LMA has a Z_2^0 amplitude of 2.20 nm

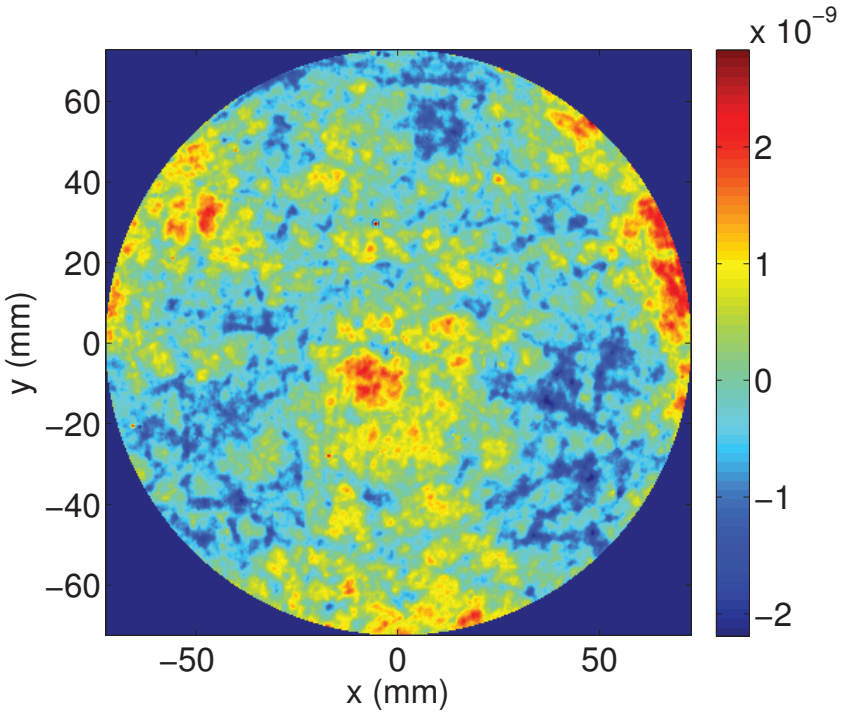

Figure 4.19: Surface figure of the flat surface (n°2) of ITM04 measured at LMA, piston, tilt, RoC and astigmatism removed. Flatness = 0.65 nm RMS.

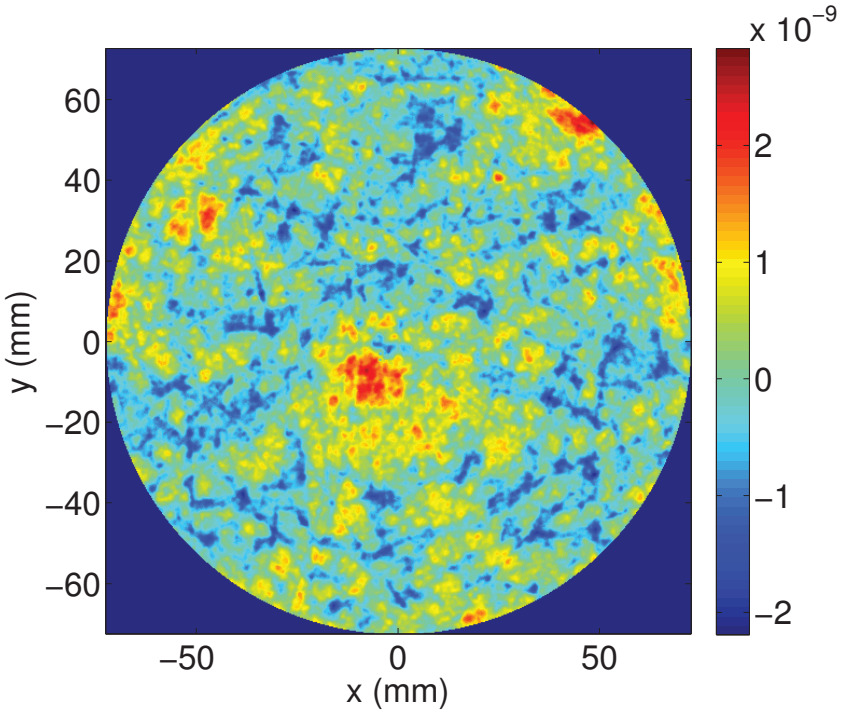

Figure 4.20: Surface figure of the plane surface (n°2) of ITM04 measured at Tinsley, piston, tilt, RoC and astigmatism removed. Flatness = 0.60 nm RMS.

whereas the measurement at Tinsley has an amplitude of 1.64 nm for the same polynomial. That is to say a difference of 0.56 nm. This difference is equivalent to a change of curvature of about 1.2 m on the radius of curvature of the Advanced Virgo end mirror (1683 m) and 0.9 m on the radius of curvature of the Advanced Virgo input mirror (1420 m). This difference is small as it is in the range of the repeatability error on the RoC measurement.

We look then at the astigmatism, the astigmatism measured at LMA is of 1.58 nm at 14.3°to be compared with the astigmatism on the Tinsley measurement which is 1.94 nm at -5.9°. The main difference is the astigmatism orientation. This could be due to the mounting of the substrate inside the sample holder that can induce deformation on the surface.

It is also interesting to compare the spectral contents of the two measurements. To do so we compute and plot the power spectral density of the two measurements, see 4.21. We see in that the two curves are very close except for the very low spatial frequencies (below 20 m^{-1}) where the contents is higher for the measurement at LMA and for the high spatial frequencies above 500 m^{-1}. In the high spatial frequencies, the measurement at LMA has a lower power. This is due to the averaging of the forty measurements that reduces the high frequency noise of the measurements.

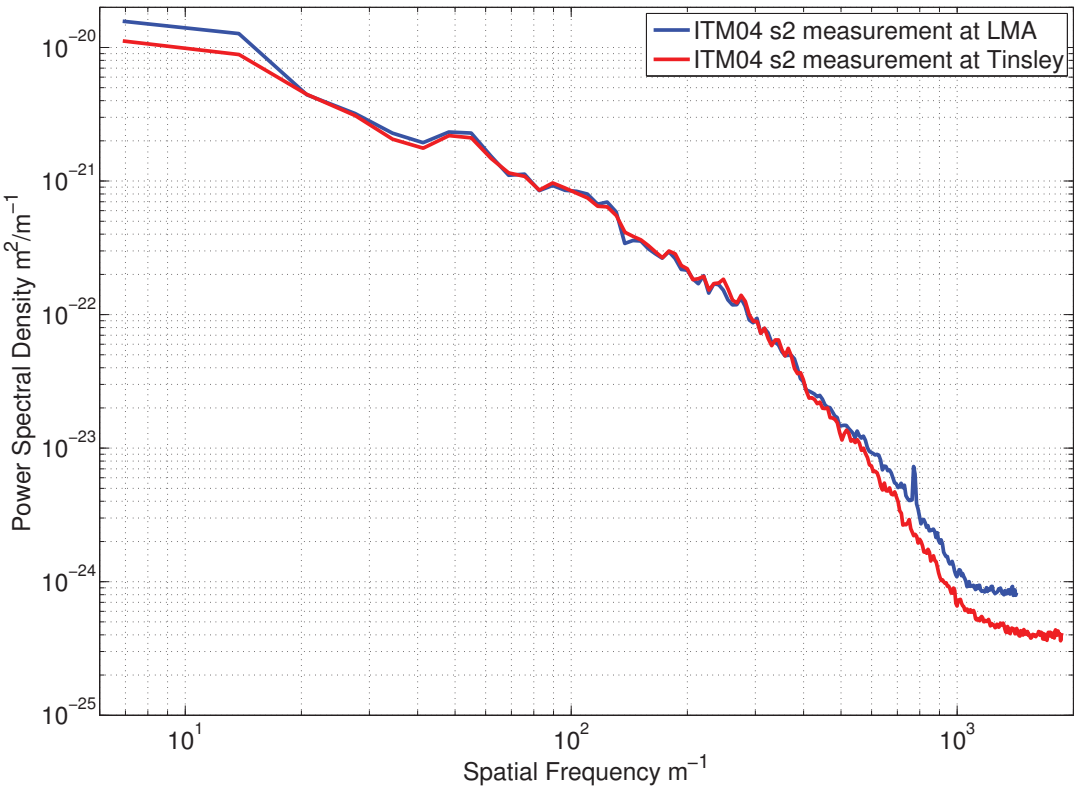

Figure 4.21: Power Spectral Density of the surface 2 of ITM04 measured at LMA (blue curve) and at Tinsley (red curve).

Anyhow, we can say that we are quite confident in the accuracy of the measurement at LMA if done in a flat-tint condition. Considering that during the measurement, the reference surface contribution is subtracted from the measurement to obtain only the contribution of the tested surface, we can say that we know our reference with a great accuracy. Indeed, if the reference surface phase-map is not well-know, it can contribute greatly to the error on the measurement especially on such sub-nanometric surface where the contribution of the reference surface in the wave-front measurement is being dominant given that it has a flatness of about 3 nm RMS.

4.7.2 Measurement of a concave surface.

About the measurement of concave surface with a very low flatness the measurement of aLIGO substrates bring to light the existence of some systematic errors. Indeed, we measured concave surfaces with a radius of curvature around 2 km with a flat reference surface. It is not the optimal condition as there are about 3 circular fringes in the field of view of the interferometer.

So we measure this surface with the same procedure as before, that is to say with an averaging of 40 measurements. We decompose the surface into Zernike polynomials, we found that the Z_2^0 polynomial has an amplitude of 676.8 nm which gives a RoC of 1941.6 m. This value has to be compared with the radius of curvature measured at Tinsley which is 1938.6 m according to the technical polishing report delivered by Tinsley [96]. The difference in the two radii of curvature measured is in the range of the repeatability error. Also the astigmatism measured by Tinsley is of 0.12 nm in amplitude while it is 1.08 nm in our measurement. There is a big discrepancy between the two measurements in the astigmatism measured. This discrepancy is significant of a problem in the measurement.

Moreover, if we look at the measurement at LMA (figure 4.22), it has a flatness of 1.23 nm RMS when the actual flatness as measured at Tinsley (figure 4.23) is only 0.15 nm RMS.

In the figure 4.22 we see a square structure which appears to be a measurement artefact as there is no such structure in the measurement done at Tinsley (see figure 4.23). This square structure is a systematic error and we do not know its origins. Given the important discrepancy between the Tinsley and LMA measurements, plotting the power spectral densities of the surfaces does not give valuable information.

It seems that this systematic error is linked to the interference pattern. Indeed, for the measurement shown in the figure 4.24 the fringes center has been shift to the bottom left of the field of view. We see that the structure follows the fringes. It means that this systematic error is related to the interference pattern. One hypothesis is that the wave-front coming

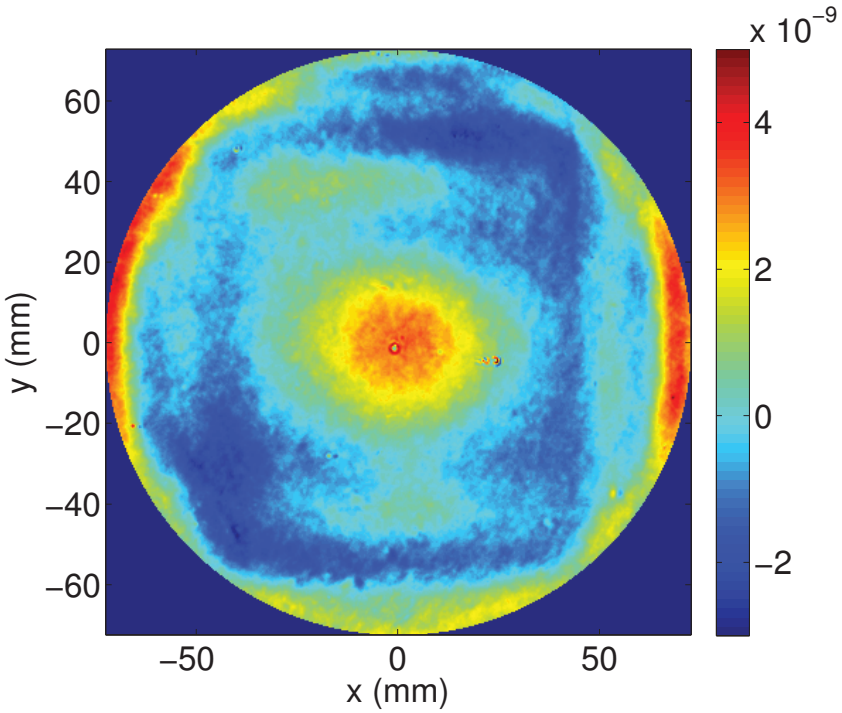

Figure 4.22: Surface figure of the curved surface (n°1) of ITM04 measured at LMA, piston, tilt, RoC removed. Flatness = 1.23 nm RMS.

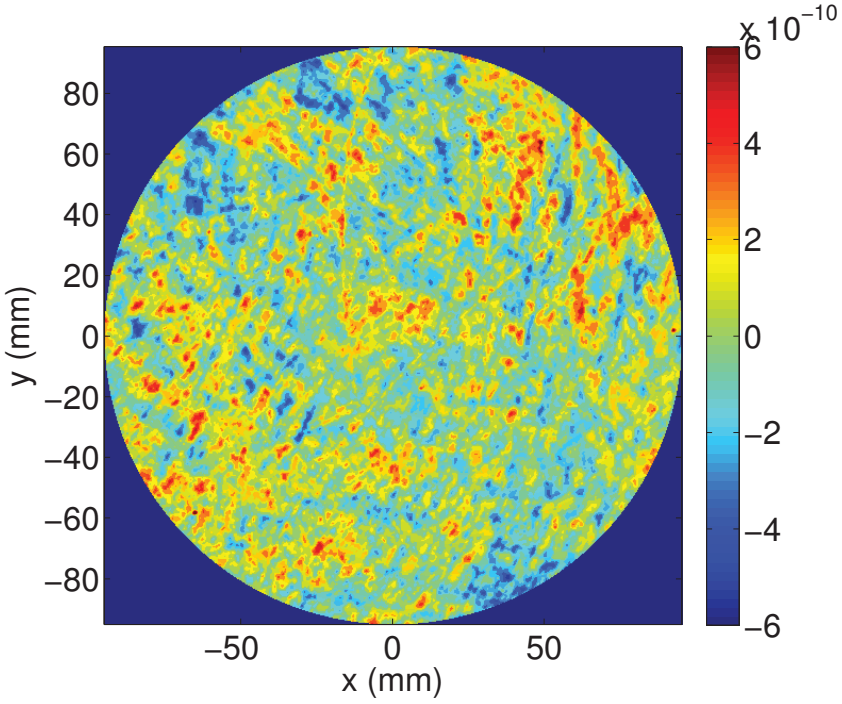

Figure 4.23: Surface figure of the curved surface (n°1) of ITM04 measured at Tinsley, piston, tilt, RoC removed. Flatness = 0.15 nm RMS.

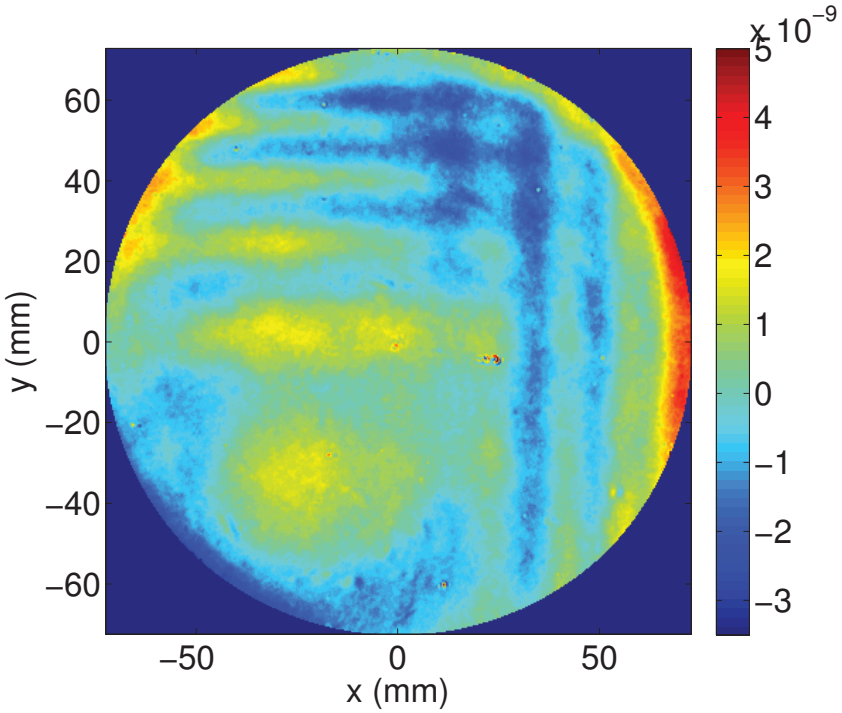

Figure 4.24: Surface figure of the curved surface (n°1) of ETM02 measured at LMA, piston, tilt, RoC removed with off-centered fringes. Flatness = 0.97 nm RMS.

from the interferometer is distorted by a square beam-splitter that is inside the phase-shift interferometer.

A way to avoid this measurement artefact would be to nulled the fringes. To do so, we need to have a reference with the same curvature as the test surface. Unfortunately at LMA, we do not have such curved reference and so we were not able to test the measurement of a concave surface in better conditions.

4.7.3 Conclusion

The measurement of the aLIGO substrate at LMA has been a very useful tool to assess the quality of the surface measurement. These substrates have a very low flatness: around 1 nm RMS on a diameter of 145 mm for the back surface of the ITMs and between 0.1 and 0.2 nm RMS on 145 mm for the front surface of the ITMs and ETMs.

We can distinguish two cases, the measurement of plane surface and the measurement of concave surface. In the first case we have been able to measure a surface with a good accuracy as what we measure is very close to the independent measurement done at Tinsley. This surface has a flatness of about 1.2 nm RMS on 145 mm and of about 0.6 nm RMS on 145 mm if one removed the residual radius of curvature and astigmatism.

On the other hand, the measurement of concave surface with a very low flatness was proven as impossible with the actual apparatus at LMA. Indeed we identified a systematic error which dominates the surface figure measurement. This systematic error is not well explained but we showed that it is linked to the interference fringes. A way to eliminate this error will be to use a curved reference with the same radius of curvature as the tested surface thus working in the optimal flat-tint condition.

4.8 Conclusion

In this chapter we have shown the basic principle of the phase-shifting interferometry to measure the surface figure of a substrate or a mirror. We have then presented the actual apparatus at LMA to measure the substrate flatness as well as the stitching technique that allows to perform measurement over a diameter larger than the pupil size of the interferometer.

Some of the noises sources as well as their effects on the surface figure measurement have been presented. Especially the environmental noises, i.e. vibrations and air turbulences. We have then shown a study on the repeatability of the measurement in two different conditions, the clean room and the plenum.

In this study we see that the repeatability measured over a 150 mm diameter in the clean room is limited by the vibrations in the case of a measurement with fringes in the field of view. We obtained in theses conditions a median value in the subtraction flatness of successive measurements of 0.21 nm RMS. This value is a limit on the precision of the measurement in theses conditions (in the clean room and with fringes in the interferogram). If we work in flat-tint condition (no fringes), the repeatability is then limited by the laminar air flux of the clean room. The median value on the repeatability becomes 0.13 nm RMS. In the plenum where the air is not controlled properly, the limiting factor in the repeatability is now the air turbulences whether there are fringes in the interferogram or not. The median value of the subtractions flatness is now 0.29 nm RMS. The air turbulences can be controlled efficiently by a local laminar air flux, it allows to obtained a repeatability of 0.13 nm RMS in the plenum and with fringes in the field of view. Working in flat-tint condition also allows to avoid the ripple noise limitation due to vibrations. To conclude, it would be preferable to move the metrology bench to the plenum because of the lower vibrations.

After that we study the reproducibility of the measurement of surface on a large diameter with stitching. We underline the role of the sample holder in the difficulty to obtained a reproducible measurement. Indeed the sample holder is a crucial element as depending on the way the substrate is hold it can induce deformations on the surface under test. These deformations are due to the weight of the substrate. A new sample holder for the 40 kg Advanced Virgo test mass should be developed. It should be designed so that the weight of the substrate is distributed largely. Doing so we should be able to reduce the induced deformation.

We also show in this chapter the measurement of some of the aLIGO substrates. These measurements could be compared with the measurement done at Tinsley (the polishing company). We can distinguished two cases, the measurement of plane surface and the measurement of curved surface. The measurement of plane surfaces is in very good agreement

with the measurement at Tinsley. It gives us confidence on the accuracy of the measurement done at LMA. On the contrary the measurement of curved surfaces bring to light the existence of a systematic error which is related to the fringes on the interference pattern. The measurement of curved surface with a very low flatness is for the moment impossible at LMA. A way to overcome this problem would be to use a reference surface with a radius of curvature identical to the test surface to be able to work in flat-tint condition.

Chapter 5

The Corrective Coating Technique

5.1 Introduction

As explained in chapter 3, the specification on the arm mirror flatness is very stringent and in order to meet this specification a technique has been developed at LMA to enhance the flatness of the substrate surface. The principle of the technique called corrective coating is to add materials on the surface where it is needed, that it is to say to fill the hole on the surface. To deposit the corrective layer of materials on the surface a robot has been built. It allows to move the substrate in front of a hole through which the silica is sputtered and deposited on the substrate. A very high precision metrology is needed to be able to correct the substrate surface with high precision.

In this chapter we will present the corrective coating technique. First we will explain its principle and then show simulations of the correction in the spatial domain. We will also present two algorithms for the computation of the correction. The first one is the algorithm developed in the early 2000 [75] and the second is a new one developed in the context of this thesis. It allows to correct surface defects smaller than the size of the elementary deposition imprint. Simulations have been performed to compare the behaviour of the two algorithms. We also run simulations to understand what is the correction diameter needed for the use in the arm cavity of the Advanced Virgo gravitational wave detector.

Then we also present the work done for the calibration of the robot and present the performances obtained in terms of positioning as well as the parameters of the deposition imprints through the hole.

Finally we present experimental results obtained on a 80 mm diameter substrate and on an initial Virgo substrate (350 mm diameter). This correction is considered as a full size test as the diameter of the substrate are the same in Virgo and Advanced Virgo. It will prove the capability of the corrective coating to lower the substrate flatness down to the level required

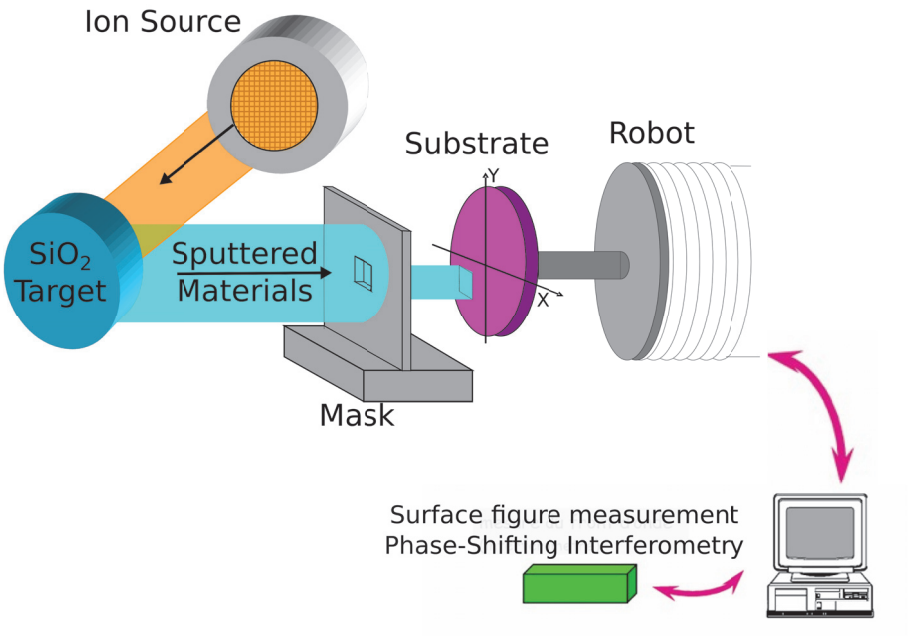

Figure 5.1: The corrective coating technique

for Advanced Virgo. Finally we simulate the round-trip losses in the Advanced Virgo arm cavity using the surface figure measured on the corrected substrate.

5.2 Principle of the correction

The principle of the correction is to add silica on the surface of the substrate in order to flatten it. In the coating machine the silica is sputtered towards the substrate mounted on a robot. The substrate is masked except for a hole which we will refer to as a mask. The robot allows to move the substrate in front of the mask so that the material is deposited on the wanted locations of the substrate. Figure 5.1 shows a scheme of the corrective coating principle. The deposition is done using the ion-beam sputtering (IBS) technique, more details can be found about this deposition technique in chapter 6.

First we need to measure the surface figure; this is done using the phase-shifting measurement technique (see chapter 4). Then we compute how much materials we need to add at each point on the surface in order to make it flat. Finally we deposit the materials on the substrate surface we want to correct. The deposited materials must be the same as the substrate, in our case it is silica. The silica is deposited through a mask. Typically the masks are square and have different dimensions. Up to now we used two square masks which are 10 mm and 21.5 mm large and one smaller circular mask with a diameter of 1.5 mm. Once the imprint of the deposition through a mask is known, we compute the motion of the

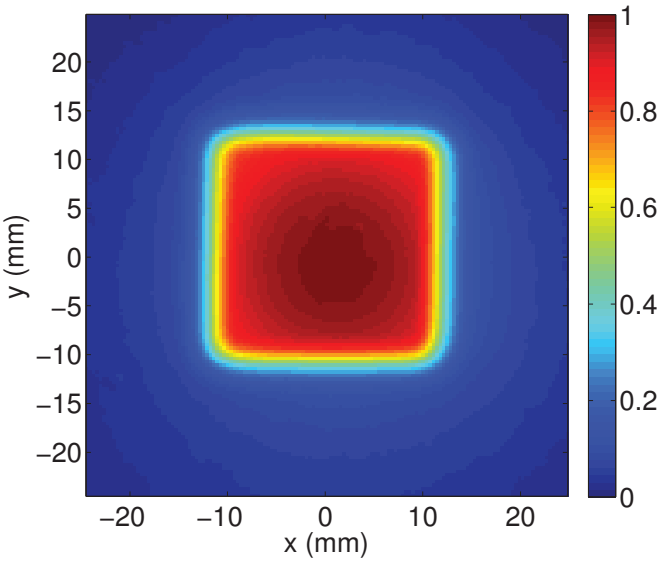

Figure 5.2: Normalized deposition imprints through a 21.5 mm square mask.

robot in space and in time that will yield to the ideal correction. Figure 5.2 shows as an example the imprints of the deposition through the 21.5 mm mask. We will present this in more details in the paragraph 5.5.

Before correction some silica is deposited on the surface outside of the active area through the small circular mask. This small silica imprints allow calibrating the positioning of the robot with respect to the substrate surface.

Typically the robot moves along a regular grid and stop for a given time at each point. The spacing of the grid has to be chosen carefully in order to avoid a too large or a too small overlapping in the coating deposition. Indeed it could results in creating a grating on the surface that would result in high diffraction losses in the arm cavities. This spacing depends strongly on the shape of the imprint deposited through the mask.

Once we have computed the correction with the appropriate robot step, we mount the substrate on the robot and start the deposition of silica on the surface with the robot moving accordingly to the computed correction.

5.3 The algorithms

An algorithm had been developed in the early 2000 for computing the correction and it has been enhanced in order to get a better correction. We will next refer to them as the classic algorithm and the optimized algorithm. The software that controls the robot, which was developed at LMA [75] includes a simulation tool that allows to compute the correction using the first algorithm. It also includes a tool to compute manual correction. These two

algorithms will be described in the next two paragraph and the results obtained in simulation will be presented in the paragraph 5.4. To compute the correction to obtain the best possible corrected surface we need to measure the surface deviation from the ideal surface. This is done using a phase-shifting interferometer as explained in chapter 4.

5.3.1 The classical algorithm

From the surface figure measurement (S) which is made over a given surface (typically 300 mm) with a given pixel size (typically 0.35 mm) one can compute the ideal correction. It is simply the ideal surface one want to obtain to which we subtract the measurement. Doing so we now have the map of the coating we want to deposit on the substrate. We will refer to it as the deposition objective map (O). Then we need to find how much we need to deposit at each point where the robot stops on the substrate to get the coating deposition the closest to the ideal one. We will refer to the positions points where the robot stop as the robot positions grid (G). The instructions (I) at each point of the robot grid is given in nanometres and is directly related to the deposition speed of the IBS machine as explained later in the paragraph 5.5. At the end, the instructions are given to the robot in seconds as the quantity of materials deposited is directly related to the deposition time.

The first algorithm developed is depicted in the figure 5.3. It gives as an instruction a first guess which is at each points of the grid (G) 5% of the deposition objective map. This 5% value is empirical, it has been found to be enough to give instructions close to the best possible one. It depends on the size of the imprint (21.5 mm) and the size of the grid (4.5 mm). We have:

$$I_1(G) = 0.05 \times O(G) \tag{5.1}$$

Then we simulate the deposition applying the instructions for each point of the grid. It gives as an output a deposition map (D), which is:

$$D = M \otimes I(G) \tag{5.2}$$

where M is the elementary deposition imprints through the mask. M is a two-dimensional normalized matrix as shown in figure 5.2.

Then we sum the deposition map (D) and the initial surface (S), it gives us a simulated corrected surface (C). Typically, we see that the initial surface has been over-corrected because of the fact that a deposition at a given location also deposits materials on the neighbour locations and the 5% factor is not exact. To take into account the effect of the neighbours we compute a neighbour coefficient (N) which is simply the deposition objective

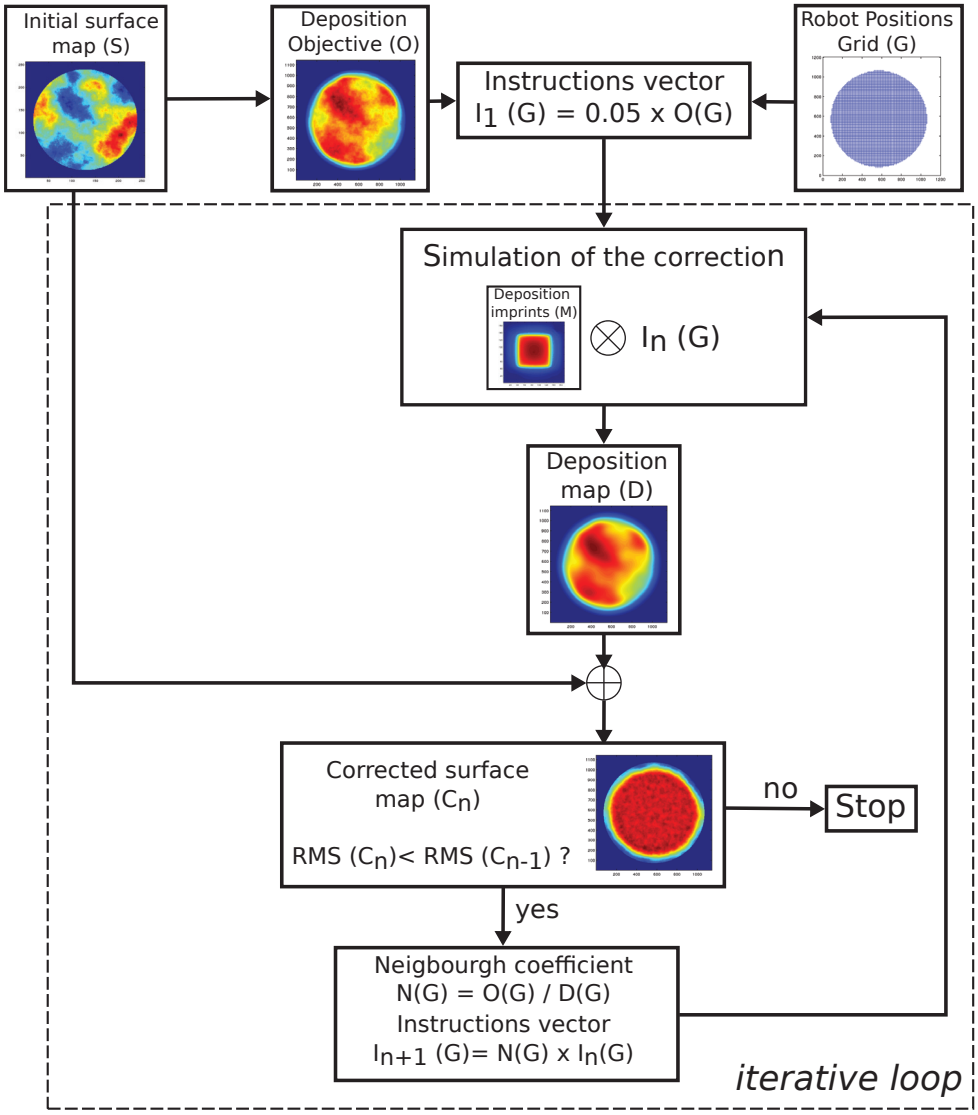

Figure 5.3: Schemes of the classical algorithm used to compute the robot instructions.

map over the deposition map at each point of the robot position grid:

$$N(G) = O(G)/D(G) \tag{5.3}$$

Then we compute a new instructions (I_{n+1}) from the previous instructions (I_n) by multiplying it by the neighbour coefficient:

$$I_{n+1}(G) = N(G) \times I_n(G) \tag{5.4}$$

With this new instructions we compute a new deposition map (D_{n+1}) that will give a new corrected surface (C_{n+1}). If the new corrected surface has a lower flatness than the older one,

we compute a new neighbour coefficient and so on. If the new corrected surface is not flatter than the previous one, we stop and choose the previous instructions. We use this technique of the neighbour coefficient iteratively to get the final corrected surface map. Unfortunately the technique does not allow to reach the perfect correction and the algorithm diverges after a few iterations.

The algorithm diverges because it does not take into account the quantity of materials deposited between the robot positions grid points. After a few iterations it starts to deposit too much materials on these uncontrolled areas.

5.3.2 The optimized algorithm

From the results of the classic algorithm we know that it is important to control how much material is deposited between the locations where the robot stops.

One can think of the problem of the correction as a system of n equations with n being the number of points of the robot positioning grid where the deposits are done. Where the unknowns are the instructions given to the robot. I is a vector $I(G)$ where to each element corresponds a position on the surface given by the robot positioning grid (G). To this vector corresponds a vector with the height of the objective deposition map at the corresponding positions of the grid G, it is $O(G)$.

The system can be solved if one knows the matrix that links the two vectors. This matrix (R) is simply the matrix that links the quantity of deposited materials on each positions of the grid G when a normalized quantity of materials is deposited on a given location of the grid G. The matrix R is computed knowing the deposition imprint through the mask. At the end the system can be described as:

$$O(G) = R \times I(G) \tag{5.5}$$

where R is a n by n matrix, I(G) and O(G) are n-dimensional vectors and n is the number of points in the robot grid G.
The system can be solved by inverting the matrix R.

$$I(G) = R^{-1} \times O(G) \tag{5.6}$$

The solution of the equation gives some of the instructions to be negative. It does not make sense on a physical point of view as we are not able to remove materials from the surface. Also simplifying the system to the points of the robot positioning grid does not take into account what happens between these points. Even if the system is solved properly it does not give a good correction because the deposition outside of the robot grid remains uncontrolled.

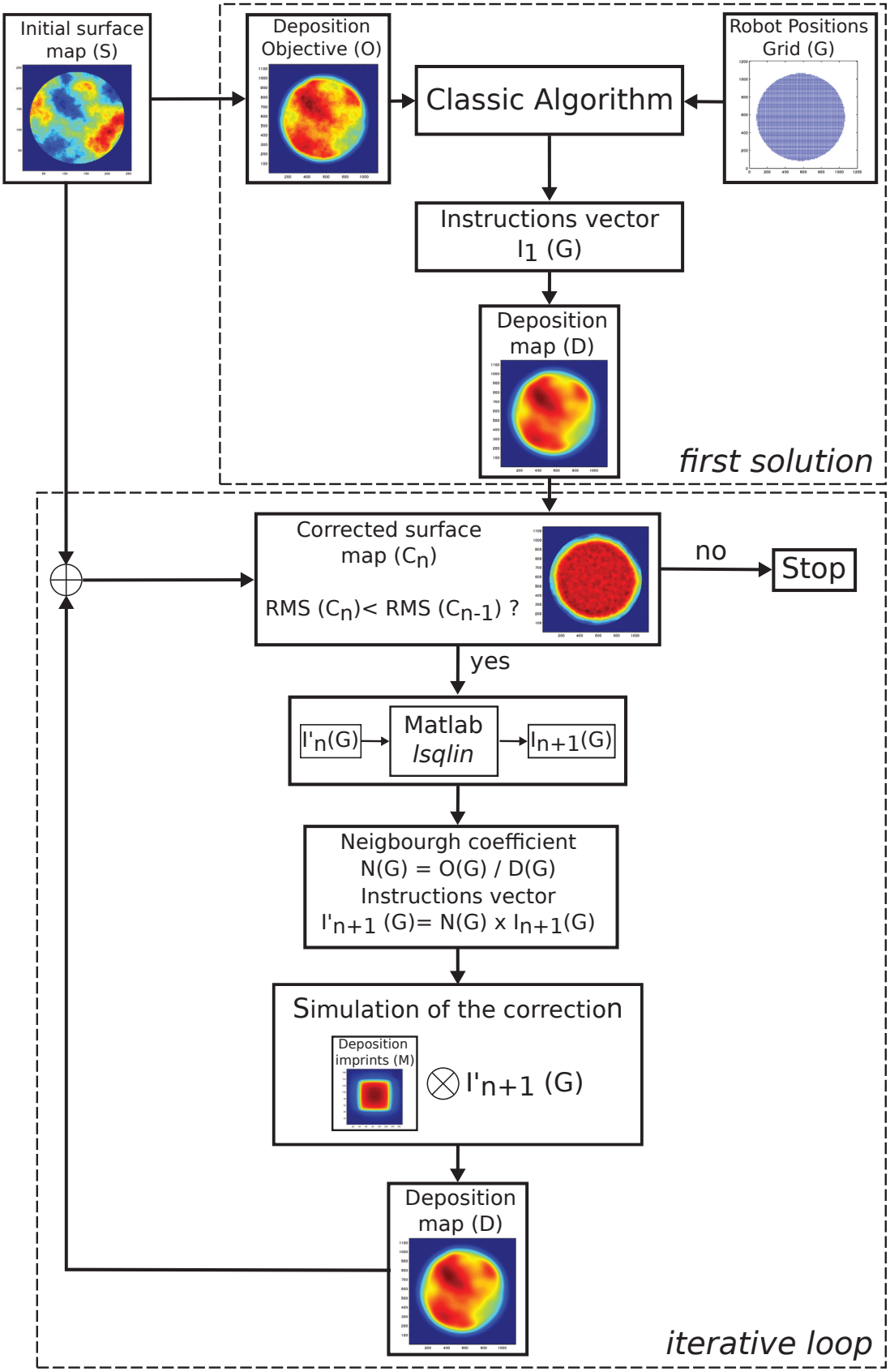

Figure 5.4: Schemes of the optimized algorithm used to compute the robot instructions.

Thus we need to control better these regions and we need to solve the system for a greater number of points on the surface map. We define then a second grid with a spacing four times smaller than the robot grid, we refer to this second grid as the control grid (G'). It means that we will control the deposition on about sixteen times more position points placed along the new grid G'. The relation matrix R between the normalized deposition height on the position points of the robot grid G and the actual deposition height on the position point of the control grid G' is now a n by m matrix, with m the number of element in the control grid (G'). The system becomes:

$$I(G) = R^{-1} \times O(G') \tag{5.7}$$

where R^{-1} is the pseudo-inverse of R, I(G) a n-dimensional vector and O(G') a m-dimensional vector. Typically n is around 3000 for a grid with a spacing of 4.5 mm in both x and y direction taking only the points inside a circle with a diameter of 290 mm and m is about 48000 for a spacing of 1.125 mm.

To resolve this system of m equations with n unknowns we have to compute the pseudo-inverse of the matrix R. The computing software MATLAB [97] allows to solve a system of linear equations with rectangular matrix using the function *lsqlin* provided in the optimization toolbox. The function allows to give constraints such as minimum and maximum values and gives as an output an approximate solution. The function offers as an option the possibility of starting from a guess. In the optimized algorithm the guess solution given to the Matlab function is the solution found with the classic algorithm.

From this guess the Matlab function provides a solution that gives a better correction than the previous algorithm. However it can be enhanced by using the technique of the neighbour coefficient previously described. Let's call the solution given by the Matlab function, I_n. We adjust the instructions with the neighbour coefficient:

$$I'_n = N \times I_n = \frac{O(G)}{D(G)} \times I_n \tag{5.8}$$

We compute the new correction, the corrected surface and we answer the question; is the corrected surface flatter than the previous one. If yes the solution is given as a guess to the Matlab function to give a new solution to the system which is then adjusted by the neighbour coefficient method. Doing this iteratively allows obtaining a coating map close from the ideal one. The algorithm converges to a minimal value typically after less than twenty iterations.

Finally this algorithm allows to control the correction more efficiently by controlling the deposition between the position points of the robot grid. The performance of the two

algorithms are compared in paragraph 5.4.2.

5.4 Simulating the corrective coating in the spatial domain.

A first set of simulations on the corrective coating has already been done in the chapter 3. It was done in the spatial frequency domain assuming that the corrective coating cut down the power spectral density below a given cut-off frequency. Here the simulations are done in the spatial domain. That is to say simulating the deposition on the surface map using the elementary imprint deposited through the mask during the calibration of the performance of the robot.

Typically the masks are square, we used two masks, one is 21.5 mm large and the other one is 10 mm large. The size of the mask will determine the level of correction one can reach in the corrective process. Indeed the smaller the mask, the smaller the defects one can correct. But as a drawback the correction is longer and is also more difficult to compute because the number of points of the robot grid G becomes very large as we reduce the robot step. The deposition through the two square masks have been done on small substrates (80 mm or 100 mm diameter). The substrates are measured before and after deposition in order to extract the imprints of the deposition only. In the simulation, the real imprints have been used to compute the correction.

5.4.1 Diameter of correction

One of the issue to deal with is the diameter of the correction. Indeed when correcting a mirror there is a risk of creating a step between the corrected region and the non corrected region. But still there is no need to correct the surface of a substrate on a too large diameter as there is only a few light impinging on the external radii of the mirror in the Advanced Virgo arm cavity. The diameter on which we need to correct the substrate depends on the size of the beam on the mirror. To avoid having a sharp step on the mirror we will make the correction such as to create a transition region between the corrected and not corrected regions of about 30 mm.

We made simulations of the corrective coating for different diameter of correction using the classic algorithm. We made simulations with the diameter of the correction going from 140 mm to 310 mm. For example a diameter of correction of 200 mm means that we correct up to a radius of 100 mm and then add a 30 mm transition region. The simulations have been done on a simulated surface which has a flatness of 2 nm RMS in the central region

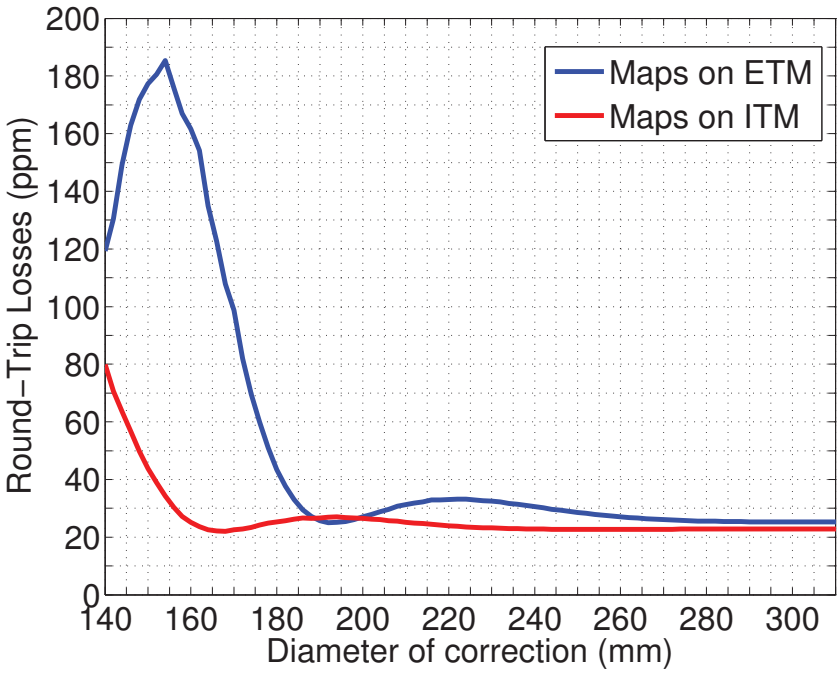

Figure 5.5: Round-Trip Losses in Advanced Virgo cavity as a function of the correction diameter for the maps on ITM (red) and ETM (blue).

(on a 150 mm diameter). In this simulation, the height of the step is between 15 and 20 nm over the 30 mm transition region. The corrected surface maps have been put in a simulation of an Advanced Virgo cavity under SIESTA first on the input mirror and then on the end mirror, the opposite mirror remaining without defects.

Then the round-trip losses have been computed, they are plotted as a function of the correction diameter in the figure 5.5. We can see that the RTL reach an asymptotic value when the diameter of the correction are respectively 220 mm and about 260 mm for the maps on the input mirror and the end mirror. Correcting the substrate on a larger diameter has no effect on the losses in the arm cavity.

So from these simulations we can say that we need to correct the substrate surface up to a diameter of 260 mm. Therefore we need to measure the surface figure on a diameter of at least 300 mm so that we can create a smooth slope on the external radii of the correction. Having a measurement over a diameter of 300 mm will also allow to add the reference positioning peak sufficiently far from the center of the mirror. At a radius of 145 mm, the positioning peaks do not induce more round-trip losses in the Advanced Virgo arm cavity.

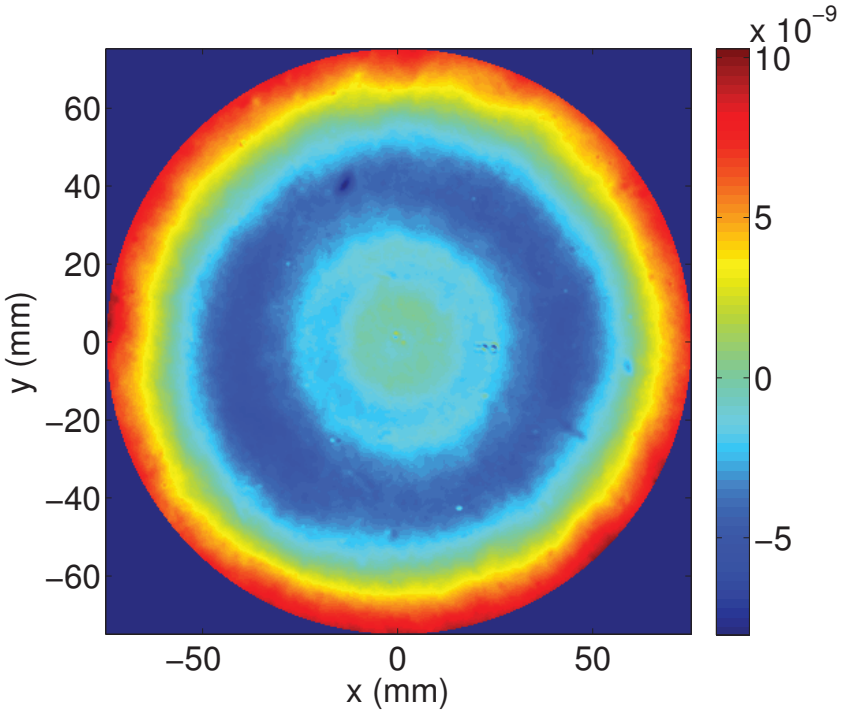

Figure 5.6: VEM02a before correction - flatness = 4.0 nm RMS.

5.4.2 Comparison of the two algorithms

The two algorithms have been tested in simulation using as input data the surface of figure of an initial Virgo substrate (called VEM02). The input data comes from a measurement before the deposition of the positioning peaks. This substrate has a radius of curvature (RoC) of about -70 km and this curvature has been removed from the measurement since it will not be corrected. It has a flatness of 4.0 nm RMS on a diameter of 150 mm and of 6.6 nm RMS on a diameter of 260 mm before correction. Figure 5.6 shows the VEM02a surface before correction on the central 150 mm.

We simulate the correction using the two algorithms presented. The table 5.1 presents the flatness of the surface before and after correction for the two algorithms on a diameter of 150 mm and 260 mm. We see that with the optimized algorithm, the flatness of the substrate surface after correction is lower than the one with the classic algorithm both on a diameter of 260 mm and 150 mm.

The power spectral densities of the surfaces before and after correction are shown on the figure 5.7. These PSDs are computed on the central 150 mm diameter. The blue curve shows the PSD of the surface before correction whereas the green and red curves show the PSD for the simulated correction with the two algorithms. We see that the corrective coating flatten the PSD below a certain spatial frequency which is related to the size of the mask for the

Table 5.1: VEM02a flatness before and after simulated correction.

	VEM02a before correction	**Simulated correction classical algorithm**	**Simulated correction optimized algorithm**
Flatness on 260 mm	6.6 nm RMS	0.54 nm RMS	0.31 nm RMS
Flatness on 150 mm	4.0 nm RMS	0.37 nm RMS	0.25 nm RMS

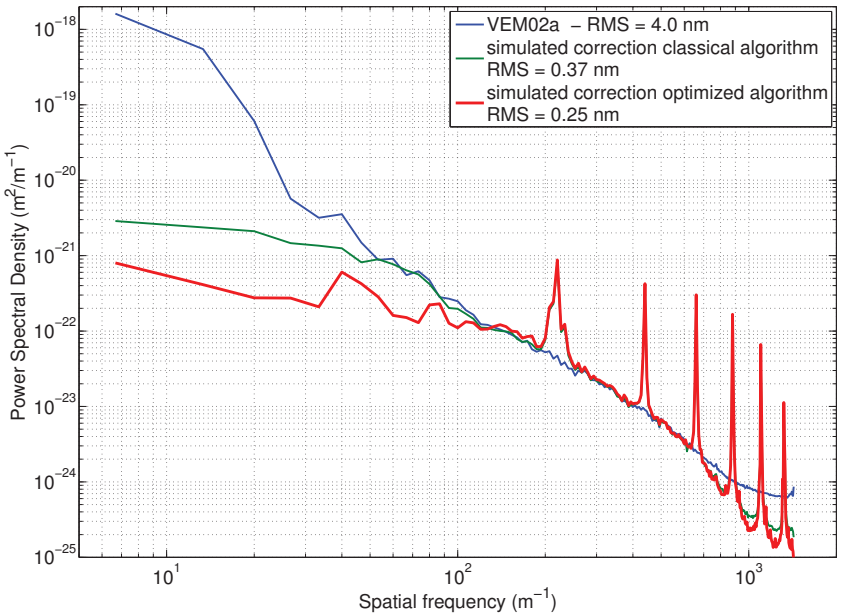

Figure 5.7: Power spectral density of the VEM02a surface and the simulated correction on 150 mm.

classic algorithm. This spatial frequency is of about 50 m^{-1}. The red curve which is the PSD of the simulated correction with the optimized algorithm is lower than the initial PSD for a wide range of spatial frequency as the cut-off frequency is a bit higher than 100 m^{-1}. This is due to the fact that we control the deposition between the robot positions grid and so we correct the surface in a more subtle way.

We also see peaks in the PSDs of the simulated correction at a frequency of 220 m^{-1} and at its harmonics. These peaks are simulation artefacts due to the fact that when simulated the correction the matrix that represents the imprints of the deposit is finite and so there is a border effect between the line of pixels where there is a deposition and the adjacent line of pixels where nothing is deposited. It adds on the final correction an artificial grid that shows as peaks in the power spectral density. This peaks should not be present in the PSD of the real correction.

Figure 5.8 shows the surface of the simulated correction for both algorithms on a diameter of 260 mm. The top figure is the substrate surface corrected with the classic algorithm whereas the bottom one is with the optimized algorithm. The color scale is between -2.5 nm and 2.5 nm for both figures. We can see that the peak to valley value is higher with the classic algorithm. We can say that the optimized algorithm gives a better correction. It has a higher frequency cut and so a more subtle correction with the same mask. It results in a considerable gain of time compared to a correction with a smaller mask.

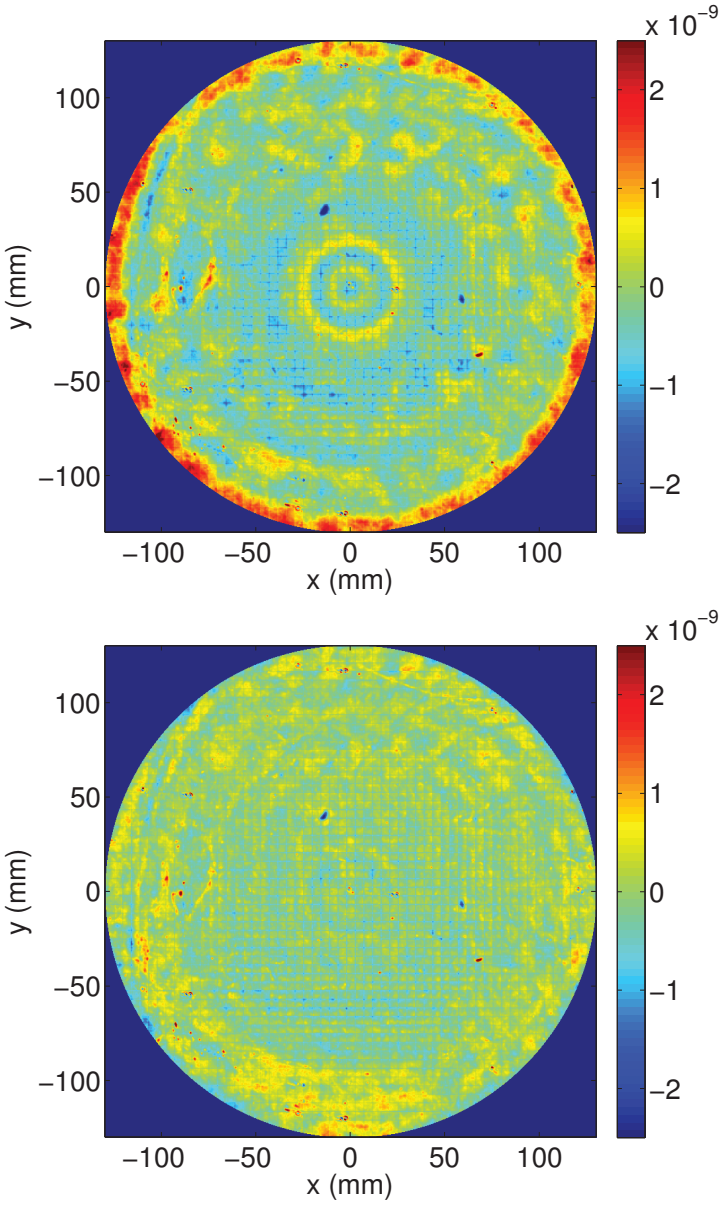

Figure 5.8: Surfaces of the simulated correction with the classic (top) and optimized (bottom) algorithms.

5.4.3 Avoid a grid effect

We can see from the figure 5.7 in the previous paragraph that the peak at 220 m^{-1} is quite large and it is not excluded that the regular spacing in the robot positioning grid creates a grating with a period equal to the robot step.

Randomization of the grid To avoid this grating effect, we add a random term on the positioning grid of the robot both in the x and y direction. We compute a new correction with the random term going from plus or minus 0.35 mm to 1.05 mm. It corresponds to n times the size of the pixel of the surface figure, with n an integer. We obtain a corrected surface with the flatness reported in the table 5.2 on 260 mm and 150 mm. We see that

Table 5.2: VEM02a flatness before and after simulated correction.

	No randomization	**random +- 0.35mm**	**random +- 0.70mm**	**random +- 1.05mm**
Flatness on 260 mm	0.31 nm RMS	0.31 nm RMS	0.31 nm RMS	0.32 nm RMS
Flatness on 150 mm	0.25 nm RMS	0.25 nm RMS	0.25 nm RMS	0.27 nm RMS

the effect on the flatness is very small when adding this randomization term. There are no significant difference in the flatness of the surface after correction.

We can look at the power spectral density of the correction with the randomization term. Figure 5.9 shows the PSD of the correction on 150 mm. We see that the peaks are attenuated with the amplitude of the randomization term especially the harmonics at the spatial frequencies of $n \times 220$ m^{-1}. The drawback is that it creates a bump around the spatial frequency of 150 m^{-1} which amplitude increases with the randomization term amplitude.

From these simulations we can say that it is not efficient to add a randomization term on the regular grid of the robot as it adds a bump in the power spectral density of the corrected surface. Anyhow we cannot exclude that the bump added is not due to the border effect due to the imprint matrix. To be sure that the peaks are an artefact of simulation we extrapolate the imprint matrix to extend the data on a larger region than the 50 mm square used previously. The mask is extrapolated and now falls down smoothly to zero instead of being cut at 4 % of the maximum height.

Therefore we compute the correction with the same instructions as before but with the extrapolated mask. The power spectral densities of the surface after correction are plotted in the figure 5.10, we see that the peaks have disappeared. We also observe that a low

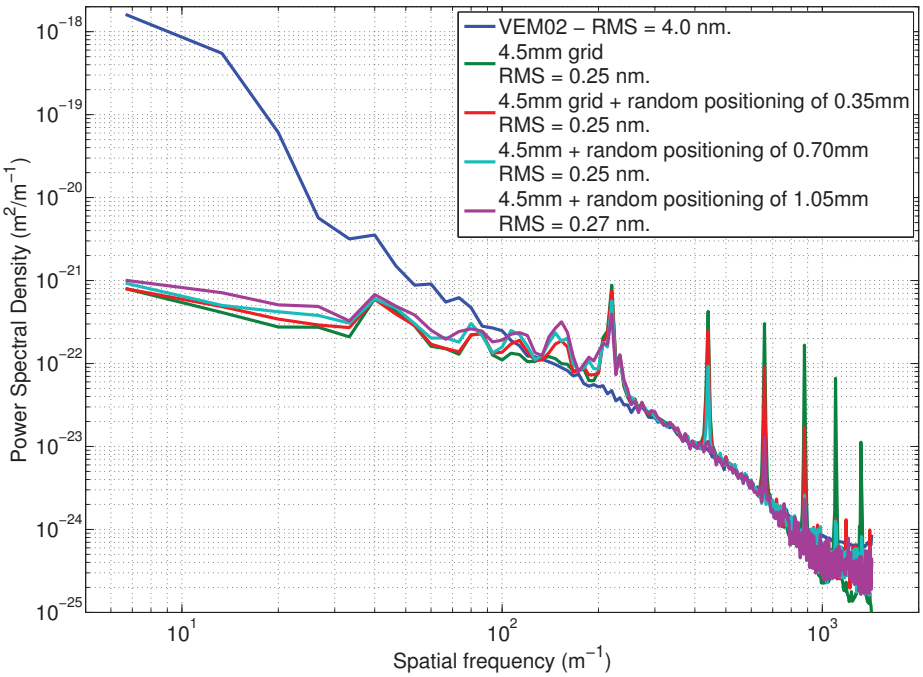

Figure 5.9: Power spectral density of the VEM02a surface and the simulated correction with and without randomization term on 150 mm.

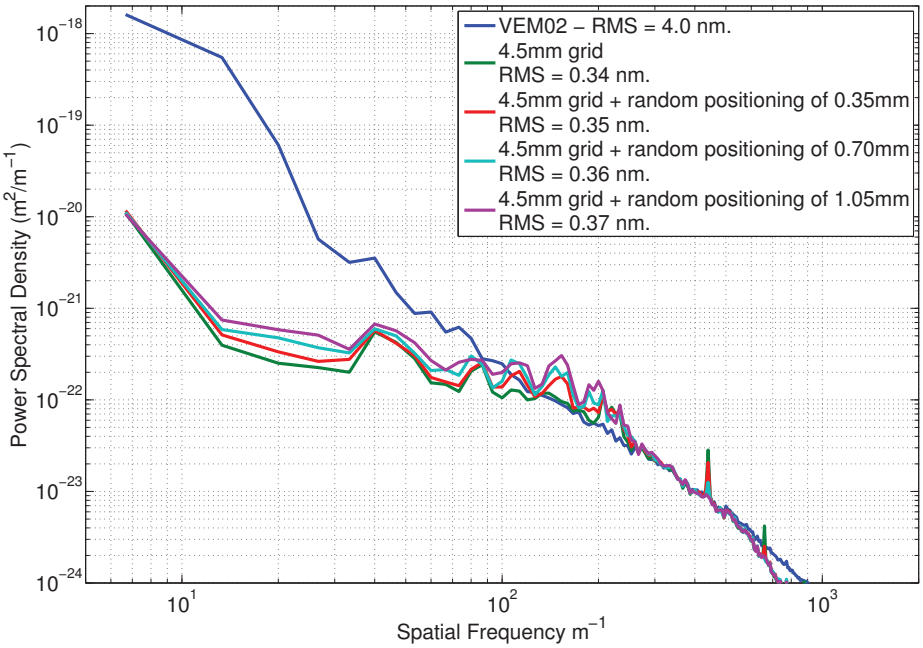

Figure 5.10: Power spectral density of the VEM02a surface and the simulated correction with and without randomization term on 150 mm and with the extrapolated mask.

frequency contribution has been added, it is due to an additional curvature. In any of the cases the Z_2^0 Zernike term added has an amplitude of about -0.45 nm on a diameter of 150 mm. If we project this value on the radius of curvature of the arm mirrors, it would change the radius of curvature by respectively 0.7 m and 0.8 m for the input and end mirrors.

Finally the bumps in the PSDs are added by the randomization term and so it is preferable to have a regular grid for the displacement of the robot.

Random grid An other way to break the grating effect is to create a random positions grid for the robot in order to avoid any grid effect. A random grid can be computed in order to have more points where we need to add more silica on the substrate surface. To do so, we draw a positions on the surface and look at how much materials is needed at this positions. Then we choose to keep this positions according to a probability law that increase with the quantity of material needed on the positions. We also reject the positions if there is already a point in the close vicinity. We choose to keep the positions so that the minimal distance between two adjacent points cannot be smaller than 2 mm. The reason to avoid having points which are too close is that it will results in instructions which are too small.

We compute the correction with the random grid, we obtain a corrected surface map with a flatness of 0.35 nm RMS on 150 mm and 0.75 nm RMS on 260 mm with the non extrapolated mask. It is not as good as what we can obtain with a regular grid. We can see in the power spectral density, see figure 5.11, an excess of power in the range 60 m^{-1} - 300 m^{-1} compared to the initial PSD. We see that the cut-off frequency of the correction in that case is about 50 m^{-1} whereas it was higher than 100 m^{-1} with a regular grid. We also see that the peaks we see in the PSD of the correction with a regular grid have disappeared both for the simulation with the extrapolated mask or not. The simulated correction with the extrapolated mask adds as before a small curvature which Z_2^0 term amplitude is -0.50 nm.

Such correction is not good as it adds high spatial frequencies defects to the surface that would directly convert into losses in a Fabry-Perot cavity as they have a spatial frequency higher than 50 m^{-1} as explained in the paragraph 3.5 of chapter 3. Finally having a correction with a random grid is not a good solution for the corrective coating technique.

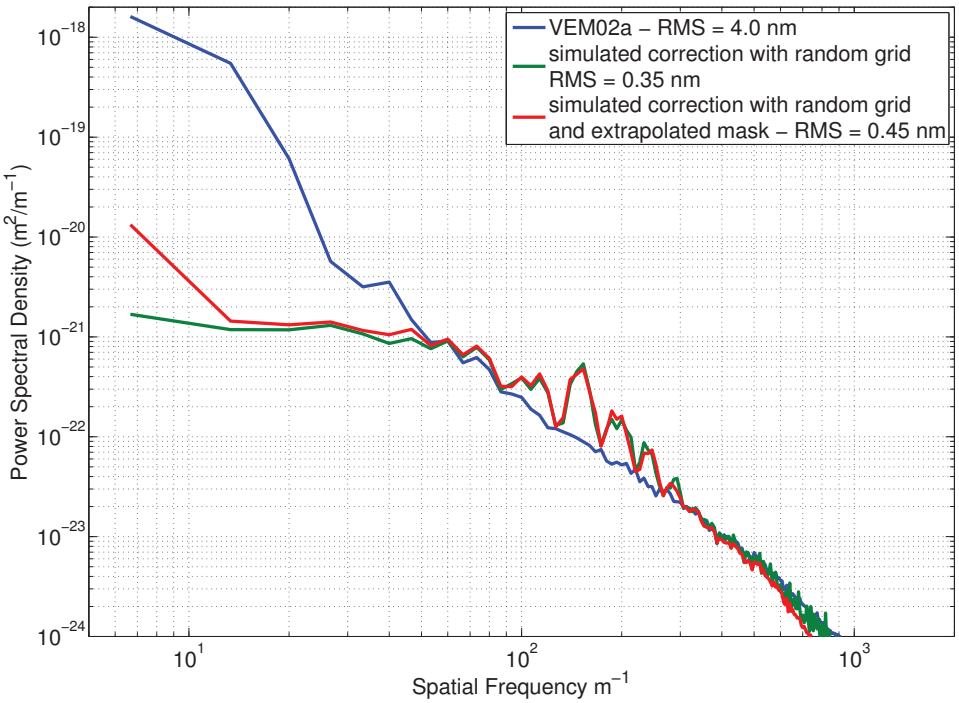

Figure 5.11: Power spectral density of the VEM02a surface (blue) and the surface after correction with random robot positioning (green) and with the extrapolated mask (red) on 150 mm.

5.5 Calibration of the robot

A robot for the correction of the Advanced Virgo substrates has been developed in collaboration between the LMA and the *Laboratoire d'Anncey-le-vieux de Physique des Particules (LAPP)*. It has been built at LAPP and it was delivered at LMA at the end of July 2011.

The robot is composed of three rotating arms (A_1, A_2, A_3) and the substrate is placed on the third arm at about 10 cm of the center of the arm A_3. The substrate is deported so that it can explore a larger region than if at the centre of the arm A_3. It also permits to add a counterweight that will reduce the oscillation of the substrate when moving. A combination of the three angles of rotation allows to position the substrates at the wanted position.

A phase of calibration is necessary to evaluate the robot performances in terms of accuracy and reproducibility of the positioning. The deposition imprint in itself has to be calibrate too with the essential parameters that are the speed of deposition and the shape of the imprints.

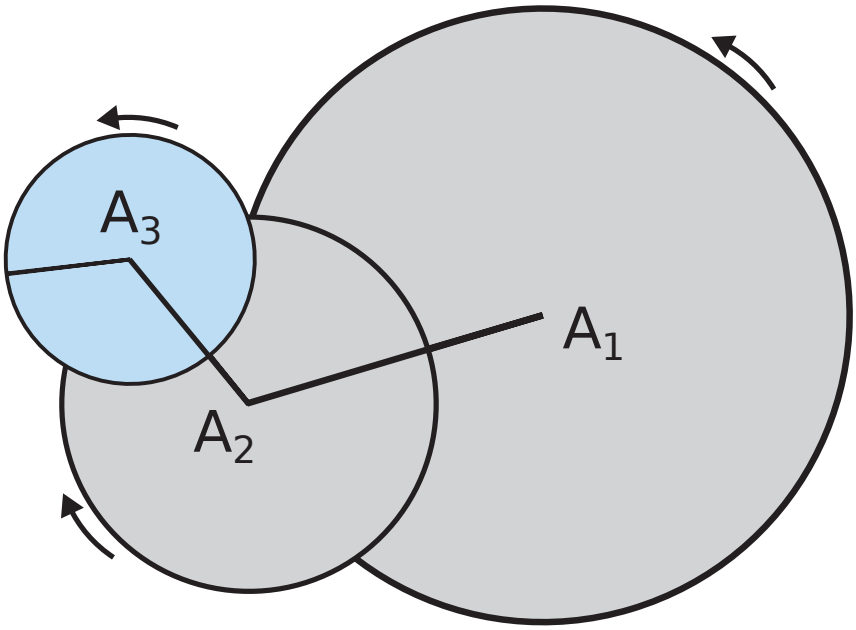

Figure 5.12: Simplified schemes of the robot with three rotating arms.

5.5.1 Positioning of the robot

To obtain an efficient correction, the positioning of the substrate in front of the mask used for the correction must be very accurate and reproducible. The positioning of the robot must be at least more accurate than the size of a pixel of the surface figure measurement of the substrate to be corrected. Given the actual apparatus at LMA to measure the substrate surface the positioning of the robot has to be with an accuracy and reproducibility better than 0.35 mm.

The robot is designed to achieve a positioning with an accuracy of 0.1 mm. We need to fine tune the parameters of the robot to achieve such accuracy. To check the precision of the positioning an apparatus has been developed at LAPP, it uses the same camera that are used on the Virgo interferometer for the local control of the mirror [98]. The camera looks at a test pattern composed of nine white dots set up in a square. From the image of the test pattern, a software developed at LAPP [99] compute the error of positioning both in the vertical and horizontal direction. A rectangular table of about 1 m by 0.5 m with n equally spaced test patterns on it has been designed so that we can check the positioning of the robot. The table is set on the center of the arm A_3. It has the same weight as the Advanced Virgo substrate. It is important that the box weights the same as the substrate we want to correct so that the robot is working in the same condition as for a future correction. A difference of weight could result in a different behaviour of the robot. Figure 5.13 shows the apparatus to measure the accuracy in the positioning of the robot.

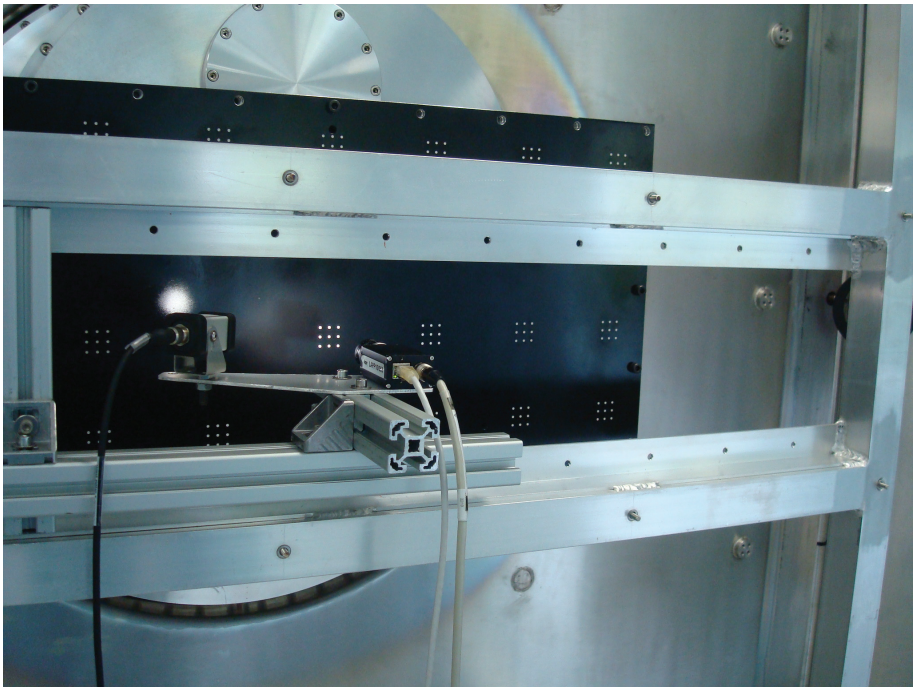

Figure 5.13: Camera set up to test the accuracy of the robot in terms of positioning.

The offset on each arms has to be set up correctly to obtain a good positioning of the robot. We make a scan of the table with the results shown in the figure 5.14. On this figure, the red circle are the targeted positions on the table. The blue crosses are the obtained positions when scanning the table. Positioning errors have been multiplied by a factor 10 on the figure so that they are visible. An error of 0.5 mm in the positioning of the robot is shown as an error of 5 mm on the figure 5.14. The camera is placed in front of the center of the robot, it is important to note that the robot will work later in an off-centred position as the mask through which the materials is deposited is set in front of one of the two sources of the coating machine. It will be set at approximately 160 mm on the left of the center of the robot. The standard deviation from the targeted position is 0.24 mm in the x-direction and 0.21 mm in the y-direction. Thus the typical error in the positioning of the robot is smaller than the pixel size of the surface figure measurement.

Then we also made some tests in the positioning of the robot in the working area, that is to say shift from the center by about 160 mm. At this position we are no more able to use the box with the test patterns. Indeed, the camera is set in the place of the mask which is at the center of the substrate that is to say deported from the center of the arm A_3 from 10 cm. In that position there are no test patterns facing the camera. Moreover the test patterns are set every 117.5 mm and 100 mm on the table in the x and y direction and we want to control the positioning in a smaller area. A fake substrate with white dots on it allow us

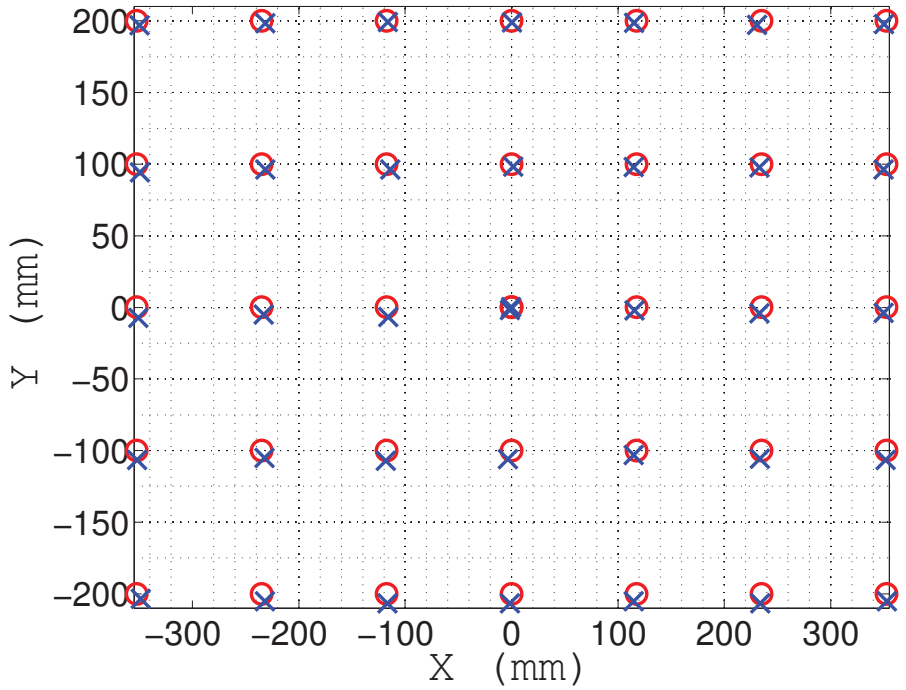

Figure 5.14: Error on the positioning of the robot, the red dots are the targeted positions and the blue crosses are the obtained positions.

to get the positioning error with the same camera. The fake substrate is put on a sample holder designed for the correction of small substrate (smaller than 150 mm). The surface of the fake substrate is set in the same plane as the future Advanced Virgo substrate and its total weight is similar to the Advanced Virgo substrate.

We used this small substrate to tune finely the robot parameters and to assess the repeatability of the robot positioning. With the fake substrate we see that the reproducibility of the robot positioning is of about 0.200 mm and 0.150 mm in the x and y directions. The reproducibility of the positioning of the robot is better than the pixel size of the substrate measurement in the working area.

For the time being, there is no shutter in front of the mask and so materials is deposited during the movement of the robot. It is important to know the movement speed of the robot. A scan has been made on a surface corresponding to a Virgo substrate with the robot stopping every 4.5 mm. We find that the average time between two positions is about 1 second.

5.5.2 Calibration of the deposit.

Once we have tuned the parameters of the robot and characterize its performances in terms of positioning, we need to calibrate the imprint of the deposition through a mask. We want to know the shape of the deposition imprint, its position compared to the positioning of the robot and the deposition speed that is to say the flux of materials deposited.

Several depositions have been done on a 100 mm diameter substrate (TC1202) with the two square mask of 10 mm and 21.5 mm. 4 deposits have been done with the 10 mm mask at 20 mm of the substrate surface (C10D20) and 1 deposit has been made at 10 mm of the substrate surface (C10D10). Another deposit has been made with the 21.5 mm at a distance of 20 mm (C21.5D20). We measure the substrate surface after those depositions and subtract the background, i.e. the measurement before deposition. We can compute the flux of materials that is sputtered through the mask, it is simply:

$$flux = \frac{D}{A \times t} \tag{5.9}$$

where D is the volume of deposited materials, A the area of the mask and t the time of deposition. This value should be constant for the different deposits. We compute the flux for the six deposits, the values are reported in the table 5.3. We see that the flux of materials deposited is constant whatever the mask size and the distance of deposition. The average value is 1.18 nm.s^{-1}.

Table 5.3: Flux of the deposition.

Deposit (run)	Flux in nm.s^{-1}
C21.5D20 (C12011)	1.21
C10D20 (C12012)	1.16
C10D10 (C12013)	1.13
C10D20 (C12018)	1.18
C10D20 (C12018)	1.13
C10D20 (C12019)	1.25

We can extract the imprint of the deposits through the two masks. Figure 5.2 shows the imprints of the deposition through the 21.5 mm mask and figure 5.15 shows the deposition imprints through the 10 mm mask. In both cases the mask is placed at a distance of 20 mm.

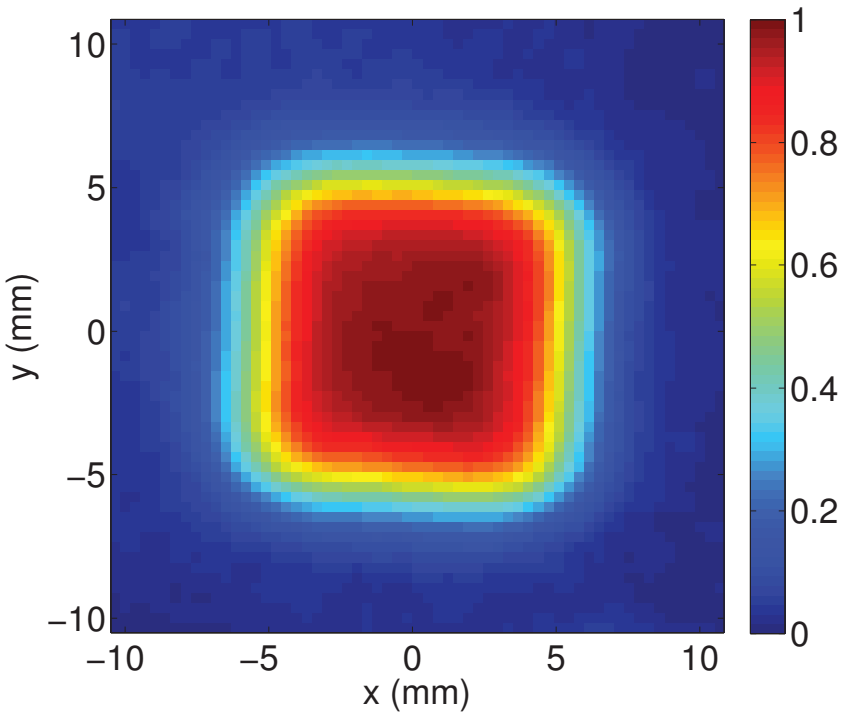

Figure 5.15: Normalized deposition imprints through a 10 mm square mask at a distance of 20 mm.

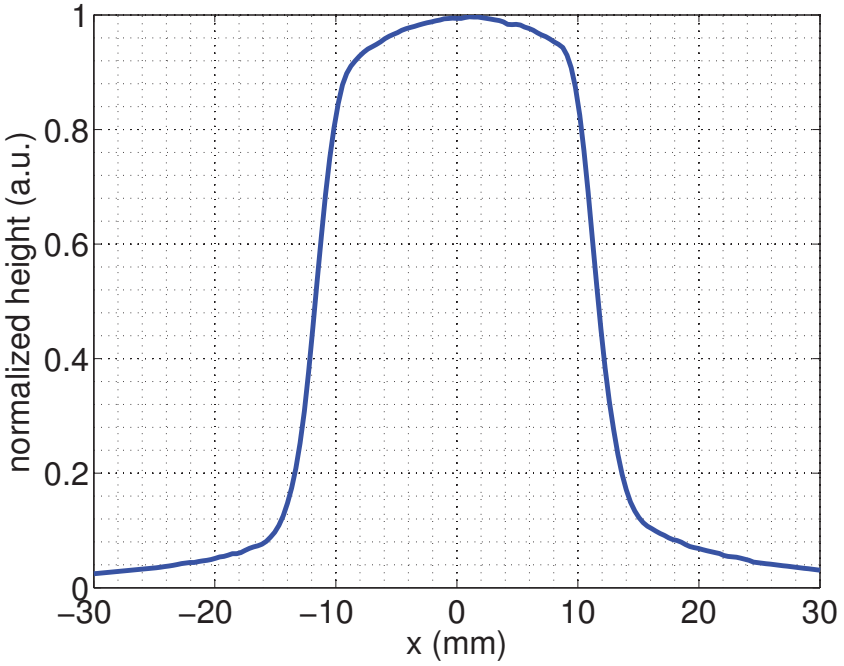

Figure 5.16: x profile of the normalized deposition imprints through the 21.5 mm square mask at 20 mm. The data are extrapolated for a radius larger than 25 mm.

If we look at the profile of the deposition imprint when using a mask of 21.5 mm (see figure 5.16), we see that it has quite a smooth shape with a rounded plateau and a width at half height of about 23.5 mm. The sides of the imprint has a slope of about 0.11 mm^{-1}, it decreases from 90% to 10% in about 7 mm. This extracted deposition imprint is used in the computation of the correction and we assume that its shape remains the same whatever the deposition time.

5.6 Experimental results

In this paragraph we will present the results obtained with the corrective coating in the flattening of silica substrates. We will first present the results on an 80 mm substrate and then show the correction of the flat surface of an initial Virgo substrate.

5.6.1 The corrective coating process

The process of the corrective coating technique from the first measurement of the substrate to the deposition of the corrective coating takes places in six steps.

1. Measurement of the substrate.
2. Deposition of three positioning peaks.
3. Measurement of the substrate with the three positioning peaks.
4. Computation of the correction.
5. Deposition of the corrective coating.
6. Measurement of the substrate after correction.

First we measure the substrate surface we want to correct. Then we deposit three peaks with a 1.5 mm diameter circular mask. We deposit through the mask during one hour at three positions on the substrate to get the three peaks. The three peaks are typically set at the bottom, the top and the right of the substrate. This three peaks will allow us to calibrate the coordinate system on the substrate according to the positioning of the robot so that we know precisely the center of the substrate. Moreover by deposing this three peaks one avoid any non repeatability in the measurement of the substrate that could be due to the metrology mount. Once we have measured the substrate with the three peaks we can compute the correction using the algorithm presented earlier in the paragraph 5.3. Then the corrective coating is deposited on the surface of the substrate we want to correct. And

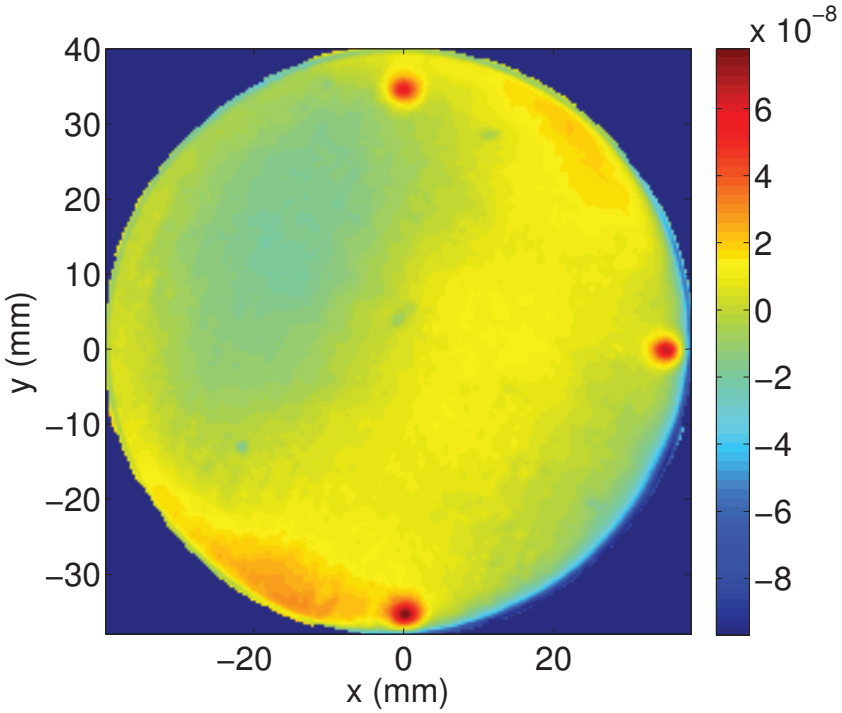

Figure 5.17: Surface of the substrate TC1203 before correction on 80 mm.

finally we measure the results of the substrate after the correction. If the correction is not good enough, we can compute again the correction and deposit a second corrective coating.

5.6.2 Correction of a 80 millimetre substrate

We made a first test of the corrective coating with the new robot on a 80 mm diameter substrate to check the whole process of the correction. The substrate has two plane surfaces with no wedge i.e. there is no angle between the planes of the two surfaces. Three peaks have been deposited at the following position during one hour:

- x = 0 mm, y = 35 mm.
- x = 0 mm, y = -35 mm.
- x = 35 mm, y = 0 mm.

Figure 5.17 displays the surface figures of the 80 mm diameter substrate with the three positioning peaks deposited in order to calibrate the coordinate system on the substrate. It has a flatness of 6.31 nm RMS on the central 60 mm diameter. The correction has been computed using the classic algorithm, it gives a surface with a flatness of 1.33 nm RMS on 60 mm. We correct the surface with a mask of 10 mm and a robot step of 4 mm.

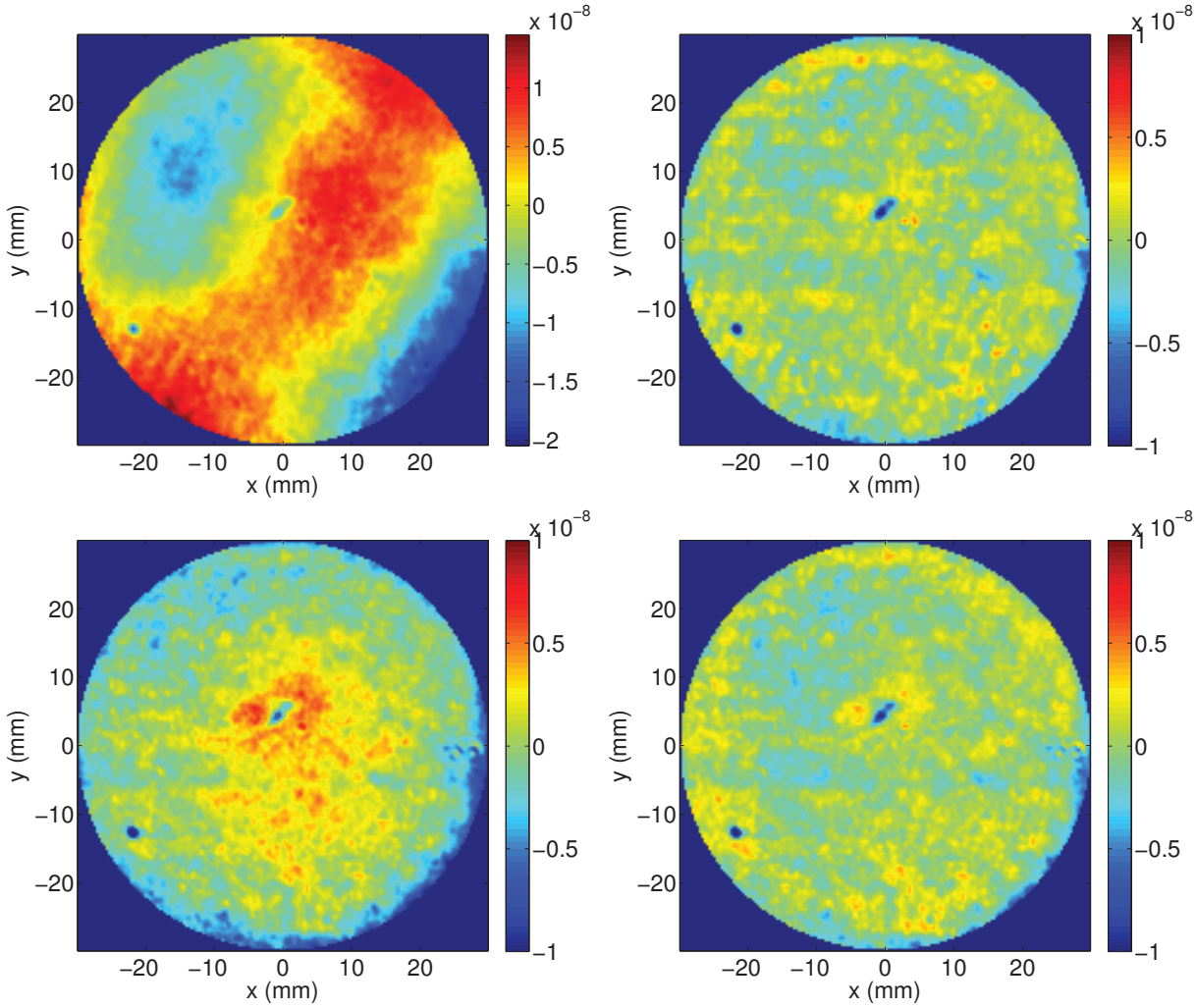

Figure 5.18: Surface of the substrate TC1203. Surface before correction (top left), simulated surface after correction (top right), experimental surface after correction (bottom left) and experimental surface after correction with residual curvature removed (bottom right).

Figure 5.18 shows the surface figure of the substrate TC1203 before and after correction. The top left figure is the surface before correction, the top right figure is the simulated surface after correction, the bottom left figure is the surface after correction and the bottom right figure is the same surface with the curvature removed.

We perform the correction in the coating machine with the robot, we measure after correction a surface with a flatness of 2.32 nm RMS on 60 mm which is mainly due to a residual radius of curvature. Indeed, if we look at the Zernike polynomial decomposition [81] of the surface, we see that the Zernike polynomial Z_{20} has an amplitude of -3.1 nm. It corresponds to a radius of curvature about -72.5 km. The flatness of the corrected surface after removal of the curvature becomes 1.45 nm RMS on 60 mm. This is quite close to the

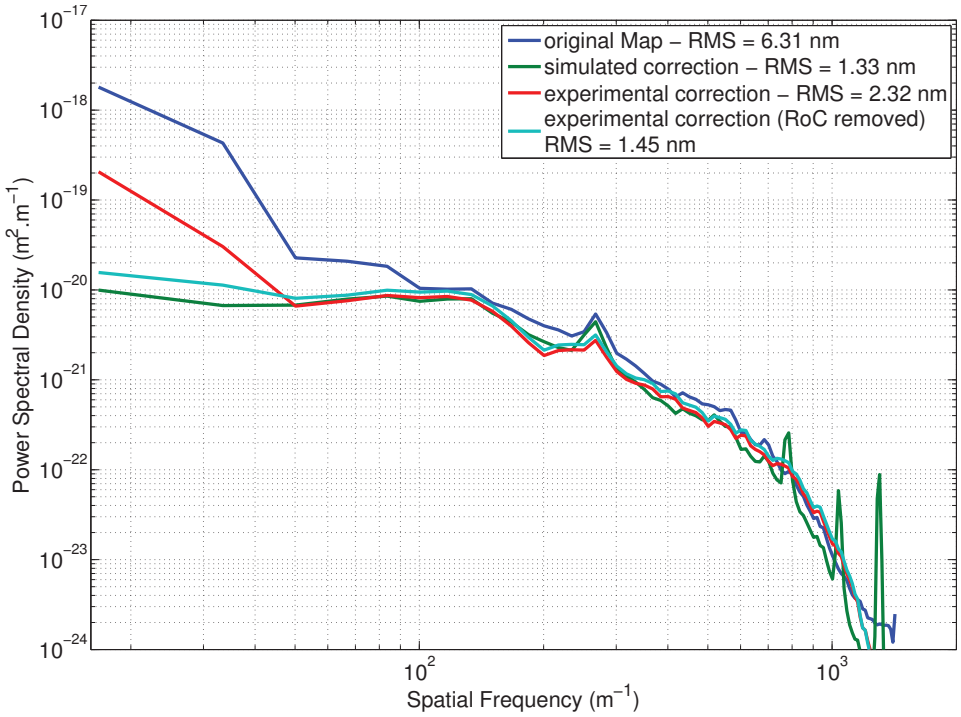

Figure 5.19: Power spectral densities of the TC1203a surface figure before correction (blue) along with the simulated surface after correction (green), the surface after experimental correction (red) and the surface after correction without curvature (cyan) on 60 mm.

simulated value (1.33 nm RMS on 60 mm). One can also see similarity in the simulated surface and the experimental surface figure with the curvature removed shown in the figure 5.18. Indeed in both surface figures we see an horizontal band between 0 and -5 mm in y which shows a lack materials.

We compute also the power spectral densities of those four surfaces, they are plotted in the figure 5.19. We see that the power spectral densities are bent down below a cut-off frequency of 100 m^{-1} as explained in the paragraph 3.6 of chapter 3. This cut-off frequency corresponds to the inverse of the size of mask (10 mm) used in the correction. The power spectral density of the surface after correction follows the one of the simulated correction above a spatial frequency of 50 m^{-1} and is higher below this spatial frequency. This excess of power at low spatial frequencies is due to the curvature of the surface. We see that the excess of power at low spatial frequency in the power spectral density of the corrected surface without curvature has disappeared.

We can see in the measurement of the substrate before correction some fringes that are due to the back surface of the substrate. Indeed the substrate is a flat-flat substrate. The reflection of the back surface contribute in the measurement of the front surface when measured by phase-shifting interferometry. To eliminate the back surface contribution, we

deposit by hand a film of soap on the back surface. It allows to reduce the reflection from the back surface but it is not perfect and there is still a small reflection that contributes to the overall measurement.

The curvature in the experimental correction could be due to an error in the initial measurement of the substrate. Indeed because of the substrates has no wedge, the back surface contribute slightly to the measurement and it could add a curvature to the measurement that is not intrinsic to the substrate front surface. The corrective coating will correct this curvature which is not part of the surface we want to correct.

It has been decided to perform a second correction on the substrate to try to correct the residual curvature seen of the surface figure after correction. Figure 5.20 shows the surface figure after the second correction measured with a thin film of soap in the back surface and with the back surface being grounded so that it is no more reflective. The surface figure with the soap has a flatness of 2.2 nm RMS while the surface figure has a flatness of 1.1 nm RMS after that the back surface has been grounded. We see that the technique of adding a film of soap on the back surface adds high frequency noises on the measurement as one can observe in the figure 5.21. We see that the power spectral density of the measurement with soap on the back surface has a high power at high frequencies because of the contribution of the back surface. After being grounded on the back surface, the high frequencies are largely reduce at level below the PSD of the initial measurement. It means that the initial measurement had a contribution coming from the back surface. The reflection of the back surface was not enough extinguish by the film of soap.

Anyhow with this test, we can validate the process of the correction presented in the paragraph 5.6.1. However a lot of care should be taken in the initial measurement of the substrate surface one wants to correct. Indeed a wrong measurement could results in a wrong correction. The level of correction depends strongly on the quality of the initial measurement.

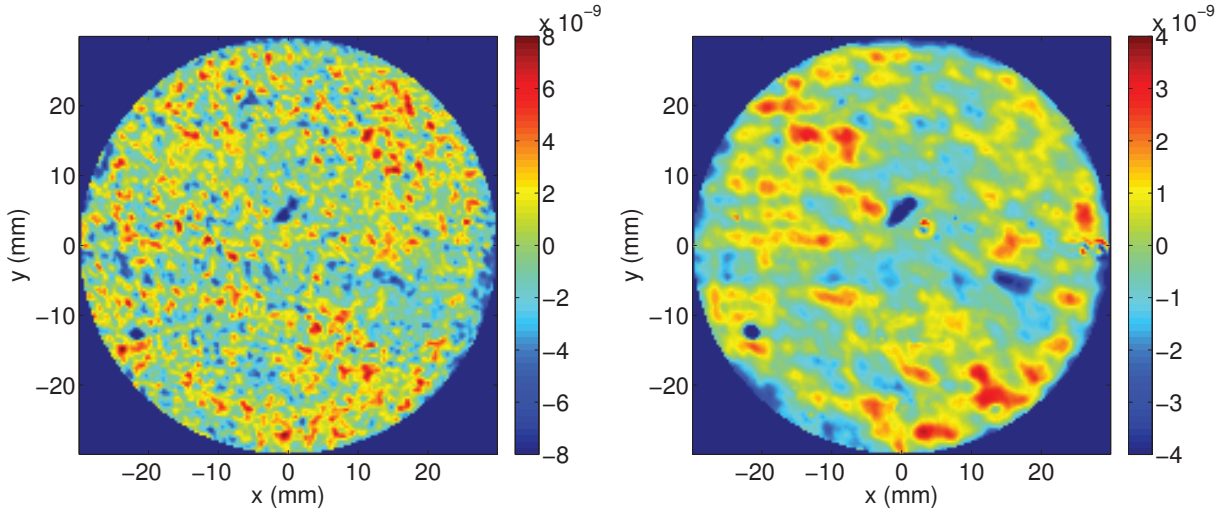

Figure 5.20: Surface of the substrate TC1203 after the second correction measured with soap on the back surface (flatness = 2.2 nm RMS) (left) and with the back surface being grounded (flatness = 1.1 nm RMS) (right).

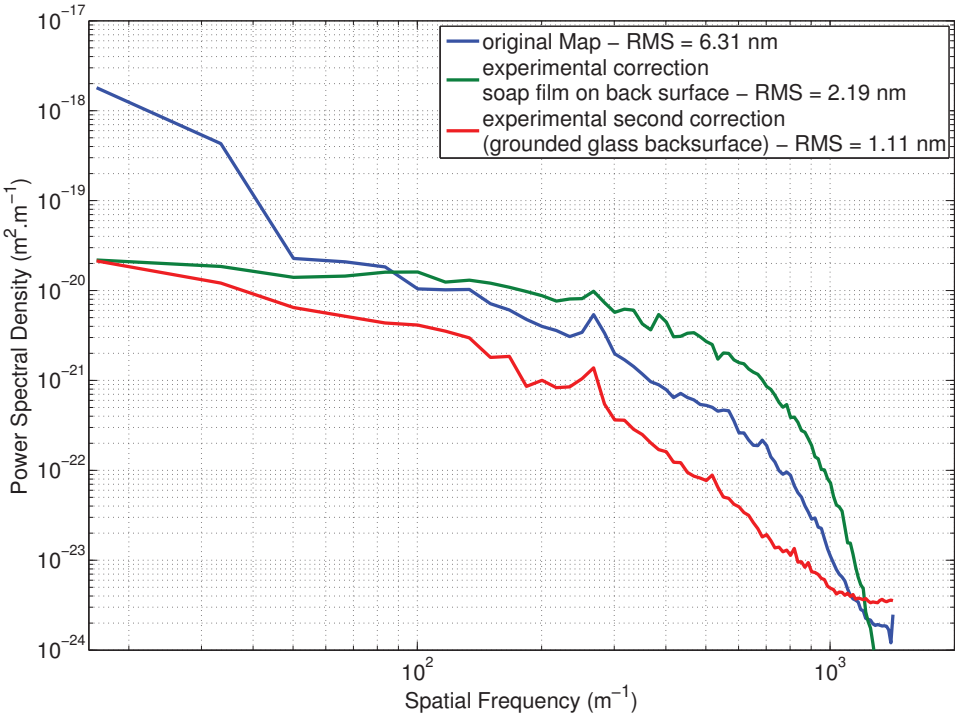

Figure 5.21: Power spectral densities of the TC1203a surface figure before the first correction (blue), after the second correction (green) and with the back surface being grounded (red) on 60 mm.

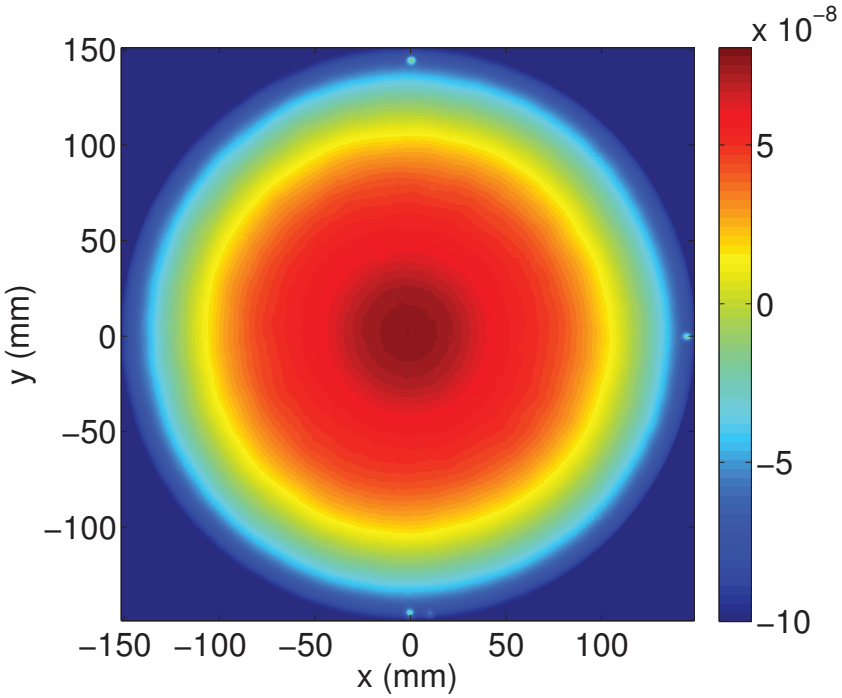

Figure 5.22: VEM02a wavefront before correction on 300 mm with the radius of curvature of -70 km.

5.6.3 A full size test: correction of a Virgo substrate

After correcting a small substrate, we decide to make a full size test on a Virgo substrate called VEM02. Considering that the metrology is limited when measuring concave surface (see chapter 4), we decided to correct the back surface of the substrate which is flat.

We measured the plane surface (a) of the VEM02 substrate, it has a radius of curvature of about -70 km on 300 mm. This curvature of -70 km corresponds to a Zernike coefficient Z_{20} with an amplitude of about 80 nm that is to say a peak to valley amplitude of 160 nm. We decided not to correct this curvature and so we subtract to each measurement a curvature of -70 km. All the surface figure shown in the following paragraph are with a -70 km curvature removed on 300 mm.

The measurement is the average of four measurements done after deposition of four reference peaks (run C12032). These measurements have been done using the stitching technique as explained in chapter 4. Figure 5.22 shows the VEM02a surface figure on 300 mm with the reference peaks. The locations and time deposition of the four reference peaks are reported in table 5.4.

Figure 5.23 presents the surface figure of the plane surface (a) of the substrate VEM02 before correction on a diameter of 260 mm with a radius of curvature of -70 km on 300 mm removed. It has a flatness of 7.0 nm RMS on 260 mm and 4.0 nm RMS on 150 mm.

Table 5.4: Locations and time deposition of the reference peaks on the VEM02a surface.

	x (mm)	y (mm)	time deposition (min)
peak 1	0	145	60
peak 2	145	0	60
peak 3	0	-145	60
peak 4	10	-145	30

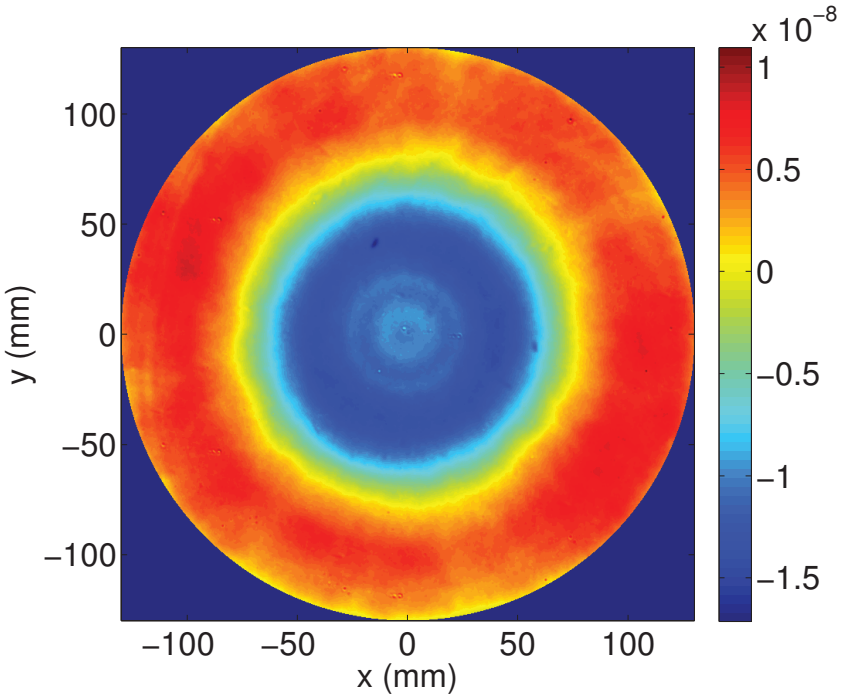

Figure 5.23: VEM02a surface figure before correction on 260 mm - flatness = 7.0 nm RMS on 260 mm and 4.0 nm RMS on 150 mm.

Ten different measurements have been done on the VEM02a surface and the reproducibility of the measurement is limited by the measurement of the astigmatism and RoC. Five of these measurements have been done before the deposition of the reference points and five have been done after. As explained in 4.6.1, the optic has been dismounted or remounted from its mount between the measurement except for the two first measurements. We have a difference in the orientation of the astigmatism measured on the surface as we find that the astigmatism angle on 150 mm is around -67.5° for the measurement before the reference peaks deposition and it is -16.8° for the four first measurements after the run C12032. The fifth measurement with the reference peaks shows an astigmatism with an angle of -65.9° similar to the measurement before the run C12032. The reason of this difference in the astigmatism orientation is the mounting of the substrate in the optics holder. The substrate in the sample

holder is never resting on the same position and so the forces that apply on it induce an extra astigmatism that depends in the way the substrate was mount. It is very delicate to mount the substrate in a reproductive way in the optics holder and the measurements were done before the improvement of the sample holder explained in 4.6.2.

So we compute the correction on the average of the four first measurements with the reference points. The correction has been computed with the non-extrapolated mask. It is mandatory to compute the correction on the measurement with the reference point as we need to know precisely the positioning of the robot on the substrate. The correction has been computed with the optimized algorithm and the instructions have been rounded to the second as the robot controlling software does not yet permit to control the timing more precisely. Also for the time being there is no shutter on the mask and so the materials is deposited during the displacement of the robot. The speed of displacement from one point to another has been estimated to be around one second. So we subtract one second to each instructions in order to take into account the materials deposited during the displacement of the robot. Adding a shutter in front of the mask would permit to give instructions with a better precision. A square mask of 21.5 mm is used for the correction with a robot step of 4.5 mm.

Figure 5.24 shows the surface after correction as predicted by the simulation with the extrapolated mask. It has a flatness of 0.43 nm RMS on 260 mm and 0.33 nm RMS on 150 mm with low astigmatism (smaller than 0.2 nm on 260 mm). The correction simulated with the extrapolated mask add a small curvature with a Z_2^0 of amplitude -0.42 nm. This small extra curvature is due to the extrapolated mask. The surface simulated with the non-extrapolated mask did not exhibit this curvature. Then we perform the correction experimentally in the coating machine we obtained the surface wavefront shown in the figure 5.25. It took about four hours to correct the surface with the 21.5 mm square mask. The measurement is again the average of four measurements done with the stitching technique. It has a flatness of 2.2 nm RMS on 260 mm and 0.90 nm RMS on 150 mm after removal of a radius of curvature of -70 km on 300 mm. The flatness of this surface is mainly dominated by a residual curvature and a strong astigmatism. Part of the residual curvature is probably added because of the non extrapolated mask used to compute the correction as we have seen in paragraph 5.4.3. The amplitude of the Z_2^0 Zernike term is about 1.1 nm on 150 mm whereas it is -0.42 nm for the correction simulated with extrapolated mask. Thus the additional curvature on the surface after the experimental correction is due to the fact that the correction was computed with the non-extrapolated mask.

The astigmatism amplitude is about 3.6 nm at 84.0°on 260 mm and of 1.3 nm at 82.2°on 150 mm compared to 1.6 nm at -16.5°on 260 mm and 0.7 nm at -35.3°on 150 mm before

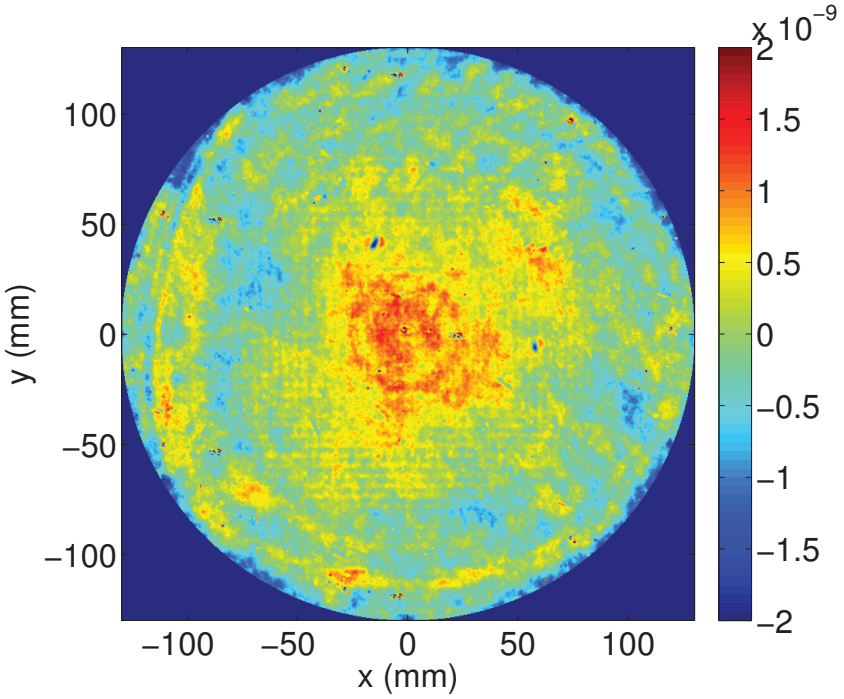

Figure 5.24: Simulated surface figure of VEM02a after correction on 260 mm - flatness = 0.43 nm RMS on 260 mm and 0.33 nm RMS on 150 mm.

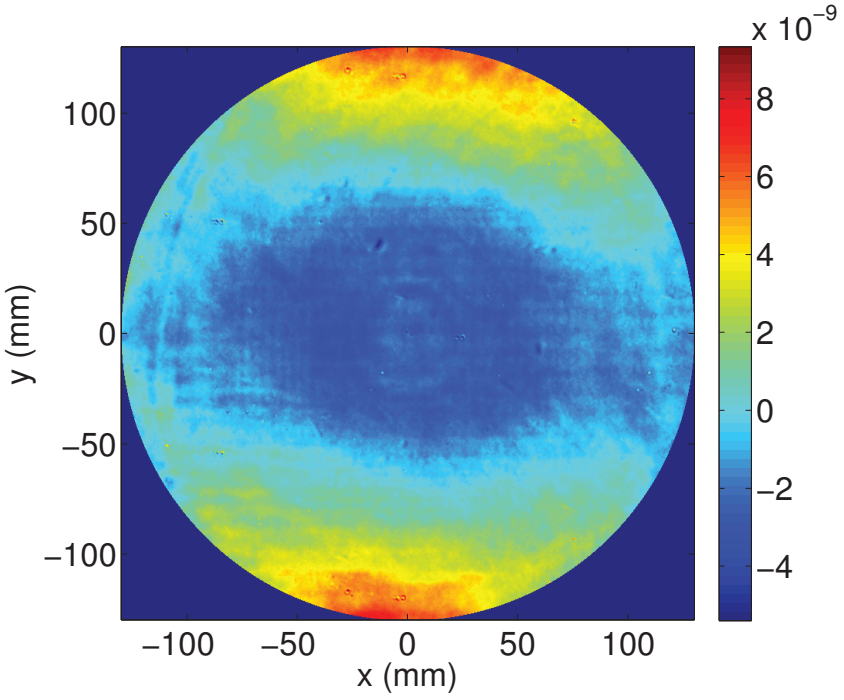

Figure 5.25: Experimental surface figure of VEM02a after correction on 260 mm - flatness = 2.2 nm RMS on 260 mm and 0.88 nm RMS on 150 mm.

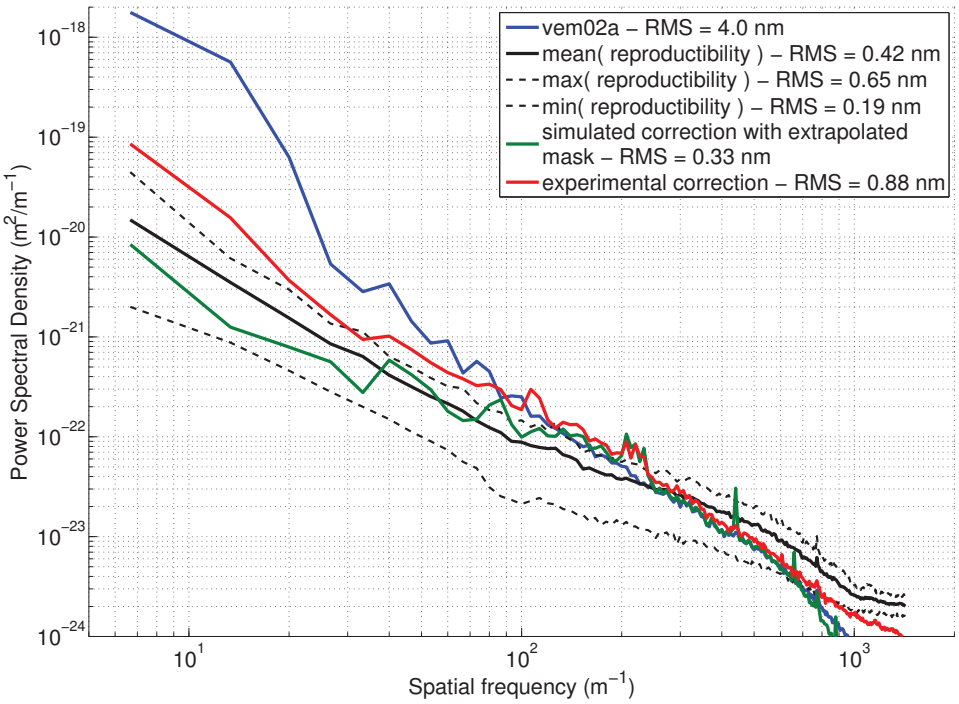

Figure 5.26: Power spectral densities of the VEM02a surface figure before correction, the reproducibility measurement, the simulated correction and the experimental correction on 150 mm.

correction. The astigmatism angle is different in the measurement before and after correction. This difference could be explained by the fact that we may have added a bit of astigmatism by correcting a wrong astigmatism.

We can look at the power spectral densities before and after the correction as well as the reproducibility of the initial measurement. Nine measurements have been done with the substrate being dismounted from the sample holder between each measurements. It results in 36 subtractions and so in 36 different PSDs. To show the reproducibility of the measurement we present three different curves, the mean, the maximum and the minimum of these 36 PSDs. Figure 5.26 shows the PSDs of the initial measurement (blue), the three curves of the reproducibility of the measurement (black), the simulated correction (green) and the experimental correction (red). We see that the PSD of the experimental correction (red curve) follow the maximum of the reproducibility and so we can say that the correction is limited by the metrology. We also see a bump around 220 m^{-1} which is due to a small grating created by the robot step of 4.5 mm. Anyhow this bump is very small in amplitude and it can be considered as negligible as it does not induce significant more round-trip losses in the Advanced Virgo arm cavity.

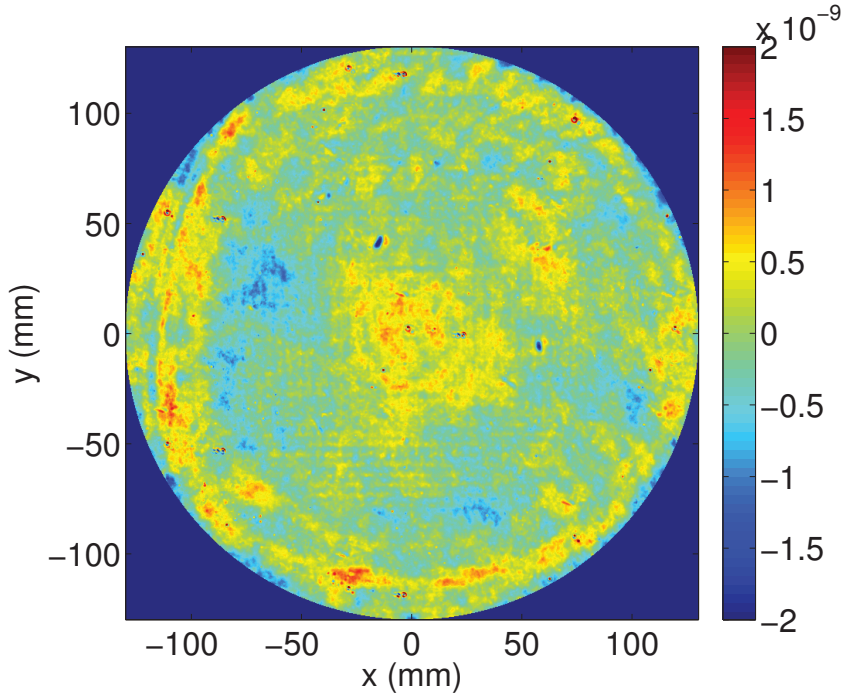

Figure 5.27: Simulated surface figure of VEM02a after correction with residual curvature and astigmatism removed on 260 mm with astigma - flatness = 0.34 nm RMS on 260 mm and 0.25 nm RMS on 150 mm.

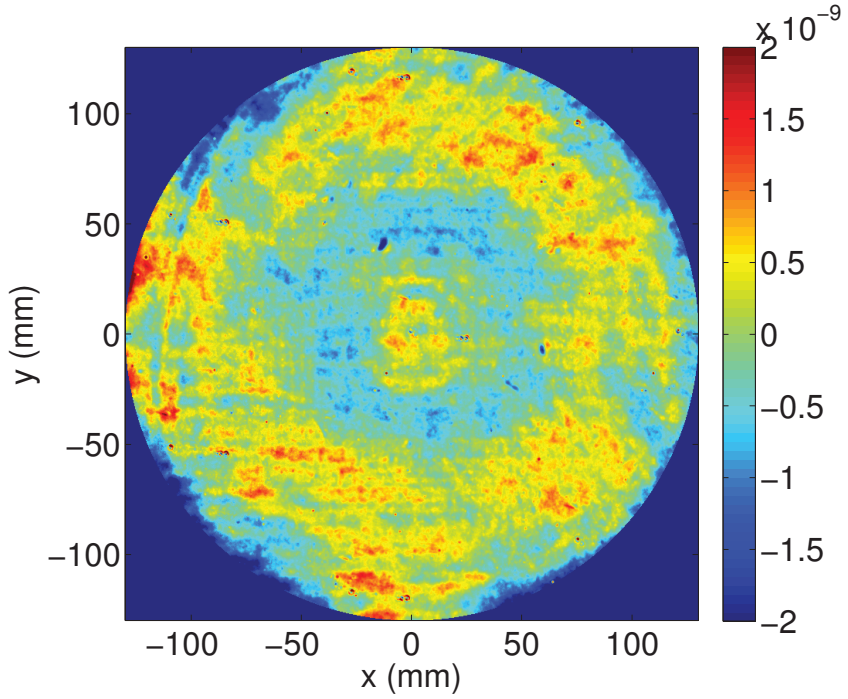

Figure 5.28: Experimental surface figure of VEM02a after correction with residual curvature and astigmatism removed on 260 mm - flatness = 0.51 nm RMS on 260 mm and 0.36 nm RMS on 150 mm.

If we subtract the residual curvature and astigmatism on the measurement of the substrate surface after correction, the flatness becomes much lower. It becomes 0.51 nm RMS on 260 mm and 0.36 nm RMS on 150 mm. It confirms that most of the RMS flatness of the surface is due to the astigmatism and curvature. Figure 5.28 shows the corrected surface figure with the astigmatism and residual curvature removed. The color axis is as before between -2 nm and 2 nm. The simulated surface figure after correction with the curvature and astigmatism removed is shown in figure 5.27. The surface flatness is of 0.34 nm RMS on a 260 mm diameter and 0.25 nm RMS on a 150 mm diameter. We see that the correction was quite efficient, even though not at the level of the simulated correction. We also can see a slight regular grid with a spacing that corresponds to the step of the robot.

We now plot the power spectral densities as before but with the astigmatism and radius of curvature subtracted in each measurement, it is the figure 5.29. We also see that the experimental correction reach the reproducibility of the measurement. Now the reproducibility of the measurement is only due to the environmental condition (vibrations, air turbulence) and to the stitching technique in itself.

From this full size test, we can say that for now the corrective coating technique is limited by our ability to measure the surface figure before correction with a great precision and reproducibility. Anyhow, it gives quite good results as we gain more than a factor four in the RMS flatness of the substrate in the central area. A better reproducibility in the measurement of optical surfaces should be achieved to increase the efficiency of the corrective coating correction.

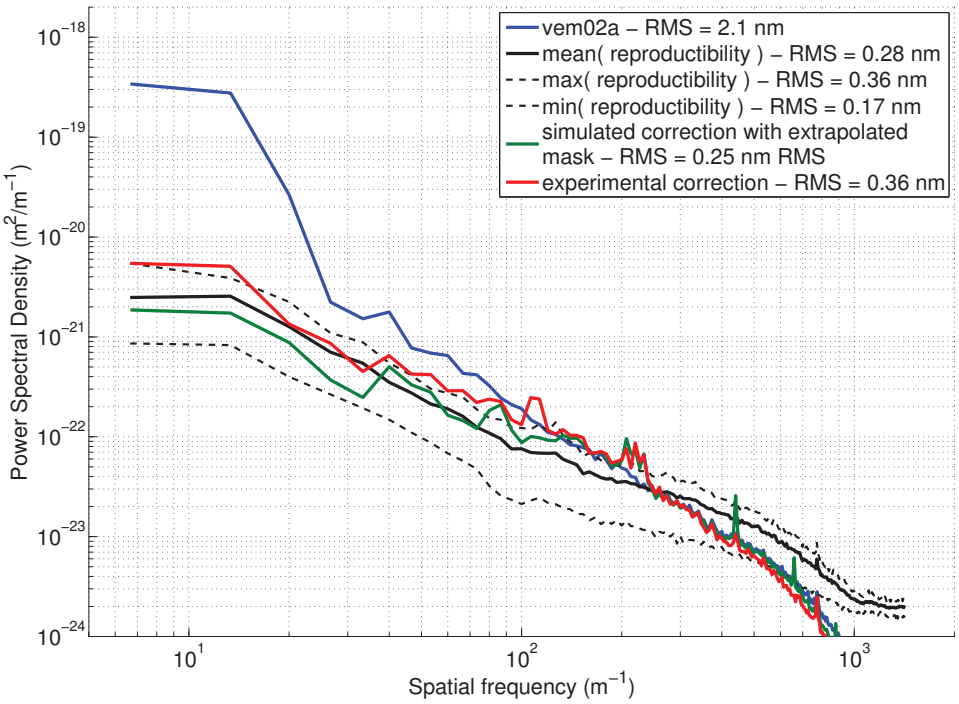

Figure 5.29: Power spectral densities of the VEM02a wavefront surface, the reproducibility measurement, the simulated correction and the experimental correction on 150 mm with RoC and astigmatism removed.

5.6.4 Losses in Advanced Virgo cavity

Finally, we want to know the effect of the surface after correction in the Advanced Virgo arm cavity in terms of losses. Therefore we use the map of the surface measured after correction in the simulations of a Fabry-Perot cavity under SIESTA. The map is put first on the ITM mirror and then on the ETM mirror with the opposite surface being perfect.

We simulate the Advanced Virgo cavity with the maps before and after correction. The maps used in these simulations are the experimental ones on 300 mm with only tilt and piston removed. It includes the residual curvature and astigmatism. The results of the simulation in terms of round-trip losses and round-trip losses projected on the TEM_{00} are reported on the table 5.5 and have been cross-check with OSCAR [100].

We see that the RTL with the surface after correction are around 13 ppm i.e. lower than the Advanced Virgo specifications. We remind that the specification is set to be lower than 50 ppm of round-trip losses in the arm cavity, that is to say 25 ppm per mirror. We also notice that the RTL on the TEM_{00} mode are very close to the total RTL. It means that the beam inside the cavity is also very close to be a perfect TEM_{00}. It also means that the cavity is quite immune to this level of astigmatism as it does not induce high losses in the cavity.

Table 5.5: RTL and RTL00 in the Advanced Virgo arm cavity with the VEM02a surface before and after correction simulated with SIESTA.

	Surface map on ITM		**Surface map on ETM**	
	RTL (ppm)	**RTL00 (ppm)**	**RTL (ppm)**	**RTL00 (ppm)**
VEM02a before correction	37.1	40.0	365.1	390.2
VEM02a after correction	12.4	12.9	12.9	13.9

There is a big difference in the round-trip losses with the surface figure before correction with the surface map on the ITM or on the ETM (37 ppm compared to 365 ppm). It is due to the size of the beam on the two mirrors. Figure 5.30 shows the surface before correction along with the beam size on the input mirror (dashed white line) and on the end mirror (solid white line). Because of the larger beam size, we observe that the laser power on the end mirror impinges where the surface height begins to rise. On the contrary most of the laser power that impinges on the input mirror is contained in flatter region. It explains the observed difference in the round-trip losses in the cavity.

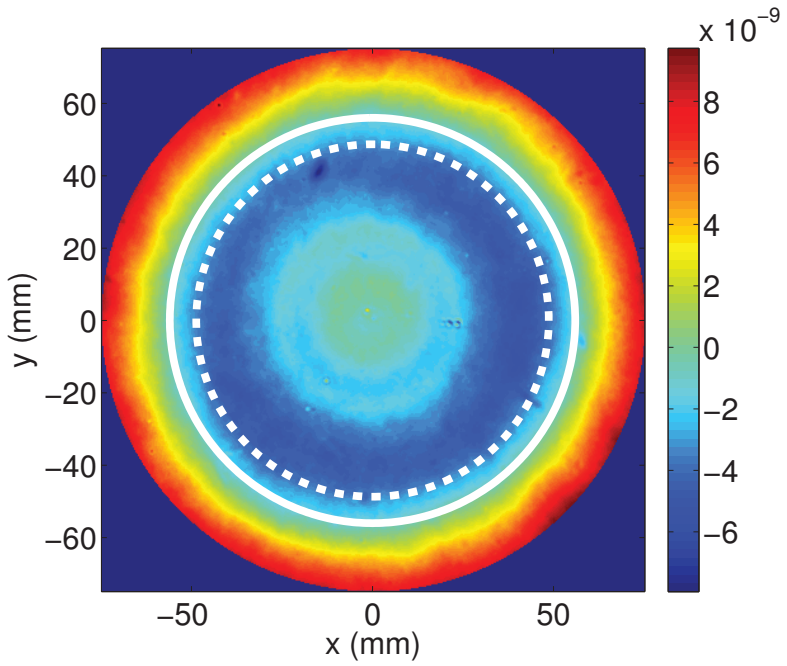

Figure 5.30: Surface figure of VEM02a before correction on 150 mm. The dashed white line represents the beam size impinging on the input mirror whereas the solid white represents the beam size impinging on the end mirror

Finally we have been able to correct a substrate surface that meet the specification on the round-trip losses in the Advanced Virgo cavity even though there is an astigmatism of about 1.3 nm on the central 150 mm diameter. This astigmatism induces a differential radius of curvature in the x and y direction of about 0.9 m and 1.3 m on a diameter of 150 mm for the Advanced Virgo input and end mirrors.

5.7 Conclusion

In this chapter, we have presented the concept and the test of the corrective coating technique. The simulation and experimental results prove the efficiency of the technique.

The goal of the corrective coating technique is to flatten the surface of a substrate. Its principle is to deposit a coating layer of the same materials as the substrate that fill in the holes of the surface.

A robot has been developed in collaboration with the LAPP and the LMA and it has been built at LAPP. This robot allows moving the substrate inside the coating chamber behind a mask through which the materials is sputtered and deposited on the surface. The robot performances are quite stringent as it should be able to move a load of about 60 kg in vacuum with a high precision. It has been shown that the positioning of the robot is precise within about 0.2 mm. This precision is enough to correct a substrate surface with a good efficiency.

The surface figure measurement of the substrate we want to correct is critical in the efficiency of the correction. The substrate surface must be measured with the best possible precision and a very good reproducibility. Indeed an error in the measurement of the surface before correction will result in a wrong correction. The actual apparatus to measure mirror surface at LMA is composed of a 6 inch phase-shifting interferometer and a stitching technique is used to measure surfaces over a diameter of 300 mm. As from now the reproducibility of the measurement is limiting the correction. It is limited because of the stitching technique and because of the optics holder which does not allow to mount the substrate with a good reproducibility.

A new algorithm to compute the correction has been developed. It allows correcting defects smaller than the size of the mask. With this new algorithm we are able to correct in simulation a surface with a flatness of 4.0 nm RMS down to 0.33 nm RMS. We also show that for Advanced Virgo it is enough to correct the substrate surface on a diameter of 260 mm. We should take care in avoiding to have a step between the corrected and uncorrected region. So we typically create a step with a slope of about 30 mm on the external radius of the correction.

A full size test has been made on a Virgo substrate. It has been corrected down to the level of about 0.9 nm RMS on 150 mm. The surface after correction is mainly dominated by an astigmatism. The correction is limited for the time being by our capability to measure the astigmatism in a reproducible way. If we remove the residual curvature and astigmatism from the surface after correction, its flatness becomes 0.36 nm RMS. Anyhow the corrected surface meets the Advanced Virgo specification on the round-trip losses in the arm cavity.

To conclude, we have shown the capability of the corrective coating to bring the substrate surface to the level of the flatness required by the Advanced Virgo interferometer.

Chapter 6

The Coating Uniformity

6.1 Introduction

The final step in the development of the mirrors for the Advanced Virgo gravitational wave detector is the deposition of the multilayer coating on top of the substrate. A multilayer coating is an alternation of thin films of high and low refractive index materials that makes the substrate highly reflective. In the Fabry-Perot arm cavities there are two kinds of mirrors the input and end mirrors, both highly reflective The other side of the substrates are coated with an anti-reflective coating. In this chapter we will focus on the deposition of the high reflective multilayer coating for the two test masses composing the arm cavity. The input mirror (IM) is designed to have a transmission of 1.4% whereas the transmission is 1 ppm only for the end mirror (EM) [23].

First, we will describe the principle of the multilayer coating technique to obtain mirrors with the required reflectivity. The principle is to deposit alternatively thin films of high and low refractive index materials with a controlled thickness. It allows the light to interfere such that the light is reflected by the mirror with the required intensity.

In the second section, we will present the technique used to deposit the materials on the substrate that is to say the Ion-Beam Sputtering (IBS) technique. The IBS technique allows to deposit thin films with very low optical and mechanical losses [101].

Then we will concentrate on the multilayer coating uniformity that becomes dominating in the overall flatness of the mirrors. We will present the different configurations of the coating chamber to obtain a very low flatness. There are three possible configurations for the coating depositions, the first one is with one mirror in the center of the chamber with a simple rotation, the second with two mirrors in simple rotation. Finally two mirrors can be coated with a planetary motion of the substrates inside the coating chamber. These three configurations will be described more extensively and we will show the results in term of

flatness obtained experimentally with the two first configurations. Then we simulate the coating deposition with a planetary motion of the substrates inside the chamber and look at the surface flatness we would obtain. We will also study the effect of the principal aberrations induced by the coating deposition (in terms of Zernike polynomials) in the round-trip losses of the Advanced Virgo arm cavities.

6.2 Multilayer coating for high reflective coating

To achieve a reflectivity of 98.6 % for the IM and a transmission of 1 ppm for the EM, we need to deposit a multilayer stack of low and high refractive index materials. The high refractive index material is titanium doped tantalum oxide (tantala) whose molecular formula is $Ti : Ta_2O_5$. The low refractive index material is the same as the substrate material that is to say silica whose molecular formula is SiO_2. The refractive index of the two materials are around 2.07 and 1.44 respectively for the titanium doped tantala and for the silica. Typically the multilayer stack is composed of doublets of quarter-wave ($\lambda/4$ where λ is the light wavelength) layer of low and high index materials plus a first $Ti : Ta_2O_5$ layer and a finishing layer of silica as shown in the figure 6.1. In the case of the aLIGO coating, the design of the coating has been optimized in order to reduce the total thickness of the tantala [102, 103]. In the HR ITM coating, the thickness of the silica is about 2.1 µm whereas the tantala thickness is about 0.7 µm.

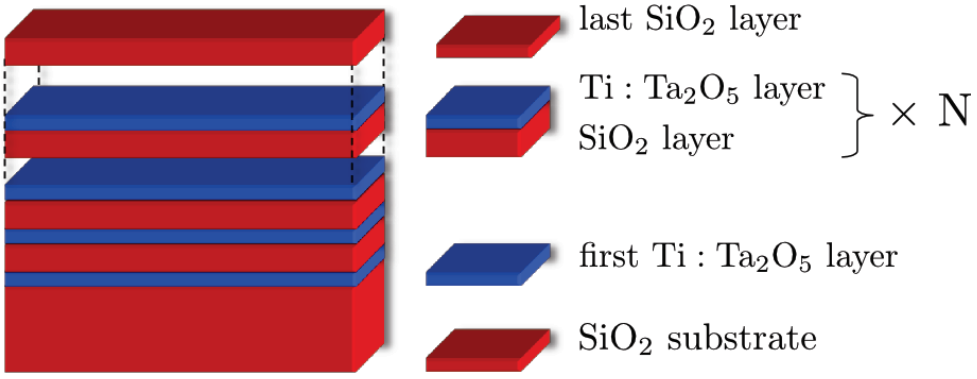

Figure 6.1: Multilayer coating composed of low and high refractive index materials.

The light impinging on such a multilayer coating interferes constructively and destructively such that the desired transmission is achieved. Basically the more doublets there are in the coating stack the more reflective is the coating.

The amplitude and intensity (a_i and I_i) of the light field passing through the multilayer stack are described in the figure 6.2 with n_i and e_i being the refractive index and thickness of the layer i.

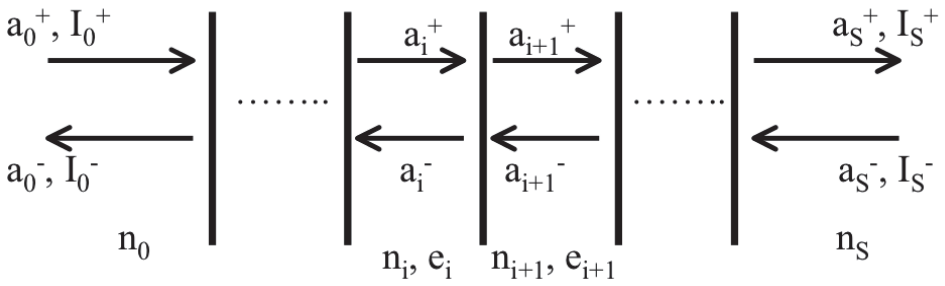

Figure 6.2: Light field propagating through a multilayer coating.

At each interface between the two materials of the multilayer stack the light field a_i is reflected and transmitted according to the laws:

$$a_r = r \cdot a_i \tag{6.1}$$

$$a_t = t \cdot a_i \tag{6.2}$$

$$\tag{6.3}$$

where a_r and a_t are respectively the reflected and transmitted field. We have at the interface between the layer i and the layer $i+1$:

$$r_{i \to i+1} = \frac{n_i - n_{i+1}}{n_i + n_{i+1}} \tag{6.4}$$

$$t_{i \to i+1} = \frac{2n_i}{n_i + n_{i+1}} \tag{6.5}$$

where n_i and n_{i+1} are the index of refraction of the two layers.

At each dioptre, the light propagating in both directions recombine. We can describe the relation between the fields at the dioptre between two layers i and $i+1$ by the relation [104]:

$$\begin{pmatrix} a_i^- \\ a_i^+ \end{pmatrix} = \begin{pmatrix} \frac{n_i+n_{i+1}}{2n_i} & \frac{n_i-n_{i+1}}{2n_i} \\ \frac{n_i-n_{i+1}}{2n_i} & \frac{n_i+n_{i+1}}{2n_i} \end{pmatrix} \cdot \begin{pmatrix} a_{i+1}^- \\ a_{i+1}^+ \end{pmatrix} = D_i \cdot \begin{pmatrix} a_{i+1}^- \\ a_{i+1}^+ \end{pmatrix} \tag{6.6}$$

When travelling through a layer the light field experienced a phase shift that depends on the thickness of the layer (e_i) and on the refractive index of the layer (n_i), we have:

$$\delta_i = \frac{2\pi \cdot n_i \cdot e_i}{\lambda} \tag{6.7}$$

with λ being the wavelength of the light.

We have the following relation between the field propagating in the two directions in the layer:

$$\begin{pmatrix} a_i^- \\ a_i^+ \end{pmatrix}_{x_i} = \begin{pmatrix} e^{-j\delta_i} & 0 \\ 0 & e^{-j\delta_i} \end{pmatrix} \cdot \begin{pmatrix} a_i^- \\ a_i^+ \end{pmatrix}_{x_{i+1}} = L_i \cdot \begin{pmatrix} a_i^- \\ a_i^+ \end{pmatrix}_{x_{i+1}} \tag{6.8}$$

where x_i is the beginning of the layer i and x_{i+1} is the end of the layer i, with $x_{i+1} - x_i = e_i$.

Finally the light field passing through the whole stack of n layers is given by the relation:

$$\begin{pmatrix} a_0^- \\ a_0^+ \end{pmatrix} = \begin{pmatrix} M_{11} & M_{12} \\ M_{21} & M_{22} \end{pmatrix} \cdot \begin{pmatrix} a_S^- \\ a_S^+ \end{pmatrix} = M \cdot \begin{pmatrix} a_S^- \\ a_S^+ \end{pmatrix} \tag{6.9}$$

where $a_0^{\pm}$ is the light field entering and leaving at the first layer and $a_S^{\pm}$ is the light field in the substrate. We have:

$$M = D_0 \cdot L_1 \cdot D_1 \cdot L_2 ... L_n \cdot D_n. \tag{6.10}$$

Typically we assume there are no light coming from the substrate ($a_s^- = 0$), the overall reflectivity and transmissivity coefficient of the multilayer coating are then:

$$r = \frac{a_0^-}{a_0^+} = \frac{M_{12}}{M_{22}} \tag{6.11}$$

$$t = \frac{a_S^+}{a_0^+} = \frac{1}{M_{22}} \tag{6.12}$$

The reflection and transmission of the coating are given by:

$$R = \frac{I_0^-}{I_0^+} = r \cdot r^* \tag{6.13}$$

$$T = \frac{I_S^+}{I_0^+} = \frac{n_S}{n_0} t \cdot t^* \tag{6.14}$$

$$\tag{6.15}$$

Using these equations we can compute the reflection and transmission of a coating knowing the thickness of each layer in the multilayer stack and the refractive index of the materials. The response of the multilayer coating depends on the wavelength of the light as the phase shift in each layer and the refractive index of the materials are wavelength dependent. As an example, the figure 6.3 shows the reflectivity of a quarter-wave coating constituted of 9 doublets of layers.

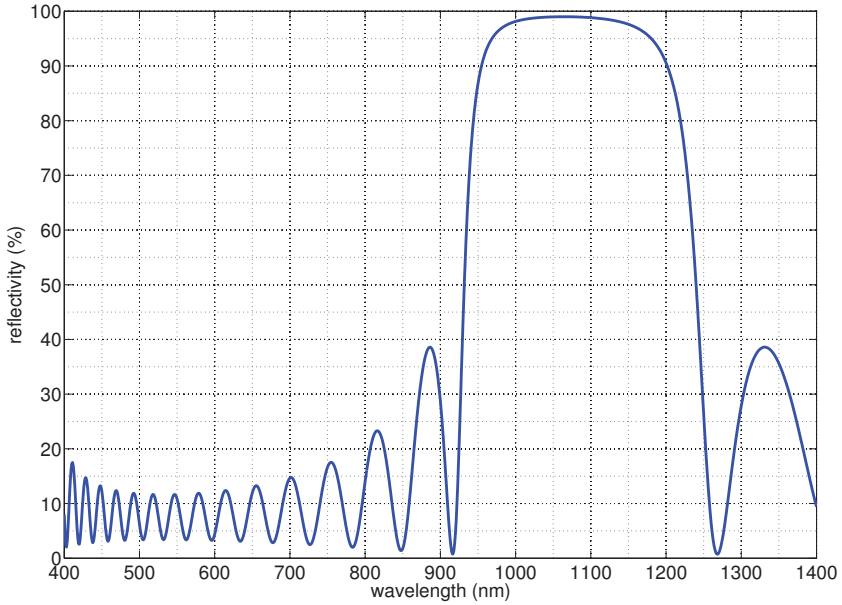

Figure 6.3: Reflectivity of a quarter-wave multilayer coating with 18 layers.

6.3 The Ion Beam Sputtering deposition technique

To deposit the stack of thin film on top of the substrate, a coating machine has been built at LMA in the early 2000s to be able to coat substrate for the gravitational wave detector Virgo [105]. A picture of the coating machine can be seen in figure 6.4. This machine uses the technique of Ion Beam Sputtering (IBS) and is able to coat mirrors over a diameter of approximately 1 m.

In the context of using the mirrors in a Michelson interferometer with Fabry-Perot arm cavities for the detection of gravitational waves it is important that the two input mirrors of the arm cavities have a very good matching in terms of transmission [106]. Indeed, if the transmission is different for the two mirrors it results in an asymmetry between the two arms of the interferometer and thus a larger sensitivity to laser frequency and amplitude noise. In order to obtain mirrors with the best matching in transmission, one has to coat the two substrates at the same time.

The Ion Beam Sputtering technique is described in [107] and the figure 6.5 shows the basic principle of the technique. The coating machine operates under vacuum. By mean of an ion source atoms are sputtered from a target made of the material one wants to deposit on the substrate. Ions are formed from a gas, typically Argon (Ar), in the source and accelerated towards the target. The ions strike the target with an energy of about 1 keV and atoms from the targets are ejected towards the substrate. This yields in a plume of materials

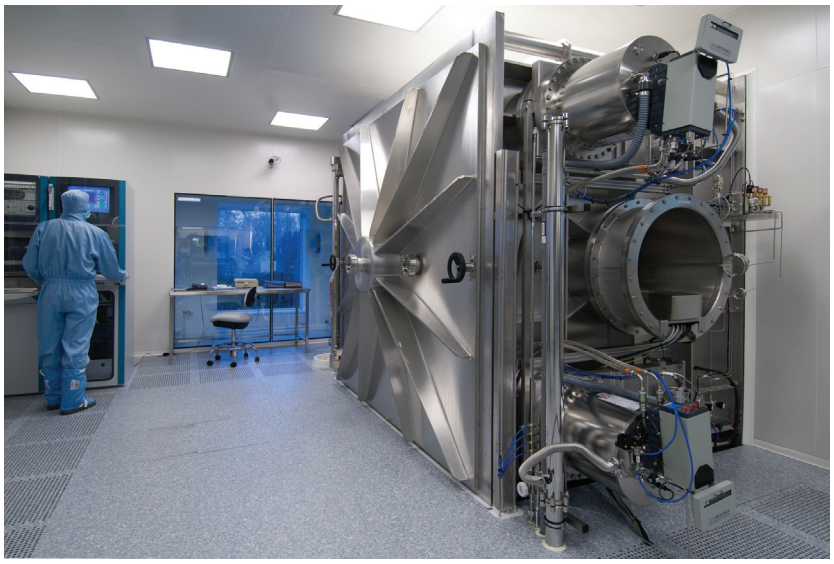

Figure 6.4: The large Ion Beam Sputtering coating machine.

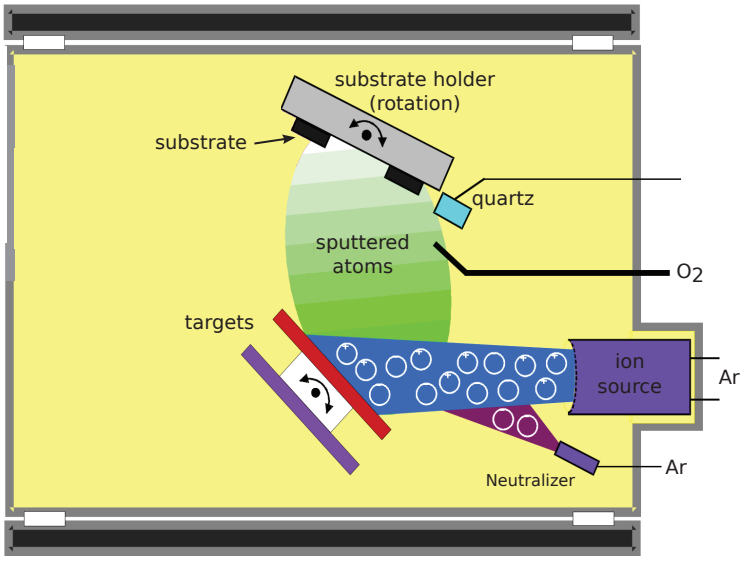

Figure 6.5: The ion beam sputtering technique.

that condense on the substrate. A neutraliser emits electron that permit to keep the ion beam electrically neutral. It avoids the accumulation of electric charges at the surface of the target. The substrate is kept in rotation in order to improve the uniformity of the coating deposition as we will see later. In the large coating machine the system is doubled with two targets of the same materials so that we are able to coat substrates having a larger diameter.

After deposition the mirrors are annealed at a temperature of a few hundreds of degrees. This annealing allows relaxing the stress induced by the coating deposition on the substrate. It also allows to stabilize the refractive index of the deposited materials [105].

Table 6.1: Specification on the high-reflective coating for the aLIGO cavity mirrors (over a 160 mm diameter aperture).

	HR ITM	**HR ETM**
Flatness	< 0.5 nm RMS	< 0.5 nm RMS
Sagitta change	< 8 nm	$<$ 8nm
Zernike terms higher than second order	< 0.5 nm	< 0.5 nm
Transmission at 1064 nm	1.4%	5 ppm $\pm$ 1
Transmission matching	$< 1\%$	-

6.4 Specifications on the coating uniformity for advanced detectors

The *Laboratoire des Matériaux Avancés* is responsible for the coating of the aLIGO arm cavity mirrors. The specifications on the coating uniformity for the input and end test masses are described in table 6.1. On a clear aperture of 160 mm in diameter, the coating shall not change the substrate sagitta by more than 8 nm, that corresponds to an amplitude of 4 nm for the Zernike term Z_2^0. Also the coating shall not add Zernike terms greater than second order with an amplitude higher than 0.5 nm. The specification on the transmission is of 1.4% for the input test masses and 5 ppm for the end test mass. The matching in transmission is defined as $M = 2|\frac{T1-T2}{T1+T2}|$ with $T1$ and $T2$ being the maximum and minimum transmission of a set of two mirrors. M should be smaller than 1% for the ITM.

For Advanced Virgo, the specifications on the coating should be about the same but over a diameter of 150 mm considering that the beams on the ITM and ETM are smaller in Advanced Virgo than in Advanced LIGO. These are very stringent specifications considering that the coating thickness is about 3 µm for the input test mass and 6 µm for the end test mass. It means that the coating uniformity should be typically less than 0.1% peak to valley value.

In the following, we will present the work done at LMA to reach a coating flatness which is compliant with these requirements.

Figure 6.6: Twin mirrors configurations.

6.5 Coating deposition with simple rotation.

6.5.1 Twin mirrors in simple rotation with masking.

The configuration with twin mirrors is used to obtain a very good matching in the transmission of the two mirrors. The two mirrors coated at the same time will have exactly the same coating deposited and so the transmission difference between the two mirrors will be minimal. It is also a gain of time as only one deposition run is needed for two mirrors.

The figure 6.6 shows a picture of the two sample holders used in the twin mirrors configuration. In this configuration the technique of masking is used. It consists in putting a mask in front of the substrate so that part of the materials plume is invisible to the substrates. Adjusting the geometry of the mask allows to obtained a better uniformity in the coating deposition as explained in [108].

Two tests mirrors have been coated, the coating was that of an ITM high-reflective coating for aLIGO with a transmission of 1.4 %. The coating has been deposited on the plane surface (n°2) of the ETM01 and on the curved surface (n°1) of the ETM02. These substrates have been coated as a test because they are made of silica that warps with annealing, i.e. their radii of curvature change and it adds astigmatism on the surfaces.

The surface figures of the two substrates after coating are similar. They have a flatness of about 1.4 nm RMS on a diameter of 150 mm. Figure 6.7 shows the surface figure of the substrate that has been coated on its flat surface (ETM01 surface n°1) on a diameter of 150

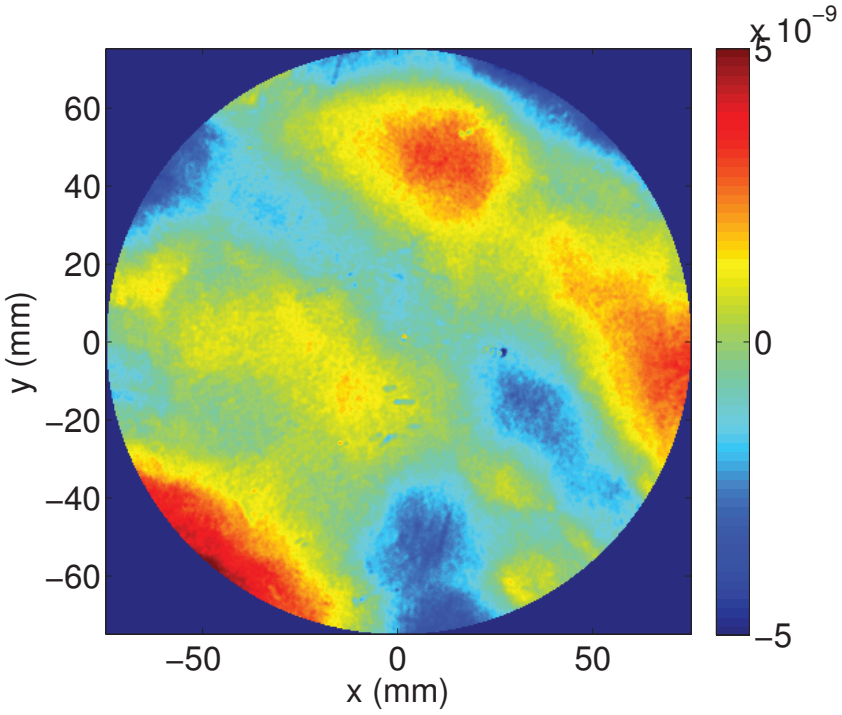

Figure 6.7: Figure of the surface n°2 of ETM01 after deposition of ITM type HR coating (T = 1.4%) with RoC removed.

mm. The radius of curvature of the surface has been removed from the data in the figure. The change of sagitta due to the coating deposition has been estimated by measuring the surface after the coating deposition and without annealing. It has been estimated to be negligible.

The surface figure after the coating deposition has been put into simulation of the Fabry-Perot arm cavity using the FFT code SIESTA to compute the expected round-trip losses induced by such surface. Two cases have been simulated, first the map has been put on the ITM with the ETM mirror remaining perfect, then the opposite has been done (map on ETM, perfect ITM). It has to be noted that only tilt and piston have been subtracted from the surface figure put into the simulation. When the map is used for the input mirror the round-trip losses are about 46 ppm while they are about 100 ppm in the case of the end mirror. These losses are too high in regards of the specification which is 50 ppm for the round-trip losses induce by the surface figures of the two mirrors. And so it is not acceptable to have such kind of the surface figure on the arm mirrors for the Advanced Virgo gravitational wave detector.

It appears that we are at the limit of the achievable coating uniformity with the masking technique and twin mirrors. Thus it has been decided to try another configuration for the coating deposition.

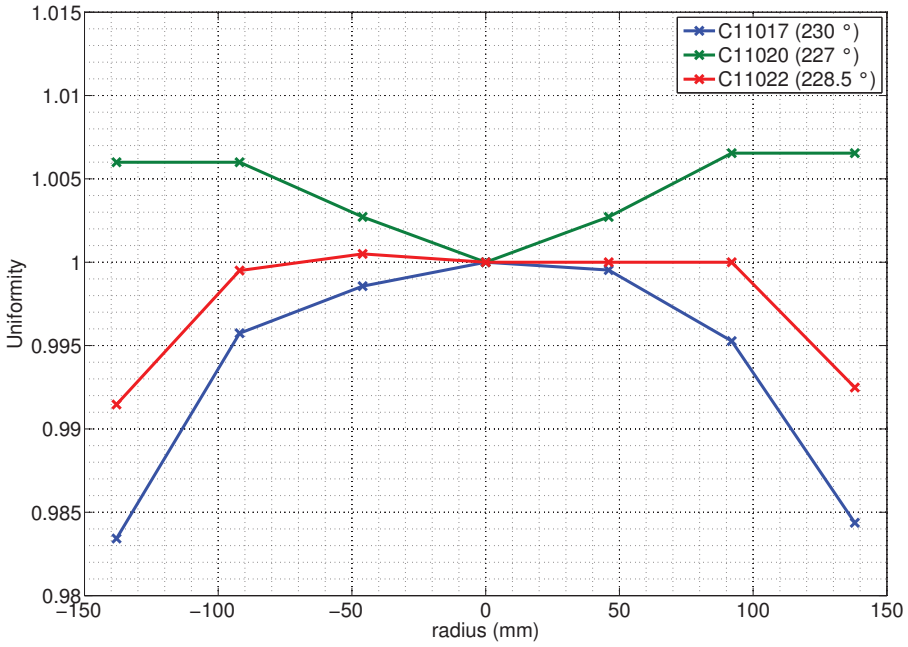

Figure 6.8: Uniformity of tantala monolayer for different target angle.

6.5.2 One mirror in simple rotation.

In order to improve the coating uniformity, the substrate has been placed at the centre of the coating machine with a simple rotation around its center. We did not use a mask in this configuration. In the coating machine we can adjust the angle between the ion beam coming from the source and the target, it modifies the shape of the sputtered materials plume. It permits to adjust and improve the uniformity of the deposited materials.

The figure 6.8 shows linear profiles of the deposition of a monolayer of tantala. To obtain these linear profiles, 1" substrates are mounted onto a fake mirror (made of aluminium). This fake mirror with the small substrates is put in the place of the substrate in the coating machine so that the plane of the 1" substrate will be the same as the full size substrate to be coated. Initially 7 substrates are put on the fake mirror on a radius. The small substrates are placed every 46 mm. Then we modified the fake mirror so that we can place 11 substrates onto the fake mirror. The substrates are then distant of 27 mm, thus permitting to obtain a more accurate coating profile. Finally we deposit the tantala monolayer with the wanted target angle and with the other parameters being the same as for a multilayer coating deposition. After deposition, each substrate is measured with a spectrophotometer. The spectrophotometer measures the transmission of the monolayer as a function of the wavelength in the range 400 to 1400 nm. By fitting the data and knowing the refraction index of the deposited material one can derived the coating thickness [107]. These linear

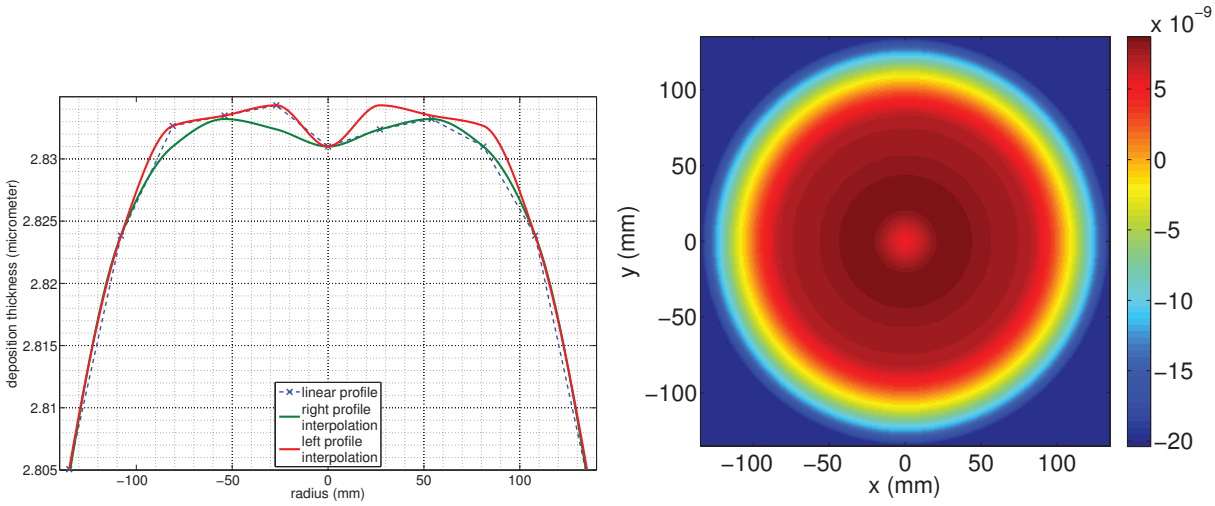

Figure 6.9: Linear profile of HR coating (left) and simulated surface map (right) for the deposition run C11068

profiles allow to adjust the uniformity of the two materials deposited for the multilayer stack. We see an asymmetry in these linear profiles, this asymmetry is not well explained. One hypothesis is that it could be due to the fake mirror which is made of aluminium. It could induce an electric field that modifies the plume shape of the deposited materials.

From these linear profiles we choose the target angles for the silica and the titanium-doped tantala. Then the ITM multilayer coating is deposited on small substrates set onto the fake mirror. This allows checking the uniformity of the coating before the deposition on a real substrate. Many deposition tests have been done with different combination of the silica and tantala target angles. Again we extract the coating thickness on each substrate. From these data, we can simulate the surface figure of the coating. Two coating maps can be simulated with one linear profile using the left or the right part of the profile as the profile are asymmetric. To simulate this surface map, we assume a circular symmetry around the substrate center (because of the substrate rotation) and so we extrapolate the linear profile on every radius of the map. Simulating these coating surface maps allows to compute the expected round-trip losses in the Advanced Virgo arm cavity. As an example the figure 6.9 shows the linear profile of one ITM HR coating and the simulated map from the left part of the profile.

Table 6.2 shows the RTL computed from the simulation of the Advanced Virgo cavity with the simulated coating surface map on the ITM and on the ETM (the opposite map being perfect) along with the target angle for the two materials. We see that even for the same deposition run the round-trip losses induced by the simulated surface can be very different depending on the side of the profile used to simulate the surface map. For example

Table 6.2: Simulated RTL in Advanced Virgo arm cavity with the simulated coating map.

Deposition Run	SiO_2 **target angle**	$Ti : Ta_2O_5$ **target angle**	**RTL (map on ITM)**	**RTL (map on ETM)**
C11029 (left profile)	53°	228.5°	10 ppm	30 ppm
C11029 (right profile)	53°	228.5°	2 ppm	3 ppm
C11055 (left profile)	52.5°	228.5°	37 ppm	118 ppm
C11055 (right profile)	52.5°	228.5°	7 ppm	104 ppm
C11064 (left profile)	53.5°	228.5°	92 ppm	183 ppm
C11064 (right profile)	53.5°	228.5°	100 ppm	80 ppm
C11068 (left profile)	53.5°	229°	128 ppm	74 ppm
C11068 (right profile)	53.5°	229°	3 ppm	12 ppm
C11069 (left profile)	53.5°	229°	83 ppm	34 ppm
C11069 (right profile)	53.5°	229°	11 ppm	121 ppm
C11095 (left profile)	53.4°	229°	135 ppm	97 ppm
C11095 (right profile)	53.4°	229°	49 ppm	91 ppm

the run C11068 give simulated round-trip losses of 202 ppm (summing the losses due to the map on the input mirror and on the end mirror) for the left profile whereas it gives only 15 ppm with the right profile.

6.5.2.1 Circular Zernike polynomials and losses in the Advanced Virgo Fabry-Perot cavity

We can find an explanation to the difference in the round-trip losses for a same profile by looking at the decomposition of the surfaces into Zernike polynomials [93]. Obviously this kind of simulated surfaces only have circular Zernike polynomials because of the circular symmetry hypothesis made in the simulation process. Table 6.3 reports the amplitude of the four first circular Zernike polynomials Z_2^0 (defocus), Z_4^0 (primary spherical), Z_6^0 (secondary spherical) and Z_8^0 (tertiary spherical) for the deposition runs reported earlier. We see that the map simulated with the right profile of the deposition run number C11068 has Zernike terms with smaller amplitudes than the map extracted from the left side of the profile. There is about a factor 3 for the primary and secondary spherical aberrations and 18 for the tertiary spherical aberration. The surface simulated from the right profile is then much more smooth than the one simulated from the left part of the profile. There are no steep gradient on the right profile compared to the left surface as we can see on the left plot of the figure 6.9.

Table 6.3: Zernike polynomials amplitude in the simulated coating map.

Deposition Run	SiO_2 **target angle**	$Ti : Ta_2O_5$ **target angle**	Z_2^0 **(in nm)**	Z_4^0 **(in nm)**	Z_6^0 **(in nm)**	Z_8^0 **(in nm)**
C11029 (left profile)	53°	228.5°	-0.39	-1.14	0.43	-0.08
C11029 (right profile)			-0.86	0.32	-0.15	0.04
C11055 (left profile)	52.5°	228.5°	4.42	-0.16	-0.62	0.37
C11055 (right profile)			4.64	1.20	-0.35	-0.20
C11064 (left profile)	53.5°	228.5°	3.66	-0.32	-0.80	0.73
C11064 (right profile)			3.01	-0.80	-0.66	0.60
C11068 (left profile)	53.5°	229°	-0.44	-0.41	0.71	-0.72
C11068 (right profile)			0.038	-1.10	0.16	-0.04
C11069 (left profile)	53.5°	229°	0.99	-0.81	0.65	-0.53
C11069 (right profile)			0.53	-2.95	0.44	0.076
C11095 (left profile)	53.4°	229°	-0.56	0.23	-0.05	0.56
C11095 (right profile)			-0.17	0.27	-0.33	0.36

What can be observed from these two tables is that the amplitude of the Zernike terms Z_6^0 and Z_8^0 seems to be linked to the round-trip losses in the Advanced Virgo arm cavity. Figure 6.10 shows the sum of the expected round-trip losses in the Advanced Virgo cavity with the surface figure map on the input mirror and on the end mirror as a function of the absolute amplitude of each circular Zernike term. From top left to bottom right are plotted the round-trip losses as a function of the absolute amplitude of the Z_2^0, Z_4^0, Z_6^0 and Z_8^0. We see no pattern relating the losses in the cavity with the Zernike terms Z_2^0 and Z_4^0. It appears to be random and the surfaces that gives RTL out of the specifications are because of the Z_6^0 and Z_8^0 term. We can say that the Zernike terms $Z_2^0$and Z_4^0 have a minor impact on the losses inside the Advanced Virgo cavity in the amplitude range simulated (up to 3 nm for Z_4^0 and up to 5 nm Z_2^0).

For the Z_2^0 terms, it can be explained easily. Its effect is to change the radius of curvature of the mirrors. For example a Z_2^0 term with an amplitude of 5 nm over a diameter of 150 mm will shift the RoC of the ITM by only 7 m and the RoC of the ETM by about 10 m. Modifying the RoC of the mirrors changes only the mode parameters of the field circulating inside the cavity from the theoretical one but it remains a TEM_{00} mode. Despite that it does not induce large round-trip losses in the cavity it can be a problem in regards of the RTL projected on the theoretical TEM_{00} and of the contrast defects. Indeed if the two cavities modes are shift in a non symmetric way, it will result in a larger contrast defects as the two beams recombining will be different. The change of sagitta of the mirrors should be kept small also in order to avoid the excitation of high order modes in the cavity [109].

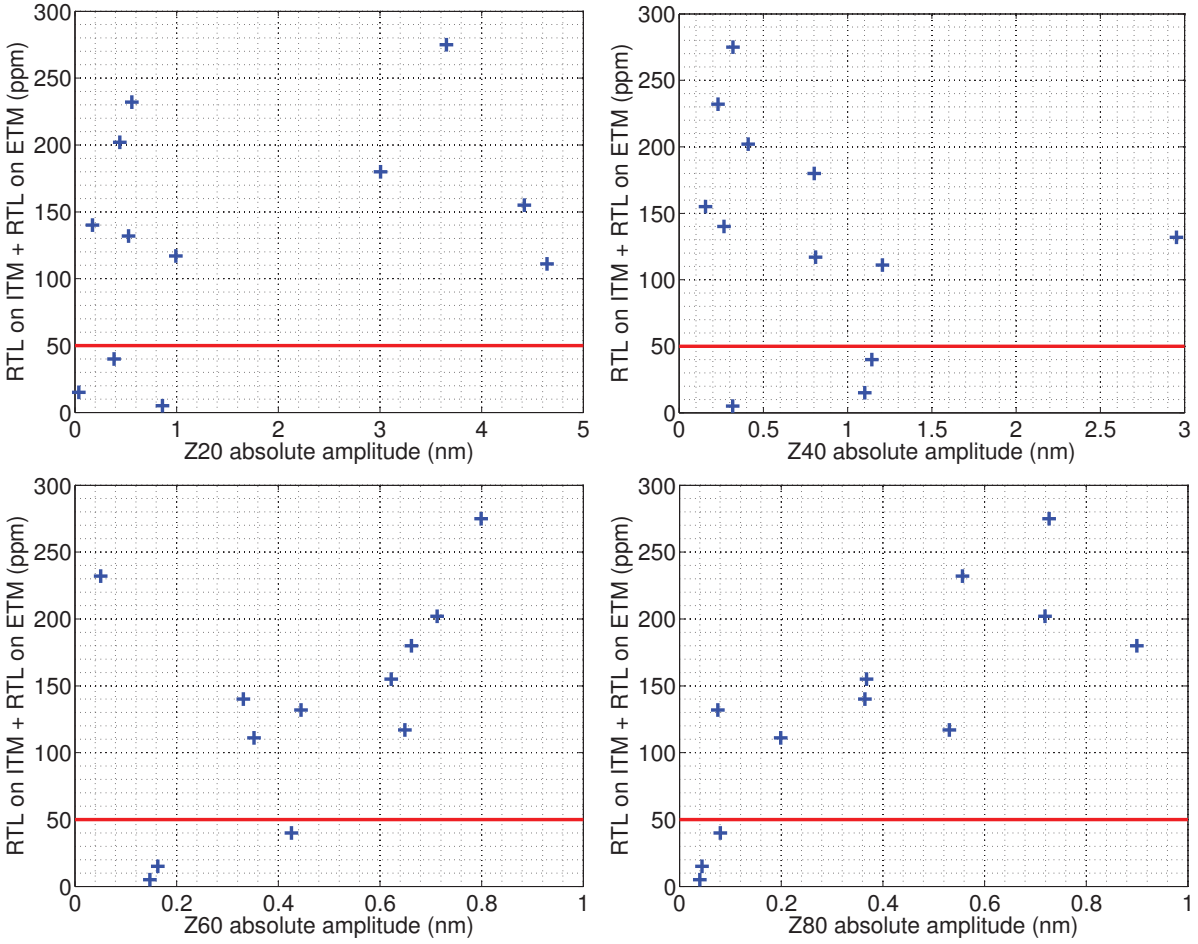

Figure 6.10: Sum of the round-trip losses in the Advanced Virgo arm cavity with the surface map on ITM and ETM (in ppm) as a function of the absolute amplitude of the Zernike polynomial (in nm) Z_2^0 (top left), Z_4^0 (top right), Z_6^0 (bottom left) and Z_8^0 (bottom right). The red line shows the 50 ppm limit.

On the contrary looking at the secondary and tertiary spherical aberration in the figure 6.10 we can see a trend in the data. It appears that the presence of secondary and tertiary spherical aberrations on the mirror surface figure induces a lot of the round-trip losses in the arm cavity. Indeed if normalised on a diameter of 150 mm, the Z_6^0 and Z_8^0 polynomials creates a "W" shape with a bump having a steep slope in the central area of the mirror where the laser power is large.

To understand the effect of the spherical aberrations (Z_p^l with $l = 0$) we simulate surfaces having Zernike polynomials Z_4^0, Z_6^0 and Z_8^0 normalised over a diameter of 150 mm with an amplitude range of -1.5 nm to 1.5 nm. The surface maps generated contain only one Zernike polynomial and it must be kept in mind that the combination of different Zernike aberration could result in a different behaviour of the cavity. The surface maps are put into simulations

of the Advanced Virgo FP arm cavity on the ITM with the opposite surface being perfect and then on the ETM with the opposite surface being perfect. We compute the round-trip losses in the cavity and we look at the high order mode contents of the field inside the cavity. It is interesting to look at the high order modes content of the field inside the cavity as it can result in a larger contrast defect at the output port of the interferometer. The results of the simulations in terms of round-trip losses an high order modes content are shown in the figure 6.11.

At the time of writing, there are no specifications on the HOM content of the field circulating in the arm cavities. As one can see from appendix B, the HOM content of the field recombining at the dark fringe should not be critical after the output mode cleaner. Indeed it would require about 4000 ppm in the HOMs in the reflected field from the arm cavities to result in 10 mW of laser power at the dark port. It is small compared to the foreseen detuning that gives 80 mW of power at the dark port. However before the OMC, a HOM content of 400 ppm in the field recombining at the dark port leads to about 490 mW of power on the dark fringe. The content in the HOM of the field at the dark port is due to the asymmetry of the beams reflected from the two cavities. Considering that the two cavities should be close one to each other, the HOM of the two reflected fields can interfere destructively at the dark port, even though probably not entirely. It should be considered also that the HOM content of the reflected field from a Fabry-Perot cavity is four times the one of the field circulating in the cavity. Having 490 mW of power at the dark fringe is compatible with the functioning of the interferometer. Thus we can estimate that the HOM content of the field circulating in the arm cavities should be less than 100 ppm. It should allow to limit the contrast defects due to the higher order modes excited in the arm cavities.

We see that the Zernike polynomial Z_4^0 on the input mirror surface induces negligible round-trip losses in the Fabry-Perot arm cavity. The end mirror surface is on the contrary sensitive to the primary spherical aberration with round-trip losses larger than 25 ppm (RTL specification per mirror) for an amplitude of the Zernike term about -1.3 nm and larger than 1.5 nm. On the input mirror, the primary spherical does not induce a large amount of high order modes inside the cavity either as it is always smaller than 15 ppm for an absolute amplitude smaller than 1.5 nm. It is very different on the end mirror as it induces quite a large amount of high order modes in the cavity with about 150 ppm for an absolute amplitude of 1.5 nm.

The secondary spherical aberration Z_6^0 yields to quite a lot of round-trip losses in the cavity. Indeed the round-trip losses become higher than the 25 ppm limit for an amplitude of about 0.9 nm. We notice that the input mirror surface is a bit more sensitive to a Z_6^0 with a negative amplitude. It is the contrary for the end mirror surface. We see that in

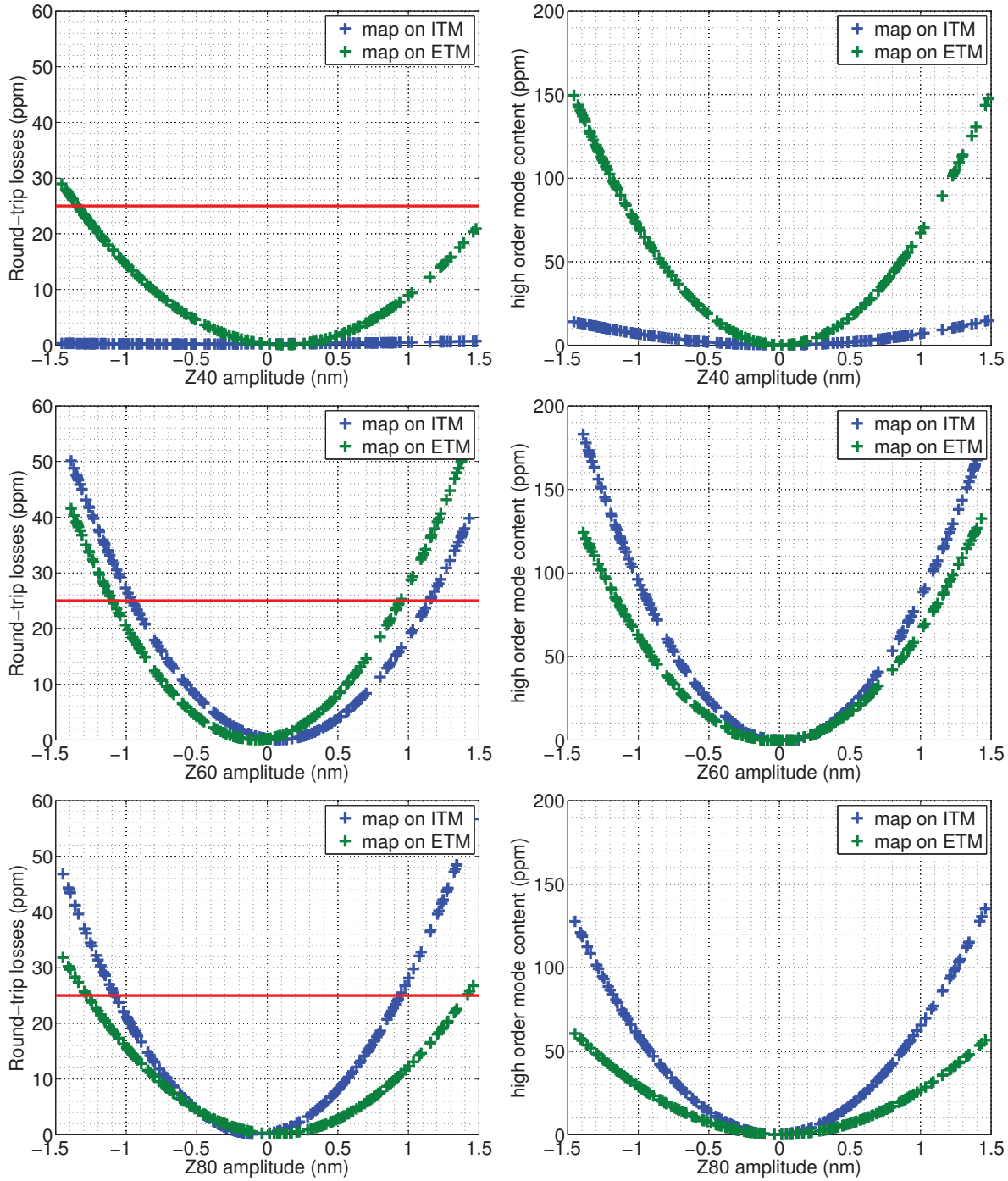

Figure 6.11: Round-trip losses and high order mode content in the Advanced Virgo arm cavity with the surface maps on the ITM (blue) and on the ETM (green). The left column shows the RTL (in ppm) as a function of the amplitude of the Zernike polynomial (in nm) Z_4^0 (top), Z_6^0 (middle) Z_8^0 (bottom), the red line shows the 25 ppm limit. The right column shows the high order mode content of the field circulating in (in ppm) as a function of the amplitude of the Zernike polynomial (in nm) Z_4^0 (top), Z_6^0 (middle) Z_8^0 (bottom).

the amplitude range tested the secondary spherical can induce up to about 190 ppm of high order modes on the input mirror. In contrary to the primary spherical aberration, the input mirror is more sensitive to the secondary spherical aberration as it yields to a larger amount of HOMs and larger round-trip losses in the Advanced Virgo arm cavity.

Concerning the tertiary spherical aberration Z_8^0, we see that the RTL are a bit smaller than for the Z_6^0 term. The Z_8^0 amplitude should be contained between -1.2 nm and 1.3 nm for the end mirror surface and between -1 nm and 0.9 nm for the input mirror surface in order to have less than 25 ppm of RTL per mirror. The amount of high order modes generated by this aberration is also a bit smaller than for the two other Zernike terms studied (except for the primary spherical on the ITM). In the amplitude range studied (-1.5 nm to 1.5 nm) we have less than 140 ppm and 60 pmm of HOMs induced by the tertiary spherical aberration respectively on the input mirror and on the end mirror. Again we see that the input mirror surface is more prone to provoke round-trip loss and to excite HOMs in the Advanced Virgo FP cavity. This is presumably due to the difference in the beam size at the input and end mirror. The bigger beam on the end mirror seems to be less sensitive to the small bump (in diameter) induced by the Z_8^0 polynomial.

More generally the amount of RTL seems to be related to the amount of HOMs in the cavity. It can be explained as follows, the HOMs excited inside the cavity are much more likely to be clipped by the mirror (because of the physical dimension of the mirrors) than the TEM_{00} mode because HOMs extend on a larger diameter.

In conclusion, we can say that the specification on the Zernike polynomials defined by aLIGO (amplitude smaller than 0.5 nm) allows to limit the round-trip losses and the amount of high order modes circulating inside the cavity. Indeed we see that for an amplitude of the Zernike terms smaller than 0.5 nm it yields to less than 10 ppm of round-trip losses per mirror in any of the cases we studied . The amount of HOMs is also limited to less than 25 ppm. These are quite small values and it seems wise to adopt the same specification for the Advanced Virgo arm mirror surface even if it should be taken with great care. These simulations also outlined the fact that the input mirror and end mirror surfaces are not sensitive to the same aberrations. For example primary spherical aberration induce very negligible round-trip losses in the cavity when on the input mirror surface. Contrarily the tertiary spherical aberration yields to more cavity losses when on the input mirror than when on the end mirror. This specificity of the mirror surfaces should be taken into account.

Also it is important to note that the simulations performed have been done for only one Zernike term at a time. The combination of different Zernike polynomials is complex and not straightforward. The round-trip losses induce by a surface being the sum of a few prominent Zernike terms cannot be taken as the sum of the round-trip losses induce by

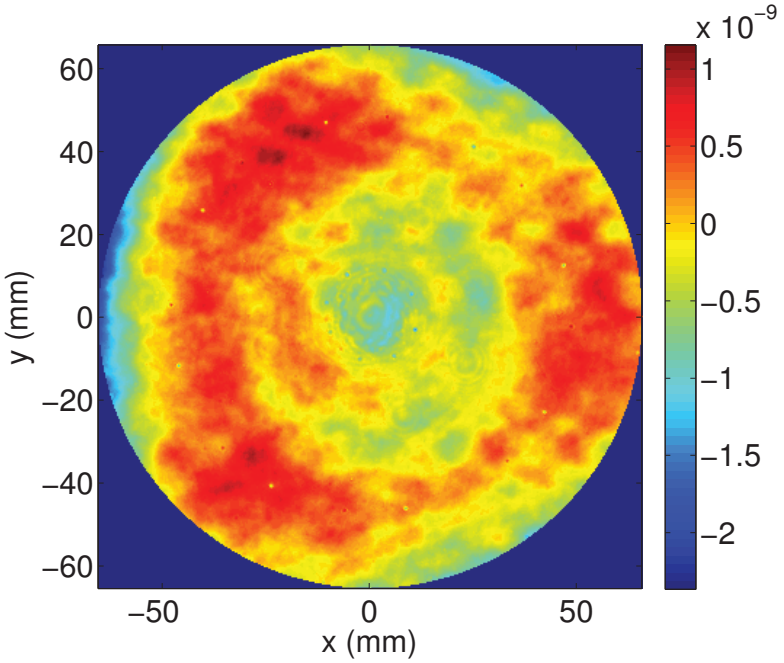

Figure 6.12: Surface figure of ETM04 surface n°1 (curved) after deposition of ITM-HR coating measured over a diameter of 150 mm measured at Caltech [110]. Piston, tilt, RoC and astigmatism removed.

different surfaces with each of the prominent Zernike terms. In other words, a surface with Zernike terms compliant with the aLIGO specification can induce large round-trip losses (right profile of C11095 for example) whereas a surface which is not compliant with the specification can induce only a few round-trip losses (left profile of C11095 for example). At the end, what matters is the overall surface figure of the mirror and not only the individual Zernike terms. The specification on the Zernike term is a good tool to limit the risk of having a lossy surface but it should only be used as a tool and not as a rule to follow blindly.

6.5.2.2 Experimental results on full size substrate

The first substrate to be coated with an HR-ITM coating was the substrate ETM04. It was coated on its curved surface (n°1) and it has been measured at Caltech [110]. Figure 6.12 shows the surface figure after deposition of the multilayer coating in simple rotation with piston, tilt, RoC and astigmatism. It has a flatness of 0.42 nm RMS on a diameter of 150 mm and a peak to valley value of 3.5 nm. We see that the surface on a diameter of 150 mm is mainly dominated by three Zernike terms. The prominent Zernike terms are; a coma in x (Z_3^1) with an amplitude of 0.45 nm, a trefoil in X (Z_3^3) with an amplitude of 0.65 nm and a primary spherical (Z_4^0) with an amplitude of -0.56 nm. The Zernike terms Z_3^3 and Z_4^0 are not compliant with the aLIGO specification.

Table 6.4: Substrate coated with an HR-ITM coating, surface figure over a diameter of 150 mm.

Substrate	**Sagitta change (in nm)**	**flatness - RoC, astigmatism**	**Predominant Zernike term**
ETM04 surface 1	-30.8 nm	0.42 nm RMS	$Z_3^1 = 0.45$ nm $Z_3^3 = 0.65$ nm $Z_4^0 = -0.56$ nm $Z_5^{-1} = -0.11$ nm
ETM05 surface 1	-27 nm	0.32 nm RMS	$Z_3^{-1} = -0.16$ nm $Z_3^{-3} = 0.13$ nm $Z_4^0 = -0.47$ nm $Z_4^2 = -0.14$ nm $Z_6^4 = -0.14$ nm $Z_8^0 = -0.12$ nm
ITM04 surface 1	1.4 nm	0.24 nm RMS	$Z_2^2 = 0.12$ nm $Z_3^1 = 0.11$ nm $Z_4^0 = -0.39$ nm $Z_4^2 = -0.10$ nm

We put this surface map with the radius of curvature and astigmatism removed into a simulation of the Advanced Virgo Fabry-Perot arm cavity. We found that the round-trip losses are 4.4 ppm with the map on the ITM and 5.2 ppm with the map on the ETM. It is interesting to see that even with a surface figure which is not compliant with the specification on the coating uniformity the round-trip losses remains in the Advanced Virgo budget loss (i.e. less than 25 ppm per mirror).

Three substrates have been coated with an HR-ITM coating and measured at the time of writing. They have been coated in the configuration with one mirror at a time in simple rotation and have been measured at Caltech by the LIGO team [110, 111, 112]. Table 6.4 reports the values of the RMS flatness on 150 mm as well as the sagitta change and some of the predominant Zernike terms in the surface figures. The flatness value reported is with the radius of curvature and astigmatism removed from the data. Only the Zernike terms with an absolute amplitude larger than 0.1 nm are reported in the table. The round-trip losses induced by the surface figure in the Advanced Virgo arm cavity are also reported both with the map on the ITM and on the ETM.

The two first HR-ITM coating have been done on ETM type substrates made of bad silica that warps with annealing. For these two substrates we see that the sagitta change is very large, this is due to the annealing process. The sagitta change reported here is not significant of the coating process for the substrates ETM04 and ETM05. The comparison of

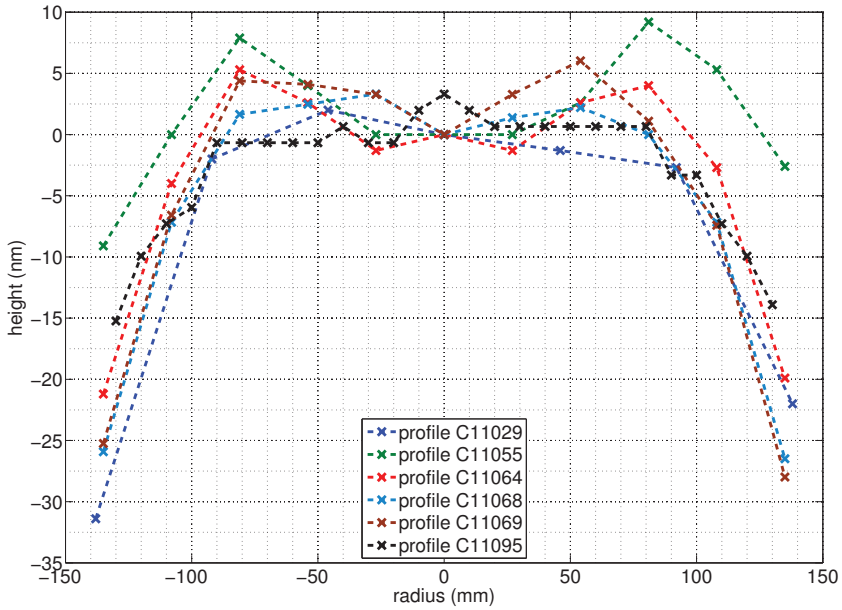

Figure 6.13: Profiles extracted from deposition on small substrates.

two measurements done at LMA before and after coating shows that the change of sagitta is of -2.6 nm for the ETM04 coating. The RoC of the ETM05 is found to be unchanged after coating with the uncertainty measurement. We see that for the coating on the substrate named ITM04 (which does not warp with annealing) the sagitta change is well within the aLIGO specification with a change of only -1.4 nm. Concerning the astigmatism, we only reported in the table the astigmatism for the coating on the ITM04 as we know it is not induce by the annealing process on the contrary of the two other mirrors. The astigmatism measured by the polishing company on the substrate ITM04 before coating was of 0.12 nm, it is now 0.16 nm. As expected the astigmatism induced by the coating deposition is very small because of circular symmetry of the process. We also notice that the highest Zernike terms in the surface figure are the ones with a circular symmetry. This is particularly true for the coating on the ITM04 where we are confident that there are no deformations due to annealing process.

Figure 6.13 compares the deposition test profiles reported in tables 6.2 and 6.3. The different depositions have been done with different target angles and on small substrates except for the run C11095 which has been done on a disk of glass having a diameter of 310 mm and measured along a radius. We notice that the profile are not symmetric, this is probably due to the fake mirror that induce an electric field that modifies the plume shape locally as explained earlier. There is also an uncertainty in the measured thickness that does not allow us to know the thickness deposited very precisely. This is true especially at the center where the thickness changes by less than 0.1 % (i.e. 3 nm). Anyhow the technique

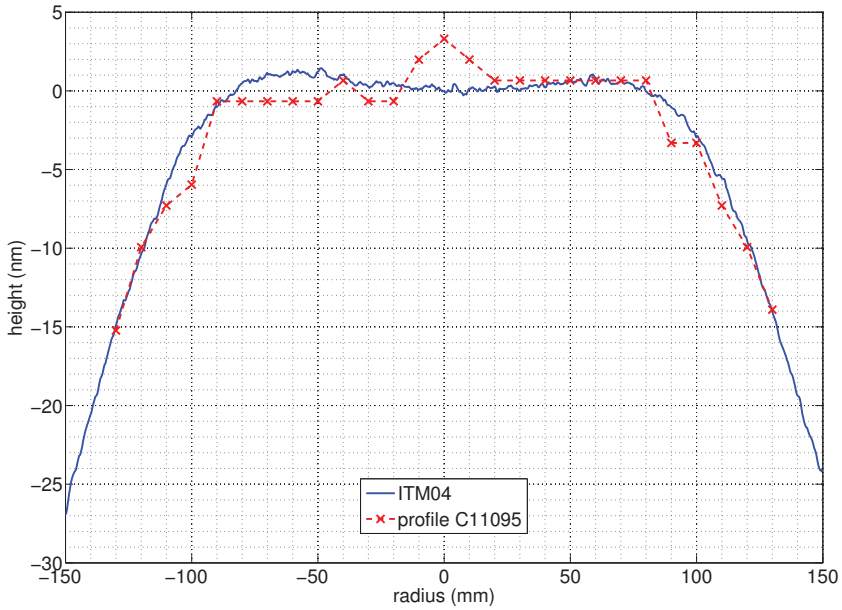

Figure 6.14: Radius profile of ITM04 after coating deposition and profile obtained from a deposition on a disk of glass with the same target angles.

allows having an estimate of the coating uniformity. To know the coating uniformity with a high precision one has to coat a real substrate.

In the figure 6.14 we show the profile in the x direction of the ITM04 after coating and the deposition test profiles done with the same target angles and parameters (C11095). The run C11095 has been done on a disk of glass and measured along a radius. We see that the profile C11095 fits quite well the profile of the coating deposited on a real substrate except at the center where we see a bump. The uncertainty on the measurement of the thickness explains the bump. We see that the profile of the ITM04 has a smaller peak to valley than the profiles of the deposition test in the central region. Generally the lower losses obtained in the Advanced Virgo cavity with the real coating compared to the simulated one can be explained by the smoother shape of the real coating compared to the profiles obtained the small sample.

Finally the round-trip losses induced by these surface figures are reported in table 6.5 along with the high order mode content of the field circulating inside the cavity. The HR-ETM coating is simulated as 2 times the surface figure of the HR-ITM coating because it is twice as thick. The cavity is simulated with the surface map on the input mirror, on the end mirror and with twice the map on the end mirror. We see that the RTL are always within the Advanced Virgo loss budget as they are smaller than 25 ppm per mirror even when the surface is doubled to simulate the HR-ETM coating. In that last case, we are at the very limit of the acceptable losses. The round-trip losses induce by coating are compliant with

Table 6.5: Round-trip losses and HOM content in the Advanced Virgo cavity with surface figure of the coated substrate :with an HR-ITM coating.

Substrate	**RTL**			**HOM**		
	ITM	**ETM**	**2 × ETM**	**ITM**	**ETM**	**2 ×ETM**
ETM04	4.3 ppm	5.1 ppm	20.8 ppm	205 ppm	273 ppm	1483 ppm
ETM05	6.4 ppm	6.0 ppm	23.8 ppm	76 ppm	125 ppm	621 ppm
ITM04	3.5 ppm	3.3 ppm	11.7 pmm	8 ppm	19 ppm	117 ppm

the Advanced Virgo loss budget. It is true even if some of the Zernike terms present in the surface figure are higher than the 0.5 nm limit set by LIGO. It reinforce the statement that the specification on the Zernike terms should be taken with some flexibility.

Anyhow, we see that in some cases the HOM content of the field circulating in the FP cavity is very large compared to the maximum 100 ppm wanted, especially for the simulated HR-ETM coating where it is already about 120 ppm in the best case. Then we need to coat the end mirror with a better uniformity in order to avoid this large amount of high order mode in the cavity.

6.6 Coating with planetary motion of the substrates

6.6.1 Principle of the planetary motion

We have seen previously the limit of the coating deposition with a single rotation in terms of coating uniformity both for twin mirrors with masking or for the configuration with one single mirror at the center of the coating machine. Especially for the end mirror coating where the coating thickness is twice that of the input mirror coating. What appears as a solution to improve the uniformity is the implementation of a planetary motion of the substrates inside the coating chamber.

Figure 6.15 shows a scheme of the planetary motion system. The point O is the center of the planetary system, the center of the substrate is at the point P and the point S represents a point on the substrate. Equations 6.16 and 6.17 describe the coordinate of the point S in polar coordinate:

$$\overline{OS} = \sqrt{d^2 + r^2 + 2dr\cos\left(\omega_s \cdot t + \Phi_s\right)} \tag{6.16}$$

$$\widehat{Ox, OS} = \arctan\left(\frac{\sin\left(\omega_s \cdot t + \Phi_s\right) \times r}{d + \cos\left(\omega_s \cdot t + \Phi_s\right) \times r}\right) + \omega_p \cdot t + \Phi_p \tag{6.17}$$

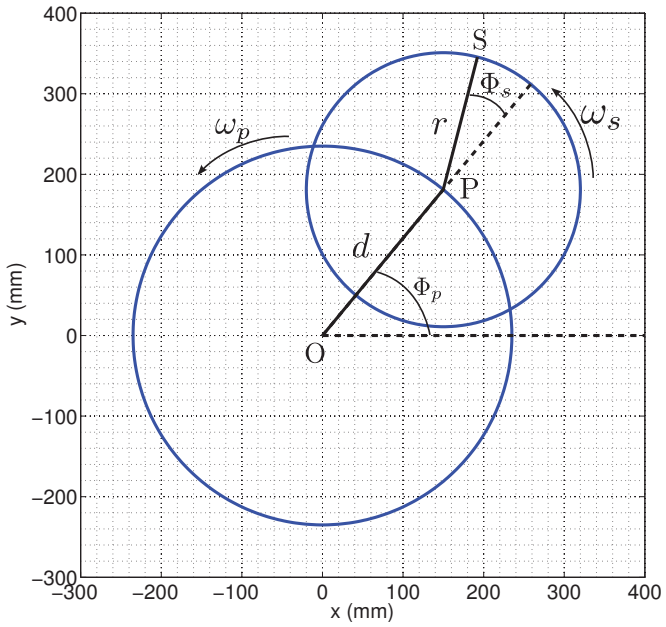

Figure 6.15: Parameters of the planetary motion.

with t being the time, ω_s and ω_p the angular velocity of the satellite and of the planet. Φ_s and Φ_p are the position at $t = 0$.

On the system there are two substrates located on both sides of the center of the system (O). There are three parameters to choose for a planetary motion system, the distance of the planet from the center of the system (d), the angular velocity of the planet ω_p and the ratio between the angular speed of the planet and the satellite; $\frac{\omega_p}{\omega_s}$. In the system studied at LMA, we have $d = 235\ mm$, $\omega_p = 2\ rpm$ (rotation per minute) and $\frac{\omega_s}{\omega_p} = \frac{158}{31}$. The angular velocity of the planet has been set to 2 rotation per minute because it is the angular velocity of the actual system. Thus we can use the motors already in use in the simple rotation system. The ratio of the two angular velocities has been set to $\frac{158}{31}$ because of the mechanical and space constraints [113].

The planetary motion of the substrates allows to improve the coating uniformity by increasing the numbers of locations seen by each point on the substrate and so averaging the quantity of materials deposited on each point. Figure 6.16 shows the trajectory inside the coating chamber of a point located at 80 mm from the center of the substrate with the planetary motion during a period of the planetary motion. We can see that this part of the substrate travels on a high number of positions on the plane where the substrate intercept the sputtered materials. The period of the system is 930 seconds with the actual parameters. It is important that the period of the planetary motion is smaller than the deposition duration of a layer. Indeed a deposition having an incomplete period degrade the uniformity of the deposition [114]. In the case of the ITM-type coating the duration of

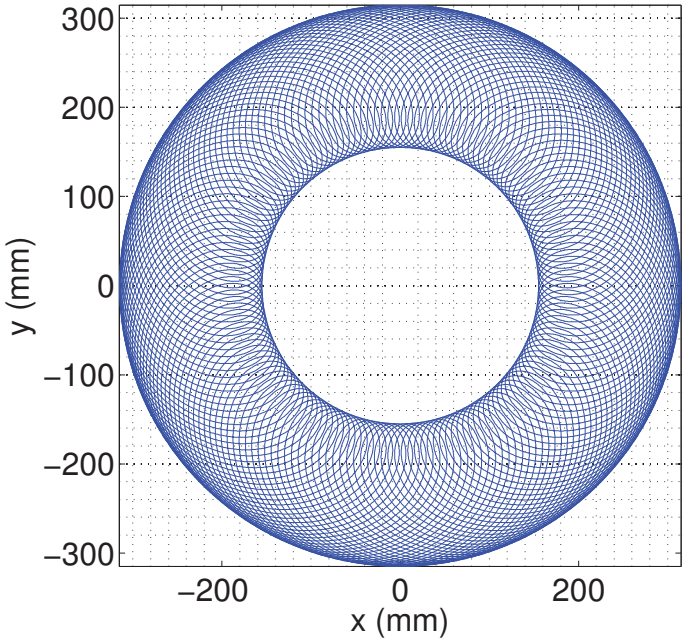

Figure 6.16: Trajectory of a point located at 80 mm of the substrate center with the planetary motion during one period.

deposition of a silica layer is between 5 and 6 times the period of the planetary motion. It is about 2.7 times the system period for the tantala layers. Despite the fact that the number of period is not a multiple of period, the combination of several layers should provide a sufficiently uniform coating. Another advantage with the planetary motion is that we are able to coat two mirrors at the same time and so we can obtain a very good matching in the transmission of the two mirrors.

Finally we simulate the deposition of the multilayer coating both for the aLIGO ITM and ETM highly reflective coating using the deposition time of actual runs and the model of the plume shape. In the following sections we will describe the modelling of the plume shape for the two materials (silica and tantala). The results of the simulation in terms of coating flatness for the configuation with planetary motion are presented thereafter. The effect on the round-trip losses in the Advanced Virgo arm cavity is also simulated with the surfaces obtained by the simulation.

6.6.2 Modeling the plume shape of the deposition

To be able to simulate the coating deposition inside the coating chamber we have to model the plume shape of each materials when sputtered towards the substrate. The technique used to model the plume shape is derived from [115].

To do so we deposit materials on an aluminium plate which is kept still during the

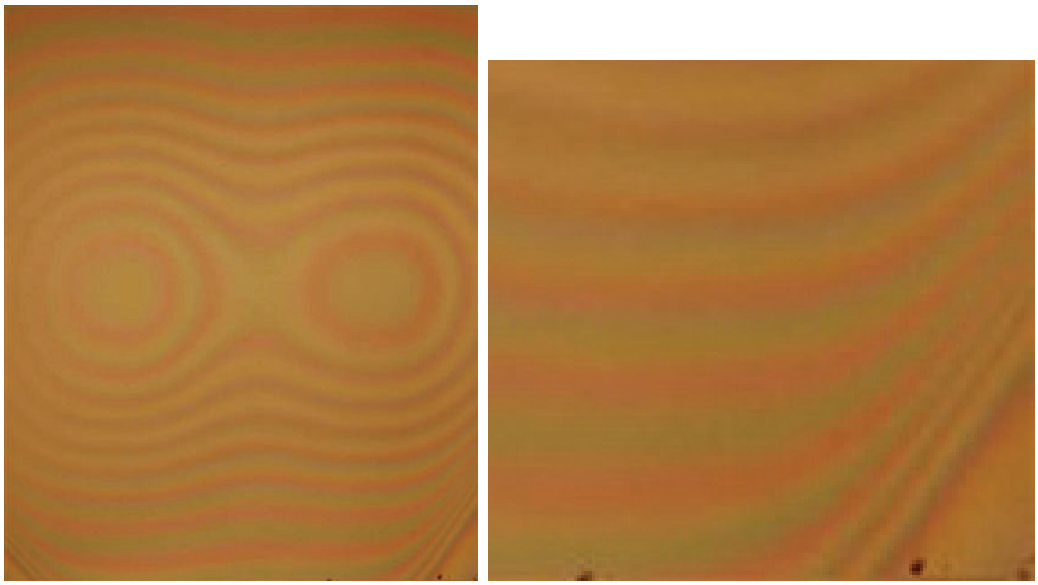

Figure 6.17: Aluminium plate with a static deposition of silica (left) and zoom on the masked region (right).

deposition. The deposition takes several hours in order to make the deposition visible to the human eye. The plate is set at the exact plane of the substrate surface to be coated. Then we take a picture of the aluminium plate with materials deposited on it as we can see in the left picture of the figure 6.17. On the picture one can see that the bottom right corner of the plate has no deposition because it was masked during the deposition process. The right picture in figure 6.17 is a zoom on this corner. Starting from the corner we can start to count the fringes given that between two fringes of the same colour there is a difference of thickness of $\frac{\lambda}{2}$ with λ being the wavelength of the colour of the fringes. The fringes can be seen as isothickness curves. The picture taken has three colour channels red, green and blue. We decompose the picture in this three channels and we count the fringes in the green and red channels. We do not use the blue channel because it is too noisy and it becomes difficult to clearly distinguish the fringes. Knowing the thickness of the deposition, we can model the deposition height on the whole aluminium plate. We model the deposition height using the data extracted from the green and red channel by a function with two Gaussian functions adjusting their parameters. The modelling function is:

$$f = \frac{1}{2\pi\sigma_{x1}\sigma_{y1}} \exp\left[-\left(\frac{(x-x_{01})^2}{2\sigma_{x1}^2} + \frac{y^2}{2\sigma_{y1}^2}\right)\right] + \frac{A}{2\pi\sigma_{x2}\sigma_{y2}} \exp\left[-\left(\frac{(x-x_{02})^2}{2\sigma_{x2}^2} + \frac{y^2}{2\sigma_{y2}^2}\right)\right] \tag{6.18}$$

There are 7 parameters to be adjusted, the positions on the x-axis of the center of the gaussian (x_{01} and x_{02}), the spreads of the gaussians in the x and y direction ($\sigma_{x1},\ \sigma_{y1},\ \sigma_{x2}$

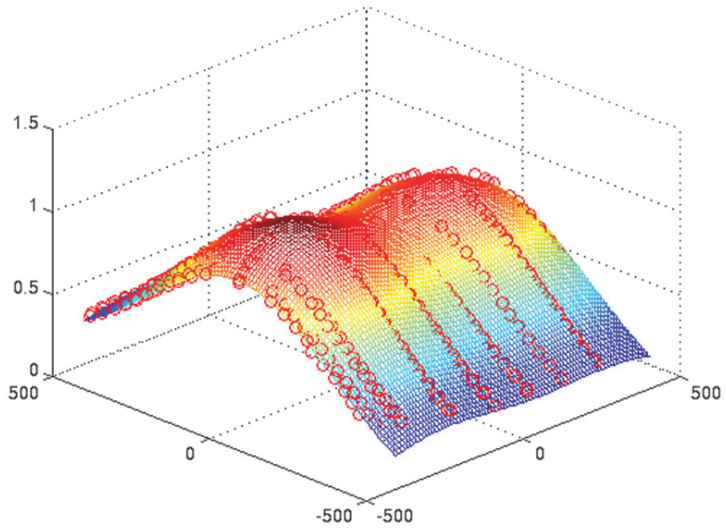

Figure 6.18: Modelisation of the plume of the sputtered silica.

and σ_{y2}) and the amplitude of one of the gaussian (A) given that we normalized the function afterwards.

Figure 6.18 shows the data points extracted from the pictures along with the modelling of the plume shape for the silica deposition. The plume shape of the sputtered materials for the two materials, tantala and silica, have been modelled. These models are then used in the simulation of the coating deposition with planetary motion.

6.6.3 Simulation of the coating deposition with planetary motion of the substrate

6.6.3.1 Principle of the simulation

To simulate the multilayer coating deposition, we compute the trajectory of different points on the substrate, typically separated by 1 mm in both x and y direction, during the deposition time of each layer. We also take into account the time when there are no deposition between the layers due to the change of target. The deposition time of each layer of silica and tantala used in the simulation is the one of the real coating deposition run C11012. During this run, 2 substrates were coated in the twin mirrors configuration with masking. A high reflective ITM-type (with a transmission of 1.4 %) was deposited during this run. We assume that the coating deposition time will be about the same in the planetary motion configuration.

Then we sum the amount of deposited materials on this trajectory using the plume shape model of each materials for each layer of the multilayer coating. We sum the overall coating thickness to obtain the final surface figure. In the two mirrors configuration a mask is set

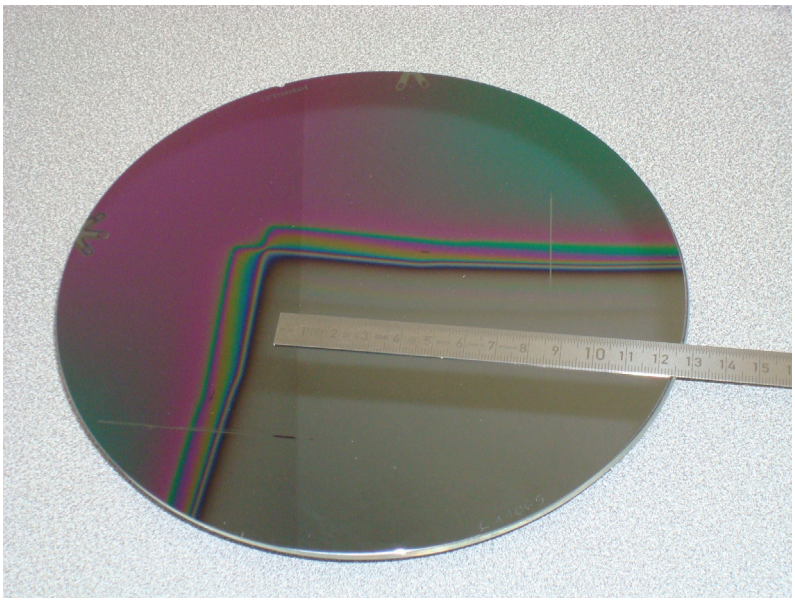

Figure 6.19: Silicon wafer coated with silica. The wafer has been partly masked during the coating deposition.

in front of the rotating substrate so that part of the materials plume shape is invisible to the substrates. This technique of masking is well-known to improve the uniformity of the coating deposition [108]. It is usually used with a simple rotation of the substrates but it can be used equally with a planetary motion. It is important to note that the masks used in the simulation are not optimized for the planetary motion and so the results shown here could be improved by adjusting the mask geometry.

The mask is placed a few centimetre in front of the substrates and so there is a shadowing effect. That is to say there is a transition between the region where the coating is maximal and the region where there is no deposited materials. We are interested in the width of this transition region. Thus to evaluate this shadowing effect we made a static deposition of silica on a silicon wafer in the coating machine with the mask. The mask was placed in front of the silicon wafer which was put in the deposition plane of the substrates. The figure 6.19 shows the silicon wafer with silica deposited on it. We can identify the different regions with the reflection of the light. The uniform coloured region is where the coating deposition is mostly uniform, the grey region is the part that was masked during the coating deposition. The fringes are due to the gradient in the coating thickness between the two regions. The average width of the transition region is 13 mm. This shadowing effect has been taken into account into the simulation by applying a linear slope between the masked and unmasked regions.

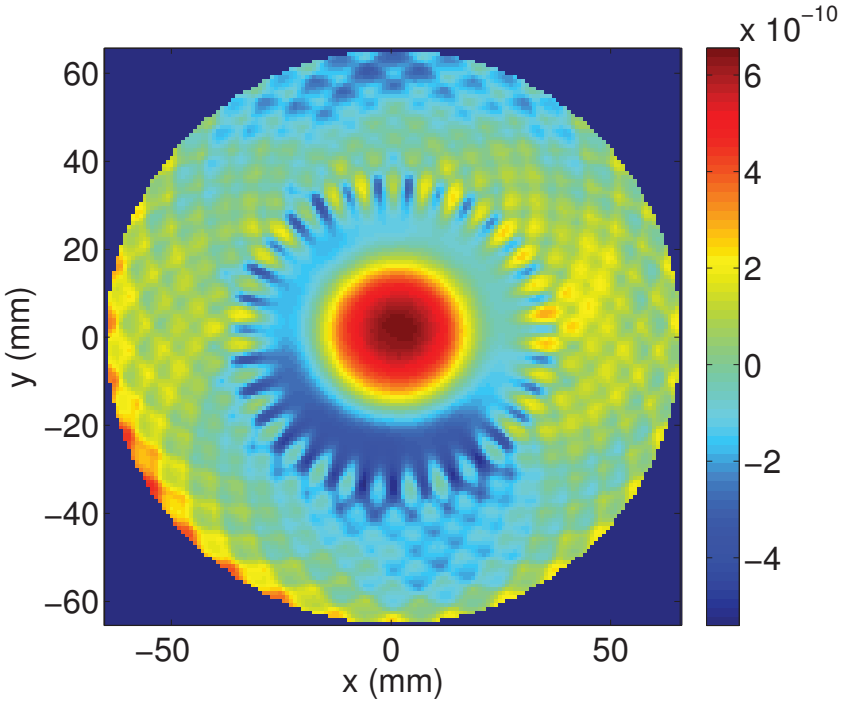

Figure 6.20: Surface figure of the simulated deposited HR-ITM coating with planetary motion of the substrates, piston, tilt and RoC removed.

6.6.3.2 Results of the simulation for the ITM and ETM HR coating

The simulation of the HR-ITM coating deposition gives a coating uniformity with the surface figure shown in figure 6.20 on a diameter of 150 mm, the residual curvature is removed from the data. The surface flatness is 0.16 nm RMS with the residual curvature removed from the data. On 150 mm the Zernike polynomial Z_2^0 has an amplitude of -0.75 nm. It would change the radius of curvature of the input mirror by only 1.1 m. This change of radius of curvature is small enough to be acceptable.

Concerning the ETM coating which has a thickness of about 6 µm with more than 2.1 µm of tantala. The surface figure of the HR-ETM simulated coating is visible in the figure 6.21 with the residual radius of curvature due to the coating removed from the data. It has a flatness of 0.32 nm RMS. The change of curvature for the end test masses on the central 150 mm would be about -2.3 m (from 1683 m to 1689.9 m) because of a Z_2^0 which has an amplitude of about -1.2 nm. Again the sagitta change is quite limited.

Concerning the Zernike Polynomials of higher order than 2, the table 6.6 shows the amplitude of the highest Zernike polynomials for the HR-ITM and HR-ETM simulated coating. They are computed over a diameter of 150 mm and only the Zernike polynomials with an amplitude higher than 0.1 nm have been reported in the table.

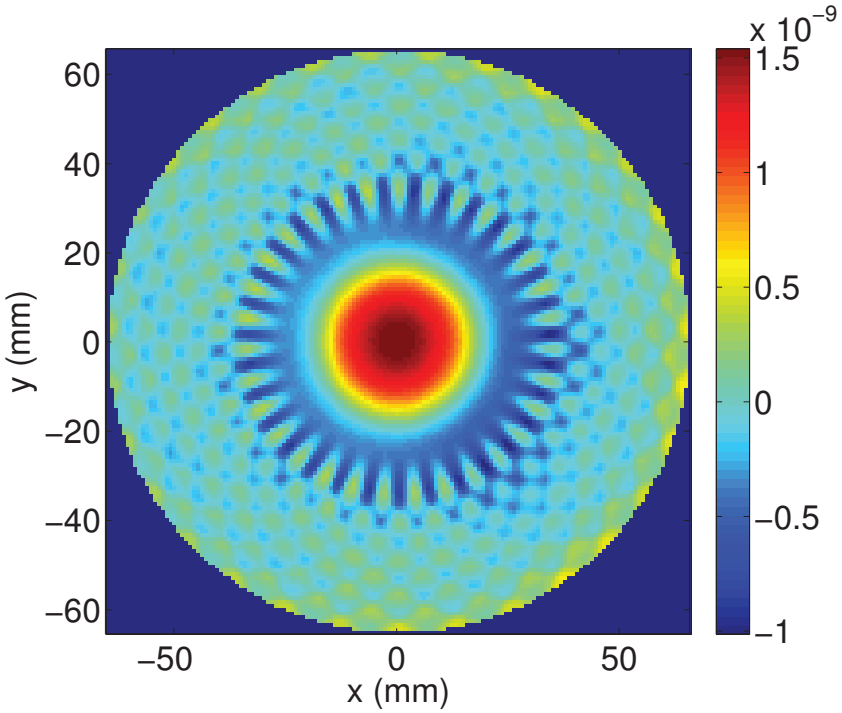

Figure 6.21: Surface figure of the simulated HR-ETM coating with planetary motion of the substrates, piston, tilt and RoC removed.

We see that there are only a few Zernike polynomials which have a high amplitude in the simulated surface figure for both kinds of coating. The highest amplitude is the Z_8^0 term with 0.55 nm for the HR-ETM surface. It should not be a problem as we have seen that this Zernike polynomial has a limited influence on the round-trip losses in the Advanced Virgo arm cavity, especially if on the ETM. Anyhow we are at the very limit of the aLIGO specification for the ETM-type coating but we should be able to improve the uniformity by adjusting the mask geometry.

Table 6.6: Zernike polynomials in the simulated HR-ITM and HR-ETM coating surface with planetary motion.

HR type ITM	**HR type ETM**
$Z_2^2 = 0.15$ nm	$Z_3^1 = 0.11$ nm
$Z_3^{-1} = -0.19$ nm	$Z_4^0 = 0.40$ nm
$Z_4^0 = 0.14$ nm	$Z_6^0 = -0.44$ nm
$Z_4^0 = -0.15$ nm	$Z_8^0 = 0.55$ nm
$Z_8^0 = 0.26$ nm	

6.6.3.3 Losses in the Advanced Virgo Fabry-Perot cavity with the simulated coating uniformity

The round-trip losses induced by such simulated surface have been computed from the simulation of the Advanced Virgo arm cavity. We tested three cases, first with the HR-ITM surface map on the IM with the opposite surface being perfect. Then with the HR-ETM surface map on the EM with the opposite surface being perfect and finally with the two simulated surfaces on each mirror. The results in terms of RTL and high order mode content of the circulating field in the Advanced Virgo arm cavity are reported in the table 6.7.

Table 6.7: Round-trip losses due to the simulated HR-ITM and HR-ETM coating surface with planetary motion.

Simulation	**RTL**	**HOM**
(ITM - perfect map)	8.3 ppm	32 ppm
(perfect map - ETM)	19.0 ppm	90 ppm
(ITM - ETM)	17.0 ppm	62 ppm

We see that the simulated surfaces with the planetary motion gives round-trip losses that are below the amount of losses acceptable for the Advanced Virgo gravitational wave detector. Indeed the expected losses with theses simulated surfaces are smaller than 25 ppm per mirror and smaller than 50 ppm for the two mirrors. It limits also greatly the amount of high order modes in the cavity with only 62 ppm for the simulation with the two surfaces. We see that the end mirror surface is again more critical because of the larger beam impinging on it and because of a larger coating thickness. It induce about two times more round-trip losses than the input mirror surface and about 3 times more HOMs. This is certainly due to the bump at the center of the surface and the surface figure could be improved by adjusting the masks geometry.

The planetary motion of the substrates during the deposition process is very promising. Indeed, the simulated surfaces have a very good uniformity and they give very low losses in the Advanced Virgo arm cavity both for ITM and ETM coating. Considering that the technique allows coating two mirrors at once these are very promising results as we expect to obtain surfaces with a very low flatness and a good transmission matching between the two mirrors coated during the same deposition run.

Considering the results of the simulation, it has been decided to implement the planetary motion system in the coating machine. The first coating deposited with the planetary motion should be performed during the summer 2012.

6.7 Conclusion

In this chapter we have shown that the coating uniformity can become predominant in the overall flatness of the mirrors composing the Fabry Perot arm cavity in Advanced gravitational wave detector. Indeed the substrate flatness should be very good and the deposition of the 3 µm and 6 µm for the ITM-type (T=1.4%) and ETM-type (T=5ppm) high reflective coating has to be very uniform. To obtain the mirrors with the required transmission, the substrates are coated with multilayer of dielectric materials of low and high refractive index (silica and titanium doped tantala).

We have presented the coating machine used for the coating deposition of the Advanced Virgo mirrors. This machine is an ion-beam sputtering machine, it allows to coat two substrates during the same deposition run thanks to its large dimension.

For the time being, two configurations can be used for the coating of the substrates. The two configurations are with a simple rotation, the first is with the substrate in the center of the machine and the second is with two substrates on both sides of the rotational axis. The twin mirrors configurations has the advantage of coating two mirrors at a time to obtain a very good matching in the mirrors transmissions. Unfortunately, we have shown that the surface figure obtained in this configuration is not good enough even with the masking technique. The single mirror configuration allows to coat substrates with an ITM type coating with a surface figure compliant with the aLIGO requirement. We are at the very limit of the technique and the deposition uniformity obtained might not be enough for the deposition of the ETM type coating as this coating is twice as thick as the ITM one.

We have also studied the effect of the firsts circular Zernike polynomials aberration that can be induced by the coating deposition. We have shown that second and tertiary spherical aberrations (Z_6^0 and Z_8^0) can be responsible for a lot of round-trip losses in the Advanced Virgo arm cavity.

Finally, we have studied the possibility of coating the substrates with a new configuration in the coating chamber. This configuration implies a planetary motion of the substrates. To study the coating uniformity with the planetary motion we have modelled the plume shape of the deposited materials. The simulation of the coating deposition gives surface figures which are compliant with the aLIGO requirements except for the Zernike polynomials Z_8^0) on the ETM type coating surface which has an amplitude of 0.55 nm. Anyhow, the expected round-trip losses induced by such surfaces in the Fabry-Perot arm cavity are well within the loss budget of Advanced Virgo as they are less than 30 ppm. The implementation of the planetary motion of the substrates inside the coating chamber is currently on going.

Conclusion and perspectives

Gravitational waves have been predicted by Einstein in the General Relativity theory. They are perturbations of the space-time metric and so far no direct detection has been reported. The only evidence of the gravitational waves existence comes from an indirect measurement done by the observation of the binary pulsar PSR1916+13 by Taylor and Hulse. First generation interferometric detectors have taken observational runs in the last years without reporting any direct detection.

Nowadays second generations detectors are in preparation with Advanced Virgo, Advanced LIGO and KAGRA. They are planned to be dual-recycling Michelson interferometer with Fabry-Perot cavities. The shot noise limits the sensitivity at high frequencies, it scales as the square root of the power in the interferometer. Thus high finesse Fabry-Perot cavities with low losses are necessary to decrease the effect of the photon shot noise on the interferometer sensitivity as well as the noises coming from the control of the other interferometer mirrors.

First, we studied the effect of the high power circulating in the Fabry-Perot cavities. Indeed, it is planned to have about 650 kW of power in the arm cavities and so the power absorption in the input mirror coating will induce a large thermal lensing effect. The thermal lensing effect degrades the recycling gain of the RF sidebands at 6 MHz used in the control of the interferometer. Different configurations of the recycling cavities have been studied and we have shown that non-degenerate cavities are much more immune to thermal lensing than marginally-recycling cavities. However the marginally stable cavities have been chosen as the reference design for Advanced Virgo.

Then we focus on the mirrors composing the Fabry-Perot arm cavities and especially on the surface figure of the mirrors. We calculate the specification on the arm mirror flatness. The surface figure of those mirrors should be sub-nanometric to limit the round-trip losses in the Fabry-Perot cavity as the requirement on the arm cavity round-trip losses is to be less than 75 ppm. To define the need in terms of mirror flatness we uses a statistical approach with thousands of simulations. Different kind of surface figures dependent on the polishing process are considered. We set the flatness specification to be less than 0.5 nm RMS in the central 150 mm diameter and less than 0.15 nm RMS in the same region in the

spatial frequency band 50 m^{-1} $-$ 1000 m^{-1}. The corrective coating technique has also been simulated in order to assess the need in terms of flatness for the substrates to be corrected. The simulations shows that we need to start with a mirror having a flatness of 1.5 nm RMS for a correction up to 50 m^{-1} or a flatness of 2 nm RMS for a correction up to 100 m^{-1}.

In the chapter 4, we have studied the measurement of the mirror surface figure. At LMA the measurement is done with a phase-shifting interferometer with a 145 mm pupil. We study the repeatability of the measurement on the same diameter. The repeatability is limited mainly by environment noises such as vibrations and air turbulences. To reduce their effects, the measurement should be taken with no fringes in the field of view and in a controlled atmosphere area. The reproducibility of the measurement with the stitching technique on a large diameter is also presented. The limits due to the stitching technique itself and due to the sample holder are shown. Finally, comparative measurements of the same sample at LMA and at Tinsley have been done. Two cases have been encountered, one is the measurement of a flat surface and the other one is the measurement of a curved surface. In the flat surface case we obtained good results as the measurement at LMA compares very well with the Tinsley measurement. On the contrary, the curved surface measurement compares poorly with the Tinsley measurement. It has bring to light a systematic error linked to the interference pattern in the field of view. Thus the measurement of the substrate and mirror surface should be done preferably with no fringes in the field of view.

Then the corrective coating technique is presented along with the results obtained in the correction of the substrates flatness. We have corrected an initial Virgo substrate on its flat surface with good results. Indeed we have corrected the substrate on a large diameter (260 mm). On the central 150 mm diameter the substrate has a flatness of 0.9 nm RMS after correction starting from a flatness of 4.0 nm RMS. The corrected surface is mainly dominated by a residual curvature and astigmatism. This is due to the measurement of the surface before correction, the reproducibility of the measurement being limited by the sample holder and stitching technique. If we remove the astigmatism and curvature of the surfaces before and after correction, the corrected surface has a flatness of 0.36 nm RMS starting from 2.1 nm RMS before correction. The correction is for now limited by the ability of measuring the substrate we have to correct. It is important to state that our ability to correct a substrate surface is driven mainly by our ability to measure the surface before correction. Thus the metrology issue is very important for the corrective coating technique. It has to be stated that the expected round-trip loss due to the corrected surface figure are compliant with the Advanced Virgo requirement even with the residual curvature and astigmatism.

Finally in the development of the mirrors, the deposition of the coating is a crucial step

to obtain mirrors with the wanted reflectivity. Indeed considering that the substrates have already a sub-nanometric flatness, the coating can become dominant in the final flatness of the mirror. The high reflective coating that are deposited on top of the substrate for the arm cavity mirrors have a total thickness of approximately 3 µm and 6 µm for the input and end mirrors. It means that the uniformity of the deposited coating should be about 0.1 % on a diameter of 150 mm. It is preferable to coat two mirrors at the same time in order to obtain the best transmission matching between the mirrors used in the two arms of the interferometer. The results on the deposition of the aLIGO substrates shows that the uniformity obtained by coating two mirrors at once in simple rotation is not enough. The flatness obtained for the mirrors coated in simple rotation at the center of the machine are compliant with the requirements for advanced gravitational waves detectors. But the expected coating uniformity of the end mirrors (that are twice as thick as input mirrors) with this technique is not good enough. The study of the planetary motion of the substrates shows that the expected coating uniformity should be compliant with the advanced detectors requirements even for the end mirror coatings. The planetary motion system will be installed in the coating machine at LMA and tested during the summer 2012 with hopefully the expected results.

Another way to lower again the mirror flatness would be to apply a corrective coating on the coated substrate. The correction on the coating is a bit more complex as one as to take into account the phase shift in the coating itself. And the multilayer coating stack should be adjusted in order to have a linear response of the phase shift when adding materials on the last layer. Preliminary computations and tests show that adding materials on a quarter-wave high reflective coating is similar to removing materials because of the coating phase shift response. Anyhow, the work presented in this thesis shows that the technique of corrective coating associated with a coating deposition with planetary motion of the substrates should allow obtaining mirrors with a surface figure compliant with the requirement for second generation gravitational wave detectors. The correction of the surface after coating deposition is another possible way to lower down the mirror flatness.

Appendix A

Zernike Polynomials

Zernike polynomials have been introduced by Zernike [92]. They are a set of orthogonal polynomials defined on a circular pupil of radius 1. They are used to describe the surface figure of mirrors or wave-front aberrations that arise from optical systems. A surface or a wave-front(W) can be expanded in a sum of orthonormal Zernike circle polynomials $Z_n^m(\rho,\theta)$ expressed in circular coordinate as follow:

$$W(\rho,\theta) = \sum_{n,m} a_n^m Z_n^m(\rho,\theta) \tag{A.1}$$

where a_n^m is the *expansion coefficients* with $a_n^m =< W(\rho,\theta)|Z_n^m(\rho,\theta) >$.
The Zernike polynomials are defined as:

$$Z_n^m(\rho,\theta) = \sqrt{2(n+1)}R_n^{|m|}(\rho)\cos(m\theta), \quad m > 0 \tag{A.2}$$

$$Z_n^m(\rho,\theta) = \sqrt{2(n+1)}R_n^{|m|}(\rho)\sin(m\theta), \quad m < 0 \tag{A.3}$$

$$Z_n^m(\rho,\theta) = \sqrt{n+1}R_n^0(\rho), \quad m = 0 \tag{A.4}$$

where $R_n^m(\rho)$ is the radial polynomial given as:

$$R_n^m(\rho) = \sum_{s=0}^{(n-m)/2} \frac{(-1)^s(n-s)!}{s!(\frac{n+m}{2}-s)!(\frac{n-m}{2}-s)!}\rho^{n-2s} \tag{A.5}$$

The indexes n and m are integers (including zero) with $n-|m| \geq 0$ and even. The n index is positive and can can be considered as the radial degree whereas the m index represents the azimuthal frequency. In table A.1 are reported the Zernike polynomials up to the secondary spherical Z_6^0. Figure A.1 shows a pyramid with the pictures of the the Zernike polynomials up to $n = 8$. The indexes n and m of each Zernike polynomials are reported on the top left of each picture along with a progressive numbering on the top right. The name of the

aberration (if any) is also mentioned at the bottom of the pictures.

Table A.1: Orthonormal Zernike circular polynomials.

n	m	$Z_n^m(\rho,\theta)$	Aberration name
0	0	1	Piston
1	1	$2\rho\cos\theta$	x tilt
1	-1	$2\rho\sin\theta$	y tilt
2	0	$\sqrt{3}(2\rho^2-1)$	Defocus/Power
2	2	$\sqrt{6}\rho^2\cos\theta$	Primary astigmatism at 0 °
2	-2	$\sqrt{6}\rho^2\cos\theta$	Primary astigmatism at 45 °
3	1	$\sqrt{8}(3\rho^3-2\rho)\cos\theta$	Primary x coma
3	-1	$\sqrt{8}(3\rho^3-2\rho)\sin\theta$	Primary y coma
3	3	$\sqrt{8}\rho^3\cos 3\theta$	Trefoil
3	-3	$\sqrt{8}\rho^3\sin 3\theta$	Trefoil
4	0	$\sqrt{5}(6\rho^6-6\rho^2+1)$	Primary spherical
4	2	$\sqrt{10}(4\rho^4-3\rho^2)\cos 2\theta$	Secondary astigmatism at 0 °
4	-2	$\sqrt{10}(4\rho^4-3\rho^2)\sin 2\theta$	Secondary astigmatism at 45 °
4	4	$\sqrt{10}\rho^4\cos 4\theta$	
4	-4	$\sqrt{10}\rho^4\sin 4\theta$	
5	1	$\sqrt{12}(10\rho^5-12\rho^3+3\rho)\cos\theta$	Secondary x coma
5	-1	$\sqrt{12}(10\rho^5-12\rho^3+3\rho)\sin\theta$	Secondary x coma
5	3	$\sqrt{12}(5\rho^5-4\rho^3)\cos 3\theta$	
5	-3	$\sqrt{12}(5\rho^5-4\rho^3)\sin 3\theta$	
5	5	$\sqrt{12}\rho^5\cos 5\theta$	
5	-5	$\sqrt{12}\rho^5\sin 5\theta$	
6	0	$\sqrt{7}(20\rho^6-30\rho^4+12\rho^2-1)$	Secondary spherical
6	2	$\sqrt{14}(15\rho^6-20\rho^4+6\rho^2)\cos 2\theta$	Tertiary astigmatism at 0 °
6	-2	$\sqrt{14}(15\rho^6-20\rho^4+6\rho^2)\sin 2\theta$	Tertiary astigmatism at 45 °
6	4	$\sqrt{14}(6\rho^6-5\rho^4)\cos 4\theta$	
6	-4	$\sqrt{14}(6\rho^6-5\rho^4)\sin 4\theta$	
6	6	$\sqrt{14\rho^6\cos 6\theta}$	
6	-6	$\sqrt{14\rho^6\sin 6\theta}$	
7	1	$4(35\rho^7-60\rho^5+30\rho^34\rho)\cos\theta$	Tertiary x coma
7	-1	$4(35\rho^7-60\rho^5+30\rho^34\rho)\sin\theta$	Tertiary y coma
7	3	$4(21\rho^7-30\rho^5+10\rho^3)\cos 3\theta$	
7	-3	$4(21\rho^7-30\rho^5+10\rho^3)\sin 3\theta$	
7	5	$4(7\rho^7-6\rho^5)\cos 5\theta$	
7	-5	$4(7\rho^7-6\rho^5)\sin 5\theta$	
7	7	$4\rho^7\cos 7\theta$	
7	-7	$4\rho^7\sin 7\theta$	
8	0	$3(70\rho^8-140\rho^6+90rho^4-20\rho^2+1)$	Tertiary spherical

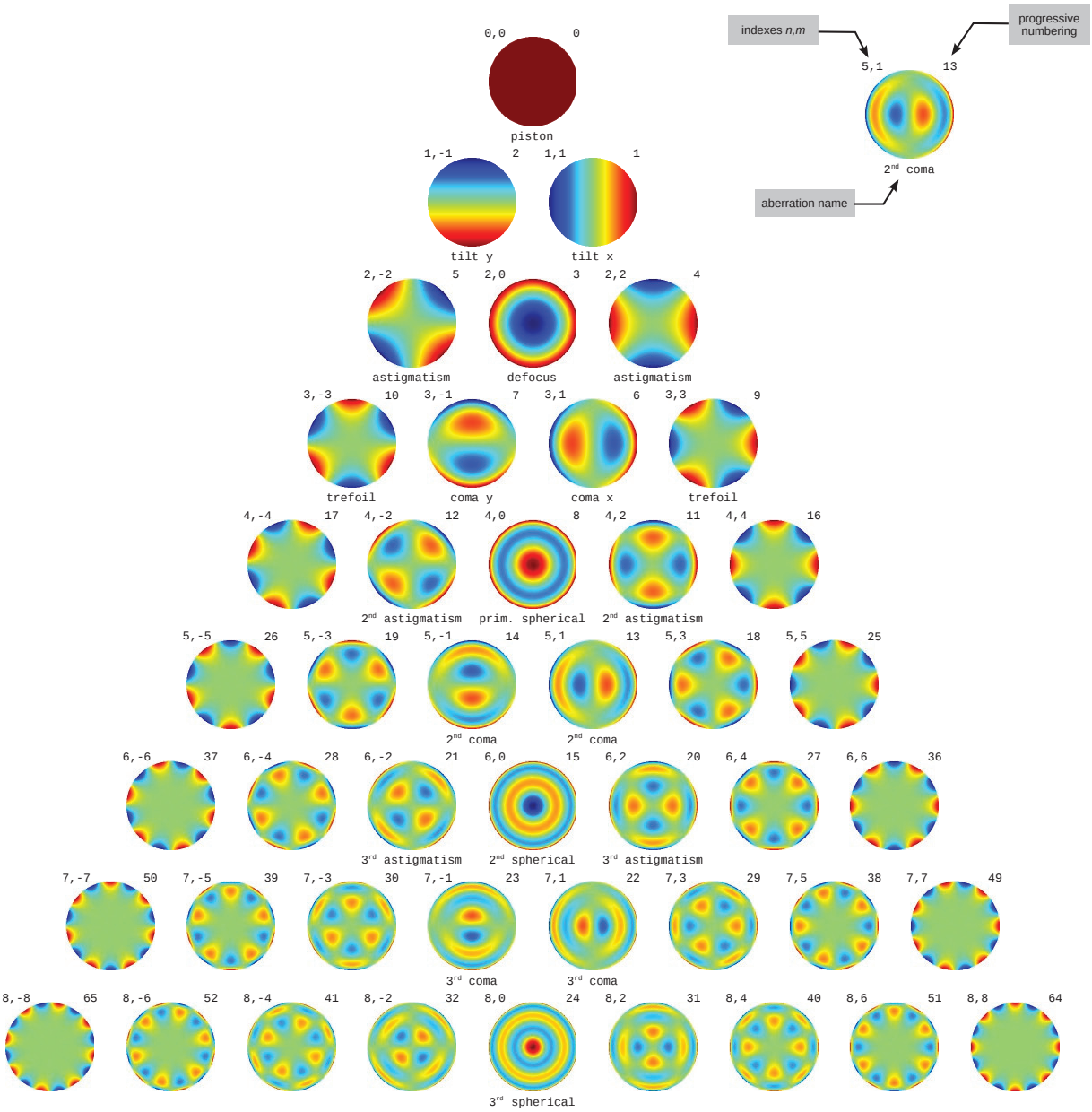

Figure A.1: Zernike Polynomials.

Appendix B

High Order Mode and Contrast Defects

In this appendix, we present a basic calculation of the power at the output port due to the high order mode content of the fields coming from the two arms.
The interferometer being tuned in dark fringe, we can express the field at the output port of the interferometer as:

$$\Psi_{DF} = \frac{1}{\sqrt{2}} [\Psi_r^y - \Psi_r^x] \tag{B.1}$$

where Ψ_r^x and Psi_r^y are the field reflected respectively from the north and west arms.

If we assume that the field Psi_r^y is a pure TEM00 mode and that the field Ψ_r^x has a high order mode Ψ_{nm} component of amplitude b, we have:

$$\Psi_r^x = a \cdot \Psi_{00} + b \cdot \Psi_{nm} \tag{B.2}$$

$$\Psi_r^y = \Psi_{00} \tag{B.3}$$

with Ψ_{00} being the pure TEM_{00} mode, Ψ_{nm} the high order mode, a and b being the content of the field in the TEM_{00} mode and in the high order mode respectively.
We can derive the field at the output port[1]:

$$\Psi_{DF} = \frac{1}{2} [(1 - a) \cdot \Psi_{00} - b \cdot \Psi_{nm}] \tag{B.4}$$

[1]We are assuming that the field impinging on the beam splitter has an amplitude equal to one.

The power P_{DF} at the output port of the interferometer tuned in dark fringe can be expressed as:

$$P_{DF} = |\Psi_{DF}|^2 \tag{B.5}$$
$$= \frac{1}{4}\left[(1-a)^2 \cdot \Psi_{00}^2 + b^2 \cdot \Psi_{nm}^2 - 2(1-a)b \times \Psi_{00} \cdot \Psi_{nm}\right] \tag{B.6}$$

The modes TEM_{00} being orthogonal with the high order modes, the scalar product $\Psi_{00} \cdot \Psi_{nm}$ is null. Thus we have:

$$P_{DF} = \frac{1}{4}\left[(1-a)^2 \cdot \Psi_{00}^2 + b^2 \cdot \Psi_{nm}^2\right] \tag{B.7}$$

Assuming that there is no power lost elsewhere the principle of energy conservation tells that:

$$a^2 + b^2 = 1 \tag{B.8}$$

The high order modes content of the field being small ($b \ll 1$) we have:

$$a = \sqrt{1-b^2} \approx 1 - \frac{1}{2}b^2 \tag{B.9}$$

After passing through the output mode cleaner (OMC), it remains only the contribution from the TEM_{00} mode so that the power at the dark fringe is:

$$P_{DF} = \frac{1}{4}(1-a)^2 \cdot P_{BS} \tag{B.10}$$
$$P_{DF} = \frac{1}{8}b^4 \cdot P_{BS} \tag{B.11}$$

where P_{BS} is the power coming from the beam-splitter.
In Advanced Virgo it is foreseen to have 80 mW of carrier power at the dark fringe induced by a very small detuning of the arm cavities. This leaking power is used for the DC read-out control. We assume that we want to have less than 10 mW due to the high order modes after the OMC. Considering that there are 4.9 kW on the beam-splitter, the content in high order modes of the fields reflected from the arm cavity should be smaller than 0.4%:

$$b^2 < \sqrt{\frac{8 \times 10\ mW}{4.9\ kW}} \tag{B.12}$$
$$b^2 < 0.4\% \tag{B.13}$$

This 4000 ppm of high order modes content should not be a problem.

If we look at the field before the OMC, the power is dominated by the HOM content of the field. We have:

$$P_{DF} = \frac{1}{4} b^2 \cdot P_{BS} \tag{B.14}$$

There are no clear specification on the power at the dark fringe before the OMC. Anyhow if we assume that the high order mode content of the field reflected from one cavity is about 400 ppm, the power at the dark fringe will be of 490 mW considering that there are 4.9 kW of power on the beam-splitter.

$$P_{DF} = \frac{1}{4} 400\ ppm \cdot 4.9\ kW \tag{B.15}$$

$$P_{DF} \approx 490\ mW \tag{B.16}$$

This 490 mW of power on the dark fringe is tolerable from the point of view of the diffused light. Considering that there is a factor four between the HOM content in the circulating and reflected field in a Fabry-Perot cavity then the HOM content of the circulating field should be less than 100 ppm.

Bibliography

[1] A. Einstein, "Die grundlage der allgemeinen relativittstheorie [adp 49, 769 (1916)]," *Annalen der Physik*, vol. 14, pp. 517–571, 2005. 5, 6

[2] R. A. Hulse and J. H. Taylor, "Discovery of a pulsar in a binary system," *Astrophys. J.*, vol. 195, pp. L51–L53, Jan. 1975. 5, 8

[3] J. Weber, "Detection and generation of gravitational waves," *Phys. Rev.*, vol. 117, pp. 306–313, Jan 1960. 5

[4] M. E. Gertsenshtein and V. I. Pustovoit, "On the detection of low frequency gravitational waves," *Sov. Phys. JETP*, vol. 16, p. 433435, 1963. 5

[5] C. Misner, K. Thorne, and J. Wheeler, *Gravitation*. No. 3 in Physics Series, W. H. Freeman, 1973. 6

[6] R. Wald, *General Relativity*. Physics/Astrophysics, University of Chicago Press, 1984. 6

[7] P. Saulson, *Fundamentals of Interferometric Gravitational Wave Detectors*. World Scientific, 1994. 7

[8] C. Cutler and K. S. Thorne, "An overview of gravitational-wave sources," in *Proceeding of the 16th general relativity and gravitation conference* (N. T. Bishop and S. D. Maharaj, eds.), pp. 72–111, World Scientific, 2002. arXiv:gr-qc/0204090v1. 7

[9] J. Abadie et al. (The LIGO Scientific Collaboration and The Virgo Collaboration), "Predictions for the rates of compact binary coalescences observable by ground-based gravitational-wave detectors," *Classical and Quantum Gravity*, vol. 27, no. 17, p. 173001, 2010. 7

[10] J. Abadie et al. (The LIGO Scientific Collaboration and The Virgo Collaboration), "Search for Gravitational Waves from Low Mass Compact Binary Coalescence in LIGO's Sixth Science Run and Virgo's Science Runs 2 and 3," *Physical Review D*, vol. 85, p. 082002, 2012. 8

[11] J. Abadie et al. (The LIGO Scientific Collaboration and The Virgo Collaboration), "Beating the spin-down limit on gravitational wave emission from the Vela pulsar," *Astrophysical Journal*, vol. 737, p. 93, 2011. 8

[12] C. D. Ott, "The gravitational-wave signature of core-collapse supernovae," *Classical and Quantum Gravity*, vol. 26, no. 6, p. 063001, 2009. 8

[13] B. P. Abbott et al. (The LIGO Scientific Collaboration and The Virgo Collaboration), "An upper limit on the stochastic gravitational-wave background of cosmological origin," *Nature*, vol. 460, 7258, pp. 990–994, 2009. 8

[14] J. M. Weisberg, J. H. Taylor, and L. A. Fowler, "Gravitational waves from an orbiting pulsar," *Scientific American*, vol. 245, no. 4, pp. 74–82, 1981. 8

[15] J. Weisberg, J.M.; Taylor, "The relativistic binary pulsar b1913+16: Thirty years of observations and analysis," in *Binary Radio Pulsars*, vol. 328, p. 25, 2005. 8, 9

[16] A. Abramovici, W. E. Althouse, R. W. P. Drever, Y. Grsel, S. Kawamura, F. J. Raab, D. Shoemaker, L. Sievers, R. E. Spero, K. S. Thorne, R. E. Vogt, R. Weiss, S. E. Whitcomb, and M. E. Zucker, "LIGO: The Laser Interferometer Gravitational-Wave Observatory," *Science*, vol. 256, no. 5055, pp. 325–333, 1992. 9

[17] C. Bradaschia, R. D. Fabbro, A. D. Virgilio, A. Giazotto, H. Kautzky, V. Montelatici, D. Passuello, A. Brillet, O. Cregut, P. Hello, C. Man, P. Manh, A. Marraud, D. Shoemaker, J. Vinet, F. Barone, L. D. Fiore, L. Milano, G. Russo, J. Aguirregabiria, H. Bel, J. Duruisseau, G. L. Denmat, P. Tourrenc, M. Capozzi, M. Longo, M. Lops, I. Pinto, G. Rotoli, T. Damour, S. Bonazzola, J. Marck, Y. Gourghoulon, L. Holloway, F. Fuligni, V. Iafolla, and G. Natale, "The VIRGO Project: A wide band antenna for gravitational wave detection," *Nuclear Instruments and Methods in Physics Research Section A: Accelerators, Spectrometers, Detectors and Associated Equipment*, vol. 289, no. 3, pp. 518 – 525, 1990. 9

[18] G. Vajente, *Analysis of sensitivity and noise sources for the Virgo gravitational wave interferometer*. PhD thesis, Scuola Normale Superiore di Pisa, 2008. 11, 12, 13, 14, 21, 35, 44

[19] S. Braccini et al., "Measurement of the seismic attenuation performance of the virgo superattenuator," *Astroparticle Physics*, vol. 23, no. 6, pp. 557 – 565, 2005. 11, 12, 21

[20] C. Fabry and A. Perot, "Theorie et applications dune nouvelle methode de spectroscopie interferentielle," *Annales de la Chimie et de Physique*, vol. 115, 1899. 13

[21] F. Acernese et al. (The Virgo Collaboration), "The virgo 3km interferometer for gravitational wave detection," *Journal of Optics A: Pure and Applied Optics*, vol. 10, no. 6, p. 064009, 2008. 14

[22] T. Accadia et al. (The Virgo Collaboration), "Status of the Virgo project," *Classical and Quantum Gravity*, vol. 28, p. 114002, 2011. Contribution to 19th International Conference on General Relativity and Gravitation (GR19), Mexico, 4-9 July 2010. 14, 24

[23] The Virgo Collaboration, "Advanced Virgo Technical Design Report," *Virgo Internal Note*, vol. VIR-0128A-12, 2012. 14, 17, 23, 24, 25, 26, 27, 29, 31, 34, 59, 64, 66, 70, 93, 169

[24] G. Cella and A. Giazotto, "Invited review article: Interferometric gravity wave detectors," *Review of Scientific Instruments*, vol. 82, no. 10, p. 101101, 2011. 16

[25] M. Lorenzini (on behalf of the Virgo Collaboration), "The monolithic suspension for the virgo interferometer," *Classical and Quantum Gravity*, vol. 27, no. 8, p. 084021, 2010. 16

[26] M. Granata, *Optical Development for Second- and Third-Generation Gravitational-Wave Detectors: Stable Recyling Cavities for Advanced Virgo and HIgher-Order Laguerre-Gauss Modes*. PhD thesis, Université Paris Diderot, Università degli Studi di Roma Tor Vergata, 2011. 16, 27

[27] "Virgo noise budget." `https://wwwcascina.virgo.infn.it/senscurve/`. 17

[28] J. Degallaix, *Compensation of strong thermal lensing in interferometric gravitational waves detectors*. PhD thesis, University of Western Australia, 2006. 18, 34, 43

[29] T. Accadia et al. (The Virgo Collaboration), "A thermal compensation system for the gravitational wave detector Virgo," in *Proc. 12th Marcel Grossmann Meeting on General Relativity* (R. T. J. T. Damour and R. Ruffini, eds.), Singapore: World Scientific, 2011. 18, 28, 35

[30] G. Vajente for the Virgo Collaboration, "Performance of the Virgo interferometer longitudinal control system during the second science run," *Astroparticle Physics*, vol. 34, pp. 521–527, 2011. 19

[31] T. Accadia et al. (The Virgo Collaboration), "The seismic Superattenuators of the Virgo gravitational waves interferometer," *Journal of Low Frequency Noise Vibration and Active Control*, vol. 30, pp. 63–79, 2011. LAL 11-151. 21

[32] LIGO Hanford website. `http://www.ligo-wa.caltech.edu/`. 22

[33] LIGO Livingston website. `http://www.ligo-la.caltech.edu/`. 22

[34] G. M. Harry and the LIGO Scientific Collaboration, "Advanced LIGO: the next generation of gravitational wave detectors," *Classical and Quantum Gravity*, vol. 27, no. 8, p. 084006, 2010. 22

[35] GEO600 website. `http://www.geo600.org/`. 22

[36] LIGO Scientific Collaboration. `http://www.ligo.org/`. 22

[37] B. Willke et al., "The GEO-HF project," *Classical and Quantum Gravity*, vol. 23, no. 8, p. S207, 2006. 22

[38] Kentaro Somiya for the KAGRA Collaboration, "Detector configuration of kagra - the japanese cryogenic gravitational-wave detector," *arXiv*, vol. arXiv:1111.7185v2, 2012. 22

[39] KAGRA website. `http://gwcenter.icrr.u-tokyo.ac.jp/en/plan`. 22

[40] J. Mizuno, K. Strain, P. Nelson, J. Chen, R. Schilling, A. Rdiger, W. Winkler, and K. Danzmann, "Resonant sideband extraction: a new configuration for interferometric gravitational wave detectors," *Physics Letters A*, vol. 175, no. 5, pp. 273 – 276, 1993. 23

[41] M. Punturo, "Advanced Virgo Sensitivity document," *Virgo Internal Note*, no. VIR-0073A-12, 2012. 23

[42] The Virgo Collaboration, "Advanced Virgo Baseline Design," *Virgo Internal Note*, vol. VIR-0027A-09, 2009. 27, 34, 35, 46, 66, 87

[43] J. Degallaix for the OSD group, "Setting the requirement for TCS," *Virgo Internal Note*, vol. VIR-0199A-12, 2012. 28

[44] V. Fafone, "AdV TCS: thermal simulations and SS update," *Virgo Internal Note*, vol. VIR-0200A-12, 2012. 29

[45] P. Hello and J.-Y. Vinet, "Simulation of thermal effects in interferometric gravitational-wave detectors," *Physics Letters A*, vol. 178, no. 56, pp. 351 – 356, 1993. 33

[46] J. Marque and G. Vajente, "Thermal effects & frequency noise," *Virgo Internal Note*, vol. VIR-0127A-09, 2009. 34

[47] V. Fafone, "TCS update," *Virgo Internal Note*, vol. VIR-0414A-11, 2011. 35

[48] G. Vajente, "Plane-concave cavities for Advanced Virgo," *Virgo Internal Note*, vol. VIR-0681A-09, 2009. 35, 46, 53

[49] A. Freise, S. Hild, and J. Marque, "Advanced Virgo design: Layout options for the non-degenerate recycling cavities," *Virgo Internal Note*, vol. VIR-0025A-09, 2009. 35, 37

[50] H. Kogelnik and T. Li, "Laser Beams and Resonators," *Applied Optics*, vol. 5, no. 10, 1966. 37, 38

[51] A. Siegman, *Lasers*. University Science Books, 1986. 37, 42

[52] M. Granata and M. Barsuglia, "Estimation of astigmatism losses in the Advanced Virgo non-degenerate recycling cavities," *Virgo Internal Note*, 2009. 38

[53] V. Fafone and A. Rocchi, "TCS: hints for a discussion," *Virgo Internal Note*, vol. VIR-0017A-10, 2010. 40, 61

[54] R. Ward, "Thoughts on Advanced Virgo arm cavity RoCs," *Virgo Internal Note*, vol. VIR-037A-10, 2010. 45

[55] H. Yamamoto, "SIS (Stationary Interferometer Simulation) manual," *LIGO Document*, vol. T070039, 2011. 45

[56] M. Barsuglia and H. Yamamoto, "Simulation of recycling cavities with static interferometer simulation (sis)," *Virgo Internal Note*, vol. VIR-0195A-10, 2010. 45

[57] G. Vajente, "Convergence of modal simulations of MSRC," *Virgo Internal Note*, vol. VIR-0292B-10, 2010. 45

[58] G. Vajente, "MIST Modal Interferometer Simulation Tool User Manual," *Virgo Internal Note*, vol. VIR-0321B-10, 2010. 45

[59] P. Rapagnani, "Design issues on multi-payload systems," *Virgo Internal Note*, vol. VIR-0350A-10, 2010. 46, 52

[60] J. Marque, "Advanced Virgo design: Layout options for the non-degenerate recycling cavities," *Virgo Internal Note*, vol. VIR-0229A-10, 2010. 47

[61] OSD group, "Recycling Cavity Design," *Virgo Internal Note*, vol. VIR-0113A-10, 2010. 56

[62] G. Vajente. Personal communication. 57

[63] H. Yamamoto, "1D PSD of mirror maps," *DCC Ligo*, vol. T1100353-v1, 2011. 65

[64] J. Degallaix, M. Galimberti, R. Bonnand, and Q. Benoit, "Defining the arm cavity loss for Advanced Virgo," *Virgo Internal Note*, vol. VIR-706A-10, 2010. 66

[65] Australian Centre for Precision Optics, CSIRO. http://www.acpo.csiro.au/index.htm. 67

[66] `http://www.asphere.com/`. 67, 119

[67] B. Oreb. Personal Communication. 67

[68] B. Caron *et al.*, "SIESTA, a time domain general purpose simulation program for the VIRGO experiment," *Astroparticle Physics*, vol. 10, no. 4, pp. 369–386, 1999. 68, 70

[69] H. Yamamoto, "Advanced LIGO optics," *Virgo Internal Note*, vol. VIR-0570A-10, 2010. 68

[70] M. Galimberti, "Characterization and simulation of mirror surfaces," *Virgo Internal Note*, vol. VIR-0038A-11, 2011. 69

[71] J. Degallaix, "OSCAR a Matlab based optical FFT code," *Journal of Physics: Conference Series*, vol. 228, no. no. 1, 012021, 2010. 70, 71

[72] B. Bochner, *Modelling the Performance of Interferometric Gravitational-Wave Detectors with Realistically Imperfect Optics*. PhD thesis, Massachusetts Institute of Technology, 1998. 71

[73] G. Vajente, "ITF recovery after input mirror installation," *Virgo Internal Note*, vol. VIR-0270A-10, 2010. 74

[74] J. Stover, *Optical Scattering: Measurement and Analysis*. Press Monographs, SPIE Optical Engineering Press, 1995. 77

[75] J. M. Mackowski, L. Pinard, L. Dogin, P. Ganau, B. Lagrange, C. Michel, and M. Morgue, "VIRGO mirrors: wavefront control," *Optical and Quantum Electronics*, vol. 31, pp. 507–514, 1999. 78, 129, 131

[76] F. Bondu, "Large virtual mirror maps," *Virgo Internal Note*, vol. VIR-0271A-10, 2009. 79

[77] P. Carré, "Installation et utilisation du comparateur photolectrique et interfrentiel du bureau international des poids et mesures," *Metrologia*, vol. 2, no. 1, p. 13, 1966. 89

[78] R. Crane, "Interference phase measurement," *Applied Optics*, vol. 8, p. 538, 1969. 89

[79] J. H. Bruning, D. R. Herriott, J. E. Gallagher, D. P. Rosenfeld, A. D. White, and D. J. Brangaccio, "Digital wavefront measuring interferometer for testing optical surfaces and lenses," *Appl. Opt.*, vol. 13, pp. 2693–2703, Nov 1974. 89

[80] J. C. Wyant, "Use of an ac heterodyne lateral shear interferometer with real-time wavefront correction systems," *Appl. Opt.*, vol. 14, pp. 2622–2626, Nov 1975. 89

[81] D. Malacara, *Optical Shop Testing*. Wiley series in pure and applied optics, Wiley-Interscience, 2007. 90, 92, 98, 153

[82] L. Pinard, R. Bonnand, J. Degallaix, R. Flaminio, M. Galimberti, and B. Sassolas, "Polishing specifications for the Advanced Virgo substrates," *Virgo Internal Note*, vol. VIR-0416B-11, 2011. 93

[83] L. L. Deck, "Fourier-transform phase-shifting interferometry," *Appl. Opt.*, vol. 42, pp. 2354–2365, May 2003. 93

[84] M. Bray, "Stitching interferometry: how and why it works," in *EUROPTO Conference on Optical Fabrication and Testing*, vol. 3739 of *Proc. SPIE*, p. 259, 1999. 93, 95

[85] B. Cimma, D. Forest, P. Ganau, B. Lagrange, J. Mackowski, C. Michel, J. Montorio, N. Morgado, R. Pignard, L. Pinard, and A. Remillieux, "Original optical metrologies of large components," in *Advances in Optical Thin Films*, vol. 5250 of *Spie Proceedings Series*, (Saint-Etienne, France), pp. 322–333, International Society for Optical Engineering, 2004. présentée par A. Remillieux. 93

[86] M. Bray, "Stitching interferometry and absolute surface shape metrology: similarities," in *Optical Manufacturing and Testing IV* (H. P. Stahl, ed.), vol. 4451 of *Proc. SPIE*, p. 375, 2001. 95

[87] K. Creath, "Error sources in phase-measuring interferometry," in *Proceedings of the International Symposium on Optical Fabrication, Testing, and Surface Evaluation*, vol. 1720 of *Proc. SPIE*, pp. 428–435, 1992. 97

[88] J. Schwider, R. Burow, K.-E. Elssner, J. Grzanna, R. Spolaczyk, and K. Merkel, "Digital wave-front measuring interferometry: some systematic error sources," *Appl. Opt.*, vol. 22, pp. 3421–3432, Nov 1983. 97

[89] P. J. de Groot, "Vibration in phase-shifting interferometry," *J. Opt. Soc. Am. A*, vol. 12, February 1995. 97

[90] European Gravitational Observatory website. `http://www.ego-gw.it/`. 98

[91] I. Fiori and F. Paoletti, "Seismic Measurements on the LMA Fizeau Interferometer Optical Bench," *Virgo Internal Note*, vol. VIR-0397A-10, June 2010. 98, 106

[92] F. Zernike, "Diffraction Theory of Knife-edge Test and its Improved Form, the Phase Contrast Method," *Mon. Not. R. Astron. Soc.*, vol. 94, pp. 377–384, 1934a. 99, 111, 119, 205

[93] "Zernike polynomials." `http://mathworld.wolfram.com/ZernikePolynomial.html`. 99, 180

[94] M. Galimberti, R. Bonnand, R. Flaminio, D. Forest, C. Michel, N. Morgado, and L. Pinard, "Status of the new bench for wavefront measurement," *Virgo Internal Note*, vol. VIR-0412A-11, 2011. 109

[95] G. Billingsley, "aLIGO Core Optics Surprises," in *LSC-Virgo Meeting*, March 2011. 119

[96] Tinsley, "Itm04 input test mass final polishing data package," LIGO Document C1000472-v2, LIGO, 2010. 122

[97] MATLAB, *version 7.11.0 (R2010b)*. Natick, Massachusetts: The MathWorks Inc., 2010. 136

[98] F. Bellachia, D. Boget, T. Carron, D. Castelazzi, G. Daguin, L. Derome, C. Drezen, R. Flaminio, X. Grave, J. Lacotte, F. Marion, L. Massonnet, R. Morand, B. Mours, V. Sannibale, and D. Verkindt, "A VME based CCD imaging system for the VIRGO interferometer control," *Nuclear Instruments and Methods in Physics Research Section A: Accelerators, Spectrometers, Detectors and Associated Equipment*, vol. 413, no. 1, pp. 151 – 160, 1998. 146

[99] E. Pacaud. Personal Communication. 146

[100] J. Degallaix. Personal Communication. 164

[101] B. Cimma, D. Forest, P. Ganau, B. Lagrange, J.-M. Mackowski, C. Michel, J.-L. Montorio, N. Morgado, R. Pignard, L. Pinard, and A. Remillieux, "Ion beam sputtering coatings on large substrates: toward an improvement of the mechanical and optical performances," *Appl. Opt.*, vol. 45, pp. 1436–1439, Mar 2006. 169

[102] I. M. Pinto, V. Pierro, M. Principe, R. DeSalvo, and R. Dannenberg, "Coating optimization status," in *LSC-VIRGO Meeting*, March 2009. 170

[103] N. Morgado, "Coating designs for advanced detectors," in *Thermal Noise Workshop*, (Cascina, Italy.), February 2012. 170

[104] H. Macleod, *Thin-Film Optical Filters*. Series in Optics and Optoelectronics, Taylor & Francis, 2009. 171

[105] The VIRGO Collaboration, "The VIRGO large mirrors: a challenge for low loss coatings," *Classical and Quantum Gravity*, vol. 21, no. 5, p. S935, 2004. 173, 174

[106] B. Sassolas, Q. Benoît, R. Flaminio, D. Forest, J. Franc, M. Galimberti, A. Lacoudre, C. Michel, J.-L. Montorio, N. Morgado, and L. Pinard, "Twin mirrors for laser interferometric gravitational-wave detectors," *Appl. Opt.*, vol. 50, pp. 1894–1899, May 2011. 173

[107] B. Sassolas, *Etude et réalisation dempilements multicouches sur des optiques asphériques de grandes dimensions pour des applications en lithographie Extrême U.V.* PhD thesis, Université Claude Bernard, Lyon 1, 2008. 173, 178

[108] B. Sassolas, R. Flaminio, J. Franc, C. Michel, J.-L. Montorio, N. Morgado, and L. Pinard, "Masking technique for coating thickness control on large and strongly curved aspherical optics," *Appl. Opt.*, vol. 48, pp. 3760–3765, Jul 2009. 176, 195

[109] R. Day, "Simulations of ITF with roughness maps," *Virgo Internal Note*, vol. VIR-0536A-11, 2011. 181

[110] G. Billingsley, "Surface figure measurement of ETM04," *DCC Ligo*, vol. E1100684-v1, 2011. 186, 187

[111] G. Billingsley, "Coating uniformity estimate based on measurement of ETM05," *DCC Ligo*, vol. E1200093-v3, 2012. 187

[112] G. Billingsley, "ITM04 Figure Measurement," *DCC Ligo*, vol. E1200265-v2, 2012. 187

[113] C. Michel. Personal communication. 191

[114] B. Sassolas, R. Bonnand, J. Degallaix, R. Flaminio, M. Galimberti, C. Michel, and L. Pinard, "Towards a planetary motion at lma," *Virgo Internal Note*, vol. VIR-0415A-11, 2011. 191

[115] M. Gross, S. Dligatch, and A. Chtanov, "Optimization of coating uniformity in an ion beam sputtering system using a modified planetary rotation method," *Appl. Opt.*, vol. 50, pp. C316–C320, Mar 2011. 192

Le détecteur d'ondes gravitationnelles Advanced Virgo : Etude de la configuration optique et développement des miroirs.

Résumé français : Les ondes gravitationnelles ont été prédites par Einstein dans sa théorie de la Relativité Générale. Elles sont des perturbations de l'espace-temps que lon essaie de mettre en évidence par interférométrie laser. Plus précisément les détecteurs sont des interféromètres de Michelson de plusieurs km de long combinés avec des cavités Fabry-Perot afin daugmenter la sensibilité de linstrument. La première génération de détecteurs (Virgo, LIGO, GEO) n'a pas permis d'obtenir une détection directe malgré plusieurs phases d'observations en concidence à la sensibilité prévue. Une seconde génération de détecteurs est actuellement en préparation avec notamment le projet européen Advanced Virgo. Ce détecteur devrait avoir une sensibilité améliorée d'un ordre de grandeur par rapport à linterféromètre Virgo. Les miroirs de l'interféromètre jouent un rôle primordial dans la sensibilité d'Advanced Virgo puisque celle-ci est limitée à dans les fréquences médianes par le bruit thermique des miroirs et aux hautes fréquences par la quantité de photons que lon arrive à collecter dans les cavités de linterféromètre. La haute puissance contenue dans les cavités Fabry-Perot induit des effets de lentille thermique importants. Cette thèse s'intéresse dans un premier temps aux effets de lentille thermique dans linterféromètre pour différentes configurations optiques. Par la suite, nous nous intéresserons aux miroirs qui composent les cavités Fabry-Perot depuis la définition des besoins en termes de planéité à la réalisation de cette planéité et à sa mesure. La planéité de ces miroirs doit tre sub-nanométrique de faon à limiter les pertes optiques dans les cavités Fabry-Perot et ainsi réduire les effets du bruit de photons et de la lumière diffusée. Nous verrons la réalisation de la correction de la planéité des substrats par la technique dite du traitement correctif. Nous étudierons aussi l'uniformité du dépôt des couches minces diélectriques nécessaires à l'obtention de surface hautement réfléchissante avec en particulier l'étude du mouvement planétaire des substrats dans la machine de dépôts.

Mots Clés : ondes gravitationnelles, interférométrie, Advanced Virgo, couches minces, cavité Fabry-Perot, traitement correctif, simulation, métrologie.

The Advanced Virgo Gravitational wave detector: Study of the optical design and development of the mirrors.

Abstract: Gravitational waves have been predicted by Einstein in his General Relativity theory. They are perturbation of the space-time metric and we try to reveal them by laser interferometry. More precisely, gravitational wave detectors are km long Michelson interferometers combined with Fabry-Perot cavities. The network of first generation detectors (Virgo, LIGO, GEO) did not permit a direct detection after several observational runs in coincidence at the nominal sensitivity. A second generation of detectors is in preparation with in particular the European project Advanced Virgo. This detector should have a sensitivity increased by an order of magnitude compared to Virgo. The interferometer mirrors play a crucial role in the Advanced Virgo sensitivity as it is limited by the mirror thermal noise in the mid-frequency region and by the amount of photons collected in the interferometer cavities at high frequencies. The high power circulating in the Fabry-Perot cavities induces important thermal lensing effect. This thesis is interested first in the thermal lensing effect in the interferometer for different optical configurations. Then we are interested in the mirrors composing the Fabry-Perot arm cavity from the calculation of the requirements in terms of flatness to the realization of the mirrors flatness and its measurement. The mirror flatness should be sub-nanometric in order to limit the optical losses in the Fabry-Perot cavities to reduce the effect of the shot noise and of the diffused light. We will see the correction of the substrates flatness by the so-called corrective coating technique. Finally, we study the uniformity of the dielectric multilayer coating deposition necessary to obtained high-reflective mirrors. We study in particular the planetary motion of the substrates in the coating machine.

Key words: gravitational waves, interferometry, Advanced Virgo, thin films, Fabry-Perot cavity, corrective coating, simulation, metrology.

INTITULE ET ADRESSE DE L'U.F.R. OU DU LABORATOIRE :

Laboratoire des Matériaux Avancés (LMA), USR 3264.

7 avenue Pierre de Coubertin

69622 Villeurbanne Cedex